Forschungszentrum Jülich

Institut für Chemie und Dynamik der Geosphäre 2:
Chemie der Belasteten Atmosphäre

Use of airborne CO measurements for Lagrangian analysis of ozone formation and transport in continental plumes

Sandra Schmitgen

Jül-3822

Use of airborne CO measurements for Lagrangian analysis of ozone formation and transport in continental plumes

Sandra Schmitgen

Berichte des Forschungszentrums Jülich ; 3822
ISSN 0944-2952
Institut für Chemie und Dynamik der Geosphäre 2:
Chemie der Belasteten Atmosphäre Jül-3822
D 5 (Diss., Bonn, Univ., 2000)

Zu beziehen durch: Forschungszentrum Jülich GmbH · Zentralbibliothek
D-52425 Jülich · Bundesrepublik Deutschland
☎ 02461/61-6102 · Telefax: 02461/61-6103 · e-mail: zb-publikation@fz-juelich.de

Abstract

The anthropogenic ozone budget is investigated in remote regions with respect to the influence of emissions of VOC and NO_x at source regions, and with regard to the relative roles of ozone formation in the polluted boundary layer (PBL) and in the free troposphere (FT). The investigation makes use of airborne measurements aboard the United Kingdom Meteorological Office (UKMO) C-130 Hercules aircraft obtained during the European project TACIA (Testing Atmospheric Chemistry in Anticyclones) and the UK project ACSOE (Atmospheric Chemistry Studies in Oceanic Environment). High resolution measurements of CO as a quasi-inert tracer of anthropogenic emissions were made and interpreted.

The experimental investigations of anthropogenic plumes in the planetary boundary layer (TACIA) and the remote free troposphere (ACSOE) are interpreted by heuristic model calculations. The model set-up, with modules for transport and chemistry, allows for a separation of these processes in the analysis. The transport module in combination with the CO observations is shown to be a useful tool for the analysis of emissions and transport. Convective transport into the free troposphere is identified by combination of the transport module with satellite data.

The interpretation of observations distant from the source regions, with respect to the influence of anthropogenic VOC and NO_x emissions on the ozone formation in a plume, is made by an indirect inverse modelling approach. The method involves extensive sensitivity studies regarding various initial VOC and NO_x concentrations, in an EKMA framework. Despite the large degree of abstraction, the results of EKMA plot calculations can be compared to the measurements with the help of CO as emission tracer and enable the dependency of the observed O_3 on anthropogenic VOC and NO_x emissions to be analysed.

A central point of this study is the use of statistical test methods for the analysis of the significance of deviations between model results and measurements. Sensitivity studies, regarding the dependence of model results on the variability of input parameters, are analysed with respect to confidence regions of the observations.

With these means, the following general conclusions regarding ozone formation in continental plumes transported into source free maritime areas are obtained:

- The layers of enhanced CO and O_3 in the FT, observed during ACSOE flight A575, can only partly be explained by in-situ production of ozone in the FT. Higher O_3 production efficiencies on a per-molecule basis of NO_x in the FT compared to the PBL are found to be compensated by the reduced NO_x availability in the free troposphere, related to CO. PBL-produced O_3 is found not only to be important close to source regions, but also for long range transport within the FT in connection with cloud venting, where it contributes to the tropospheric budget of ozone.

- The O_3 formation within the PBL depends on a multitude of parameters. It is shown for the example of the TACIA flight A581, that the natural variability and uncertainties of these parameters are still too high for an unambiguous interpretation of observed O_3 formation in a continental plume with respect to anthropogenic NO_x and VOC emissions. This complicates the task of estimating the influence of export of pollution-derived ozone and its precursors on the remote troposphere.

Table of Contents

1 Introduction

Although only 10 percent of the total ozone column is located in the troposphere, tropospheric ozone has a major impact on the global atmosphere because it is a greenhouse gas, and because, in the presence of water vapour, it is the primary source for hydroxyl radicals (OH) [*Logan et al.*, 1981; *Thompson*, 1992]. Hydroxyl radicals are responsible for the oxidative removal of many trace gases that influence climate and/or the stratospheric ozone layer.

Tropospheric ozone has both natural and anthropogenic sources. The primary natural source is intrusion from the stratosphere [*Danielsen and Mohnen*, 1977]. The anthropogenic source is photochemical production from so-called precursors, mainly hydrocarbons, CO and NO_x, emitted by industrial and transportation combustion sources, as suggested for the first time by [*Haagen-Smit*, 1952]. Quantifying this anthropogenic source of ozone and assessing its global influence is a major research topic in tropospheric chemistry.

Recent field studies have shown that anthropogenic emissions of ozone precursors lead to large-scale production of ozone which, through long-range transport in the free troposphere, influences the ozone concentrations in large regions of the troposphere [*WMO*, 1999]. However, significant uncertainties remain in the budget of tropospheric ozone, its precursors, and the chemical and transport processes involved. In remote areas the relative contributions to the budget from ozone exported from the polluted continental boundary layer, as well as ozone produced from long-lived precursors during the transport in the free troposphere, plus eventual intrusion from the stratosphere, are still poorly understood.

The chemical composition of an air mass away from the continental source regions is determined by the anthropogenic emission flux it has received, as well as the meteorological and chemical processing it has undergone. Thus, in order to gain deeper insight into how emissions, and chemical and transport processes influence the formation of ozone in ageing anthropogenic plumes, the relative contributions of these processes have to be distinguished.

This can be achieved by the use of a quasi conservative tracer like the anthropogenic pollutant CO, which is barely reactive (lifetime of about 1 month in summer) and co-emitted with shorter lived ozone precursors, VOC and NO_x, from fossil fuel combustion.

Thus, it can be used as an effective tracer for the transport of anthropogenic emissions, providing the opportunity to learn about the meteorological history of the sampled air parcel as well as the emissions it has received [*Fishman and Seiler*, 1983; *Parrish et al.*, 1991]. This offers a valuable constraint for quantifying the anthropogenic source of ozone.

Within this work, anthropogenic ozone is investigated in remote regions with respect to the influence of emissions of VOC and NO_x, and with regard to the relative roles of ozone formation in the polluted boundary layer and in the free troposphere.

The investigation makes use of airborne measurements aboard the United Kingdom Meteorological Office (UKMO) C-130 Hercules aircraft obtained during the European project TACIA (Testing Atmospheric Chemistry in Anticyclones) and the UK project ACSOE (Atmospheric Chemistry Studies in Oceanic Environment). High resolution measurements of CO as a quasi inert tracer of anthropogenic emissions were made as part of this work during these campaigns.

The experimental investigations of anthropogenic plumes in the planetary boundary layer (TACIA) and the remote free troposphere (ACSOE) are interpreted by heuristic model calculations, which allow for the analysis of the significance of the results. Thus, CO is used for both quantifying the anthropogenic emission input and learning more about the transport of the observed anthropogenic plumes.

2 Theoretical background

The Earth's troposphere acts like a chemical reactor in which emissions of reduced trace gases from various biogenic and anthropogenic sources are transported by winds, turbulence and convection, chemically processed, and converted to products. In contrast to a well stirred reactor, reactants and products are not homogeneously distributed in the atmosphere. Oxidative (i.e. chemical processing) and transport time scales are often of similar magnitude. Thus, for a quantitative understanding of atmospheric chemistry, and especially for the interpretation of trace gas measurements distant from the sources, both transport and chemistry have to be considered, including the coupling between them [*Kley*, 1997].

2.1 Tropospheric photochemistry

The daytime tropospheric chemistry is characterised by degradation of volatile organic compounds (VOC) and other reduced trace gases through oxidation by the hydroxyl (OH) radical in the presence of oxides of nitrogen (NO_x). The most important photooxidant formed in this process is ozone. The photochemistry of ozone formation is well understood in principle. The standard textbook for a review is that by [*Finlayson-Pitts and Pitts*, 1986]. More detailed description of the chemistry is for example given by [*Atkinson*, 1990; *Paulson*, 1995; *Seinfeld*, 1995]. Thus, in this chapter only the basic outlines of the principles necessary to understand the data interpretation shall be presented.

2.1.1 The families of NO_x and O_x

Ozone is produced in the atmosphere by reaction of atomic oxygen ($O(^3P)$) with molecular oxygen. In the troposphere, the principal source for $O(^3P)$-atoms is the photolysis of nitrogen dioxide (NO_2):

(R 2.1) $$NO_2 + h\nu \ (\lambda < 420\,nm) \rightarrow NO + O(^3P)$$

(R 2.2) $$O(^3P) + O_2 + M \rightarrow O_3 + M$$

During daytime the conversion of NO to NO_2 occurs to a large extend through reaction with ozone itself:

(R 2.3) $$NO + O_3 \rightarrow NO_2 + O_2$$

A fast photochemical equilibrium through (R 2.1), (R 2.2) and (R 2.3) between O_3, NO and NO_2 is established on a time scale of 1 to 2 minutes such that

(2.1) $$[O_3] = \frac{JNO_2 \cdot [NO_2]}{k_{NO,O_3} \cdot [NO]}$$

where JNO_2 is the photolysis frequency of NO_2 and $k_{NO, O3}$ is the temperature dependent rate coefficient for the reaction of NO with O_3.

Because of this so-called photostationary state, a family of species called $NO_x = NO + NO_2$ was defined which is conservative with respect to changes in JNO_2 and ozone [*Leighton*, 1961]. In the same way and for the same reason the oxidant O_x was defined as $O_x = O_3 + NO_2$ [*Guicherit*, 1988; *Kley et al.*, 1994]. The rate of inter-conversion between members of a family is far greater than the rate of production or loss of a family member from outside the family. Thus the concept of the chemical family makes it easier to separate production and loss terms from those of conversion.

2.1.2 Photooxidant formation

Figure 2.1 shows a schematic view of the processes relevant to tropospheric ozone production. In order to achieve photooxidant formation, equivalent to a net ozone gain, NO has to be oxidised to NO_2 without consumption of an ozone molecule. This can happen through the reaction of NO with hydroperoxy (HO_2) or organic peroxy radicals (RO_2). The peroxy radicals again are formed during the oxidation of VOC, and other reduced trace gases, with the hydroxyl (OH) radical. The principal reaction scheme is illustrated by the oxidation of alkanes (abbreviated as RH). Carbonyl products are denoted R'CHO where R' denotes an organic fragment having one carbon atom fewer than R [*Brasseur et al.*, 1999].

(R 2.4) $$RH + OH \rightarrow R + H_2O$$

(R 2.5) $$R + O_2 + M \rightarrow RO_2 + M$$

(R 2.6) $$RO_2 + NO \rightarrow RO + NO_2$$

(R 2.7) $$RO + O_2 \rightarrow HO_2 + R'CHO$$

(R 2.8) $$HO_2 + NO \rightarrow OH + NO_2$$

(R 2.9) $2(NO_2 + h\nu \rightarrow NO + O(^3P))$

(R 2.10) $2(O(^3P) + O_2 + M \rightarrow O_3 + M)$

Overall: $RH + 4O_2 + h\nu \rightarrow R'CHO + H_2O + 2O_3$

Carbonyls produced in reaction (R 2.7), can photolyse to produce additional peroxy radicals which react with NO and, in turn, may increase the yield of ozone per oxidised RH.

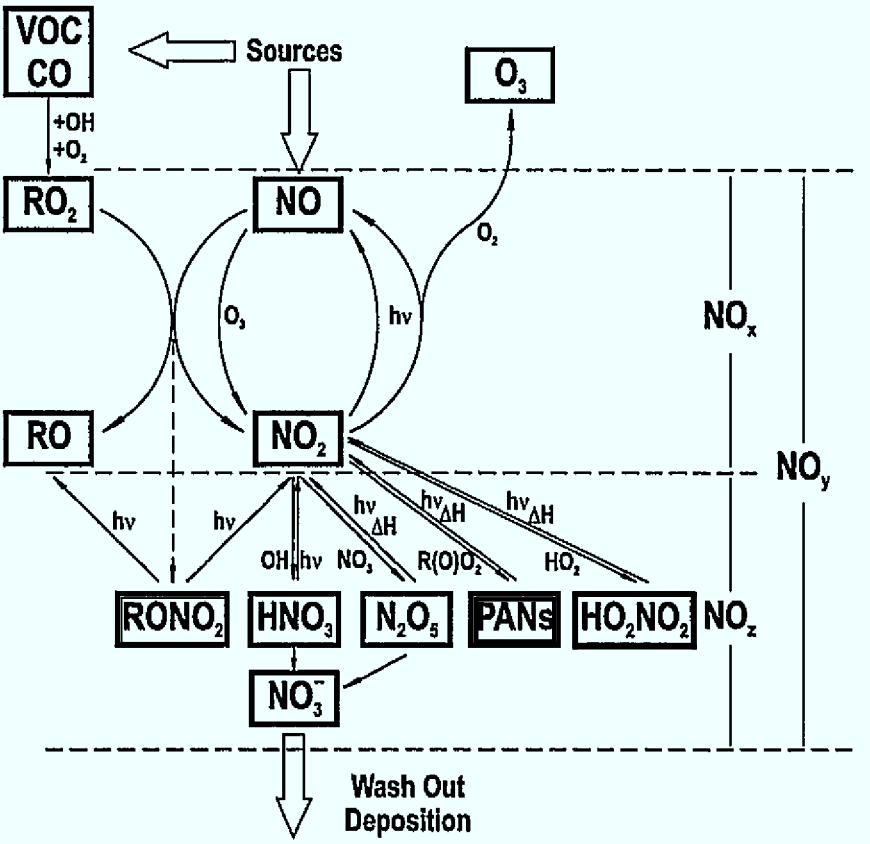

Figure 2.1: Schematic view of photochemical ozone production in the presence of VOC and NO_x (from [*Volz-Thomas et al.*, 1995])

VOC, CO and NO_x are commonly referred to as ozone precursors. Because of its long lifetime (compare chapter 2.3) CO becomes important in remote regions with very small availability of VOC. In this work it can be neglected as an ozone precursor compared to VOC, which react much faster with OH. As illustrated in Figure 2.1, the degradation of VOC produces free radicals, which in the presence of radiation form O_3 in the NO_x cycle. Thereby, VOC are consumed while NO_x acts as a catalyst. However, there are simultaneous reactions in the atmosphere that consume NO_x. An important loss for NO_2 and radicals is the reaction of NO_2 with OH. The product nitric acid is readily removed from the atmosphere through wet and dry deposition.

(R 2.11) $NO_2 + OH + M \rightarrow HNO_3 + M$

In Figure 2.1 the sum of all oxidised nitrogen species is referred to as NO_y, which is subdivided into the photochemical active NO_x and its oxidation products NO_z. However, not all NO_z species are subject to deposition. They can also act as a reservoir of NO_x and RO_2 radicals. Especially peroxyacetylnitrate (PAN), which forms during the oxidation of hydrocarbons in presence of NO_2, can be transported over long distances in the free troposphere because of its long lifetime at low temperatures. By photolysis or thermally decomposition at warmer temperatures PAN releases NO_x and RO_2 back into the reactive VOC/NO_x system [*Seinfeld*, 1995].

(R 2.12) $$CH_3C(O)O_2NO_2\ (=PAN) + M \rightleftharpoons CH_3C(O)O_2 + NO_2 + M$$

2.1.3 Relative roles of VOC and NO_x in ozone formation

The dependence of ozone formation on the ratio of VOC to NO_x is usually presented by an ozone isopleth plot. These so-called EKMA (Empirical Kinetic Modelling Approach) diagrams go back to the nineteen-seventies when they were first used by the U.S. Environmental Protection Agency (EPA) to asses the effect of NO_x and VOC emission control strategies on ozone formation [*Dodge*, 1977]. Figure 2.2 gives a typical EKMA plot showing peak ozone concentrations as function of initial VOC and NO_x concentrations.

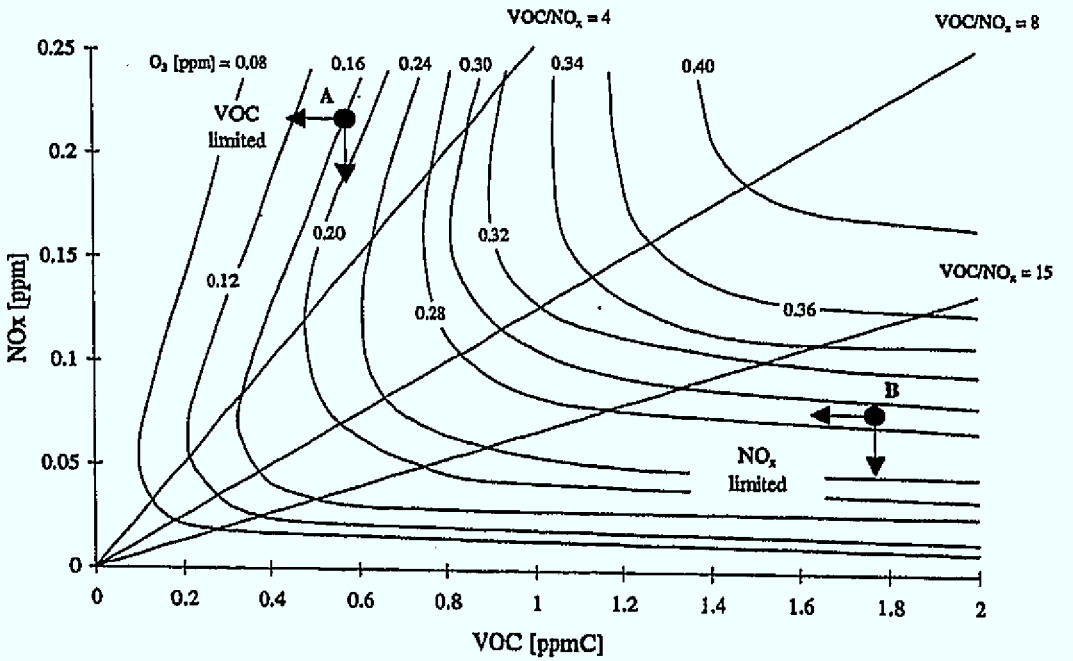

Figure 2.2: Example of an ozone isopleth diagram illustrating calculated peak ozone concentrations generated from different initial VOC/NO_x ratios. The straight lines denote different initial VOC/NO_x ratios [*Dodge*, 1977]

The plot shows that for low VOC/NO_x ratios (e.g. point A), ozone increases with increasing VOC and decreases with increasing NO_x. This regime is called VOC-limited or NO_x-saturated. In contrast, for high VOC/NO_x ratios, referred to as the NO_x-limited regime, ozone increases with increasing NO_x and shows relatively little change in response to increased VOC (e.g. point B).

In the following the highly non-linear process of ozone formation in relation to NO_x and VOC shall be discussed, mainly following [*Sillman*, 1999].

The whole chain reaction of ozone formation is radical driven, whereby the hydroxyl radical is the key reactive species. The initial attack of VOC by OH is typically the rate-limiting step in the degradation cycle [*Seinfeld*, 1995]. The split into NO_x-limited and VOC-limited regimes is closely associated with sources and sinks of radicals [*Sillman*, 1999].

Free radicals are formed by photolysis of ozone itself, formaldehyde and other intermediate organics:

(R 2.13) $O_3 + h\nu \xrightarrow{[H_2O]} 2\,OH + O_2$

(R 2.14) $HCHO + h\nu \xrightarrow{[2O_2]} 2\,HO_2 + CO$

They are removed by reactions that produce peroxides and nitric acid:

(R 2.15) $HO_2 + HO_2 \rightarrow H_2O_2 + O_2$

(R 2.16) $RO_2 + HO_2 \rightarrow ROOH + O_2$

(R 2.11) $OH + NO_2 + M \rightarrow HNO_3 + M$

When HNO_3 represents the dominant sink for HO_x = OH + HO_2, the OH concentration is determined by the equilibrium of reactions (R 2.13) and (R 2.11) and thus decreases with increasing NO_x. In this case the initial attack of VOC by OH (R 2.4) is the rate-limiting step in the ozone formation, which consequently increases with increasing VOC and decreases with increasing NO_x. This is the VOC-limited regime. When peroxides represent the dominant sink for free radicals, the sum of HO_2 + RO_2 is relatively insensitive to changes in NO_x or VOC. The rate of ozone formation, approximately equal to the rate of reactions (R 2.6) and (R 2.8), increases with increasing NO_x and is largely unaffected by VOC. This is the NO_x-limited regime.

From this argument it follows that the rate of formation of peroxides relative to the rate of formation of HNO_3 is closely associated with the split between NO_x- and VOC-limited

regimes. That provides the basis for using peroxides and nitric acid as "indicators" for NO_x-VOC chemistry [*Sillman*, 1995].

Nevertheless, NO_x-VOC chemistry is not only affected by the initial ratio of VOC/NO_x as illustrated by isopleth plots, but also by other factors which are mainly: the reactivity of the VOC mix where the role of biogenic hydrocarbons adds additional uncertainty, the extent of photochemical ageing, and meteorological parameters like available sunlight and water vapour concentration.

2.1.4 Ozone destruction

Just as ozone can be photochemically produced in the troposphere, it can be destroyed. The photolysis of O_3 in the presence of water vapour (R 2.13), the main source of OH radicals, is at the same time one of the most important sinks of ozone ([*Liu et al.*, 1980]). In the Planetary Boundary Layer (PBL), particularly in the tropics where the water vapour concentrations are the highest, the photolysis of ozone is the dominating loss process. In NO-poor environments the loss rate of ozone is enhanced because oxidation of carbon monoxide to carbon dioxide by the OH radical produced in (R 2.13) in turn leads to destruction of another ozone molecule [*Crutzen*, 1979]:

(R 2.17) $\quad CO + OH \rightarrow H + CO_2$

(R 2.18) $\quad H + O_2 + M \rightarrow HO_2 + M$

(R 2.19) $\quad HO_2 + O_3 \rightarrow OH + 2\,O_2$

Net: $\quad CO + O_3 \rightarrow CO_2 + O_2$

These reactions constitute a cycle that destroys CO and O_3 molecules without loss of HO_x radicals. At low water vapour concentrations (that is with increasing altitude), the loss reaction of ozone with HO_2 becomes more likely than the photolysis, which is a sink for O_3 only in presence of water vapour.

In more polluted regions the destruction of NO_2 with OH (R 2.11), followed by wet and dry deposition of HNO_3, adds to the loss of ozone. Due to the fast equilibrium (2.1) between O_3 and NO_2, the loss of NO_2 is then equivalent to a loss of ozone. This loss can be effective in polluted regions with NO_x concentrations large enough that a significant fraction of O_3 is tied up as NO_2 [*Kley*, 1994].

In addition to chemical reactions and photolysis, ozone is removed from the atmosphere by dry and wet deposition. Ozone is a non-specific oxidiser so that most solid surfaces act as ozone sinks. The deposition velocity of ozone depends on the surface type as well as meteorological parameters, and thus it is found to vary strongly. Generally, the deposition of ozone over land is nearly an order of magnitude faster than over water surfaces, thus deposition is one of the important loss processes for ozone in the continental PBL.

2.2 Atmospheric dynamics

The Earth's atmosphere is in a continual state of motion. It systematically circulates, with material moving from one place to another. This circulation has important implications for atmospheric chemistry in the transport and diffusion of trace constituents through the atmosphere. Atmospheric dynamics influence the trace gas composition of the troposphere over a large range of length and time scales. While molecular diffusion can be neglected, the effect of large scale advection, turbulent mixing and convective transport on trace gas distributions will be discussed in the following.

2.2.1 Large scale advection

Primarily, the atmosphere is set into motion by variations and local imbalances of the radiation budget of the atmosphere. In the tropics, the absorbed solar radiation per unit area exceeds the outgoing infra-red radiation, while in the polar latitudes there is less incoming radiation than is lost to space. These local imbalances in the radiation budget are compensated by dynamic transports of heat within the atmosphere and oceans [*James*, 1996].

Figure 2.3 shows the nature of the general circulation of the atmosphere. Besides the thermal circulation, its mean pattern is determined by the so-called Coriolis force, an effect associated with the Earth's rotation. At either side of the equator a thermal circulation is located in which warm tropical air rises and cool air at low altitudes flows towards the equator from higher latitudes. As the uplifted air flows poleward, it cools by radiation. At about 30° latitude in both hemispheres the cooled denser air subsides, closing the so-called Hadley circulation. The Coriolis effect on these cells leads to easterly winds, called the trade winds. The same situation occurs in the polar regions, in which warm air from the temperate zone moves northward in the upper levels, eventually cooling by radiation and subsiding at the poles.

Between roughly 30° and 60° N and S lies the midlatitude region, where influences of both tropical and polar regions are felt. The flows there are far less ordered than in the tropics because of strong influences by wandering high and low pressure systems. In the midlatitudes, much of the poleward heat transfer is accomplished by the movement of tropical and subtropical air masses toward the poles and of polar air masses toward the equator. The zones of contact between air masses are termed warm fronts and cold fronts, the designation depending on the nature of the air masses being advected. In these frontal regions, redistribution of lower and upper troposphere air masses can occur, causing important changes in the background photochemistry (e.g. [*Bethan et al.*, 1998]).

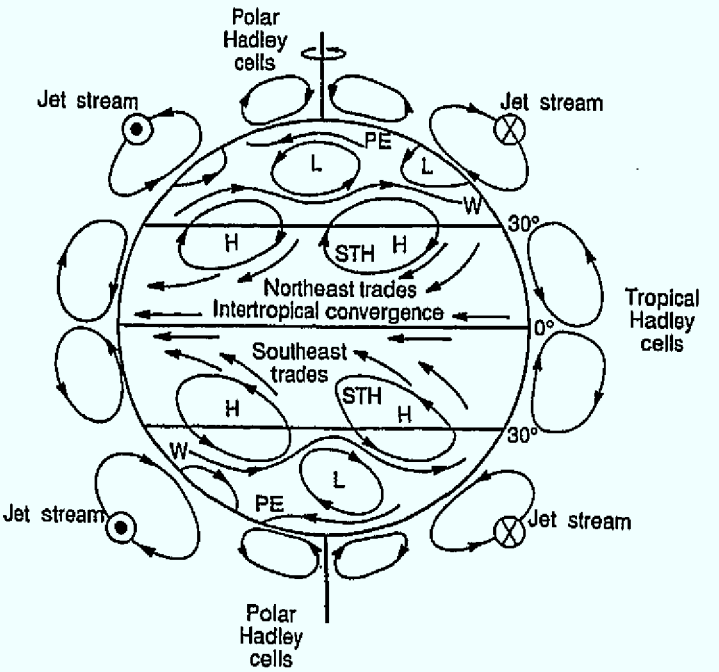

Figure 2.3: Principal features of the atmospheric circulation. The highs (H) and lows (L) are primarily lower atmospheric features, whereas the Hadley cells can extend vertically as much as 10 to 20 km throughout the troposphere and partially into the stratosphere. W, westerlies; PE, polar easterlies; STH, subtropical highs. [*Graedel and Crutzen*, 1993]

Again due to the Coriolis forces, air which converges towards low pressure systems will produce an inward spiraling motion, termed cyclonic circulation. Similarly, a flow diverging from a high pressure region will spiral outward. Such a region is called anticyclone. In the Northern Hemisphere the motion of air is counterclockwise around a cyclone and clockwise around an anticyclone.

In the temperate regions like Europe, there are many migratory cyclones and anticyclones. These have a lifetime of a few days, dimensions of some 100 to 1000 km, and drift with the general westerly flow in these regions. Cyclones are usually associated with rising air

ahead of the low pressure centre, often leading to strong winds, cloudy skies and precipitation, which leads to wash out and deposition of trace gases[1]. On the other hand, anticyclones are characterised by subsidence and adiabatic warming of the air, leading to clear skies, light winds and fair weather. Thus it is the anticyclonic conditions which favour the build up of high levels of ozone in the midlatitudes, due to the accumulation of precursors in the stable conditions, accompanied by high photolysis rates associated with clear skies.

Besides the development of weather systems, these so-called synoptic scale processes mainly affect atmospheric chemistry by advective transport, which may import trace species that originated far away.

2.2.2 Turbulence and mixing

Besides advective transport along large scale wind fields, the development of trace gas concentrations strongly depends on their dispersion in the atmosphere. Dispersion is largely determined by the fact that the atmospheric flow is turbulent. Regarding turbulence, the troposphere can be distinguished into two main layers. The planetary boundary layer (PBL) is defined as the turbulent domain of the atmosphere adjacent to the ground, in which the flow field is strongly influenced directly by interaction with the surface of the earth [*Holton*, 1992]. In the free troposphere (FT), i.e. the region above the PBL, turbulence can mainly be ignored in an approximate treatment of synoptic-scale motions, with the exception of jet streams, fronts and convective clouds[2].

The influence of the surface in the boundary layer leads to the development of turbulent eddies. Such shear-induced eddies, caused by the strong velocity shear of winds near the surface, together with convective eddies caused by surface heating, transfer momentum to the surface and transfer heat (sensible and latent[3]) away from the surface. Eddies cause nearby air parcels[4] to drift apart and thus mix properties like momentum, potential temperature, water vapour and trace gases across the boundary layer. The depth of the planetary boundary layer may range from as little as 30 m in conditions of large static sta-

[1] Compare Figure 2.1
[2] Compare chapter 2.2.3
[3] The excess surface heat can be transferred to the atmosphere either directly as 'sensible heat' or indirectly as 'latent heat' by evaporation of water, which releases the heat again when the water vapour condenses.
[4] An 'air parcel' is regarded as a volume element that is very small compared with the volume of the atmosphere, but still contains a large number of molecules.

bility[5] to more than 3 km in highly convective conditions. Turbulent eddies in the PBL have similar scales in the horizontal and vertical. The maximum eddy length scale is thus limited to a few kilometers by the boundary layer depth.

If a convective boundary layer is topped by a stable layer, turbulent mixing can lead to formation of a well mixed layer. Such boundary layers occur commonly over land in anti-cyclonic conditions during the day when the surface heating by the sun is strong and results in convective turbulence. In a well mixed boundary layer the wind speed and potential temperature are nearly independent of height. Trace constituents, which are almost all released at or close to the surface, become vertically dispersed over the height of the mixed layer, called mixing height (MH), within a time scale of about an hour [*Seibert et al.*, 2000]. Further transport into the free troposphere is strongly suppressed by the barrier of the stable layer in between.

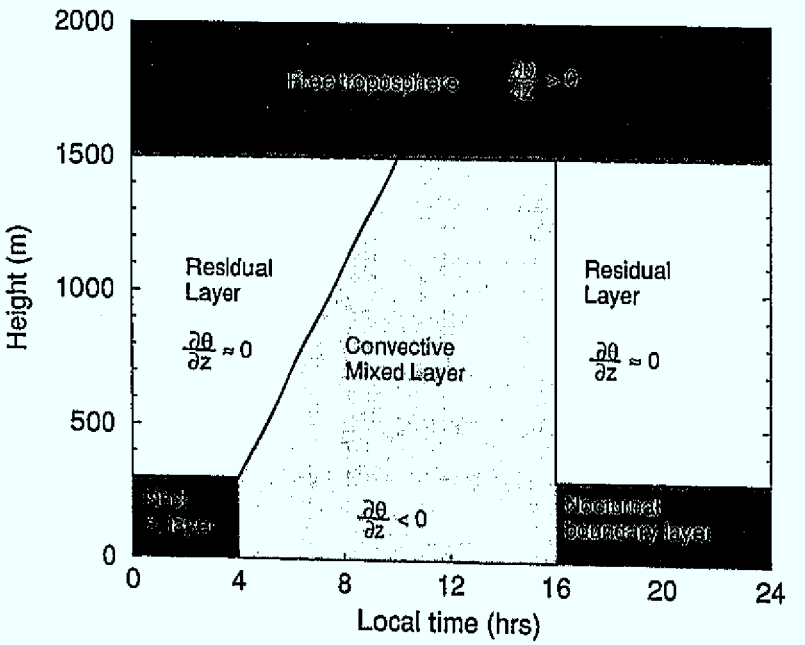

Figure 2.4: Diurnal cycle in the planetary boundary layer height. Figure is after [*Stull*, 1988].

During the night the land surface cools by radiation, thus suppressing turbulence, and a stable boundary layer develops where the potential temperature gradient is positive. The

[5] A dry atmosphere is called statically stable, if a rising air parcel is cooler than its surroundings, thus tending to return to its origin. Provided adiabatic rise of the air parcel, i.e. without heat exchange with the surroundings, this criterion is equivalent to an increase of the potential temperature of the surrounding air with height. Thereby the potential temperature θ is the temperature that a parcel of dry air would have if it were expanded or compressed adiabatically to a standard pressure (usually taken as 1000 mb).

statically stable: $d\theta/dz > 0$

statically unstable: $d\theta/dz < 0$

height of the nocturnal boundary layer is limited to a few hundred meters. The overlying air, which is separated from the nocturnal boundary layer by an inversion, is slightly stable or statically neutral. During the development of the daytime mixed layer, the night-time neutral layer air is incorporated into the convective layer up to the daily maximum height of the mixed layer. Because of this re-incorporation, the night-time layer is called the residual layer. Figure 2.4 shows a sketch of the diurnal variation over land of the planetary boundary layer.

2.2.3 Vertical transport and convection

The preceding section has focused on how emissions released at, or close to, the surface can be effectively mixed within the PBL. This section is concerned with vertical transport of trace gases throughout the free troposphere. Global estimates suggest that the entire PBL is vented about 90 times a year [*Cotton et al.*, 1995], with a large fraction of the vented air reaching the upper troposphere.

Above the PBL the potential temperature normally increases with height, thus inhibiting further vertical mixing. In this case vertical transport of trace gases in the free troposphere is limited to synoptic scale motions, which typically have a vertical velocity component of the order of a few centimetres per second [*Holton*, 1992]. Thus vertical mixing throughout the free troposphere takes about 1 month on average [*Kley*, 1997]. However, vertical transport can occur within 1 hour when moist boundary layer air is lifted to the upper troposphere in the cores of convective cumulus clouds. Convective clouds appear as isolated thunderstorms or convective systems, as well as along frontal regions of extratropical cyclones. Associated with the latter are organised flows of ascending air ahead of the surface warm front (cold conveyor belt), respectively ahead of the surface cold front (warm conveyor belt) which can transport boundary layer air in the upper troposphere [*Bethan et al.*, 1998; *Stohl*, 2000]. Nevertheless, the efficient vertical transport of pollutants in conjunction with frontal systems is largely dominated by the presence of clouds [*Chaumerliac et al.*, 1992], which is discussed in more detail below.

If a parcel of moist air is forced to rise, it will eventually become saturated. A further forced rise will then cause condensation and latent heat release, with a result that the temperature of the parcel decreases less with increasing altitude than for a dry air parcel. Thus the parcel may reach a level where it becomes warmer relative to its environment and can

freely accelerate upwards. The level at which this occurs is called the level of free convection (LFC) [*Holton*, 1992]. This moist convection leads to the development of high cumulus clouds, which are generally composed of a number of short lived rising towers, produced again by elements of ascending buoyant air called thermals. Rising thermals are highly turbulent and entrain environmental air, thus modifying the cloud air through mixing. As convective storms can range in scale from isolated thunderstorms to large mesoscale convective complexes (MCCs), the fraction of boundary layer air pumped into the free troposphere by convective cells varies. Transport of large quantities of relatively undiluted boundary layer air has been observed [*Dickerson et al.*, 1987], as well as cells which draw air from only above the boundary layer [*Pickering et al.*, 1988]. Figure 2.5 shows the vertical redistribution of a boundary layer tracer as simulated by the Goddard Cumulus Ensemble Model [*Tao and Simpson*, 1993] for a prototype convective event [*Thompson et al.*, 1994]. In this case some boundary layer air is transported as high as 15-16 km, and a peak in the redistributed tracer appears from 8 to 10 km, whereby the overall fraction of PBL air transported to the free troposphere is around 45% .

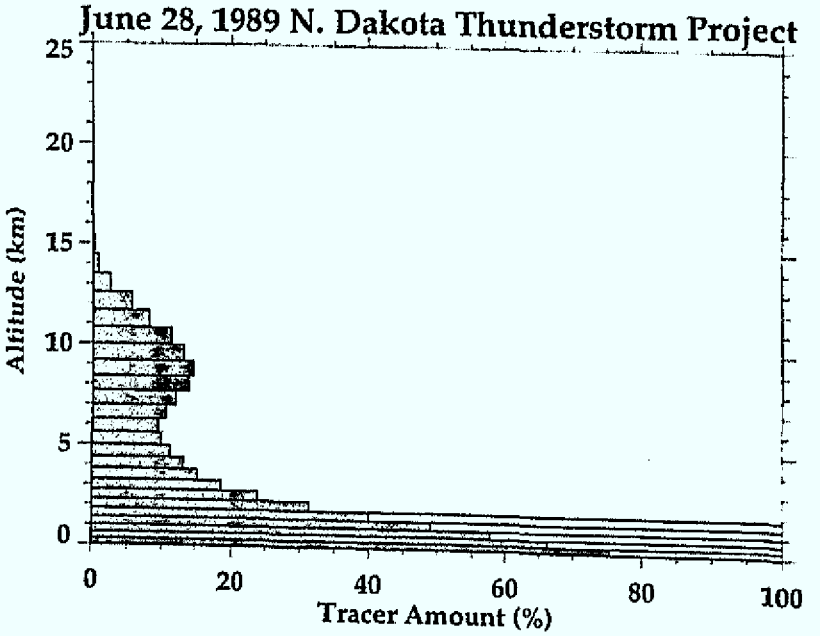

Figure 2.5: Vertical redistribution of boundary layer tracer for the June 28, 1989, North Dakota Thunderstorm Project (NDTP) convective event as simulated by the Goddard Cumulus Ensemble Model. Values of tracer were initially set to 100% in each of the five sublayers comprising the boundary layer, as indicated by the open bars. Shaded bars represent the distribution after 2.5 hours of simulated convective redistribution. [*Thompson et al.*, 1994]

Convective clouds are one of the most effective mechanisms for transporting O_3 and O_3 precursors (NO_x, VOC, CO) to the free troposphere (e.g. [*Gidel*, 1983; *Lelieveld and Crutzen*, 1994]). This has important consequences for the global tropospheric ozone distri-

bution. While soluble gases, such as HNO_3 and H_2O_2, are mainly washed out during the transport, the insoluble O_3 precursors, once transported to the free troposphere by convection, can enhance the production of O_3 in the middle-to-upper troposphere. Ventilation of highly polluted boundary layer air transports NO_x to the layers with lower mixing ratios, where after dilution it can produce O_3 more efficiently on a per-molecule basis [*Liu et al.*, 1987]. The resulting O_3 can spread over large geographic regions, rather than being confined to the PBL where loss processes are much more rapid [*Pickering et al.*, 1992].

2.3 Significance of CO in tropospheric chemistry and transport

Carbon monoxide (CO) plays several important roles in the troposphere. It has long been recognised as a major urban air pollutant and in high concentrations is known to adversely affect health [*Seinfeld*, 1986]. Furthermore, in remote regions CO provides one of the important precursors to photochemical ozone production, or, depending on the local abundance of nitrogen oxides, participates in reactions that decrease ozone[6] [*Logan et al.*, 1981]. On a global scale, through its reaction with the hydroxyl (OH) radical, CO is a critical component in the troposphere's overall oxidative capacity [*Crutzen and Zimmerman*, 1991]. The reaction with OH, (R 2.17), is the primary removal process of CO from the atmosphere, which is slow enough that the lifetime of CO is of the order of 1-3 months [*Parrish et al.*, 1991; *Seinfeld*, 1986].

Global atmospheric CO concentrations show spatial variations with respect to latitude, altitude and oceans versus continents [*Conny*, 1998]. Surface mixing ratios in the remote southern Hemisphere are more spatially uniform than in the northern hemisphere with average values near 40-60 ppb. In the northern hemisphere, higher average CO concentrations of typically 90-200 ppb are reported [*Novelli et al.*, 1992], with much more spatial and temporal variability and up to several ppm in polluted cities [*Röckmann et al.*, 1998]. The gradients in the CO distribution reflect interhemispheric differences in the CO sources, which are mainly located in land areas of the northern hemisphere, as well as differences in the removal rates depending on the available OH concentrations.

The major emission sources of CO are well known, although the exact magnitudes and distributions are still relatively uncertain. The principal sources are emissions from fossil fuel combustion and other industrial activities, and production in the atmosphere during the

[6] e.g. (R 2.17) – (R 2.19)

oxidation of methane and higher hydrocarbons, of both natural and anthropogenic origin. Less important sources include direct emissions from the oceans and from vegetation [*Warneck*, 1988]. On a global scale contributions from CH_4 oxidation, fossil fuel combustion, biomass burning and biogenic hydrocarbon oxidation exhibit similar emission rates [*Khalil and Rasmussen*, 1990; *Muller*, 1992]. Nevertheless, besides the CH_4 oxidation which leads to a global background of approximately 35 ppb CO [*Saylor et al.*, 1999], the significance of the major CO sources depends strongly on the geographical region and season. As shown by regional CO emission estimates from 1 September to 15 October 1984 in Table 2.1 [*Saylor et al.*, 1999], biomass burning and oxidation of biogenic hydrocarbons have strong impact on the CO emissions in equatorial regions, while the CO emissions of North America and Europe are dominated by anthropogenic fossil fuel combustion.

Table 2.1: Global CO emissions (Tg CO) estimates for major emission categories from 1 September to 15 October 1984 [*Saylor et al.*, 1999]. Fossil fuel and industrial also includes CO resulting from oxidation of anthropogenic hydrocarbons, while biogenic hydrocarbons includes CO from the oxidation of biogenic hydrocarbons and direct emissions of CO from plants. CH_4 oxidation is not included in the table.

Region	Fossil fuel and industrial	Biomass burning	Biogenic hydrocarbons	Regional totals
North America	27.4	0.0	5.2	32.6
South America	3.3	17.8	18.8	39.9
Europe	25.2	0.0	1.0	26.2
Africa	4.4	27.8	13.2	45.4
Asia-Oceania	24.4	2.6	14.4	41.4
Total	84.7	48.2	52.6	185.5

The long tropospheric lifetime of CO, together with its mainly anthropogenic sources in Europe and North America, allows it to be treated as a nearly inert tracer for recent anthropogenic emissions of CO [*Fishman and Seiler*, 1983]. Hence, use can be made of the fact that there is a correspondence between the amount of CO and the shorter lived ozone precursors VOC and NO_x emitted from fossil fuel combustion according to emission inventories. Thus, measurements of CO simultaneous with other atmospheric species provide the opportunity to learn about the history of the sampled air parcel, both with regard to the emissions that it has received and the photochemical transformation to which it has been subjected [*Parrish et al.*, 1991].

The measurement of such a tracer becomes especially important for the analysis and interpretation of airborne trace gas measurements in the context of the approximately similar

time scales of tropospheric chemistry and transport processes, as discussed before. When the observation area is far away from the source regions, the knowledge of the history of the air masses (including origin, anthropogenic and biogenic emission input) as well as the relative importance of mixing and dilution compared to the chemical reaction rates, becomes essential. In this work the use of airborne CO measurements for Lagrangian analysis of the history of the measured air parcels will be presented.

3 Experimental

As part of this work, airborne measurements of CO were conducted during the atmospheric chemistry projects TACIA and ACSOE in August and September 1997. Both campaigns were centred around measurements aboard the research aircraft Hercules C-130, which is owned and maintained by the Meteorological Research Flight (MRF) of the United Kingdom Meteorological Office (UKMO).

3.1 Instrumentation

The aircraft is a converted military transport plane that, due to its large size (36.6 m length) and payload capability (~17 tons), allows the installation of many instruments measuring the composition of the atmosphere simultaneously. It has a typical ceiling altitude of 10000 m, and a minimum altitude of about 15 m over the ocean. The speed is typically 150 m/s for transits and 100 m/s for measurements. Profile descents and ascents are flown at constant airspeed and rate of descent (ascent). The latter being typically 300 m/min above 1500 m and 150 m/min below this altitude. Special air sample pipes (inner diameter ~ 8 cm) are installed at both sides of the aircraft with about 30 cm distance to the walls, to avoid any contamination of the probed air by contact with the aircraft skin.

3.1.1 Measurement of CO

Airborne measurement of carbon monoxide as a tracer requires rapid time response with high precision [*Albritton et al.*, 1990]. The precision should be sufficient to detect aged air masses with CO concentrations only a few parts per billion in excess of the atmospheric background in the free troposphere. At the same time, a fast response instrument is needed to investigate atmospheric structures on small spatial scales. Of the techniques used so far, only tunable diode laser absorption spectroscopy (TDLAS) [*Sachse et al.*, 1987], and resonance fluorescence (RF) in the fourth positive band of CO (hereinafter denoted VURF) [*Gerbig et al.*, 1996; *Volz and Kley*, 1985], yield sufficient sensitivity with a time resolution of 1s, to fulfil these requirements. One significant advantage of the VURF instrument is its much simpler operation compared to the TDLAS method. *Gerbig et al.* [1999b] give a detailed description of the VURF instrument deployed aboard the UK Met Office C-130 aircraft. Therefore, only a short overview over the instrument and its performance during the TACIA and ACSOE campaigns is presented here.

3.1.1.1 The CO instrument

The basic mechanism of the CO measurements by RF in the fourth positive band of CO is given by the reactions (R 3.1) to (R 3.3). After excitation (R 3.1) the CO molecules are deactivated by fluorescence (R 3.2) or by collision with other molecules, for example N_2 and O_2 (R 3.3).

(R 3.1) $$CO(X^1\Sigma, v''=0)+h\nu \rightarrow CO(A^1\Pi, v')$$

(R 3.2) $$CO(A^1\Pi, v')\rightarrow CO(X^1\Sigma, v'')+h\nu$$

(R 3.3) $$CO(A^1\Pi, v')+M \rightarrow CO(X^1\Sigma, v'')+M$$

A schematic of the VURF instrument as deployed on the Hercules C-130 is shown in Figure 3.1. The instrument consists of three principle components: a CO resonance radiation source, an optical filter, and a sample fluorescence detection cell.

Radiation from a CO resonance lamp, employing a RF discharge in a mixture of 0.25 % CO_2 in Argon, is used to electronically excite ambient CO. The appropriate wavelength interval around 150 nm is selected in an N_2-purged optical filter consisting of two dielectric coated mirrors in combination with two CaF_2 lenses, which image the lamp into the fluorescence chamber. Suprasil optics image the fluorescence radiation onto the PMT cathode, where it is detected at a right angle to the excitation radiation.

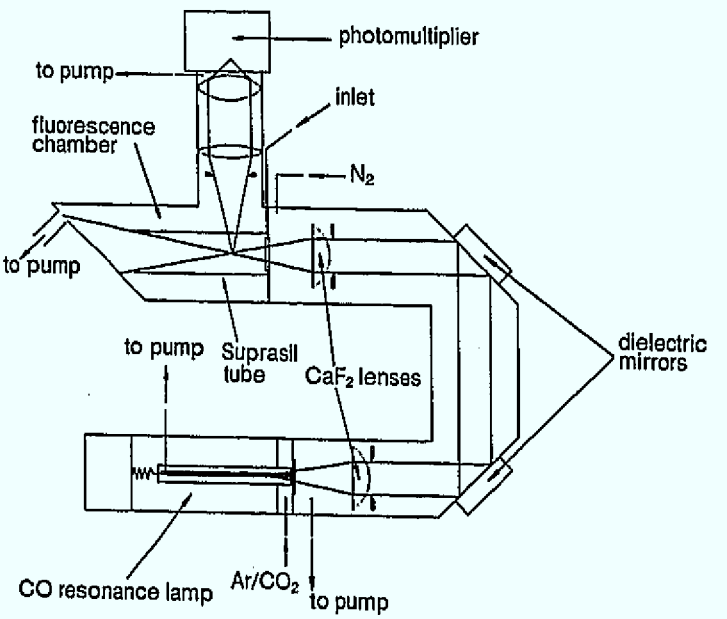

Figure 3.1: Schematic of the VURF instrument [*Gerbig et al.*, 1999b]

The intensity of the fluorescence radiation, Φ_{fl}, is given by:

$$\Phi_{fl} = A \cdot \frac{\sigma_{CO} \Phi_{ex} [CO(X^1\Sigma)]}{1 + k_q[M] \cdot \tau} \tag{3.1}$$

where A is a proportionality constant, representing the geometry of the imaging system, σ_{CO} is the absorption cross section of CO, Φ_{ex} is the intensity of the exciting radiation, $[CO(X^1\Sigma)]$ is the concentration of CO in the ground state[7], k_q is the rate constant of the quenching reaction (R 3.3), [M] is the concentration of collision partners, and τ is the radiative lifetime of the excited state.

The pressures in the chamber and the lamp, the flow rates of CO_2/Ar and nitrogen through the lamp and optical filters, as well as the temperatures of lamp, fluorescence chamber and PMT, are stabilised to avoid their influence on the resonance fluorescence signal. With the intensity of the excitation radiation constant, the fluorescence radiation is then proportional to the CO concentration. Nevertheless the counting rate measured by the PMT consists not only of the resonance fluorescence from CO, but also of a background signal, which is determined by the sampling of CO-free air. In addition to stray light, e.g. from the walls of the fluorescence chamber, continuum resonance Raman scattering by oxygen molecules is the principal source of the instrument background [*Gerbig et al.*, 1996]. Since this Raman background has a similar spectral distribution to the CO fluorescence, this effect places a physical limit on the precision of the fluorescence measurement technique.

Figure 3.2 shows the gasflow system of the VURF instrument aboard the Hercules C-130. The sample gas is taken from the starboard air sampling pipe (ASP) of the aircraft using a PFA tube with 1/8 inch OD and a length of about 15 m. The pressure in the fluorescence chamber is controlled by a piezo-driven valve close to the ASP at 7.5 ± 0.1 mbar for ambient pressures between 1013 and 175 mbar, which keeps the variation of the CO signal below 0.5 %. To avoid interference of atmospheric water vapour due to absorption of the fluorescence radiation (a mixing ratio of 2 % H_2O causes a decrease in the fluorescence signal of 10 %), the sampled air is dried by passing it over a bed of Drierite ($CaSO_4$ with humidity indicator).

[7] For the employed intensity of the exciting radiation the partition of CO in excited states can be neglected

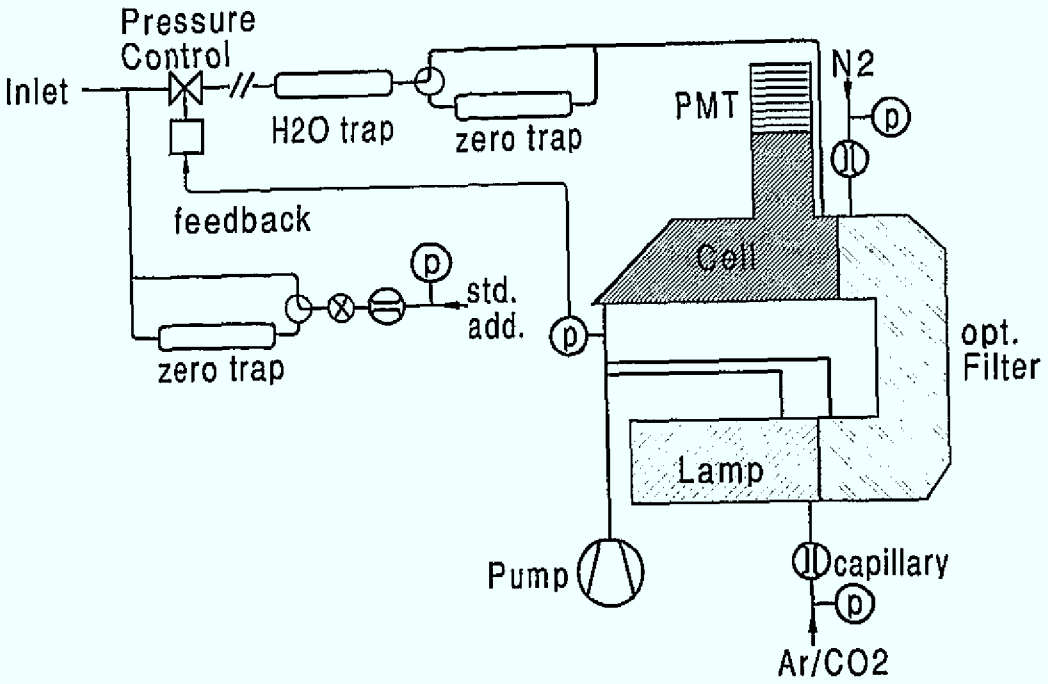

Figure 3.2: Schematic of the pipe layout used for the CO detector deployed on Hercules C-130.

In situ calibration of the instrument is achieved by injecting a standard (440 ppb CO in air) into the sampling line close to and upstream of the control valve, at flow rates slightly higher than the sample flow rate. The in-flight standard was compared with a primary standard (1 ppm in air; Messer Griesheim) before each flight. To determine the background signal, the calibration standard was passed through a Hopcalite scrubber, which quantitatively removes CO to levels < 1 ppb. In addition the background signal is determined by switching a Hopcalite scrubber into the sample flow between the inlet tube and the fluorescence chamber. This enables detection of possible errors due to leaks within the inlet tube or the water trap.

3.1.1.2 Performance during the campaign

In Table 3.1 the performance of the CO instrument during the intensive flying periods of TACIA and ACSOE is summarised. In-flight calibrations and zeros lasting roughly 3 minutes (including about 1 minute for additional internal zero measurement) were performed about every 20-30 minutes during level runs between the profiles. This yields a maximum data coverage of about 90 % which was approximately reached during most of the flights.

On average the accuracy during the TACIA and ACSOE project in Summer 1997 was 3.0 ppb for 100 ppb and 1 s data. The overall accuracy depends on the accuracy of the calibration standard as well as on the precision. The precision was calculated from background and sensitivity drift during each flight (ca. 1.2 ppb), and from the statistical error deter-

mined by counting statistics. On the assumption that the counting rates follow poisson statistics, the statistical error is given by the square root of the counting rate itself (ca. 1.6 ppb). The accuracy of the calibration standard is given by the accuracy of the primary standard (2 %, specification by Messer Griesheim), and the error in the comparison between in-flight standard and primary standard (1 %).

Table 3.1: Overview of CO instrument measurement characteristics during TACIA and ACSOE in 1997

Flight No	Data coverage [%]	Accuracy @ 100 ppb and 1s [ppb]	Background [ppb]
A569	88	3.4	67
A570	85	3.0	68
A571	89	3.0	65
A572	86	3.0	64
A574	84	2.9	66
A575	84	3.1	64
A576	80	3.2	65
A577	88	3.0	64
A579	87	3.2	63
A580	85	2.9	63
A581	89	3.0	63
total	**86**	**3.0**	**65**

3.1.1.3 Intercomparison with NOAA WP-3

An interaircraft instrument intercomparison was conducted during the ACSOE flight A577 on 18 September in the central Atlantic between the U.K. Meteorological Office C-130 flying from the Azores and the US NOAA WP-3 flying from Newfoundland [*Holloway et al.*, 2000]. The intercomparison flight plan consisted of four approximately north-south constant altitude legs of about 20 minutes each. Time was allowed at the beginning and the end of each leg for instrument calibration. At the conclusion of the final leg, each aircraft descended to its lowest altitude, and then climbed in unison. The distance of the two aircrafts averaged 110 m in the horizontal and 9.7 m in the vertical.

The CO instrument aboard the NOAA WP-3 uses the same physical technique (VUV fluorescence), but its implemented design differs largely from the VURF instrument aboard the C-130 [*Holloway et al.*, 2000]. Table 3.2 compares the instrument measurement character-

istics of the two instruments. The CO data were exchanged through an independent third party, so the results represent a double blind intercomparison. The NOAA WP-3 data were retrospectively corrected for dependence of the mixing ratio on water vapour (-0.85 ± 0.19 % / % H_2O), as the NOAA instrument measures in ambient humidity not in dry air, as well as for an error in their field standard (10.37 ppm instead of 9.9 ppm). Only the corrected data are presented here. A more detailed discussion of the intercomparison can be found in [*Holloway et al.*, 2000].

Table 3.2: Instrument measurement characteristics for the intercomparison

	Jülich C-130	**NOAA WP-3**
Sensitivity (photon counts s-1 per ppb CO)	73 cps/ppb	79 cps/ppb
Background	64 ppb	124 ppb
Precision (@ 100 ppb and 5 s)	1.5 ppb	2.2 ppb
Accuracy (@ 100 ppb and 5 s)	2.7 ppb	3.0 ppb

The results in Figure 3.3 show a good agreement within the sum of the squares of the instruments' accuracy (4.1 %) and precision (2.7 %). The ratio of the WP-3 to C-130 results gives an average value of 1.034 with a standard deviation of 2.5 %. Extrapolation by a linear fit is not conducted here because of the limited dynamic range of encountered CO mixing ratios.

Nevertheless, there are two noticeable spikes in the CO mixing ratios recorded by the WP-3 instrument, at approximately 15:22 and 15:24 GMT, that are not present in the C-130 record. As the features do not appear at the corresponding altitude during the previous descent, one has to assume that the C-130 record is correct. Possible explanations for the spikes could be that real variations in ambient CO were only sampled by the WP-3 instrument, or that an artifact of this instrument, like short term increase of discharge lamp intensity, causes such spikes [*Holloway et al.*, 2000].

In summary, the results of the intercomparison are consistent with the estimated precision and accuracy of the C-130 and WP-3 instrument. This degree of agreement lends confidence to the results of the VURF instrument aboard the C-130 being within the estimated accuracy.

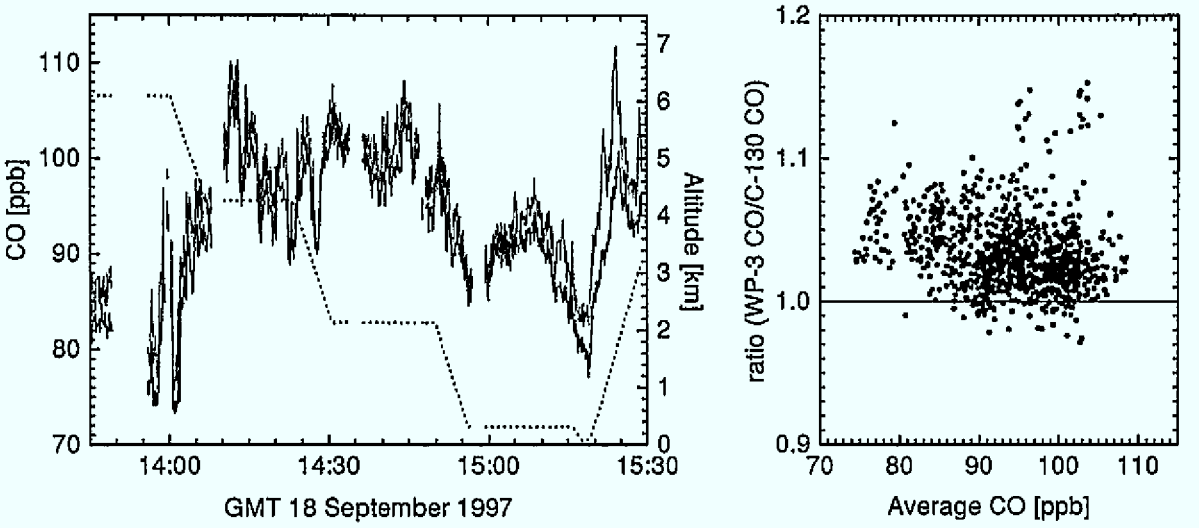

Figure 3.3: Left: Time series of 5-second average measurements of CO. The solid lines give the C-130 (darker) and the WP-3 (lighter) results and the dotted line is the aircraft altitude. Right: Ratios of coincident 5-second average CO measurements as a function of average CO concentration.

3.1.2 Further instrumentation

Besides CO a suite of several chemical species, aerosol concentrations, photolysis rates and meteorological parameters were measured during the campaigns. Table 3.3 gives an overview of the measured parameters of interest for this work, the principle of operation of the instruments, as well as their specifications. A detailed description of the instrumentation can be found in [*Hov et al.*, 1998]. Here, some information about the performance of the instruments during the campaign, and the achieved accuracy of the measurements used in the following chapters, will be given.

Meteorological and position parameters, as well as ozone and particles, are part of the standard equipment for measurements from MRF. The atmospheric chemistry group from MRF also provided an electron capture gas chromatograph with three channels to measure PAN. Unfortunately, problems during the measurements and with the calibration prohibited quantitative results.

NO, NO_2 and NO_y were measured simultaneously by the University of East Anglia (UEA, Norwich) with a four-channel chemiluminescence analyser based on a design described by [*Bauguitte*, 1998]. A fourth channel was intended to detect NO_y-HNO_3, thus providing a measure of HNO_3. Due to technical problems this fourth channel was used as a second NO_y detector. HNO_3 losses at the NO_y inlet were discovered during a comparison flight with the NOAA WP-3. Subsequent inlet tests have indicated that the NO_y instrument was

essentially sampling NO_y-HNO_3, i.e. NO_x and organic nitrates [*S.Bauguitte*, personal communication].

During missions flown in the ACSOE campaign, an electronic fault developed in the NO chemiluminescence detector (CLD), preventing it from operating at its best performance. Abnormally high variability in the background/zero counts, partly due to rapid ambient water vapour changes during ascent/descent, degraded NO measurements precision and accuracy (see Table 3.3). The propagation of uncertainties (photocounting and systematic) indicated a precision for the one second frequency NO CLD signal of 40 pptv. The detection limit for NO is estimated to be approximately 50 pptv. Nitric oxide data below 100 pptv are reported with reduced quality. For this campaign NO_2 measurements were only retrieved for joint ACSOE/TACIA flight A581, when the vicinity of continental sources provided tropospheric NO_x mixing ratios greater than the instrument detection limits for NO and NO_2 [*S.Bauguitte*, personal communication].

Formaldehyde and peroxide measurements were also provided from the University of East Anglia, with both instruments based on fluorimetric methods. The formaldehyde instrument was flown for the first time during TACIA. While the general accuracy of the instrument is 25-30%, problems with the instrument's zero during some of the ACSOE flights led to an estimated accuracy of 60% for these flights. This became apparent by an offset of 400 ppt noted during the intercomparison flight with the NOAA WP-3. Due to a low time resolution, the formaldehyde measurements give a weighted five-minute running mean of the atmospheric HCHO concentration. Thus, small atmospheric features will be underestimated in concentration and "smeared out" by the measurement.

Peroxide was measured with two channels, allowing for the determination of hydrogen peroxide (H_2O_2) and organic peroxides. Only for the flight A581 was the organic peroxide channel missing, so effectively the sum of H_2O_2 and organic peroxides was measured for this flight.

Hydrocarbons were collected by pressurisation of evacuated 1.6 litre summapolished stainless steel canisters. The canisters were always purged and filled during horizontal runs at constant altitude. A total of 163 flask samples were analysed during the TACIA 1997 summer campaign (NILU, Norway) and 99 flask samples during the ACSOE campaign in September 1997 (UEA, UK). The samples were analysed for C_2-C_8 hydrocarbons by gas chromatography with flame ionisation detection. The comparison with the NOAA WP-3

revealed that the alkanes (ethane and propane) and acetylene measured during the ACSOE campaign tended to be up to a factor of two lower than what was measured by NOAA.

Radiometers were fitted for the determination of the rate of photolysis of NO_2 and the rate of photolysis of ozone, leading to the formation of excited state oxygen atoms (O^1D). The performance of the jNO_2 radiometers, provided by the Research Centre Jülich (FZJ), has been described following earlier flights [*Volz-Thomas et al.*, 1996]. The airborne jO^1D radiometers were deployed for the first time during the ACSOE flights in September. The accuracy of the data was estimated at 30%.

Table 3.3: Instrumentation for the TACIA and ACSOE flights in summer 1997

Measured parameter	Time resolution	Accuracy	Detection limits	Principle of Operation	Laboratory	Instrument scientist
Ozone	4 s	2 %	2 ppb (2σ)	UV photometer	MRF	K.Dewey
CO	1 s	3 % or 3 ppb	< 3 ppb in 1 s	CO resonance fluorescence	FZJ	S.Schmitgen
NO	1 s	11 % @ 100 ppt 6 % @ 1 ppb	40 ppt in 1 s	Chemiluminescence	UEA	S.Bauguitte
NO_2	10 s	59 % @ 200 ppt 17 % @ 1 ppb	~100 ppt in 10 s	Photolysis to NO + chemiluminescence	UEA	S.Bauguitte
NO_y	1 s	17 % @ 200 ppt 8 % @ 1 ppb	70 ppt in 1 s	Catalytic reduction to NO + chemiluminescence	UEA	S.Bauguitte
Speciated peroxides (inorganic and organic)	1 s	10 - 15%	40 ppt	Fluorimetry [*Lazrus et al.*, 1986; *Penkett et al.*, 1995]	UEA	B.Bandy
HCHO	5 min	25 – 30 %	150 ppt in 5 min	Fluorimetry	UEA	G.Mills
PAN	2 min	no quant. Results		Gas chromatography (GC)	MRF	H.Richer
Hydrocarbons (VOC)	1-3 min	average: 15% (dependent on species)	dependent on species	Grab sample and subsequent GC-FID analysis	NILU (TACIA), UEA (ACSOE)	N.Schmidbauer, R.Burgess
Aerosol size spectrum	16 Hz	> 10 %	0.1 µm	Passive cavity aerosol sampling probe (PMS model PCASP-100X)	MRF	Standard instrumentation
Condensation particles		10 %	~ 3 nm	Ultrafine condensation particle counter (TSI INC Model A3025)	MRF	Standard instrumentation
$j(NO_2)$	1 s	8 %	$< 10^{-5}$ s^{-1}	Photometer [*Volz-Thomas et al.*, 1996]	FZJ and MRF	C.Gerbig
$j(O^1D)$	1 s	~ 30 %	$\sim 10^{-7}$ s^{-1}	Photometer [*Junkermann et al.*, 1989]	UL	P.Monks
Static pressure	< 1 s	0.3 %	< 100 hPa	Capacitance, Rosemount 1201F	MRF	Standard instr.
Wind velocity components	32 Hz	Vert.: 0.1 m/s hori.: 0.5 m/s	0-150 m/s	INS, OMEGA, GPS and Loran	MRF	Standard instrumentation
Temperature	32 Hz	0.3 K	-80 to +40°C	Platin resistance thermometers, Rosemount 102BL	MRF	Standard instr.
Dew point temperature	1-30s	better than 1 K	-80 to +30°C	Lyman-alpha fluorescence, Chilled mirror (General Eastern 1011B)	MRF	Standard instrumentation
Total water content	64 Hz	0.15 g/kg	0-20 g/kg	Lyman-alpha absorption hygrometer	MRF	Standard instr.

3.2 Flight description

TACIA flights in August-September 1997

The TACIA project consisted of 11 flight days in September 1996 and August-September 1997. In this work only the flights in 1997, i.e. four scientific flights and one instrumental test flight, are discussed. These flights took place in close proximity to the European continent, either over the North Sea or the Atlantic Ocean close to Great Britain.

Summertime continental air masses from central Europe were followed as they moved over the sea in the lower troposphere. The preferred flight track was westward over the Atlantic on the outer edge of an anticyclone, or over the North Sea in air masses coming off the British Isles or the European continent. Areas of cloud and precipitation were avoided as far as possible [*Hov et al.*, 1998]. To get a nearly 3-dimensional picture of the air mass, it was intercepted at different distances from the land by flying a sawtooth pattern (profiles between about 15 and 1500 m) parallel to the coast. Within each of these profiles short horizontal runs were carried out in order to fill bottles and calibrate instrumentation at constant altitude.

Originally a Lagrangian type of flight was intended to investigate the concentration of the hydroxyl radical and the rate of ozone production from the individual production and loss processes. Therefore the same air mass would have to be investigated several times (at least twice) in different distances of the coast, equivalent to different transport times. Unfortunately, the meteorological conditions and aircraft availability prevented the accomplishment of a Lagrangian type investigation of a European plume.

ACSOE flights in September 1997

As part of the ACSOE programme two aircraft field campaigns took place over the North Atlantic. The C-130 was based on Santa Maria, Azores, (37°N, 25°W) during April 1997 and September 1997. The CO instrument was flown only during the September campaign, for which the results are presented.

The objective of the ACSOE programme was to observe the chemical composition in tropospheric air over the North Atlantic Ocean, remote from strong anthropogenic sources. In particular, perturbations which have taken place to the major oxidising species, ozone, peroxides and free radical, as a result of long range transport of anthropogenic emissions

should be quantified [*Sturges et al.*, 1996]. Long range transport is mainly observed in the free troposphere due to the longer lifetimes of trace gases. Additionally, air at low levels with origin in the marine PBL was studied with respect to the chemical removal, with altitude, of compounds emitted from the sea. Therefore, the flight pattern during ACSOE consisted mainly of deep profiles between about 15m and 8km. The operation area was chosen in order to allow for measurements of the atmospheric composition in well-defined meteorological regimes.

In Table 3.4 an overview of the dates, numbering, duration of missions, description of flight operating area, weather situation, and scientific rationale for the TACIA and ACSOE flights in summer 1997 is given. The flight paths of these flights are shown in Figure 3.4 with the colours indicating the flight altitude. From this map the different regions of the atmosphere investigated during the two campaigns become obvious. During the TACIA flights mainly fresh pollution was investigated in the lower part of the troposphere close to the European continent. Whereas the ACSOE flights investigate the atmospheric composition up to about 8 km altitude over the Northern Atlantic far away from the source regions.

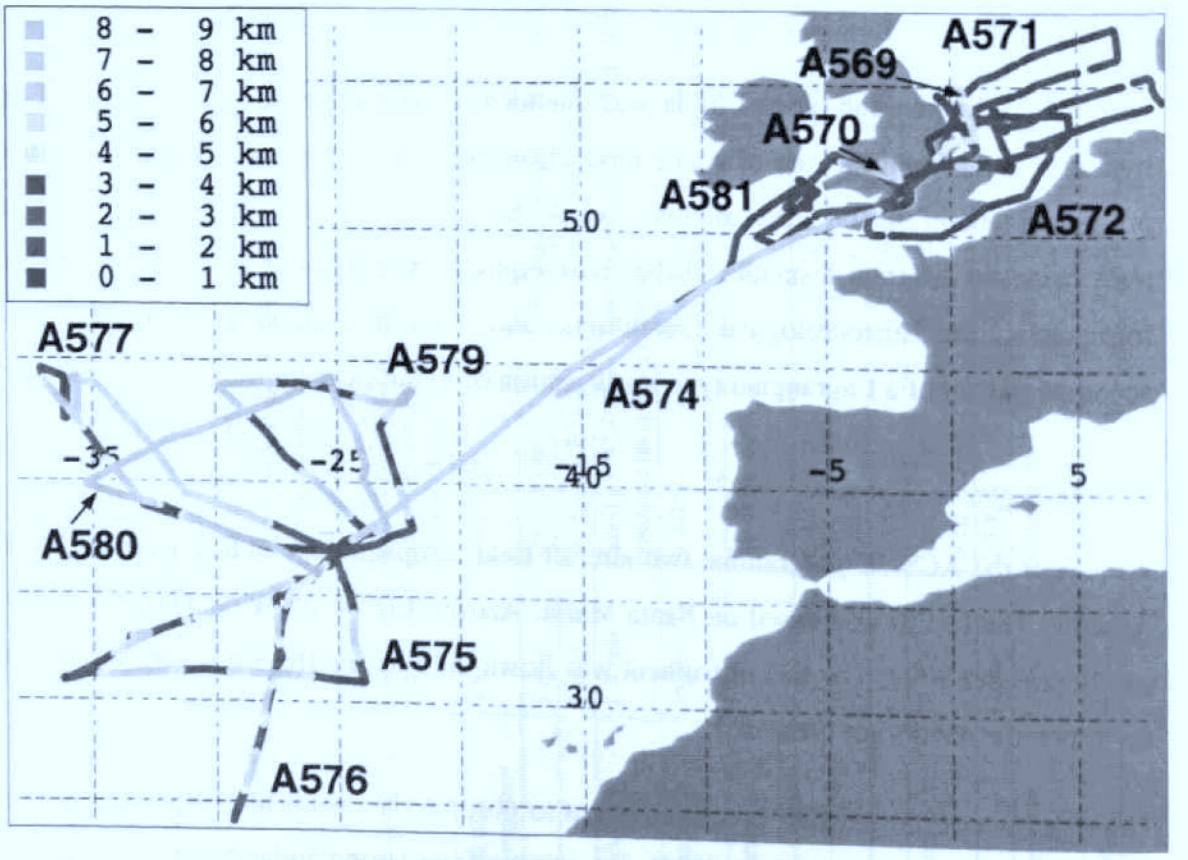

Figure 3.4: Flight tracks of the C-130 aircraft during the TACIA and ACSOE campaigns in August and September 1997. The colours indicate the flight altitude.

Table 3.4: Overview of the C-130 TACIA and ACSOE flights in summer 1997.

Date	Flight No	Project	Duration	Operation area	Weather situation	Scientific rationale
15.08.97	A570	TACIA	5h 3min	Profiling E of Teeside and along UK coast	High pressure ridge over N. coast of continental Europe into S. North Sea, stagnant flow	Plume characterisation
18.08.97	A571	TACIA	6h 45min	S. part of North Sea profiles and stacks	Anticyclone over Scandinavia, slight outflow over North Sea from continental Europe	Measure chemical composition of polluted continental plume at different distances from the coast
19.08.97	A572	TACIA	7h 24min	S. North Sea, British Channel and S. Irish Sea, across England, profiles and stacks	Anticyclone over Scandinavia, several fronts approaching from W.	Polluted continental plume characterisation
13.09.97	A574	ACSOE	4h 24min	Transit from UK to Azores	Trough west of Azores (former Hurricane Erica), high pressure ridge from Azores to western France	Instrument test and model validation
14.09.97	A575	ACSOE	7h 18min	Northeast Atlantic Ocean, Southwest of the Azores	Trough west of Azores (former Hurricane Erica), high pressure ridge from Azores to western France	Investigation of tropical air and air originating over the US
16.09.97	A576	ACSOE	6h 17min	Northeast Atlantic Ocean, Southwest of the Azores	Dominated by Tropical Storm Erica (former Hurricane)	Flight investigating outflow from Hurricane Erica
18.09.97	A577	ACSOE	7h 17min	Northeast Atlantic Ocean, Northwest of the Azores, profiles back to Azores	Operational axis (40-44°N, 35°W) just in front (east) of a frontal system and trough	Intercomparison flight with NOAA WP-3
20.09.97	A579	ACSOE	6h 1min	Northeast Atlantic Ocean, North of the Azores	Frontal system moving to the west, band of convective clouds, frontal zone ill-defined and not very active	Frontal crossing flight
21.09.97	A580	ACSOE	5h 29min	Northeast Atlantic Ocean, Northwest of the Azores	Low pressure system at 40-50°N, 10-30°W; Trough at 500 hPa	Intercomparison with DLR Falcon, Investigation of high altitude air with possible US West coast origin
23.09.97	A581	ACSOE / TACIA	6h 52min	Ferry flight Azores-UK, profiles and stacks in Bristol Channel and SW approaches to UK	Anticyclone over UK	Polluted continental plume characterisation

3.3 Results

More than a hundred vertical profiles were measured during the TACIA and ACSOE campaigns in summer 1997. To show this huge amount of data would by far exceed the frame of this work, and is not necessary. Therefore, only a statistical overview of the data is given showing the different chemical signatures of the air masses observed during TACIA and ACSOE. Individual profiles are shown in the following discussion chapters where they are deemed beneficial for the interpretation.

As the overall aim of this work is to analyse ozone and precursors in air masses influenced by anthropogenic emissions, the observations will be analysed for the observed O_3/CO ratio, which indicates photochemical production of O_3 in ageing plumes since the time of emission. Another measure for the degree of photochemical processing in the plume is the degradation of individual VOC. This will be discussed in relation to CO as a tracer for the emissions.

3.3.1 Statistical overview of the TACIA and ACSOE flight data in summer 1997

Figure 3.5 – 3.7 present the variability and characteristic chemical signatures of the observed air masses during TACIA and ACSOE in a statistical overview. The data of each of the two campaigns were partitioned into altitude intervals of 1 km each, for which the parameters of the statistical distributions are plotted. Shown are the mixing ratios of CO, O_3, NO_x, NO_y, the sum of measured VOC, peroxide and formaldehyde, as well as the relative humidity. Additionally, a background mixing ratio of ozone was determined, defined as ozone mixing ratios that were associated with CO concentrations of less than 80 ppb. As NO_2 data were not available for the ACSOE campaign, the NO_x was estimated from NO and O_3 data using the photostationary steady state assumption[8]. Consequently, the NO_x mixing ratios during ACSOE have to be considered with caution, especially as the NO measurements were close to the detection limit.

[8] Compare chapter 2.1.1

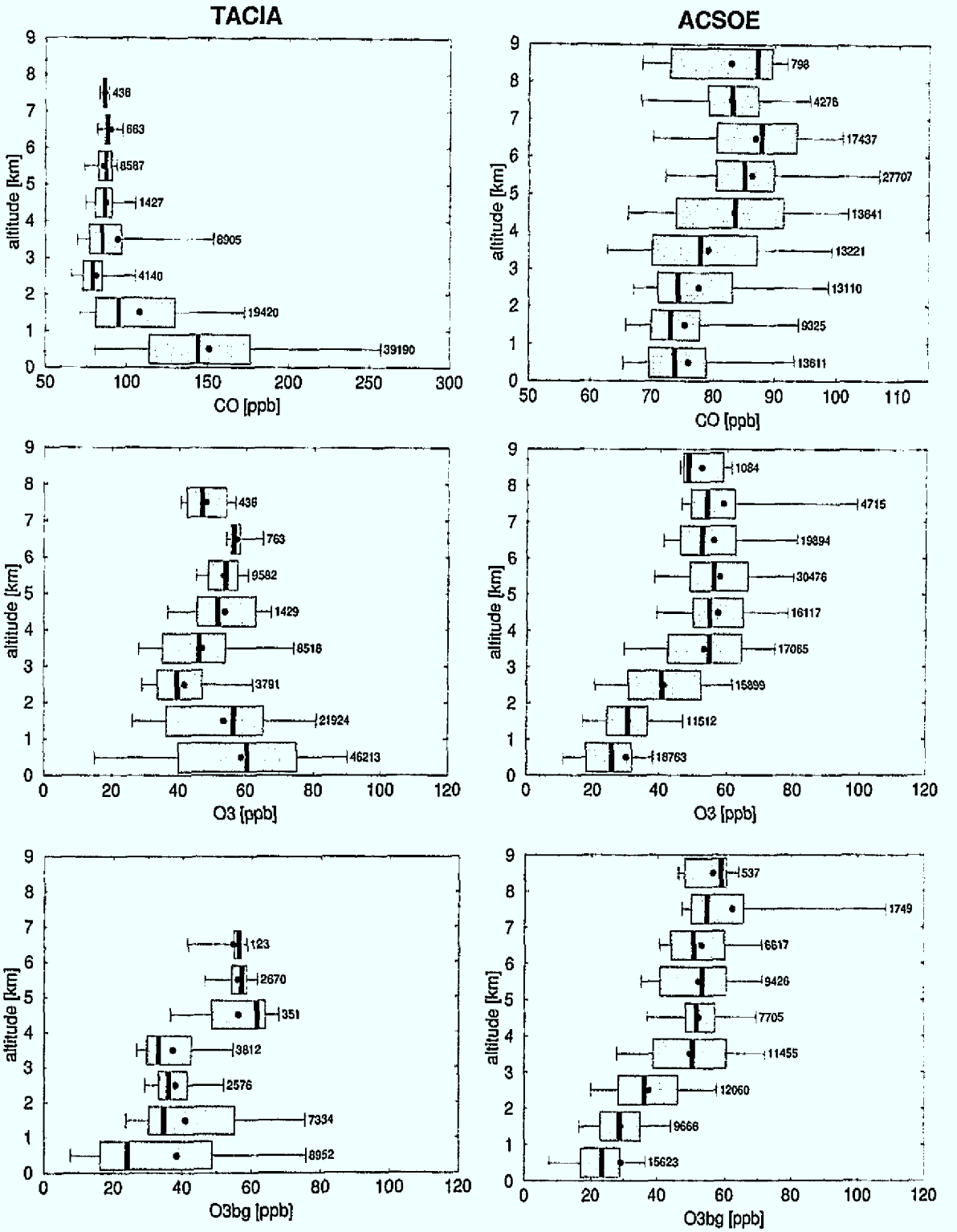

Figure 3.5: Mixing ratios of CO (upper row) and ozone (middle row) during the TACIA (left) and ACSOE (right) campaigns in summer 1997 for different altitude classes. The lowest panels shows the background ozone, defined by associated CO mixing ratios smaller than 80 ppb. The central 50% of the distribution are given by the box, the 5 and 95 percentiles by the bars. The bar within the box marks the median, and the dot the mean of the distribution. The numbers are the number of measurements included in the distribution. Note the different scales for CO.

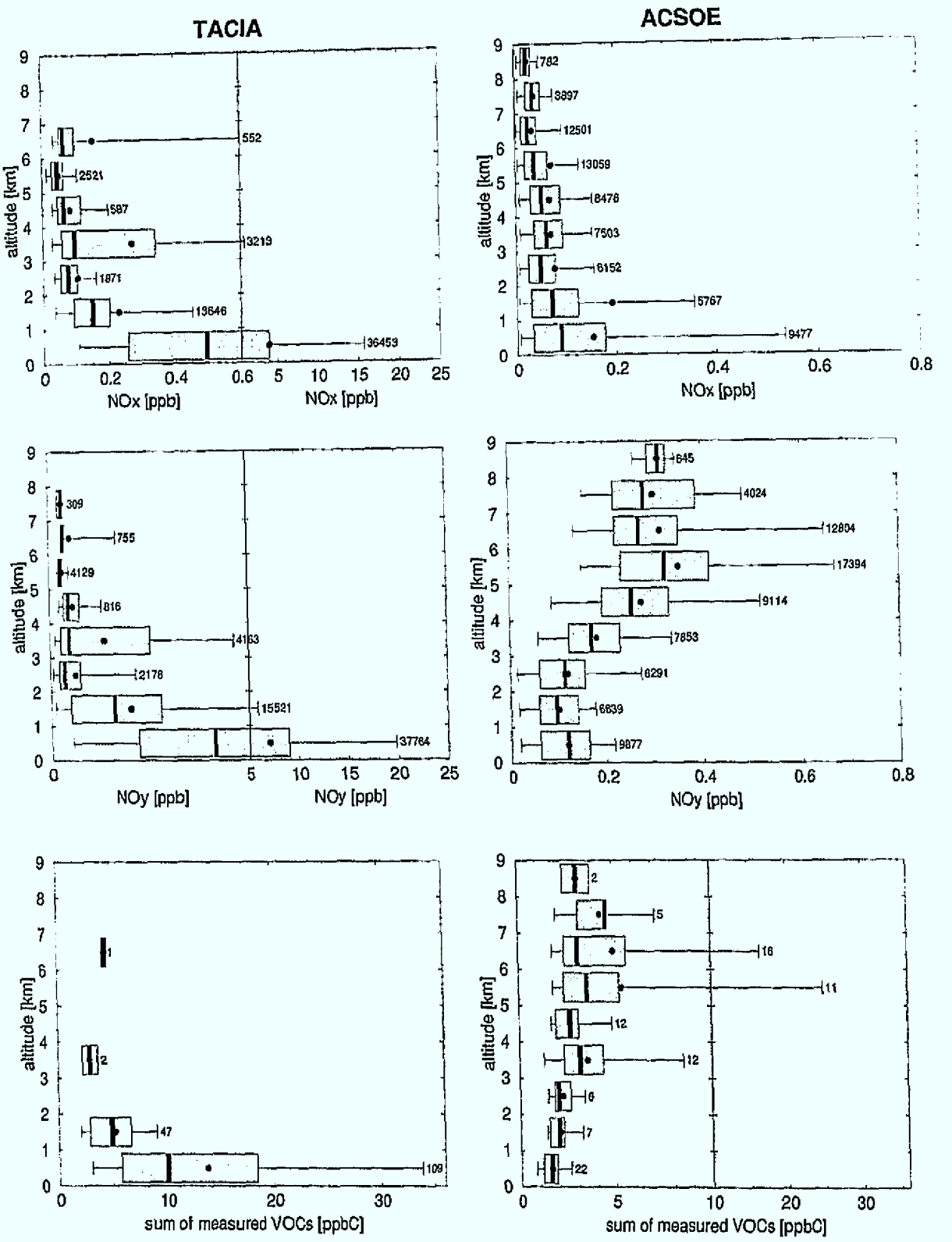

Figure 3.6: Mixing ratios of NO_x (upper row), NO_y (middle row) and the sum of measured VOC (lower row) during the TACIA (left) and ACSOE (right) campaigns in summer 1997 for different altitude classes. Symbols as in Figure 3.5. Note the changes in scale.

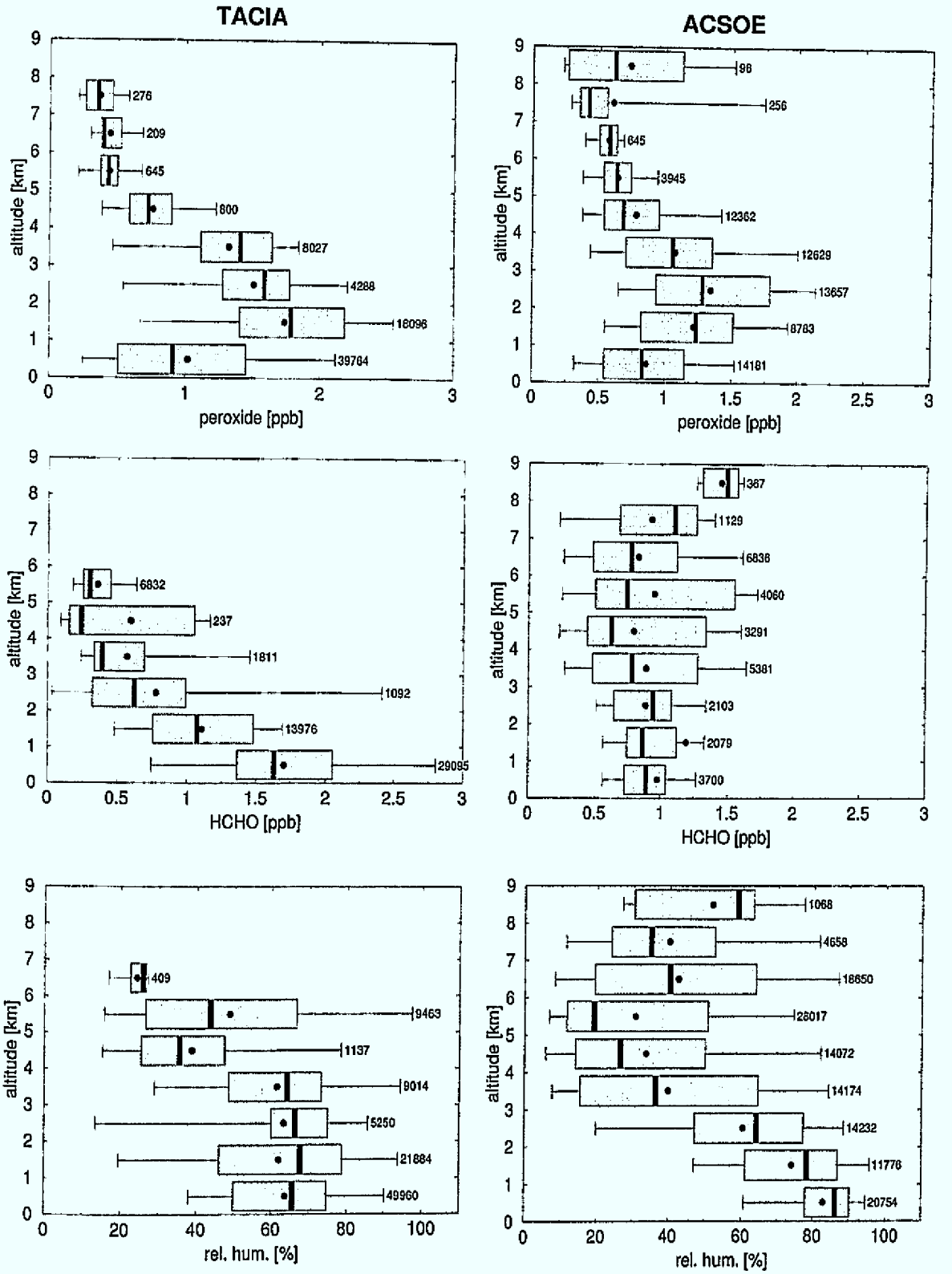

Figure 3.7: Mixing ratios of peroxide (upper row), formaldehyde (middle row) and the relative humidity (lower row) during the TACIA (left) and ACSOE (right) campaigns in summer 1997 for different altitude classes. Symbols as in Figure 3.5.

The continental influence during the TACIA flights is clearly exhibited by elevated mixing ratios of CO, NO_x, NO_y, VOCs and formaldehyde in the lowest 1-2 km altitude. Associated with these ozone precursors are ozone mixing ratios that are increased by around 20 ppb compared to the background ozone. At higher altitudes the CO mixing ratios during TACIA vary only slightly above a background concentration of about 75 ppb, corresponding to the lowest five percentiles. Some enhancement was found at 3-4 km, associated with elevated NO_x and NO_y, which had led to ozone production as indicated by mixing ratios about 10 ppb above the background. Besides this, the overall ozone values at higher altitudes were similar or even lower than the background ozone. This indicates that the mean ozone distribution observed during TACIA is strongly influenced by photochemically production in the lower altitude plumes from Europe, but at higher altitudes it is given by background ozone of probably upper tropospheric or stratospheric origin.

The highest mixing ratios of peroxide during TACIA were found between 1 and 2 km, with a clear drop in the lowest kilometre. This could be due to both deposition, which is an important loss process for peroxide, as well as the high observed NO_x concentrations in the lowest kilometre, which lead to VOC-sensitive photochemistry with low peroxide concentrations[9].

During ACSOE the large distance from the source regions led to low concentrations of CO, NO_x, NO_y, VOCs and formaldehyde in the lower troposphere. Here the ozone precursors were largely removed by photochemical processing, wash out and deposition. The ozone concentrations were close to background values.

However, at higher altitudes enhanced mixing ratios of the ozone precursors CO, NO_y and hydrocarbons are found during ACSOE. Comparison of the ozone mixing ratios at this altitude (4-7 km) with the background ozone reveals an increase in ozone (although difficult to make out in Figure 3.5). The rather low relative humidity at these altitude classes suggests an upper tropospheric origin of these air masses, whereupon the ozone concentrations would normally be attributed to stratospheric influence. Nevertheless, the combination of emission trace gases and ozone enhancement clearly points to large-scale production of ozone from anthropogenic precursors. The upward transport of continental air masses by convective processes is thought to account for these observations, which have also been found elsewhere (e.g. [*Dickerson et al.*, 1987; *Pickering et al.*, 1988; 1989;

[9] Compare chapter 2.1.3

1992; 1993]). The low humidity can then be explained by subsequent descent of the air masses to the region of observation. The process of ozone formation at the time of observation should have already ceased, as indicated by the mixing ratios of NO_x, which are close to the detection limit of the instrument.

Peroxide concentrations at higher altitudes with relatively dry air are mostly below 0.7 ppb during ACSOE. Higher concentrations around 1.3 ppb are found below about 4km where the humidity increases towards the surface. In the lowest kilometre the peroxide concentration decreases, presumably as a result of dry deposition.

The HCHO measurements during ACSOE, although shown in Figure 3.7, have to be regarded with caution due to accuracy problems of the instrument during the ACSOE campaign[10]. Thus they are not included in the discussion.

3.3.2 O_3/CO ratio of the TACIA and ACSOE flight data in summer 1997

CO is an effective tracer for the transport of anthropogenic emissions in remote areas [*Fishman and Seiler*, 1983]. Positive correlations of O_3 with CO have been used to estimate the amount of ozone photochemically produced in an ageing plume since the time of emission [*Parrish et al.*, 1993]. On the other hand, negative correlations of O_3 to CO indicate ozone of stratospheric origin, which is marked by elevated O_3 with low CO [*Hipskind et al.*, 1987].

Figure 3.8 shows the relationships between O_3 and CO for the four TACIA flights in August-September 1997. Plotted in the figure are 10 s means of the measured ozone and CO mixing ratios. This averaging time was chosen, as it reduces the amount of presented data, but does not significantly change the observed correlations, thus enabling more clarity.

Considering all data of the flights, plotted as solid and open circles, a general increase of O_3 with CO is found, indicating a photochemical origin of the observed ozone. However, the overall correlation is low, since during the flights air masses of different origin were investigated. The objective during TACIA was to estimate the production and export of ozone from the continental boundary layer to the oceanic environment. Therefore, data has been selected with recent origin in the PBL that are already sufficiently photochemically

[10] Compare chapter 3.1.2

aged to realise their O_3 production potential. These data are marked by the solid circles in Figure 3.8.

Air of recent origin in the boundary layer was thereby selected by including only data observed in the lowest 4 km altitude, with the additional criterion of a relative humidity above 50%. Realisation of the O_3 production potential can be diagnosed by the NO_x/NO_y concentration ratio [*Trainer*, 1993], which gives a measure of the chemical processing of the air mass. *Chin et al.* [1994] suggested a threshold of $NO_x/NO_y < 0.3$ as criterion of photochemically aged air for the analysis of O_3-CO correlations. Here, $NO_x/NO_y < 0.1$ was found to be a better criterion to exclude data with elevated CO but low O_3, representing fresh pollution plumes, for all the flights. Nevertheless, the correlation and slope are rather insensitive to small changes in the NO_x/NO_y criterion, as was also found by *Chin et al.* [1994].

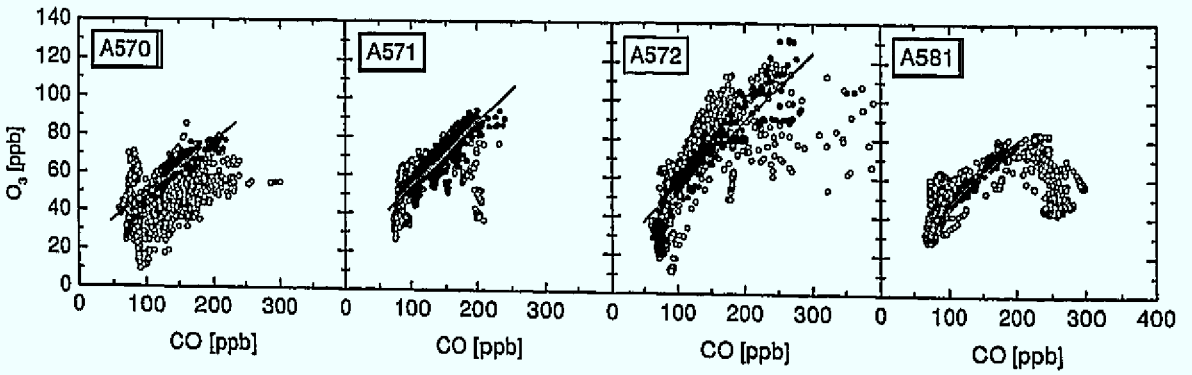

Figure 3.8: O_3-CO relationships found during the TACIA flights in August-September 1997. Shown are 10 s means. The filled symbols mark data at 0-4 km altitude, with rel. humidity > 50% and $NO_x/NO_y < 0.1$, which constitute the linear regression.

The results of a linear regression analysis for the thus selected O_3 and CO measured during the TACIA flights are shown in Table 3.5. For the regression the measured one second data were used. The results show that the constrains to select ageing boundary layer plumes produce strong correlated data with r-square values ranging from 0.78 to 0.92. The slopes found for the different flights are consistent, ranging from 0.26 to 0.35 $ppbO_3/ppbCO$. These slopes are similar to the average summertime slope of 0.3 to 0.4 reported by *Parrish et al.* [1998] at four Atlantic Canadian surface sites.

Table 3.5: Linear regression parameters for O_3-CO correlations from measured 1 s data during the TACIA flights in August-September 1997. Only data at 0-4 km altitude, with relative humidity > 50% and $NO_x/NO_y < 0.1$ are included in the regression.

Flight No.	Slope (O_3 per CO)	r-square	Number of data
A570	0.26 ± 0.01	0.78	1640
A571	0.32 ± 0.01	0.78	9061
A572	0.35 ± 0.01	0.79	3240
A581	0.31 ± 0.01	0.92	875

Rather different from these results are the O_3-CO relationships found during the ACSOE flights in September 1997, as shown in Figure 3.9. As before, 10 s means of the measured ozone and CO mixing ratios are plotted. First it should be noted that the range of observed CO during ACSOE, with about 60-120 ppb, is much smaller than the CO mixing ratios for TACIA shown in Figure 3.8, which reach up to 400 ppb. The majority of the measured CO data, especially in the flights A579 and A580, represent clean tropospheric background air where no overall correlation between ozone and CO is found. Nevertheless, as discussed in chapter 3.3.1, air masses with ozone production from anthropogenic precursors have been observed at the altitude range of 4-7 km. Therefore, data of this altitude range have been selected, and are marked by solid circles in Figure 3.9.

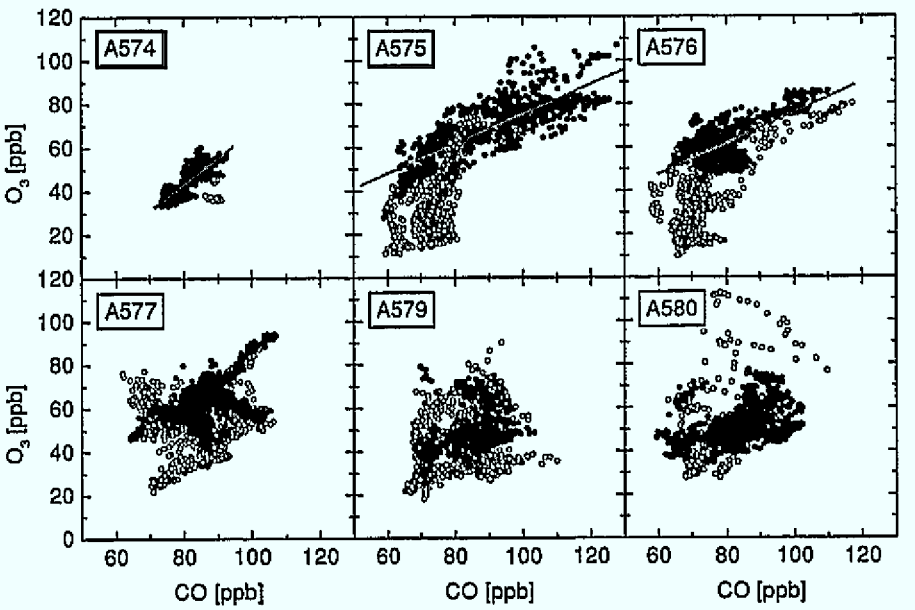

Figure 3.9: O_3-CO relationships found during the ACSOE flights in September 1997. Shown are 10 s means. The filled symbols mark data at 4-7 km altitude, which constitute the linear regression.

Indeed, for this altitude range a clear positive correlation between ozone and CO is found during the flights A574, A575 and A576, indicating photochemical origin of the observed ozone. The linear regression parameters for these correlations are shown in Table 3.6. While the range of observed CO during the flight A574 is very small, the CO observed during the flight A575 indicates air masses with pronounced anthropogenic emission input. This is observed again during the flight A576, although with a slightly smaller range of CO mixing ratios. The slopes found for the photochemically produced ozone in the free troposphere with 0.68 – 1.10 $ppbO_3$/ppbCO are significantly higher compared to the slopes found in the lower troposphere close to the European continent during TACIA. Similar slopes for continentally influenced summertime air masses in the free troposphere have for example been found during measurements over the middle Atlantic[11] [*Gerbig et al.*, 1997]. The larger slopes compared to those obtained in the PBL indicate a more efficient production of ozone from NO_x on a per-molecule basis in the free troposphere due to the longer lifetime of NO_x, as is for example suggested by *Liu et al.* [1987].

Table 3.6: Linear regression parameters for O_3-CO correlations from measured 1 s data during the ACSOE flights in September 1997. Only data at 4-7 km altitude are included in the regression.

Flight No.	Slope (O3 per CO)	r-square	Number of data
A574	1.10 ± 0.01	0.67	7756
A575	0.68 ± 0.01	0.68	10482
A576	0.69 ± 0.01	0.51	6497
A577	Not correlated		13897
A579	Not correlated		6908
A580	Not correlated		13233

For the flights A577, A579 and A580 no overall correlation between ozone and CO in the investigated altitude range of 4-7 km was found. Nevertheless, detailed analysis of the data reveals that individual layers still often show positive or negative correlations between O_3 and CO, indicating different air mass origin. This can, for example, be seen on the O_3-CO relationship for the flight A577, where the positive correlations indicate air masses with continental origin, while the negative correlations can be explained by ozone of stratospheric origin.

[11] These measurements were obtained as part of the European research project OCTA [*McKenna et al.*, 1995].

3.3.3 Individual hydrocarbons during TACIA and ACSOE in summer 1997

The emissions of volatile organic compounds (VOC) contain a large number of species with tropospheric lifetimes ranging from a few hours to a few months. The emitted VOC are subject to both dilution and chemical removal as the plume ages. The latter is dominated by oxidation of the VOC with the OH radical. Since most VOC are coemitted with CO and the latter is a quasi inert tracer on time scales of a few days, the measured CO concentrations can serve to account for dilution of the VOC, i.e. to separate chemical degradation of the VOC from physical dilution. Thus, the degradation of individual hydrocarbons related to CO gives a rough estimation of the time since emission.

The ratio of $VOC_i/(CO\text{-}CO_{bg})$ is compared in Figure 3.10 for VOC_i measured in the anthropogenic plumes observed during TACIA and ACSOE. A plume is defined by significantly elevated CO mixing ratios above CO_{bg}, the background concentration of CO, which in turn was defined by the lowest five percentiles of the measurements during the respective campaign. This differs for TACIA and ACSOE due to the different observation areas. For TACIA a background concentration of 75 ppb was found, and the plume observations were defined when CO increased more than 20 ppb over CO_{bg}. During ACSOE the CO mixing ratios were generally lower and less variable, resulting in elevated CO mixing ratios were already defined by an elevation of 15 ppb above CO_{bg} = 65 ppb. Only alkanes are included in the analysis, as most of the alkenes and other VOC (besides the long lived acetylene and benzene) did not show any functional relation to the measured CO concentrations. The lack of agreement of these compounds has been noted and addressed previously with this data set [*Hov et al.*, 1998; *Richer et al.*, 2000] and with other data sets (e.g. [*Penkett et al.*, 1993]), and will not be analysed further in this work.

For the ACSOE campaign only the alkanes observed during flight A575 showed a functional relation to CO and are therefore included into the analysis. This leaves a total of only 13 flask samples included in the statistical distribution in Figure 3.10 for the ACSOE flights, compared to 135 bottle samples for TACIA. Nevertheless, general differences in the degree of degradation of hydrocarbons observed during TACIA and ACSOE are clearly marked. During TACIA, a wide range of different photochemical ages of the air masses were observed, as indicated by the range between the 5 and 95 percentiles of the alkanes normalised to the CO concentrations. The wide variability in $VOC/(CO\text{-}CO_{bg})$ found for the alkanes with lifetimes on the time scale of days (i.e. butane Table 3.7) indi-

cates that the time since emission for air masses observed during TACIA ranges from several hours to several days.

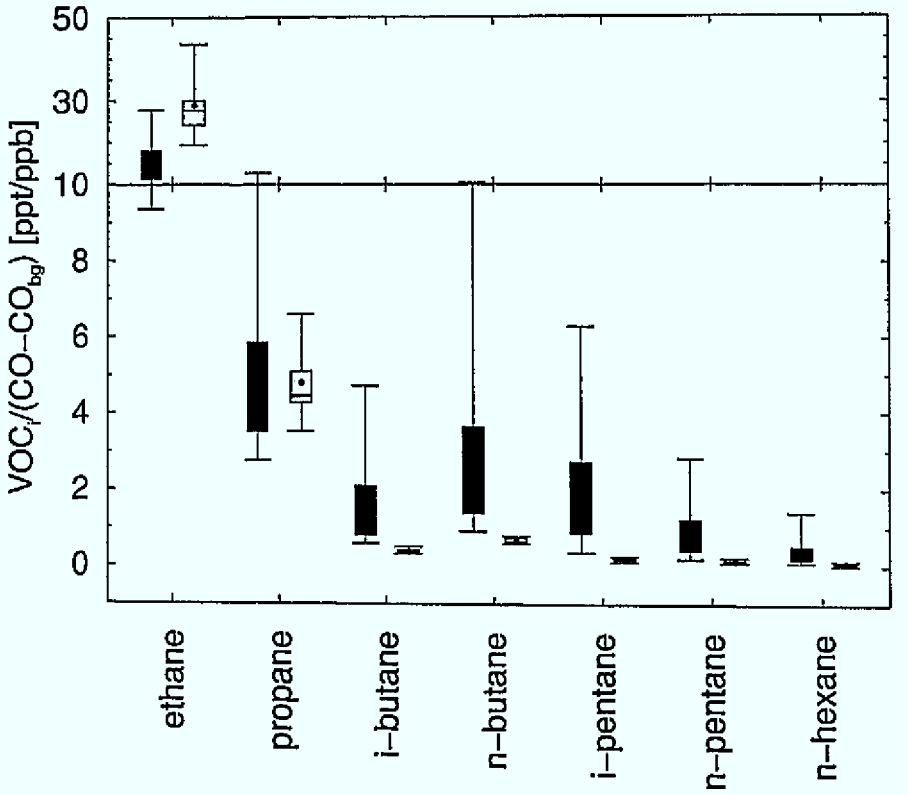

Figure 3.10: Statistical distribution of VOC$_i$/(CO-CO$_{bg}$) for alkanes measured during TACIA (dark grey) and ACSOE (light grey) The central 50% of the distribution is given by the box, the 5 and 95 percentiles by the bars. The bar within the box marks the median, and the dot the mean of the distribution.

During the ACSOE flight A575 (light grey bars in Figure 3.10) the hydrocarbons with lifetimes up to about 3 days were already largely removed, as can be seen for the extremely narrow bars of i-butane to n-hexane. Nevertheless, they were still elevated above the detection limit, particularly for i-butane and n-butane, and still revealed a functional relation to the CO concentrations. Together with the ratio of propane/(CO-CO$_{bg}$), which does not differ much from the observations during TACIA, this indicates emissions occurred several days ago, but not much more.

This analysis can only give a rough estimation of the time since emission for the plumes observed during TACIA and ACSOE. For a closer analysis, the initial distribution of the individual hydrocarbons at the time of emission, and the actual OH concentrations, would have to be considered. Nevertheless, the prerequisite for a detailed analysis of VOC degradation in continental plumes is a high quality data set. Due to the uncertainties in the VOC data quality during ACSOE, highlighted by the intercomparison with the NOAA WP-3

aircraft, such a detailed analysis was refrained from[12]. Nevertheless, the marked difference in photochemical age of the air masses observed during TACIA and ACSOE is already evident from this analysis.

Table 3.7: Rate constants of the alkanes in Figure 3.10 for degradation by OH, k_{OH}, [*Atkinson et al.*, 1997] and average lifetimes in days, calculated for an OH concentration of [OH]=2x10^{6}molecules cm^{-3}.

Species	k_{OH} [cm^3·s^{-1}]	τ_{OH} [d]
ethane	2.57*10^{-13}	22.52
propane	1.12*10^{-12}	5.17
i-butane	2.19*10^{-12}	2.64
n-butane	2.44*10^{-12}	2.37
i-pentane	3.70*10^{-12}	1.56
n-pentane	4.00*10^{-12}	1.45
n-hexane	5.45*10^{-12}	1.06

[12] Compare chapter 3.1.2

4 Model of chemistry and transport

The aim of this study is to gain deeper insight in how emissions, and chemical and transport processes lead to the observed chemical compositions in ageing plumes. In order to be able to do this, the time history of the air masses needs to be known. Since measurements in the same air parcel of the plume for different times could not be made, reconstruction of the time history can only be obtained by using available information about the meteorology, emission inputs and photochemical processing. The combination of this information leads to a model description that approximates the real processes in the atmosphere.

A heuristic model is described in this chapter, which is a tool for the analysis of the history of the air masses observed during the flight. The model formulation is chosen with modules for transport and chemistry, allowing for a separation of these processes in the analysis.

4.1 Transport characteristics

Numerical methods to compute the time history of air pollutant concentrations are usually divided into two broad categories. Eulerian models consider fixed boxes and represent transport by air flowing between these boxes. In Lagrangian models the boxes, representing air parcels, move along with the flow of the air and transport is represented by the changing location of these boxes. Eulerian methods are typically applied when fields of air pollutant concentrations are to calculate, requiring solutions at all grid points. Lagrangian methods are designed to study the history of individual air parcel by following their trajectory, which is represented by advection along the wind fields. Thus, they can be used to establish a source-receptor relationship for the interpretation of point measurements, or series of point measurements during a flight. Therefore, a Lagrangian trajectory model approach is chosen to investigate the time history of the specific air masses observed during the flights.

4.1.1 The transport module

The simplest approach for a Lagrangian box model is to consider individual trajectories. If the task is to calculate the concentration of a species at a specific location in the flow, then a trajectory is usually calculated from this location backwards in time. Next, an air parcel,

represented by an infinitesimal box, is moved forward in time along this trajectory and changes in the concentration caused by emission, chemical processing and deposition are calculated. A problem with this approach is the neglect of mixing between air masses. Also, position errors in the trajectory calculation are problematic. Position errors of 20% of the distance travelled have been found to be typical for trajectories computed from analysed wind fields [*Stohl*, 1998]. In regions with spatially inhomogeneous emissions this can lead to large errors in the calculated concentrations.

Therefore, in this study an extended approach is chosen by considering not only one single air parcel. Instead, a volume in form of a box is defined, with the geographical/time location of the observation as the box centre. This volume, which is scaled to the horizontal and vertical resolution of the wind fields[13], will be referred to in the following as receptor box. The distances between the receptor box and the source regions are assumed large enough that trace species arriving in the receptor box are approximately homogeneously mixed. Then all back trajectories calculated from an arbitrary starting point in the receptor box represent air parcels with possible contribution to the measured concentration in the centre of the box.

In practise, this influencing volume is approximated by a box spanned by seven back trajectories starting at the time t_0 from the receptor box: one from the centre of the box, and six from the middle of each of the box faces. At each point in time t, with $t < t_0$, a new box is defined by the outer edges of this trajectory cluster, as illustrated in Figure 4.1. The resulting box will typically become larger the further back in time the trajectories are calculated.

This is mainly determined by the degree of coherency of the airstream [*Stohl*, 2000]. High coherency implies that the wind vectors at all faces of the box are parallel, whence the box remains defined to its size, and mixing with neighbouring air masses is inhibited. On the other hand, for low coherency of the airstream the trajectories at the faces are determined by different wind vectors. Low coherency implies that neighbouring particles get separated from each other. In absence of turbulence and convection, this leads to filaments that may be conserved over long times. But with the assumption of turbulence leading to a well mixed receptor box, it gives an approximation for the mixing of air masses on the way to the receptor box.

[13] Here a box size of 0.5° x 0.5° and 100 m height is chosen. Compare chapter 4.1.2.

Additionally, the uncertainty of the trajectories accumulates over the time of backward integration, thus leading on average to larger boxes further back in time.

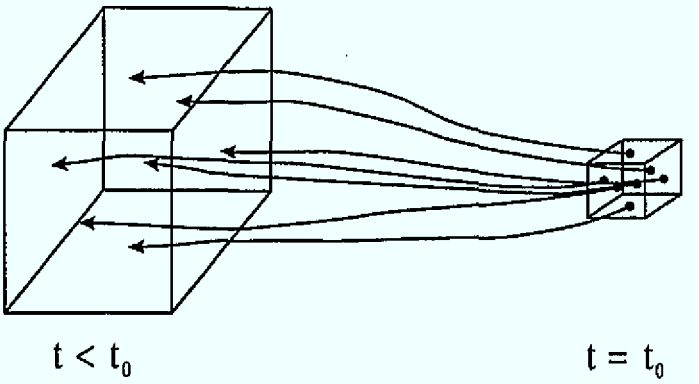

Figure 4.1: Model for the estimation of the influencing volume of a box at the time t_0 for the time $t < t_0$ by a cluster of back trajectories starting from the faces of the box at the time t_0. The box at the time $t < t_0$ is defined by the smallest rectangular box containing all trajectories.

All air parcels within the box at the time t are interpreted as having the same probability for contribution to the concentration in the receptor box, while outside the box the probability is set to zero, following a simple "top-hat" approach [*Draxler and Hess*, 1998]. As within the receptor box the air masses are assumed to be mixed, the air masses in the box at $t < t_0$ will mix on their way. This is parameterised in the model by the simplification of instantaneous mixing within the box at every time step.

The next point to consider is the vertical parameterisation of emission input into the box. Emissions are assumed to be picked up by air masses that move within the mixing layer only. They are also assumed to be instantaneously diluted over the mixing height, MH, with the simplified assumption of a homogenous mixed boundary layer up to the daily maximum of the mixing height[14] and no input of emissions above this. This approach assumes that the nocturnal residual layer is completely re-incorporated into the mixing layer each morning[15].

If the vertical extension of the influencing box is completely within the mixing layer, the emission input in the box is given by the volumetric emission rate into the mixing layer. For boxes that are only partly within the mixing layer, the "box height" is used to dilute the tracer from the part of the box within mixed layer to the total box. Boxes that are completely in the free troposphere, do not see any emission input.

[14] The determination of the maximum mixing height used in the model is described in chapter 4.1.4
[15] Compare Chapter 2.2.2 and Figure 2.4

The volumetric emission input of a species X in the box is then defined by the following equation:

$$
\begin{aligned}
\left.\frac{d[X]}{dt}\right|_{emis} &= \frac{\iint_A F_X(t)\,dA}{\rho \cdot A \cdot h_{MH}(t)} && \text{if } h_{max} \le h_{MH} \\
\left.\frac{d[X]}{dt}\right|_{emis} &= \frac{\iint_A F_X(t)\,dA}{\rho \cdot A \cdot h_{MH}(t)} \cdot \frac{(h_{MH}(t) - h_{min}(t))}{(h_{max}(t) - h_{min}(t))} && \text{if } h_{max} > h_{MH} > h_{min} \\
\left.\frac{d[X]}{dt}\right|_{emis} &= 0 && \text{if } h_{min} > h_{MH}
\end{aligned}
\tag{4.1}
$$

where F_X is the emission flux in molecules per hour and square meter, A is the horizontal area covered by the box, h_{MH} is the daily maximum mixing layer height, h_{min} and h_{max} give the respective minimum and maximum altitudes of the box defined by the trajectory cluster, and ρ is the number density of air (1 atm and 298K).

4.1.2 Trajectories

The module is based on 10-day, three-dimensional back trajectories, kindly provided by the University of Cambridge [*M. Evans*, personal communication]. They have been calculated from the European Centre for Medium range Weather Forecasting (ECMWF) T106 L31 analyses (corresponding to a horizontal resolution of approximately 1.25° by 1.25° and 31 vertical levels) [*ECMWF*, 1995], using a code developed by [*Methven*, 1997]. The trajectories are available with a six hour time step, which corresponds to the availability of the wind fields. For the calculation of the trajectories, the fields are linearly interpolated in time between these periods. The position of the trajectory is evaluated every 36 minutes and integration is achieved using a 4^{th} order Runge-Kutta method [*Evans*, 1999]. The trajectories cover the whole flight track starting at the respective flight times with a separate trajectory calculated whenever the aircraft moves up or down by 100 m or by 0.25° laterally. For every starting point thus defined, the receptor box was initialised by six points, separated by 0.25° in the north, south, east and west directions and 50 m above and below the central starting point. For these points, clusters of trajectories were calculated.

4.1.3 Emissions

Emission input in the boxes is taken from the EMEP (Co-operative Program for Monitoring and Evaluation of the Long Range Transmission of Air Pollutants in Europe) emission

inventory for 1996 [*Berge*, 1997]. Outside the EMEP model domain (which covers Europe and Russia west of the Ural), emissions are taken from the GEIA (Global Emissions Inventory Activity) inventory based on the year 1985 [*Benkovitz et al.*, 1996].

The EMEP inventory has a grid resolution of 50 km. The time steps of the trajectories are adjusted to this resolution by linearly interpolating the trajectories from six hours to one hour steps. By following this procedure the distance between two time steps of a trajectory is smaller, on average, than the emission grid size, so that the number of hits gives the residence time over a grid cell, and thus the emission input.

Anthropogenic emissions are considered for CO, NO_x and total VOC. The GEIA inventory, with a resolution of 1° x 1°, provides only NO_x and SO_2 emissions. For this domain the mass of anthropogenic VOC emissions are set equal to that of NO_x, and the CO emissions as 3.5 times the NO_x emissions by mass (NO_x as NO_2), and are given the same spatial distribution as NO_x. These ratios are based on the National Acid Precipitation Assessment Program (NAPAP) inventory for the eastern United States, and on a global emission inventory complied by [*Hough*, 1991], following the suggestions by [*Flatoy et al.*, 1996]. The NO_x emissions are assumed to be 90% NO and 10% NO_2. The speciation of the VOC emissions needed for the chemistry scheme is described in chapter 4.2.1.

Table 4.1: Weekly variations in the emissions of CO, NO_x and total VOC.

	CO activity factor	NO_x activity factor	VOC activity factor
Weekday	1.04	1.05	1.13
Saturday	0.91	0.88	0.80
Sunday	0.90	0.86	0.57

The EMEP inventory provides annual total emissions for each grid cell. Seasonal variations are not taken into account for this study, because for this time of year (September) seasonal variations assumed by [*Flatoy et al.*, 1996] are approximately equal to the annual average. Diurnal and weekly variations in the emission pattern are allowed for by multiplication with activity factors, considering the local time of the central trajectory of the cluster [*Memmesheimer et al.*, 1991]. The diurnal variations are set equal for all emitted species, whereas the factors to distinguish weekdays from weekends vary between the species. They are analysed from emissions ratios given by the project EUROTRAC/GENEMIS

[*Ebel et al.*, 1997] for Germany, Netherlands, Belgium, France and UK for weekdays versus Saturday and Sunday [*M. Beekmann*, personal communication].

4.1.4 Mixing height

There are two general possibilities for the practical determination of the mixing height MH, namely direct derivation from vertical profile measurements or the application of parameterisations and simple models based on operationally available data [*Seibert et al.*, 2000]. The operational determination of the MH is non trivial since usually the parameterisation schemes have deficiencies. For the analysis of the flight data in this work the mixing layer heights were taken from ECMWF fields of potential temperature. The method is based on the advanced parcel method, which determines the MH as the equilibrium level of an air parcel with the potential temperature θ at ground level plus an excess temperature $\delta\theta$ of 1K [*Menut et al.*, 2000][16].

In Figure 4.2 and Figure 4.3 fields of daily maximum mixing layer heights used in the model runs are shown for the relevant periods in August and September 1997. The fields of MH are available every three hours for a domain reaching from 15°W to 25°E and 40°N to 60°N. From these fields the respective daily maximum values at each grid point were determined and used in the model. The assumption of using the maximum daily mixing layer height provides complete re-incorporation of the nocturnal boundary layer during the day. Since the nocturnal boundary layer develops in the evening before midnight, the daily maximum value was not applied for emissions from midnight to midnight at the given day, but from 20 GMT the evening before to 20 GMT on the day itself. On the last day it has to be taken into account if the incorporation takes place before the time of observation. In case of a flight in the morning hours, or if the air masses leave the continental region during the night, thus staying stably stratified over the ocean, the maximum daily mixing height indicated over the emission areas will not be reached. This is taken into account for the detailed analysis of flight A581, where a strong inversion layer around 300 m height was observed during the flight and introduced into the model as mixing layer height for the last day, starting at 20 GMT the evening before.

[16] The fields of accordingly calculated mixing layer heights are kindly provided by *R.Vautard*, Laboratoire de Météorologie Dynamique, CNRS, Paris.

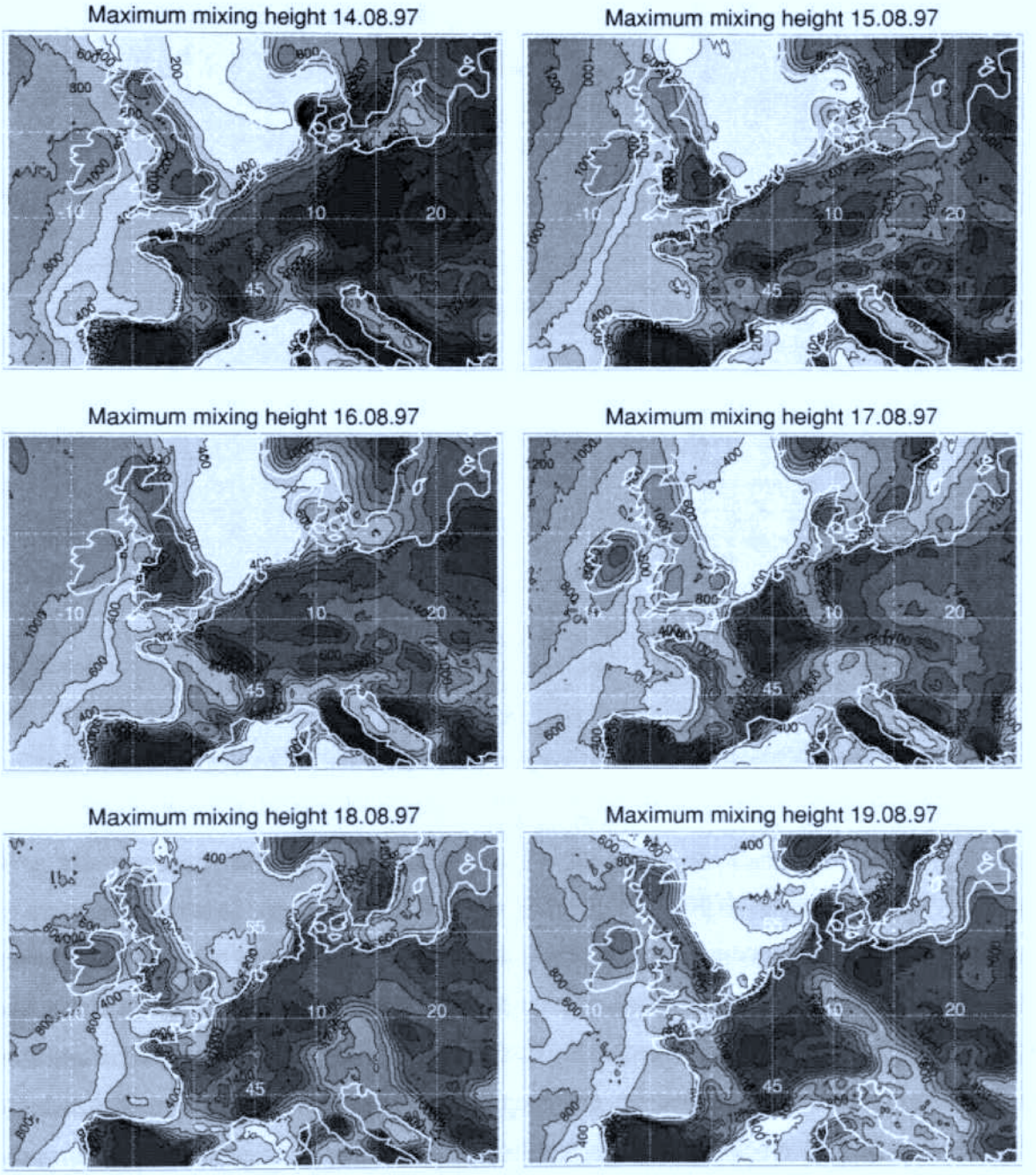

Figure 4.2: Fields of daily maximum MH from 14.-19.08.97 as diagnosed from ECMWF fields of potential temperatures [*Menut et al.*, 2000]. The lightest grey corresponds to a MH of 200 m, the darkest grey to a MH of 2000 m, with isolines every 200 m.

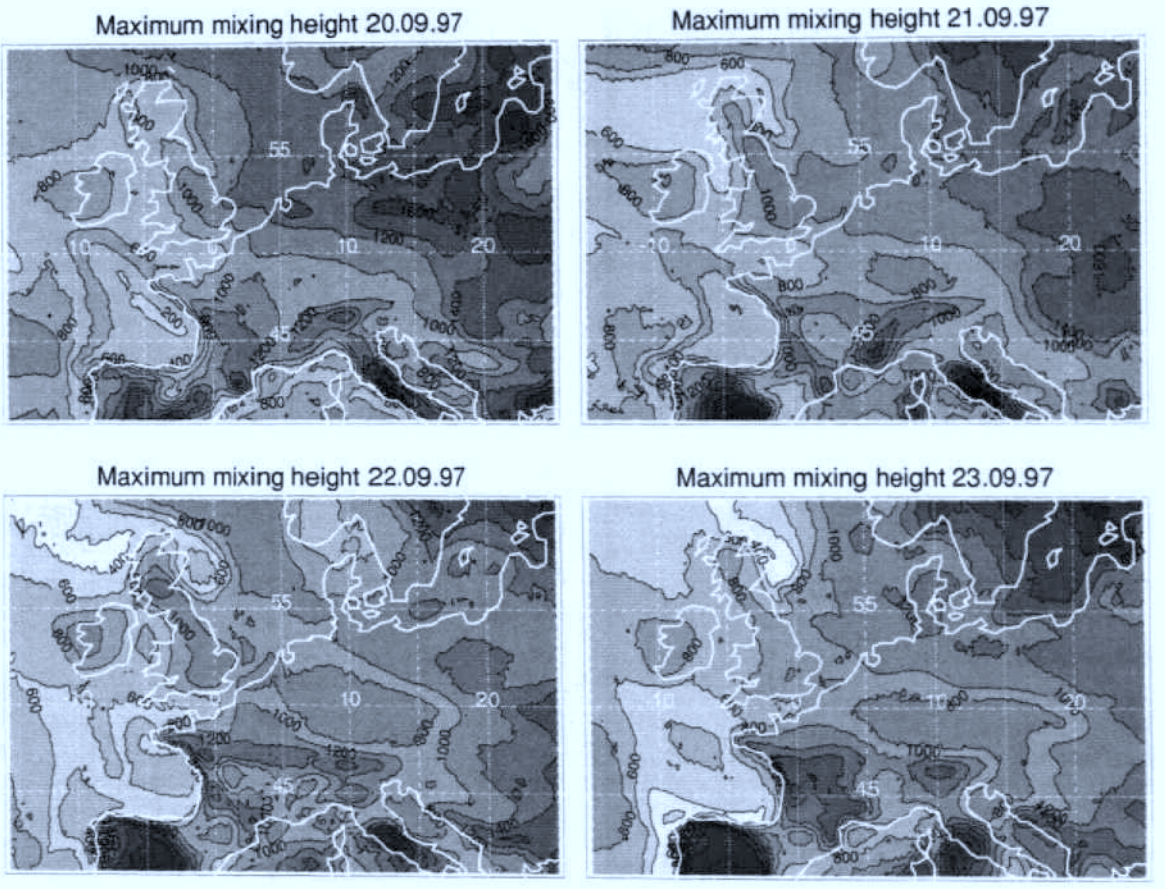

Figure 4.3: Fields of daily maximum MH from 20.-23.09.97 as diagnosed from ECMWF fields of potential temperatures [*Menut et al.*, 2000]. Levels as in Figure 4.2.

4.1.5 Limitations of the transport module

In this work the turbulence is not explicitly treated. Instead, the initial box size is set large enough that synoptic scale motions dominate over subgrid turbulent dispersion. The resolution of the model is thereby limited to the box size, which here is similar to the resolution of the emission inventory. However, emission plumes close to the source region, which have not yet spread over the size of the box, will thus not be represented within the transport module. Attempts for a better parameterisation of the initial box growth by subgrid representation of turbulence according to a particle dispersion model, which treats turbulence in a stochastic way, is currently being developed as an improved version of the transport module described here, in order to study CO_2 fluxes in the continental U.S. [*Gerbig et al.*, 1999].

Mixing and dilution is parameterised by the growth backward in time of the box defined by the trajectory cluster. Thereby tracer emissions are instantaneously diluted over the size of the box at each timestep. This is reasonable for an inert tracer for which it makes no difference in this trajectory approach whether the different air masses are first mixed and then transported or first transported and then mixed during the transport. However, because of

the non-linearity of the photochemistry of ozone production, this approach may not be completely valid when applied to chemistry modelling.

A more refined approach would be to use multiple boxes with explicit mixing between them [*Stevenson et al.*, 1998]. Such an approach would, however, significantly add to the dynamical complexity of the model and require a very large amount of model development. Therefore, it was decided to tolerate the simplification of instantaneous mixing. This gives a reasonable approximation as long as the mixing in the horizontal direction does not greatly exceed the resolution of the emission grid, which gives a lower limit for explicit horizontal mixing parameterisation possible in the model. Necessary conditions for this approach are stable weather conditions with a well defined flow situation, and limitation of the transport to a few days over emitting regions. Such conditions were aimed for in the study of anticyclonic outflow from Europe during the TACIA project.

Vertical diffusion in the model is assumed to be rapid with instantaneous mixing over the vertical extend of the mixing height. In a well mixed boundary layer, a complete turn over of the mixed layer takes place within a time scale of about one hour [*Seibert et al.*, 2000][17]. Thus, vertical mixing times are equivalent to the time step of the transport model. However, this approach does not represent residual layer above the nocturnal inversion. A two layer approach would be necessary to correctly describe the night time chemistry [*Derwent and Jenkin*, 1991] . In order to investigate differences between the single layer approach and a two (or multi) layer formulation, *M. Beekmann* [personal communication] has operated the trajectory-chemistry model MELCHIOR (Modéle Lagrangien de la Chimie de l'Ozone l'Èchelle Régionale) [*Lattuati*, 1997] in a single box mode and as a column with several vertical layers for the TACIA flight A581. Only minor differences resulted.

A more general limitation of the trajectory model approach is given by the fact that the ECMWF wind fields used to create the trajectories do not represent all scales of atmospheric motion. For example convective processes, which represent an important mechanism for vertical transport of trace gases to the free troposphere[18], are typically sub-scale processes that are not represented in the wind fields. This problem is discussed in detail in chapter 6.

[17] Compare chapter 2.2.2
[18] Compare chapter 2.2.3

4.2 Chemistry characteristics

The idea is to use the transport module, together with its emission inputs, as initialisation for a chemical box model. The chemical box model is then restarted at each and every time step of the transport module with the new meteorological and emission parameters from the transport module, as well as the chemical box model output from the last time step. The location of the moving air mass (latitude, longitude and pressure) and additional meteorological parameters such as pressure, temperature and specific humidity are taken from information content at the location of the centre of the trajectory box in the transport module. The temperature and pressure are used to calculate chemical rate constants; the specific humidity forces the water vapour concentration in the chemical box model.

The concentration of a species X is calculated in the model by forward integration of the following differential equation which contains the rates of chemical production, chemical loss, emission and deposition at each time step:

$$\frac{d[X]}{dt} = P - L \cdot [X] + \left.\frac{d[X]}{dt}\right|_{emis} + \left.\frac{d[X]}{dt}\right|_{dep} \qquad (4.2)$$

[X] is the concentration of the species,

P is the instantaneous production rate of the species by photochemistry,

L is the local removal rate of the species by photochemistry,

$\left.\frac{d[X]}{dt}\right|_{emis}$ is the emission input calculated from (4.1),

$\left.\frac{d[X]}{dt}\right|_{dep}$ is the loss due to dry deposition calculated from (4.4).

4.2.1 Chemistry scheme

The chemistry scheme is the "Regional Atmospheric Chemistry Mechanism" (RACM), which is described in [*Stockwell et al.*, 1997]. It is an updated and expanded version of the gas-phase chemical mechanism of the Regional Acid Deposition Model (RADM2) [*Stockwell et al.*, 1990], that is used in many atmospheric chemistry models [*Chang et al.*, 1989; *Hass et al.*, 1995; *Vogel et al.*, 1995]. The mechanism includes 17 stable inorganic species, 4 inorganic intermediates, 32 stable organic species, and 24 organic intermediates in 237 reactions. Heterogeneous and aqueous phase reactions are not included.

Hydrocarbons are represented using lumped species, aggregating the hundreds of VOCs in the real atmosphere into 16 anthropogenic and 3 biogenic model species. The grouping of these lumped species is based on the magnitudes of the emission rates, similarities in functional groups and the compound's reactivity toward OH [*Middleton et al.*, 1990; *Stockwell et al.*, 1997; *Stockwell et al.*, 1990].

4.2.2 Aggregation of VOC emissions

For speciation of the VOC emissions, an aggregated German urban split from the VOC database [*Mannschreck et al.*, 2000] is used[19]. The species given in this split are grouped together into the VOC classes of the RACM mechanism. To take into account the differences in reactivity of the species grouped into a class, aggregation factors according to [*Stockwell et al.*, 1990] are applied. The factor is the ratio of the fraction of the chemical species *i* which reacts with OH during the day to the fraction of the model species *m* which reacts [*Stockwell et al.*, 1997]:

$$\mathrm{Agg}_i = \frac{1-\exp\left(-\mathrm{k}_{i,\mathrm{OH}}\int[\mathrm{OH}]dt\right)}{1-\exp\left(-\mathrm{k}_{m,\mathrm{OH}}\int[\mathrm{OH}]dt\right)} \qquad (4.3)$$

For the daily average integrated OH radical concentration, $\int[\mathrm{OH}]dt$ in (4.3), a value of 1.63×10^{11} s cm^{-3} was used [*Stockwell et al.*, 1990].

Since carbonyls and organic acids are not represented in the VOC emission database, they are added to the VOC split based on data from the programme GENEMIS [*Ebel et al.*, 1997]. The VOC split used for the RACM model calculations is shown in Table 4.2.

[19] This split is composed from data by [*Abraham et al.*, ; *Bruckmann et al.*, 1983; *Bruckmann et al.*, 1988; *Ellermann et al.*, 1995; *Schmitz et al.*, 1997; *Thijsse and van Oss*, 1997; *Umweltschutz*, 1994]

Table 4.2: Specification of the total (non methane) VOC emissions into the RACM model species in volume percent. The sum differs from one hundred percent due to the application of aggregation factors [*Stockwell et al.*, 1990].

RACM class	Definition	ppb %
ETH	Ethane	7.1
HC3	Alkanes, alcohols, esthers, and alkynes with OH rate constant (298 K, 1 atm) less than 3.4×10^{-12} cm^3s^{-1}	15.5
HC5	Alkanes, alcohols, esthers, and alkynes with OH rate constant (298 K, 1 atm) between 3.4×10^{-12} cm^3s^{-1} and 6.8×10^{-12} cm^3s^{-1}	14.8
HC8	Alkanes, alcohols, esthers, and alkynes with OH rate constant (298 K, 1 atm) greater than 6.8×10^{-12} cm^3s^{-1}	1.1
ETE	Ethene	7.4
OLT	Terminal alkenes	4.1
OLI	Internal alkenes	0.5
DIEN	Butadiene and other anthropogenic dienes	0.1
TOL	Toluene and less reactive aromatics	4.5
XYL	Xylene and more reactive aromatics	4.7
CSL	Cresol and other hydroxy substituted aromatics	1.4
HCHO	Formaldehyde	4.5
ALD	Acetaldehyde and higher aldehydes	12.1
KET	Ketones	4.2
ORA2	Acetic acid and higher acids	9.2
ISO	Isoprene	0.6

4.2.3 Photolysis rates

The rate coefficients for the 23 different photolysis reactions in the RACM mechanism are computed with the associated program 'photoRACM'. Actinic fluxes are calculated from a radiative transfer model based on the delta-Eddington technique [*Joseph et al.*, 1976; *Madronich*, 1987] as described by [*Stockwell et al.*, 1990]. This method approximates the directional dependence of the radiance by two components (the Eddington approximation), one being isotropic and the other depending on the cosine of the direction of propagation. The model assumes seasonally averaged ozone and aerosol spatial distributions for the continental US. The actinic flux is calculated over a grid of 130 spectral intervals, varying in width between 1 and 10 nm depending on the changes in light absorption by O_3 and variations in the Rayleigh scattering. The photolysis rates are then determined by integra-

tion of the actinic flux with the absorption cross sections and the photodissociation quantum yields over the spectral range.

Cloud parameterisation is allowed for in the radiative transfer model, but in this work it was run for clear sky conditions only. For clear sky conditions photoRACM divides the region from the surface of the earth to the top of the atmosphere into 50 layers of 1 km each, allowing calculation of photolysis rates for each of these layers.

Comparison of different photolysis models with airborne measurements of the photolysis frequency of NO_2 have shown significant underestimation of the photolysis rates in higher altitudes by the delta-Eddington model [*Volz-Thomas et al.*, 1996]. This is attributed to the simplification of constant angular distribution of scattered light, which according to more detailed models (e.g. the discrete ordinate model TUV (Tropospheric Ultraviolet-Visible radiation model)[20]) changes considerably with altitude. Therefore the photolysis rates obtained from photoRACM were adjusted with height dependent factors by comparison with the discrete-ordinate-model TUV, which showed good agreement with the measurements. Online use of TUV in the chemical box model was refrained from because of its significantly higher computing times, and since TUV does not contain all photolysis rates used in RACM, especially for the lumped classes.

In order to allow a comparison, diurnal cycles from TUV and photoRACM were calculated for 50°N and 5°W, for each altitude level up to 12 km. The mean factor between TUV and photoRACM rate coefficients at a given height for small zenith angles was normalised to the photoRACM values at ground level, and stored for correction of the photolysis rates calculated along the trajectories. Underestimation of about 10-20% by photoRACM were found at higher altitudes, consistent with the observations of [*Volz-Thomas et al.*, 1996].

4.2.4 Deposition

Deposition is an important loss process for ozone and for many other emitted or photochemically produced species. Table 4.3 shows the deposition velocities v_d employed in the model runs. They are adapted from [*Lattuati*, 1997], with a revision of the deposition velocities for O_3 and NO_2 in consideration of surface resistances after [*Weseley*, 1989]. The velocities are parameterised depending on whether the trajectory is above land or sea, by using a land-sea mask with a resolution of approximately 0.5°. Above land, the deposition

[20] Courtesy of S. Madronich, National Center for Atmospheric Research (NCAR), calculus as done *by Stamner et al.* [1988].

velocities are subdivided into values for day and night to capture the differences given by stomata opening of the plants. A more detailed parameterisation of land-use and meteorological parameters is beyond the scope of the model approach. Thus, it has to be kept in mind that only an average representation of the deposition can be achieved.

As long as a trajectory is within the mixing layer the loss of a species mixing ratio is given as

$$\left.\frac{d[X]}{dt}\right|_{dep} = -\frac{v_d \cdot [X]}{h} \qquad (4.4)$$

where h is the mixing height of the layer.

Table 4.3: Deposition velocities [cm/s] used in the model.

Species	Deposition velocity v_d [cm/s]		
	Continental day	Continental night	Ocean
O_3	0.8	0.2	0.1
NO_2	0.55	0.05	0.05
Carbonyls	0.6	0.03	0.1
Organic acids	0.6	0.03	0.1
Organic nitrogen (PAN etc.)	0.35	0.0	0.0
HONO	1.5	1.5	1.0
HNO_3	1.5	1.5	1.0
HNO_4	1.5	1.5	1.0
H_2O_2	1.0	1.0	1.0
Organic peroxides	0.5	0.5	0.5

Wet deposition, the scavenging of trace gases due to absorption into water droplets and rainfall, is not included in the model. For anticyclonic conditions, with typically clear sky, as investigated for the TACIA project, the lack of wet deposition should have no impact on the results.

4.2.5 Initial concentrations

Initialisation of model species is required for CO, O_3, NO, NO_2, NO_y, total VOC, H_2O_2 and HCHO. Oxygen, nitrogen, methane and hydrogen are set to their climatological values, and all other species are initialised at zero concentrations.

The initial chemical composition of the trajectories can either be described directly or can be taken from larger scale Eulerian models. For the TACIA section of this work, the model initialisation was obtained with values taken from the MCT model of the University of Bergen [*Flatoy et al.*, 1995] ten days prior to the measurement.

5 Discussion of transport and chemistry during TACIA

Chemical processing in the European plumes observed in the lower troposphere over the Atlantic or North Sea will be discussed in this section. The objective is to elucidate the relative roles of VOC and NO_x emissions for photochemical ozone formation in the plume and also to see if the measured ozone precursor concentrations and the VOC/NO_x ratios are in accord with current European emission inventories.

5.1 Tracer analysis for the validation of the transport

In this chapter the objective is to establish a source–receptor relationship, which reveals the relative influence of emission areas and the travel time between source and receptor region.

As discussed in chapter 2.3 CO acts as a nearly inert tracer for recent anthropogenic emissions. Its lifetime of the order of 1-3 months is short enough that, on the one hand, concentration differences should still reflect different emissions and, on the other hand, long enough to use CO as a conservative tracer of emissions on time scales of a few days, for which photochemical decay and production can be ignored without making a significant error [*Chatfield et al.*, 1998]. In other words this enables the analyse of the dynamic history of the measured air masses without having to consider photochemical processing. Then, using CO as an inert tracer in a numerical transport model, comparison with the measurements will allow the investigation of the transport including emission input and travel times. Subsequently, this will form the basis of further analysis of photochemical processing.

For the tracer experiment, chemical production and decay are shut off in the model described in chapter 4. Since CO is not subject to deposition, only the transport module of the model was used for this part of the investigation.

5.1.1 *Discussion of the results for the* TACIA flights in 1997

The transport of CO as an inert tracer was modelled for the TACIA flights A570, A571, A572 and A581. For comparison of the observed CO data with the model results, the one-second data are averaged over the corresponding boxes given by the trajectory clusters along the flight track. A mean regional background concentration of 75 ppb CO, corre-

sponding to the lowest 5 percentiles of the measurements during TACIA[21], was added to the model results.

5.1.1.1 Divergence of the trajectory clusters

A free parameter in the transport module is the number of days the clusters of back trajectories are calculated for. Thus, before discussing the results for the individual flights it is important to investigate how many days backward in time the transport model is reasonable to run. Ten-day back trajectories were available, which is still short compared to the photochemical lifetime of CO. Nevertheless, the position error of the trajectories increases with their length. On average these errors, together with the divergence of the wind fields, lead to a growth of the boxes containing all trajectories of a cluster at a time. Therefore, the average size of the boxes gives a measure for the information that can be obtained. If the size of the box of a cluster becomes too large, only an approximate constant background will be added by running the model further back in time.

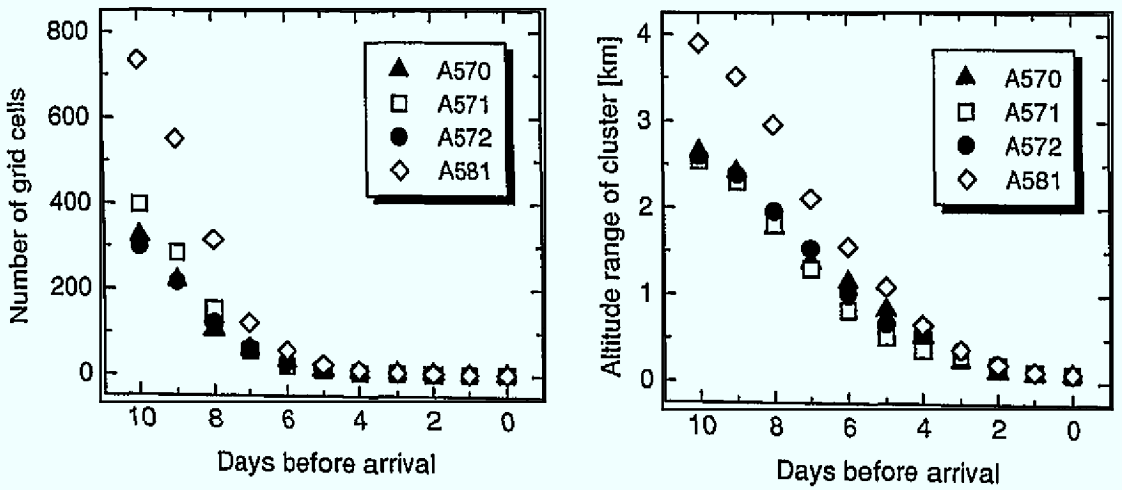

Figure 5.1: Median size of the boxes defined by the trajectory clusters as a function of the days before arrival. Left plot: median number of grid cells from which the emissions are averaged (with 50 km grid). Right plot: median altitude range of the clusters.

Figure 5.1 shows the median[22] sizes of the boxes defined by the trajectory clusters as a function of the days before arrival. The results are comparable for all analysed flights. The

[21] Compare the statistical distribution of CO data during TACIA in Figure 3.5.
[22] The median and not the arithmetic mean is used here as the size of the boxes is rather lognormal than normal distributed. Compare as well chapter 5.2.4.2 for the lognormal distribution.

number of grid cells[23] within a box shows approximately an exponential growth with time. Since, the time constant of the growth is around two days, the trajectory clusters are confined to a few grid cells during the first four days before arrival at the location of the measurement, as is shown in Figure 5.1. For more than seven or eight days before arrival the size of the boxes becomes so large that emissions from more than 100 grid cells are averaged corresponding to an area of around 250 000 km². Thus the emission input is largely averaged over rural and urban areas. For such conditions the only information that can still be obtained is whether the cluster is still within the mixing height over an continental area, or in clean air over the oceans or the free troposphere without any emission input. Since at the same time the altitude range of the clusters exceeds the mixing height of 1-2 km, no more differential diagnostic information can be obtained from this either.

Thus, for the investigated flights the transport model yields information about the history of the air masses only for seven to eight days back in time on average. Further back, the trajectory clusters become rather undefined and their accuracy is extremely questionable. The number of days that the transport model was run backward in time was determined for every flight by finding the best correlation between modelled and measured CO values.

5.1.1.2 A570, 15.08.97: Profiling east of Teeside, and along UK east coast

Example trajectories for flight A570 on 15th August 1997 are shown in Figure 5.2. Plotted are the trajectories marking the mean position of the boxes for every 10th trajectory cluster along the flight track. The flight took place over Great Britain and the North Sea close to the British coast in a very weak high pressure system with light westerly winds. As can be seen from the trajectories, the observed air masses at all altitudes originate from the North Atlantic and pass over Britain only during the last day prior to the measurements.

Accordingly, the best correlation between modelled and measured CO was found when the CO transport model was run for only one day prior to the measurement. The results for this are presented in Figure 5.3. Compared are the time series of measured and modelled mixing ratios, and their statistical distribution over the altitude. For the latter, the data were grouped into 500 m altitude intervals. The time series plot also shows the aircraft altitude at the time of measurement. For altitudes above 2 km the model yields only background

[23] The underlying grid is defined by the grid of the EMEP emission inventory with a resolution of approximately 50 km.

concentrations consistent with the measurements. Most part of the flight, from approximately 10:45 to 14:15 GMT, took place within the PBL over or close to Great Britain. For this flight section the measurements exhibit strong variations in the CO mixing ratio with vertical gradients as large as 65ppb/10m, indicative of fresh plumes which had not yet substantially mixed with the surrounding air.

On average, modelled CO mixing ratios are close to the measured CO levels inside the PBL. However, the simulated variability is smaller than that observed and the point-to-point correlation between measured and simulated CO mixing ratios is very low (r^2=0.36). This is probably due to the proximity of the sources which cannot be resolved by the model due to the finite resolution of emission data and meteorological input for the trajectory calculations. A high resolution emission inventory of the UK, and trajectory calculations based on a mesoscale model, would be necessary to obtain better representation of the local emission sources.

The statistical distribution (right panel of Figure 5.3) exhibits further deficits of the modelled CO mixing ratios. While the measured CO mixing ratios reveal a substantial drop close to the surface, the modelled values increase. Since the surface trajectories cross Great Britain with nearly the same wind direction as the trajectories at higher altitudes, this means that the measured low surface values cannot be obtained with the assumption of a well mixed boundary layer in the model. A possible explanation would be that a local sea-breeze, which is not represented in the model, may yield in cleaner air at the lowest levels, since the measured low CO mixing ratios are mainly observed close to the surface over the sea.

Another striking feature from the distribution plot is that the measured CO values show significant vertical mixing of pollution up to about 2 km, while the modelled CO mixing ratio drops to background level already at around 1.5 km. Therefore, the model mixing height over Great Britain is too low for this situation.

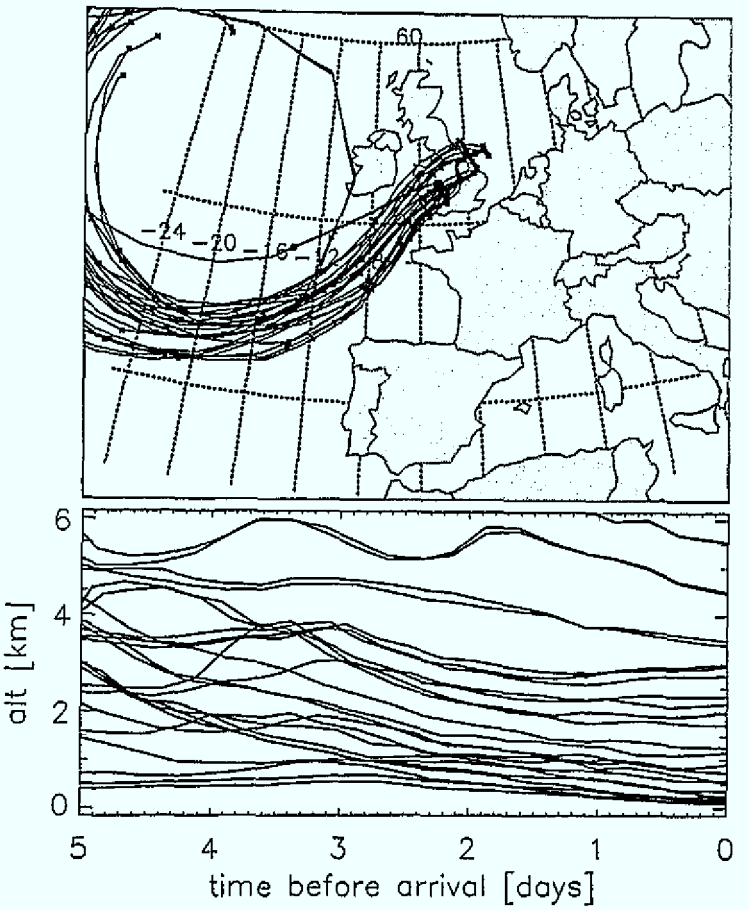

Figure 5.2: Example trajectories of the mean position of the clusters for flight A570 on 15th August 1997. The thick black line shows the flight path of the plane. Crosses mark every 24 hours along horizontal displacement of the trajectories.

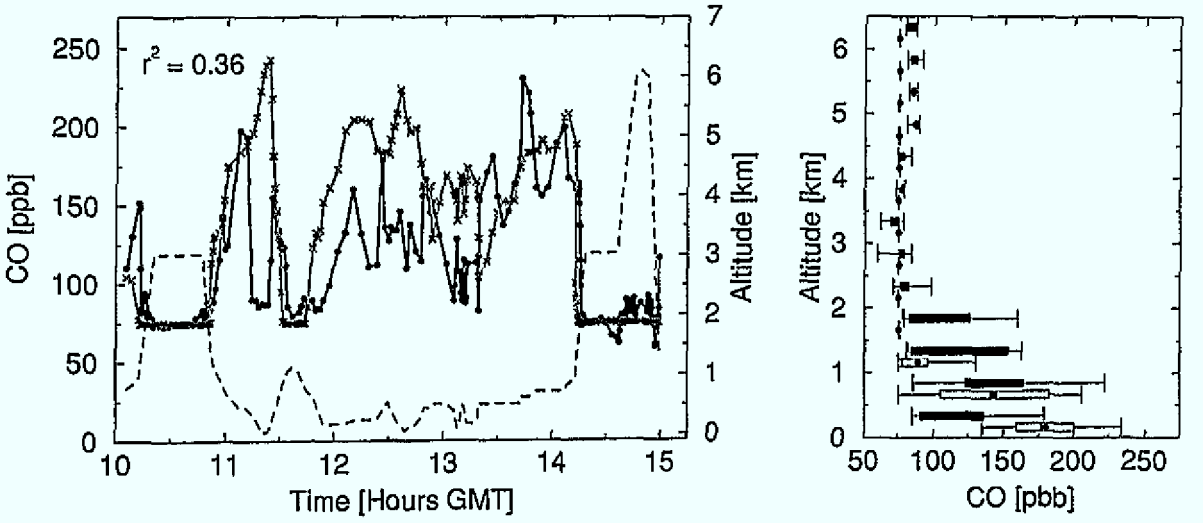

Figure 5.3: Measured and modelled CO mixing ratios for flight A570. Left panel: time series with modelled CO as grey crosses, measurements as black circles. The dashed line shows the aircraft altitude. Right panel: distribution of modelled (lighter grey) and measured (darker grey) CO mixing ratios for altitude classes of 500 m each. The central 50% are given by the box, the 5 and 95 percentiles by the bars. The bar within the box marks the median, and the dot the mean of the distribution.

5.1.1.3 A571, 18.08.97: Profiles over the North Sea at different distances from the coast

The flight A571 on 18th August 1997 took place over the south part of the North Sea with the aim of measuring the chemical composition of a continental plume at different travel distances from the coast. The flight pattern involved several traverses with low level profiles at increasing distance from northern Germany. The meteorological situation was given by a rather large but weak high system pressure extending over Europe, with the centre of the anticyclone over Scandinavia [*Evans*, 1999]. This led to a weak outflow of air from Northern Germany and the Netherlands over the North Sea, with light or almost stagnant winds. The example trajectories in Figure 5.4 show this outflow. Considerable variation existed, with part of the trajectories looping over the North Sea and then staying over the European continent for at least ten days before the measurement. Because of this long residence time, the transport model was run 8 days back in time. A longer model run does not improve the results any further because the trajectories become extremely questionable[24].

The visual comparison of modelled and measured CO mixing ratios in the time series in Figure 5.5 reveals a general agreement between observed and modelled values, although the point-to-point correlation is very weak (r^2=0.26). The good general agreement is due to a good coincidence of variations of measured and modelled CO levels as far as the emission inventory at low spatial resolution is concerned. However, the amplitudes of measured and modelled CO mixing ratios are still differerent. This can also be seen in the distribution plot (Figure 5.5, right panel), which shows that the mean CO values at the different height levels agree remarkably well while the form of the distribution varies. The modelled distribution shows spikes of high CO mixing ratios, which lead to 95 percentile values far above the measurements, close to the surface, and again at 2-2.5 km altitude. The strong variability in the modelled CO mixing ratios is caused by the extremely low wind speeds. The trajectory clusters that produce the spikes of high CO mixing ratios were found to loop, or stay almost stagnant, over strongly emitting areas such as the heavily industrialised Manchester (UK) region or the "Ruhrgebiet" in Germany.

[24] Compare chapter 5.1.1.1

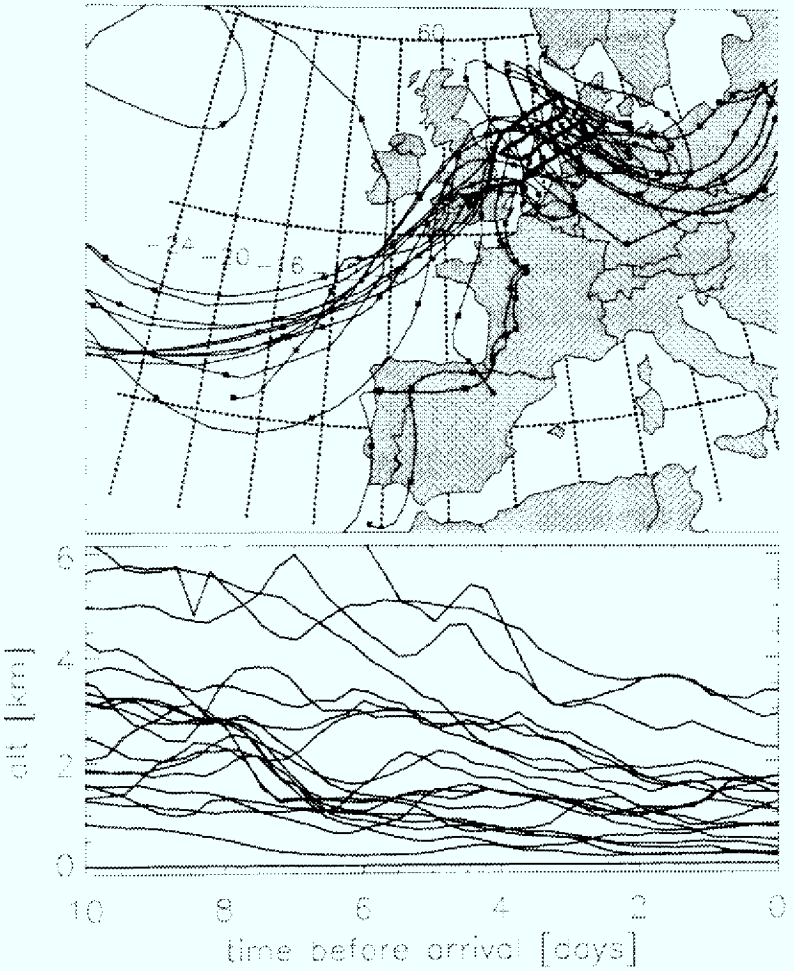

Figure 5.4: Example trajectories of the mean position of the clusters for flight A571 on 18th August 1997. The thick black line shows the flight path of the plane. Crosses mark every 24 hours along horizontal displacement of the trajectories.

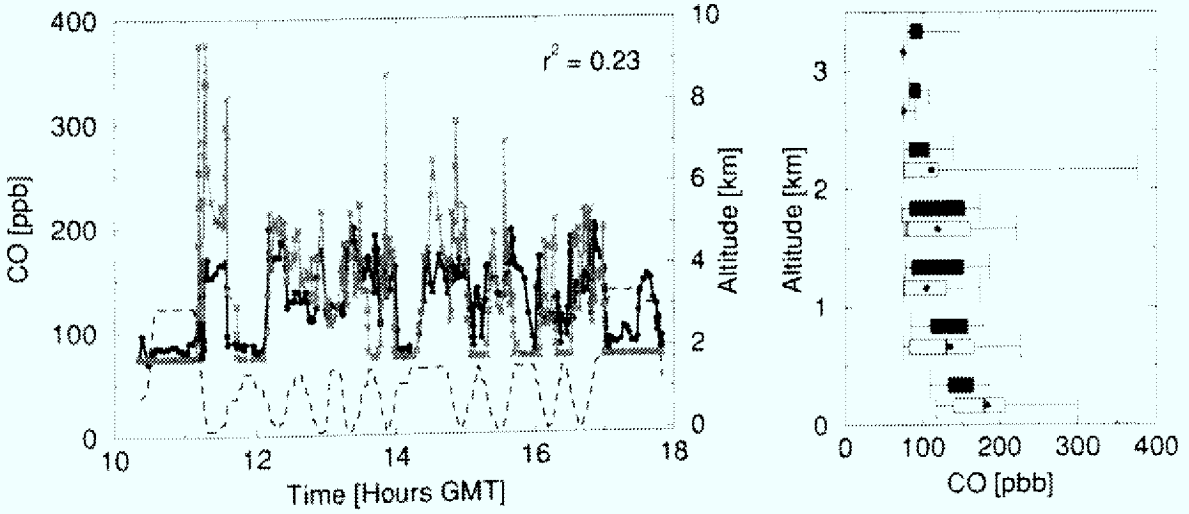

Figure 5.5: Measured and modelled CO mixing ratios for flight A571. Left panel: time series with modelled CO as grey crosses, measurements as black circles. The dashed line shows the aircraft altitude. Right panel: distribution of modelled (lighter grey) and measured (darker grey) CO mixing ratios for altitude classes of 500 m each. The central 50% are given by the box, the 5 and 95 percentiles by the bars. The bar within the box marks the median, and the dot the mean of the distribution.

That these narrow spikes do not match measured CO mixing ratios is not surprising, as it takes only very slight changes in the trajectory position to miss highly emitting but spatially concentrated source regions. In addition, the overall somewhat smaller variability in the measured CO mixing ratios indicates mixing of air masses that are heavily loaded from anthropogenic sources, with cleaner air from nearby less-or-non emitting regions. Also, at very low wind speeds turbulent diffusion might be no longer negligible, thus leading to limitations in the applicability of the model for the meteorological situation of this flight.

On average for this flight the model mixing height seems to represent the meteorological situation well, as can be seen by the good agreement of the mean concentrations in the statistical distribution over the height. In particular, the model statistically reproduces the measured mixing of CO emissions up to 1.5-2.5 km altitude. Nevertheless, at some parts during the flight (e.g. at 15:45 – 16:00 GMT) the model shows background concentrations already at 1.5 km in contrast to the measurements which exhibit similar CO mixing ratios as in the lower flight levels. This indicates problems with the parametrisation of the MH or the accuracy of the trajectory height for these parts. Since the CO concentrations are integrated over emissions of several days, it is not possible to attribute this problem to one cause.

The enhanced CO mixing ratios observed at 17: 30 – 17:50 GMT at around 3 km altitude during the return transit back over England, are not reproduced by the model. The trajectories show that these air masses were transported with westerly winds over the Atlantic. The enhanced CO mixing ratios at this part of the flight indicate long range transport of air pollutants from far away source regions, probably the American continent. That this is not resolved by the model is not surprising, as the emissions probably have occurred more than 10 days back in time, thus outside the model domain.

In summary, while no explicit source-receptor relationship for a given observation point defined by a trajectory cluster can be established under these low wind conditions, the model does reveal its ability to reproduce the main levels of CO mixing ratios.

5.1.1.4 A572, 19.08.97: Profiles along the English Channel into the North Sea; crossing of a warm front over the west side of Great Britain

One day later, on 19th August 1997, the meteorological situation was still determined by the anticyclone over Scandinavia, but a warm front had intruded and was stretching down

the west side of Great Britain. On flight A572 a series of profiles were conducted between the surface and 2 km altitude along the English channel up into the North Sea and then crossing the warm front over the Irish Sea. The example trajectories in Figure 5.6 show this twofold situation with the anticyclonic flow around Scandinavia over the North Sea and air masses of south-westerly origin over the channel and Great Britain. Again, very low wind speeds are connected with the high pressure system, leading to long residence times of the air masses over Northern Germany, the Benelux countries and Northern France. A model run starting 7 days prior to the flight yields the best compromise between additional emission information and increasing inaccuracy of the trajectories at longer times.

In accordance with the flight pattern, the time series of modelled and measured CO mixing ratios in Figure 5.7 will be discussed in three parts. The first part of the flight over the British channel, until about 15:00 GMT, took place in close proximity to emission areas. This leads to the observation of relatively fresh plumes with elevated CO, particularly close to the surface. The model generally reproduces these plumes, but overestimates their magnitude. As discussed already for flight A570 this is not surprising, as the model is at the limit of its resolution capability in this proximity to the sources. Erroneous local emission inventories, slightly wrong wind directions or wind speeds, as well as the lack of explicit parameterisation of the variability of the mixing height and turbulent diffusion, they may all cause substantial errors in the estimate of the local CO mixing ratios.

The second part, from about 15:00 to 17:00 GMT, investigating the anticyclonic flow over the North Sea, exhibits generally good agreement between model and measurement. Only a layer of rather clean air observed from about 16:30-16:45 GMT is not represented in the model calculations. This could be due to a local decrease of the mixing height that is not represented in the daily maximum MH fields used for the model calculations.

For the third part of the flight, from about 17:00 to 20:00 GMT, crossing the warm front in the west of Great Britain at different altitudes, the model yields only background values even for low flight levels, generally consistent with the measurements. The trajectories show that the encountered air originated from the clean southern Atlantic. Similar to flight A571, a plume of elevated CO measured at about 3 km altitude, which is probably attributable to long-range transport, is not captured by the model.

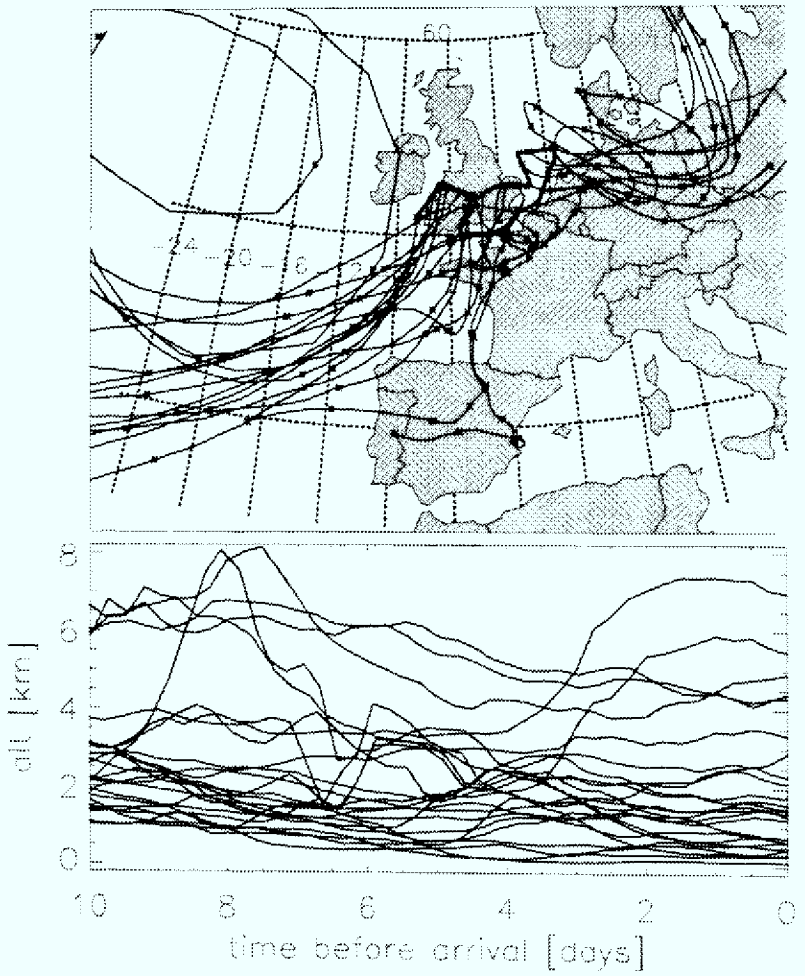
60
50
40
30
20
10
0
-10
-20
-30
-40
-50
-60
-70
-80
-90
-100
-110
-120
-130
-140
-150
-160
-170
-180
-190
-200
-210
-220
-230
-240
-250
-260
-270
-280
-290
-300
-310
-320
-330
-340
-350
-360
-370
-380
-390
-400

The statistical comparison of the profiles (Figure 5.7, right panel) generally renders a good agreement between measured and modelled time series. The model's overestimation of CO mixing ratios over the British channel leads to an overestimation of the amplitude of CO mixing ratios in the lower levels in the mean. Observed CO variations at altitudes > 3km are not captured by the model.

5.1.1.5 A581, 23.09.97: Ferry flight Azores-UK; profiles south west of Great Britain

Flight A581 on 23rd September 1997 did not take place during the main TACIA campaign in August 1997, but on the flight back from the Azores to Great Britain at the end of the ACSOE summer campaign. The first part of A581, until the south-western approaches to the United Kingdom were reached, was a ferry flight in the mid troposphere. Thereafter, a saw-tooth profiling flight track was flown in and out of the atmospheric boundary layer, over the Bristol Channel and the South-Western Approaches [*Hov et al.*, 1998]. While a low pressure system with associated trough and frontal features was crossed during the transit, the boundary layer profiles were flown at approximately right angles to an anticyclonic flow out of continental Europe. A high pressure system had been centred over the north east of Great Britain / North Sea for about 5 days. Thus, a flow of air around the anticyclone across northern Europe had sufficient time to develop [*Richer et al.*, 2000]. This flow over polluted regions of Germany, the Netherlands, Belgium, southern England and northern France is shown by the example trajectories in Figure 5.8. A model run starting 4-5 days prior to the measurements is appropriate to capture this flow.

Specific for this flight, the observed pollution was found to be trapped by two inversions[25], one at 200 - 400 m and one at 900 – 1200 m. Mesoscale model calculations with the French model Meso-NH [*Bougeault et al.*, 1995], as well as comparison with radiosonde data, show that the low level inversion developed over the European continent and southern England on the evening prior to the flight [*J. Kowol-Santen*, personal communication]. Thus, the lowest layer represents the nocturnal boundary layer, which stays stably stratified over the ocean at the day of the flight. This situation was included in the model calculations by fixing the mixing height to 300 m for t > 20:00 GMT on 22nd September.

[25] This is discussed in more detail in chapter 5.2.1.

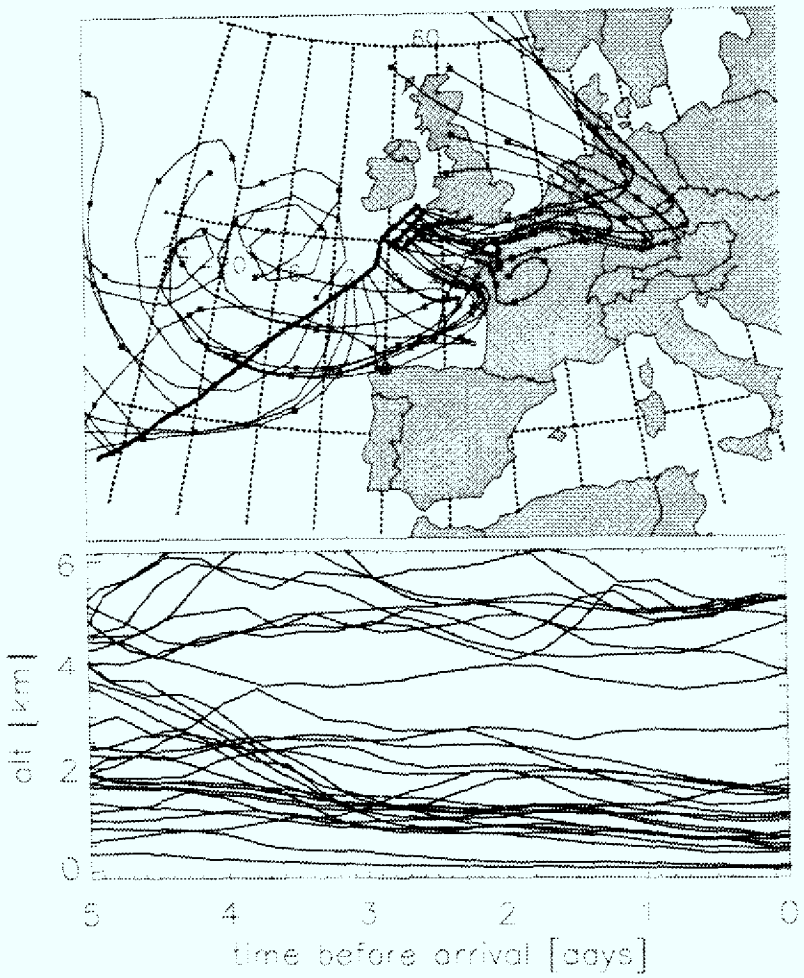

Figure 5.8: Example trajectories of the mean position of the clusters for flight A581 on 23rd September 1997. The thick black line shows the flight path of the plane. Crosses mark every 24 hours along horizontal displacement of the trajectories.

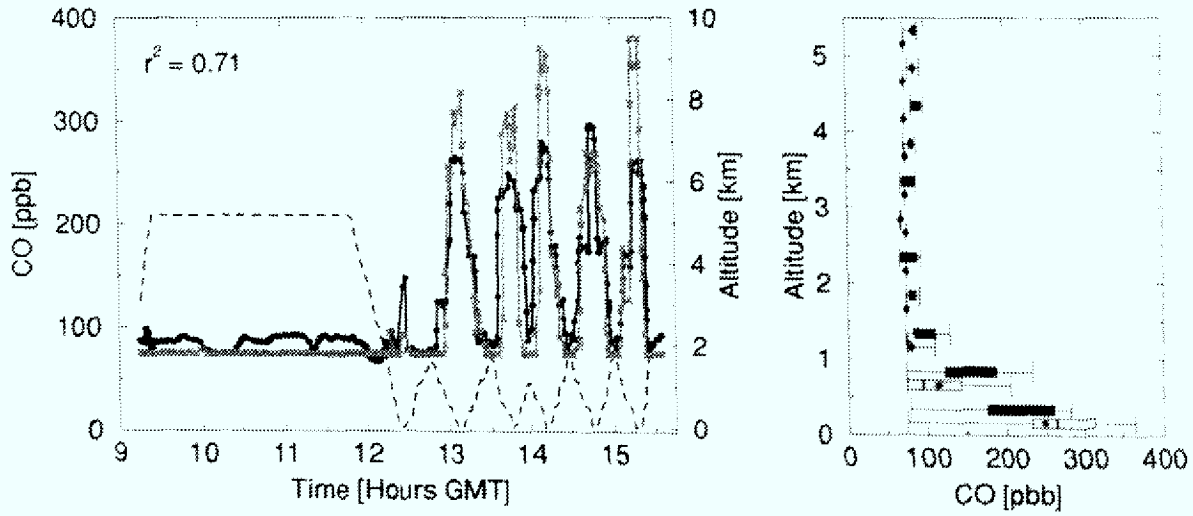

Figure 5.9: Measured and modelled CO mixing ratios for flight A581. Left panel: time series with modelled CO as grey crosses, measurements as black circles. The dashed line shows the aircraft altitude. Right panel: distribution of modelled (lighter grey) and measured (darker grey) CO mixing ratios for altitude classes of 500 m each. The central 50% are given by the box, the 5 and 95 percentiles by the bars. The bar within the box marks the median, and the dot the mean of the distribution.

The time series in Figure 5.9 generally show a strong contrast between polluted boundary layer air and clean background values in the free troposphere. This contrast is generally captured by the model, which leads to a good correlation of modelled to measured CO mixing ratios with r^2=0.71. Additionally, distinct layers in the measured CO mixing ratio within the polluted boundary layer are found, separated by the above-mentioned low level temperature inversion. This can best be seen in Figure 5.9 for the profiles between 14:30 and 15:00 GMT. The highest mixing ratios of CO up to 300 ppb are observed close to the surface, with a sharp drop to mixing ratios of about 170 to 230 ppb above the inversion at around 300 m. Above the second inversion free tropospheric background values are found of about 75 ppb. For ease of discussion below the three resulting layers are in the following referred to as the surface layer (SL), the mid boundary layer or mid PBL(MPBL), and the free troposphere (FT).

Despite the good correlation, the statistical distribution (Figure 5.9, right panel) exhibits major differences of model results to the measurement. The model overestimates the CO mixing ratios in the lowest level and produces a too fast decrease of the mixing ratios with height. This indicates that the modelled mixing height was too low. In the time series this can clearly be seen in the profiles between 13:30 and 14:15 GMT, where the modelled CO drops already to background values, while the measurement still shows mid PBL CO mixing ratios.

For the elucidation of possible problems with the maximum mixing heights used in the model, temperature and relative humidity profiles, taken from aboard of commercial flights as part of the MOZAIC program [*Marenco et al.*, 1998] will be used.

In Figure 5.10, profiles of temperature and relative humidity are shown for 20th September 1997, 17:20 GMT near the airport of Frankfurt a.M., and at Paris for 21st September 1997, 16:35 GMT. Both profiles show high relative humidity below 1250 to 1500 m altitude and a precipitous drop above, plus a strong temperature inversion at these altitudes. This indicates a well mixed boundary layer that is capped by strong temperature inversions above 1.4 and 1.3 km. Figure 5.10 also contains dashed horizontal lines that indicate the maximum mixing height from the diagnosed ECMWF fields of potential temperatures (Figure 4.3) for the appropriate day and position. Obviously, the fields give a major underestimation of the mixing height in these cases. From this point-to-point comparison it cannot be concluded whether there is a general underestimation of the mixing height or if only parts of the diagnosed fields of mixing heights should be corrected. Guided by the relative posi-

tions of actual to ECMWF-derived inversion heights, the complete fields of daily mixing heights used in the transport model were multiplied by the factor 1.5 and the model was rerun with the corrected MH values.

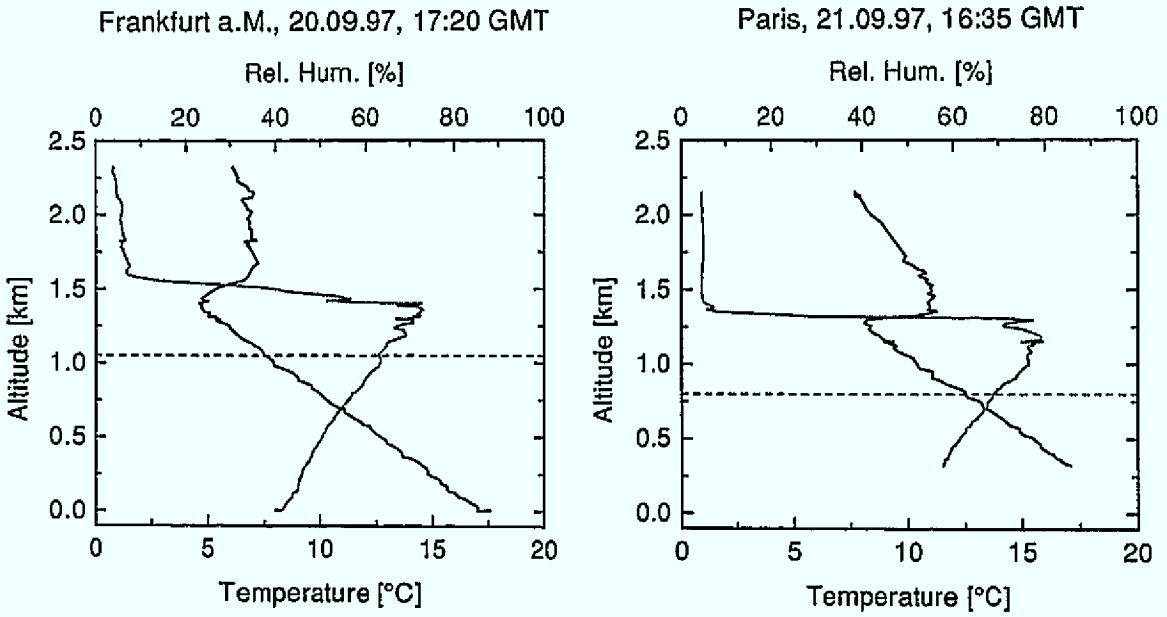

Figure 5.10: Profiles of temperature (black) and relative humidity (grey) measured aboard commercial aircraft as part of the MOZAIC program [*Marenco et al.*, 1998]. Shown are afternoon profiles in Frankfurt a.M. on 20th September and Paris on 21st September 1997. The dashed line gives the respective daily maximum MH from the modelled fields.

The results shown in Figure 5.11 strongly support this approach. A much better agreement between modelled and measured CO mixing ratios is achieved for the time-wise as well as the statistical comparison. Now, the distribution of modelled CO values closely follows the measured mean, median and maximum values, although for 0.5 – 1.5 km altitude the CO distribution is still centred slightly too low. In the time series the gradients between the different layers are very well captured as well. The successful correction is reflected in an improved correlation coefficient (r^2=0.84) between modelled and measured values.

Some deviations are found in the magnitude of the surface layer CO mixing ratios. The model overestimates the CO levels for the profiles at the north eastern edge of the sampling region (14:10 and 15:20 GMT), and underestimates them at the south western edge (13:10 and 14:45 GMT). As already discussed for the flights A570 and A572, this reflects the limitations of the model in reproducing plumes close to the concentrated source regions. A closer examination of the trajectories starting in the surface layer shows that the northern ones see recent emissions from southern England, while the southern ones just miss these emission areas by crossing over the British channel. Thus the erroneous magni-

tudes may be due to slightly wrong wind directions in the trajectory calculation or the lack of turbulence parameterisation, which prevents a horizontal dispersion of the English plume.

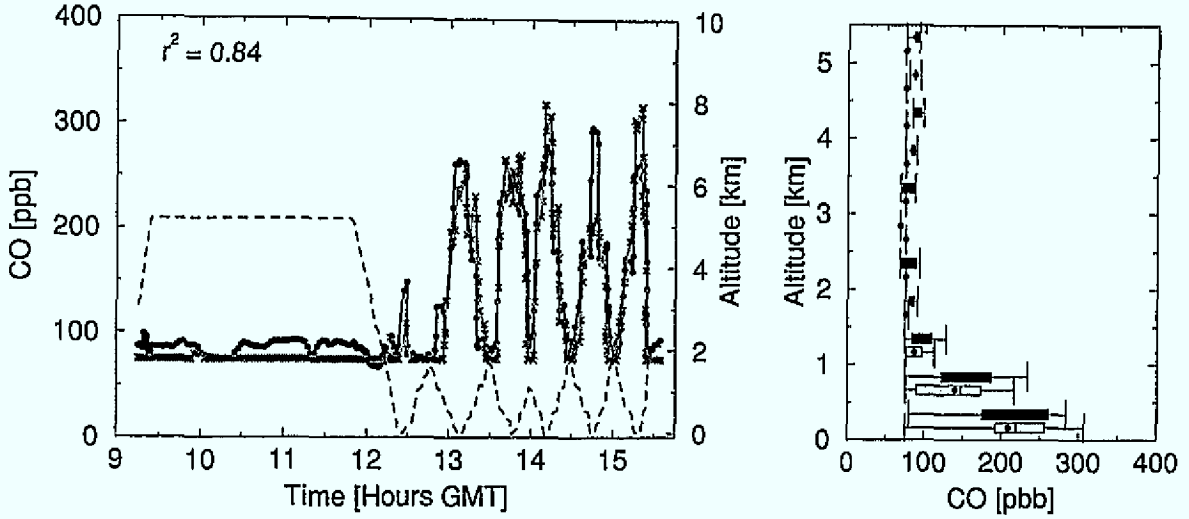

Figure 5.11: Measured and modelled CO mixing ratios for flight A581, with MH multiplied by factor 1.5. Left panel: time series with modelled CO as grey crosses, measurements as black circles. The dashed line shows the aircraft altitude. Right panel: distribution of modelled (lighter grey) and measured (darker grey) CO mixing ratios for altitude classes of 500 m each. The central 50% are given by the box, the 5 and 95 percentiles by the bars. The bar within the box marks the median, and the dot the mean of the distribution.

5.1.2 Summary of transport model performance

Despite the problems discussed in the previous sections, the newly developed model is a useful tool for description of the export of European emissions. The analysis of the statistical distribution over the flight altitudes shows that the CO budget is satisfactorily reproduced in the model runs, implying a generally good accuracy of the emission inventory for CO and the back trajectories. Difficulties are noted close to emission areas, where the resolution of the model is not appropriate, and for cases with poorly defined winds, especially with very low wind speeds. In the latter case, besides problems with the accuracy of the trajectories, turbulent diffusion might be no longer negligible against the divergence of the wind fields.

A key input parameter for the model is the mixing height. As continuous profile measurements for the operational determination of geographical fields of mixing layer heights are not generally available, the use of numerical model output is indispensable. Obviously, the results then strongly depend on the characteristics of the model, especially its boundary layer formulation and vertical resolution. A comparison of different methods for the determination of the mixing height [*Seibert et al.*, 2000] has shown deficiencies of all tested

parameterisation schemes under certain conditions. For this work, the correction of the available fields of mixing heights with a correction factor obtained from comparison with aircraft profiles, seems a reasonable compromise.

A general validation of the transport model approach is not possible in this work because of the limited number of flights and weather situations covered by these flights. An improved version of the transport model, with higher resolution of trajectories and emission inventories close to the target region, has been developed at Harvard University, MA, USA, against long-term tower and aircraft measurements of CO [*Gerbig et al.*, 1999a]. There, the model reproduces the variations of the measured CO well. In the new version the model explains 50 % of the CO variance of the tower measurements in 1996 (r^2=0.5), whereupon during winter the explained variance reaches 65 % and more. The exceptions are during summer, when small-scale convective redistribution and other sources of CO such as oxidation of biogenic hydrocarbons, may play a role, but are not included in the model Overall, the model proves to be a helpful tool for further understanding point measurements of tracers like CO.

5.1.3 Conclusions from the tracer analysis

The aim of the transport analysis was to establish a source-receptor relationship that allows the investigation the chemical processing and ozone production during the transport of the air masses. In order to allow for analysis of the chemical processing, the transport conditions should be as simple as possible and well understood.

As shown in the tracer experiment, the air masses investigated during the TACIA flights come form a large, continental size emission area, to which, in comparison, the transport time into an emission-free area over the ocean is small. Consequently, the emission area cannot be treated as a point source, but the superposition of emissions from different sources and with different transport times has to be taken into account. Consequently, only those measurements are valuable for *chemical* model calculations, where the transport module is able to reproduce the integrated CO information reliably, and thus provides the needed time- and space-resolved emission information.

In the August flights (A570, A572) the proximity of the source regions and the low wind speeds lead to mismatches of the observed and modelled plumes. Although statistically the CO budget observed during the flights is satisfactorily represented in the model runs, the

history of emission loading and transport is questionable for individual air masses. One question at this point is whether the measurements of CO as tracer of anthropogenic emissions would enable the correction of erroneous emission loadings in the model run. Unfortunately, this is prohibited due to the complex source distribution. A correction of the modelled emissions by the measured CO mixing ratios would only be possible if the source distribution and its relative contributions are well known. This could, for example, be the case if the source region is far enough away to be considered as a point source, or if homogenous emission input can be assumed on average. Unfortunately, neither was the case for the August flights. Therefore, *chemical* modelling for *these* flights would not elucidate the relative roles of VOC and NO_x emissions in the formation of ozone in the plume, as deviations between modelled and measured chemical species cannot be distinguished between transport and chemical explanations.

The situation is different for flight A581 on 23rd September 1997. For this flight a very good agreement between measured and modelled CO mixing ratios is found, which indicates a good presentation of the transport situation by the model. This is mainly due to the stable flow situation that developed around the high pressure system centred over the north east of England. The approximations regarding mixing and dilution, as assumed in the transport module, are reasonable and justified for this flight. In addition, the transport of the air masses over the European continent is limited to 3-4 days, for which the trajectories under these meteorological conditions yield sufficiently good accuracy to represent the transport. Therefore, flight A581 will be further investigated in the context of chemical modelling in the following.

5.2 Investigation of ozone production within the PBL for the TACIA flight A581

In this chapter the chemical composition of a continental European plume as it moves over the sea is analysed with respect to the relative roles of VOC and NO_x in the formation of ozone. In particular, the question is discussed of whether it is possible to learn more about the emissions and the VOC/NO_x ratios of these ozone precursors from the observation of the plume composition.

The analysis of ozone formation requires not only a non-ambiguous transport situation to be described by the model, but also a meteorological situation which is favourable for

photochemical ozone production. In the first paragraph, these conditions and chemical observations will be described in more detail, before analysing the chemical progression of the plume by model calculations.

5.2.1 Observations

The observations for flight A581 exhibit a clear signature of photochemical O_3 production. This was shown in the O_3/CO relationship discussed in chapter 3.3.2 (Figure 3.8), where for CO mixing ratios up to about 100 ppb a strong correlation between O_3 and CO with a slope of 0.34 ppbO_3/ppbCO was found. In this plot the decrease of O_3 for CO mixing ratios between 200 and 300 ppb is conspicuous. This will be analysed more closely using the measured vertical profiles.

5.2.1.1 Vertical profiles

A total of 12 low-level vertical profiles in three traverses were carried out in the observation area (SW Approaches and Bristol Channel), with 30 bottles for hydrocarbon analysis sampled during short horizontal runs at different altitudes (Figure 5.12).

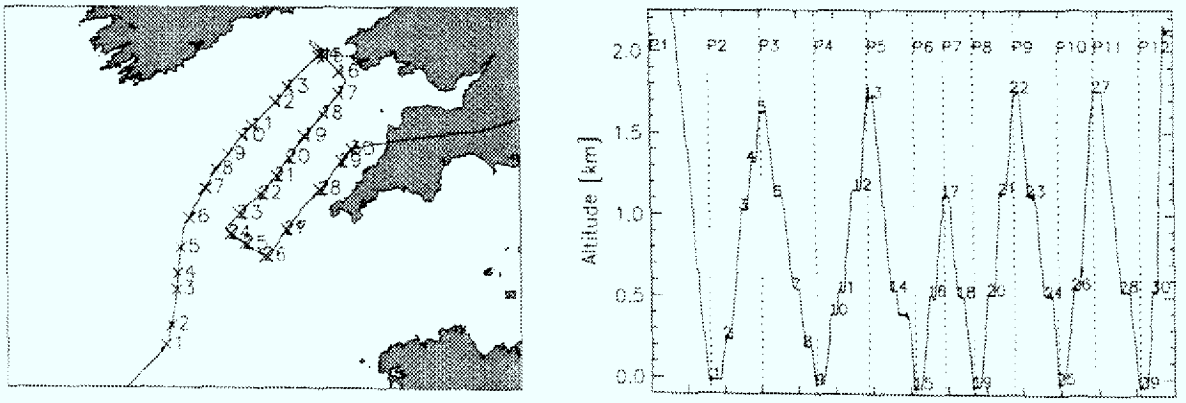

Figure 5.12: Flight track with bottle filling positions (1-30) and profile numbers (P1-P12) for flight A581.

An example of a typical profile measured during flight A581 (profile 10) is shown in Figure 5.13. It shows the three distinct layers in the measured CO mixing ratios, as already discussed in chapter 5.1.1.5, with background values in the FT, mixing ratios around 200 ppb in the MPBL, and the highest mixing ratios up to 300 ppb in the surface layer. As with the other trace gas measurements, distinct changes in the mixing ratios were notable between the layers. O_3 was found to have the highest mixing ratios of around 80 ppb in the MPBL, decreasing to mixing ratios of less than 60 ppb in the SL. This corresponds to the

decrease of O_3 at high CO mixing ratios found in the O_3/CO relationship (Figure 3.8). The decrease of ozone in the surface layer in accompanied by high NO_x mixing ratios of about 8 ppb.

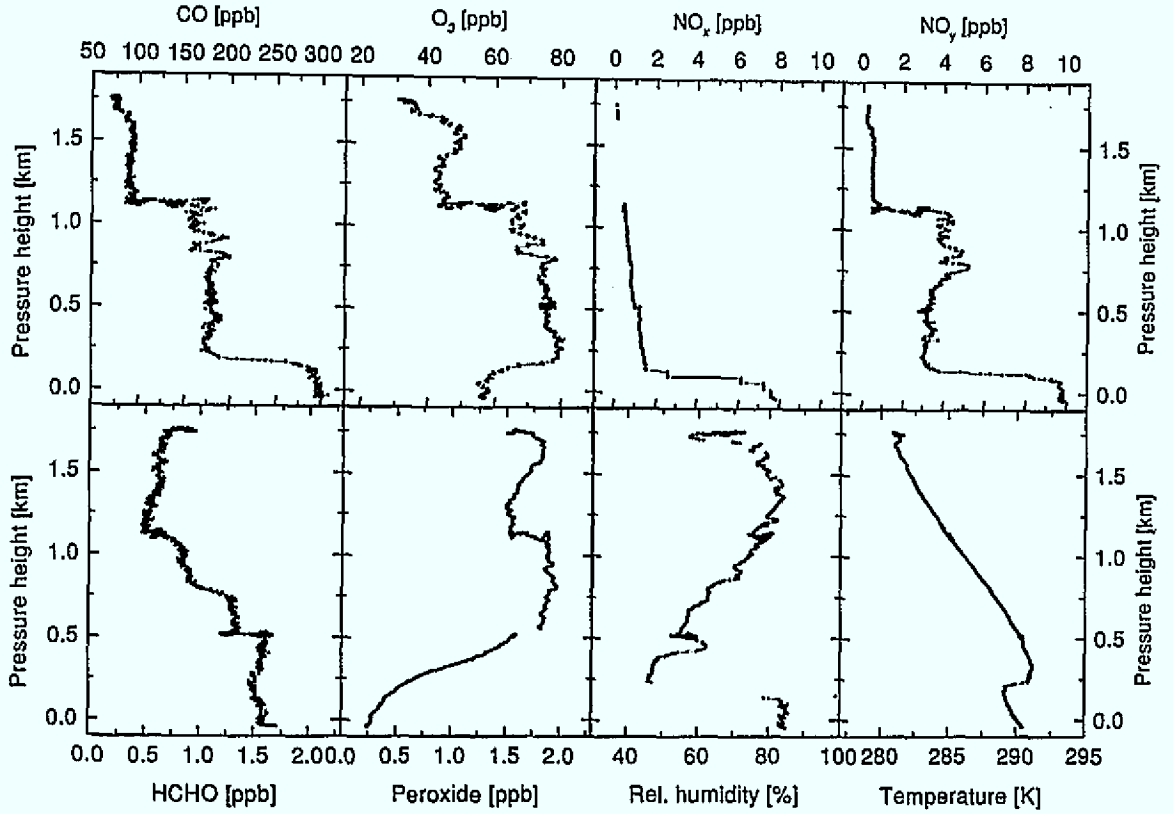

Figure 5.13: Typical profile (profile 10) of flight A581 showing CO, O_3, NO_x, NO_y, HCHO, peroxide, relative humidity and temperature.

Nevertheless, the NO_x mixing ratios in the surface layer are not high enough to explain the decrease in ozone by titration with NO. On the other hand, the differences between the NO_x and NO_y profiles of Figure 5.1, indicate a marked difference of photochemical age between the MPBL and SL. While the NO_y mixing ratios mainly reproduce the structure of the CO profile, NO_x shows nearly as high mixing ratios as the observed NO_y in the SL, but is about a factor 5-10 lower in the MPBL. The decrease is very likely caused by chemical ageing of the MPBL air mass as NO_x undergoes reactions during the evolution of the plume.

Qualitatively the same conclusion can be drawn from the analysis of the ratios of individual hydrocarbons detected in the 30 flask samples collected during this flight. The decline of shorter-lived alkanes relative to CO as a measure for the emission strength, indicates a higher chemical age of the air masses in the MPBL than in the SL [*Richer et al.*, 2000].

Due to a problem with the organic channel of the peroxide instrument for flight A581, effectively the sum of H_2O_2 and organic peroxides was measured. This sum will be referred to in the following as peroxide. Peroxide shows a decrease of mixing ratios towards the surface. This could be due to deposition which is an important loss process for peroxides. Also, at high NO_x mixing ratios the production of peroxide is suppressed because HNO_3 is the dominant OH radical sink under these conditions[26]. This again indicates fresh pollution in the surface layer, thus the photochemistry is still within the VOC limited regime.

While the mixing ratios of formaldehyde within the plume are high compared to the values in the free troposphere, no significant difference between HCHO mixing ratios in the SL and the MPBL were observed. However, it cannot be ascertained whether this is for chemical reasons, as the time resolution of the formaldehyde measurements (5 min.) is comparable to the duration of the measurements in the surface layer, where, consequently, gradients in the mixing ratios can only partly be resolved.

5.2.1.2 Partitioning of the data into classes

Although there is clearly some variability between the observations for different profiles, generally the layering described for Figure 5.13 has been found for most of the profiles. Therefore, the data can be clustered into three classes, corresponding to the layers SL, MPBL and FT.

In the following, only data measured at the flask sampling locations will be discussed, since the measurements of VOC is essential for the investigation of the relative roles of VOC and NO_x in the O_3 production. This data can be attributed to the different layers as follows: the surface layer (SL) with bottle samples obtained at about 30 m altitude, the mid boundary layer (MPBL) sampled at around 600 m, and the free troposphere (FT) sampled above the second inversion at more than 1.2 km. Not included are data from the first two profiles as the double layered structure was not apparent until profile 3, and some bottle samples obtained at interim altitudes could not clearly be attributed to one of the layers.

[26] Compare chapter 2.1.3

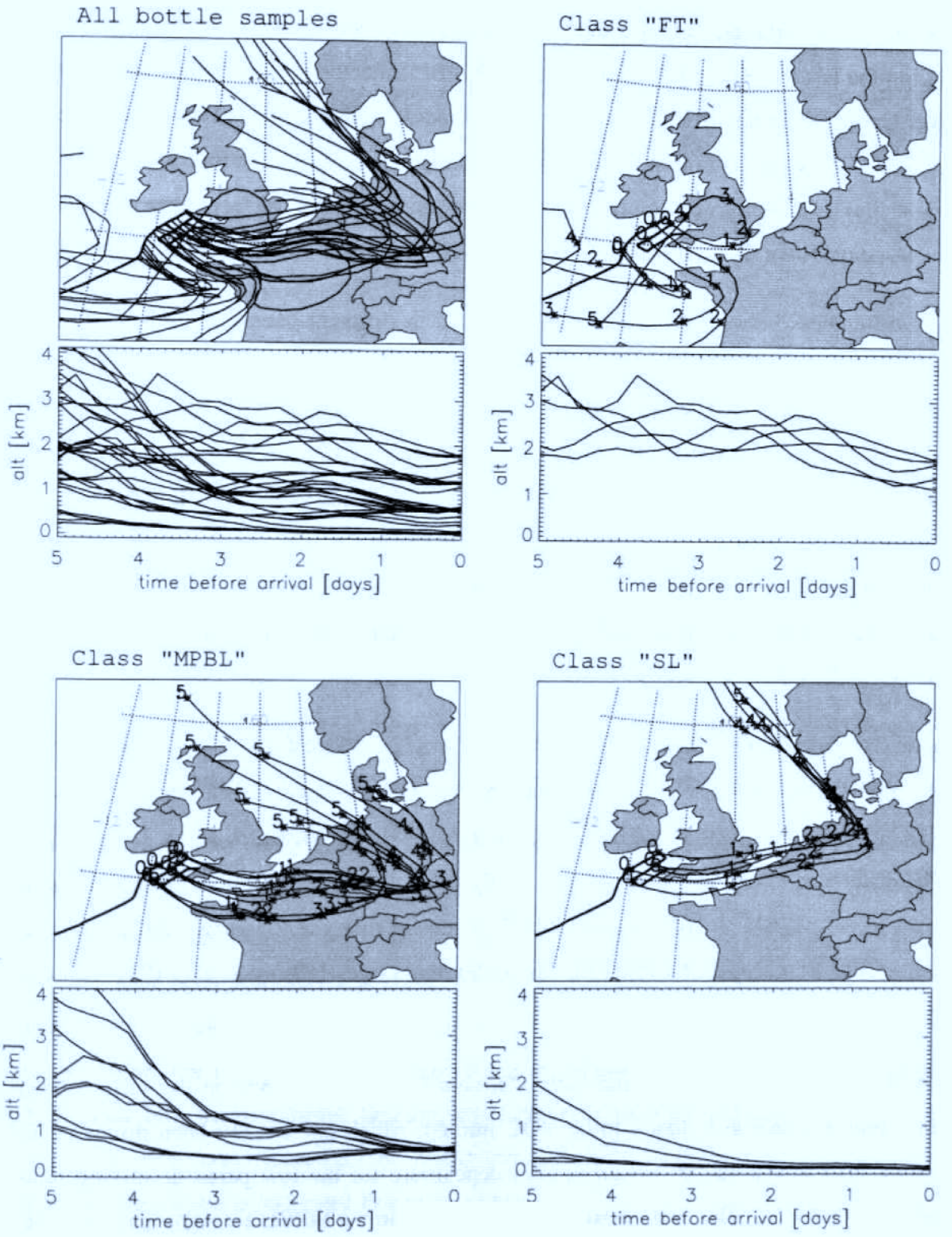

Figure 5.14: Five-day back trajectories for the bottle sample locations of flight A581 (23rd September 1997). Shown are the trajectories for all bottle sample as well as for the classes: free troposphere (FT), mid boundary layer (MPBL), and surface layer (SL). Crosses and numbers mark the days before arrival.

In Figure 5.14 the 5-day-back trajectories for the bottle samples are plotted, as well as their partitioning into the different classes. It shows that this way of clustering leads to quite homogeneous groups for the MPBL and SL. The surface layer trajectories cross Northern

Germany, Netherlands, Belgium and then Southern England[27], staying close to the surface during the last three days before arrival. The MPBL trajectories travel much further south over Germany before crossing Northern France and the British Channel up to the observation area. They collect emissions within the mixing layer over the European continent for about four days, before being separated from the surface by the surface layer inversion at the last day. The trajectories in the free troposphere do not see any European emissions.

The differences between the classes are reflected in different chemical signatures of the data. In Figure 5.15 the mean and standard deviation of the data in the three classes are plotted against the mean altitude of the class. The distinct concentration gradients observed between the layers in profile 10 (Figure 5.13) are also apparent in the mean values of the data. Generally, the surface layer is marked by significantly higher precursor concentrations (CO, NO_x, VOC) than the MPBL. However, the highest O_3 and O_x mixing ratios are found in the MPBL and not in the SL. As discussed already for Figure 5.13, NO_x mixing ratios are clearly lower in the MPBL than NO_y, indicating a higher chemical age of the air masses in the MPBL than those in the SL.

Indicators for different chemical processing in the SL and MPBL are given by comparison of VOC and NO_x in the two layers. While in the SL a mean ratio of $VOC/NO_x \approx 5$ ppbC/ppb is found, this ratio increases in the MPBL to about 18 ppbC/ppb. The difference in the VOC/NO_x ratio is likely to be due to the chemical ageing of the air mass in the MPBL, as NO_x is more rapidly removed than the longer lived hydrocarbons and so the VOC/NO_x ratio increases as an air mass ages [*Klemp et al.*, 1997; *Sillman*, 1999].

For the low VOC/NO_x ratios and high NO_x concentrations observed in the surface layer, the ozone production is likely to be VOC limited, which has already been discussed for Figure 5.13 as a possible reason, besides deposition, for the low peroxide mixing ratios observed in the SL. The mean peroxide mixing ratios in the MPBL are significantly higher, although they show a rather large variability. Together with the higher VOC/NO_x ratios this indicates that these air masses have already experienced chemical processing and are now in the transition to the NO_x limited regime of ozone production.

[27] Only the most southerly bottle sample trajectory does not hit southern England. Nevertheless the measured NO_x to NO_y ratio as well as the sampled hydrocarbons indicate very recent emission input for the observed air mass. This indicates that this air mass has also received English emissions and the trajectory direction is slightly wrong.

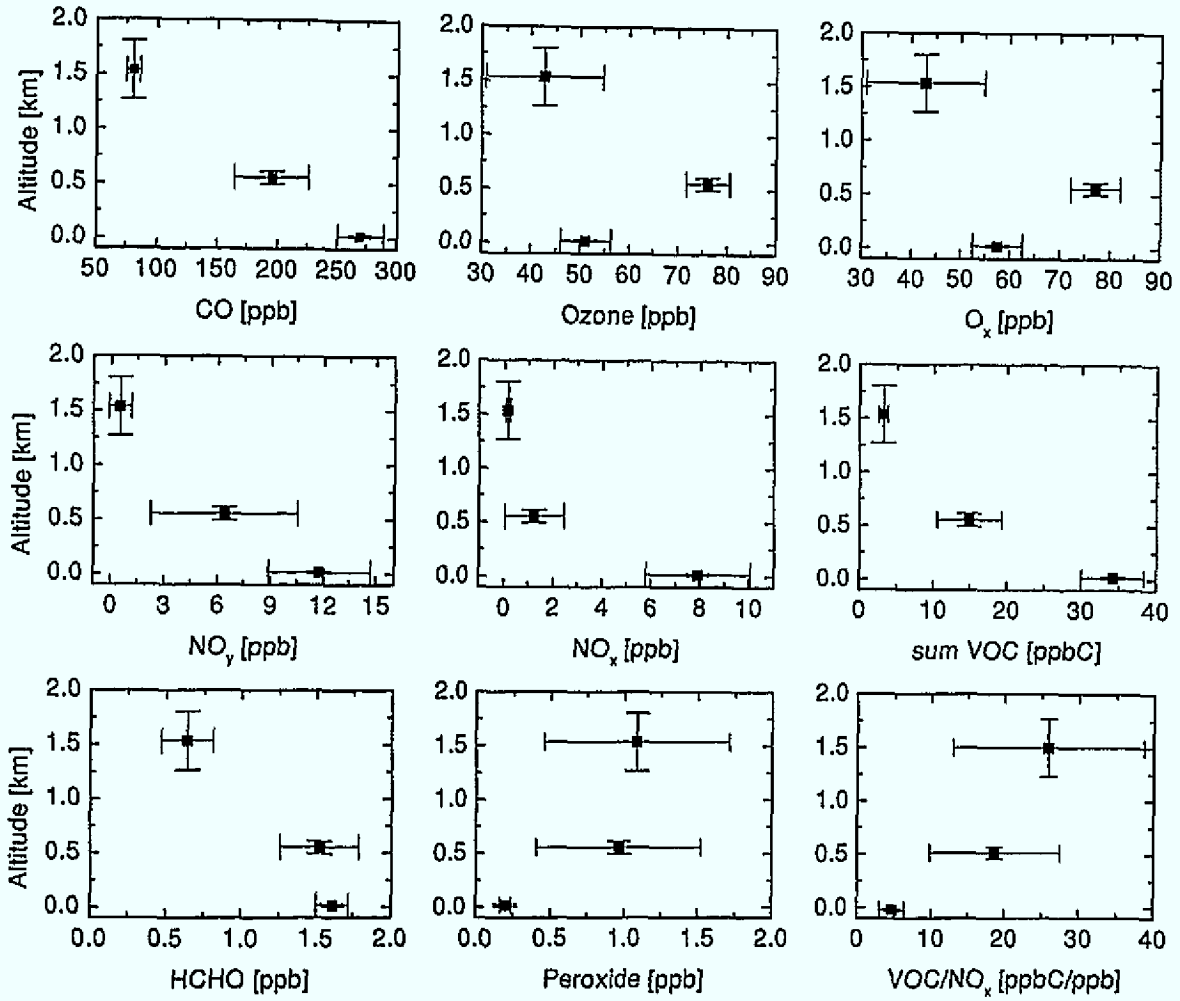

Figure 5.15: *Flight A581 on 23rdSeptember 1997. Mean observations and standard deviation in the three classes, SL, MPBL, and FT.*

For the determination of the NO_x-VOC limitation of a plume, several so-called chemical indicators have been proposed (e.g. O_3/NO_y, O_3/NO_z, H_2O_2/HNO_3 [*Sillman, 1995*]). These indicators are not used in this study, as they are mainly based on the oxidation products of NO_x which are not available here because of the uncertainty of the measured partition of HNO_3 in the NO_y measurements. Besides, these chemical indicators are only strictly valid in the vicinity of a point source and for negligible deposition and removal processes, which is not the case for the investigated European plume.

5.2.2 Description of the model run

The CO tracer study and the observations of ozone and precursors show that during flight A581 a European plume was investigated, in which already a significant amount of ozone had been produced, at least in the MPBL. The chemical processing within the plume, leading to the observations at the bottle sample locations, will be investigated by model

runs. Thus, 30 trajectory clusters starting from the flask sample locations were used to drive the photochemical model described in chapter 4. In the following, initialisation and certain approximations assumed in the model runs are discussed.

5.2.2.1 Mixing and dilution

As discussed in chapter 4.1.5, the simplification of instantaneous mixing between different air masses in the model gives a reasonable approximation in stable weather conditions with a clear flow situation and within the limitation of the transport to a few days over emitting regions. The prerequisite that horizontal mixing should not significantly change the trace gas composition compared to chemical processing in the plume is satisfied for the investigated flight. The plume originated from an anticyclonic flow around a high pressure system centred for about 5 days over the north east of Great Britain / North Sea, as described in chapter 5.1.1.5. This is a very stable meteorological situation, during which clean air masses descended from the northern Atlantic or polar region and collected emissions from the polluted regions of central Europe during the last 3-4 days before the measurements.

5.2.2.2 Photolysis rates

Another advantage arising from this meteorological situation is the clear sky condition connected with the anticyclone. METEOSAT satellite images and ECMWF analysed cloud fields show that there was no cloud during the transport of the air masses over continental Europe. Thus, the calculation of photolysis rates for clear sky conditions is a reasonable assumption. Only in the observation area over the Atlantic was there thin cirrus overhead, varying in amount from less than one octa to eight octas. Also, low level clouds were mostly absent but there was notable haze in the observation area [*Richer et al.*, 2000]. The impact on ozone production from cloud-related changes in photolysis rates should be small.

5.2.2.3 Deposition

Deposition is realised in the model calculations by first-order loss reactions, with the rate determined by the deposition velocity and the mixing height. Ideally, this would require an adaptation of the chemical box model for every change in deposition velocities and assumed mixing height. However, to keep the time expense affordable, the mixing height

used for deposition was fixed to 1250 m over the continent, and to 300 m for the surface layer on the last day before the measurements.

5.2.2.4 Initial concentrations

The initial chemical compositions of the trajectories were taken from the MCT model of the University of Bergen [*Flatoy et al.*, 1995] ten days prior to the measurement. To avoid influence on the model results from the uncertainty of the position of a single trajectory after ten days of backward integration, the initial concentrations are averaged over all trajectories associated to a class. The classes are defined by trajectories starting in the (1) SL, (2) MPBL, (3) free troposphere, and (4) trajectories that do not clearly belong to one of the other classes.

$NO_z = NO_y\text{-}NO_x$ is assumed in the initialisation to be composed of 50% HNO_3 and 50% PAN. For the initial VOC_i mixing ratios, a background mix was assumed according to the observations in the free troposphere of 44% ETH, 25% HC3, 11% HC5, 6% ETE and 14% TOL on a per-molecule basis. The box model run was started with these initial concentrations ten days prior to the measurement, with the emission input over Europe only during the last four and a half days. This provides a spin-up time of the model run which reduces the dependency of the results on the initialisation.

5.2.3 Results from the model calculation

5.2.3.1 Chemical tracers

The model results for the measured chemical species will be presented in two different ways. Comparison of the modelled with the measured time series is presented in Figure 5.16, and the relation of various modelled and measured species to CO is presented in Figure 5.17. The flight altitude is plotted in the upper left panel of Figure 5.16. The degree of correlation (r^2) is shown on the individual panels of the time series plots. This serves as a measure of the model's ability to reproduce the observed trace gas gradients. Comparing the different tracer-CO relationships (Figure 5.17) is helpful for assessing how well the model reproduces the processes controlling the concentrations of species with respect to variations in the emissions. These two ways of presenting the results are conducive to the interpretation and will be discussed together.

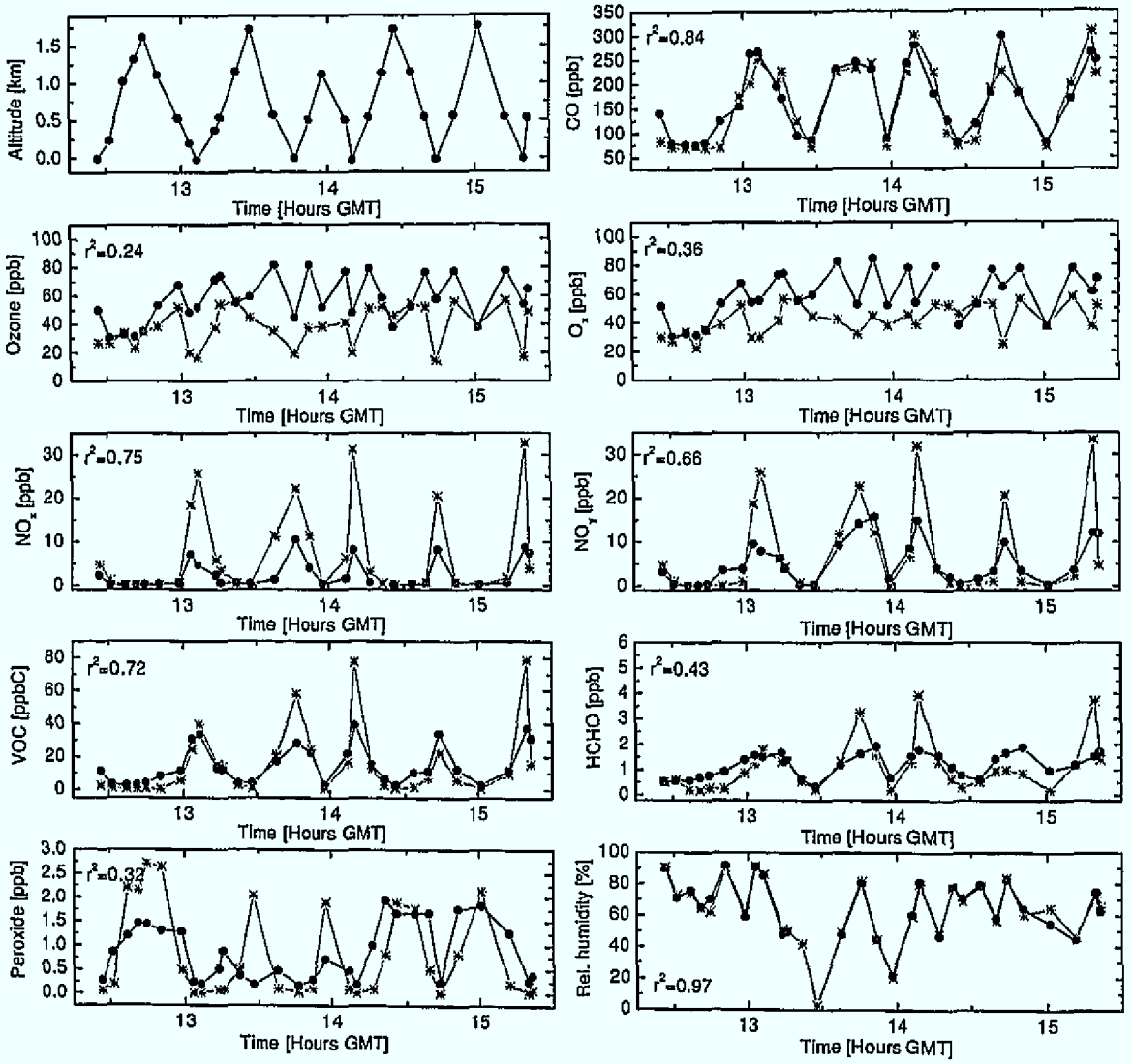

Figure 5.16: Time series of measured (black circles) and modelled (grey stars) values at the bottle sample locations of flight A581 (23rd September 1997). VOC means the sum of all measured VOC. For NO_y the measurement is compared to modelled NO_y-HNO_3. The upper left panel shows the flight altitude.

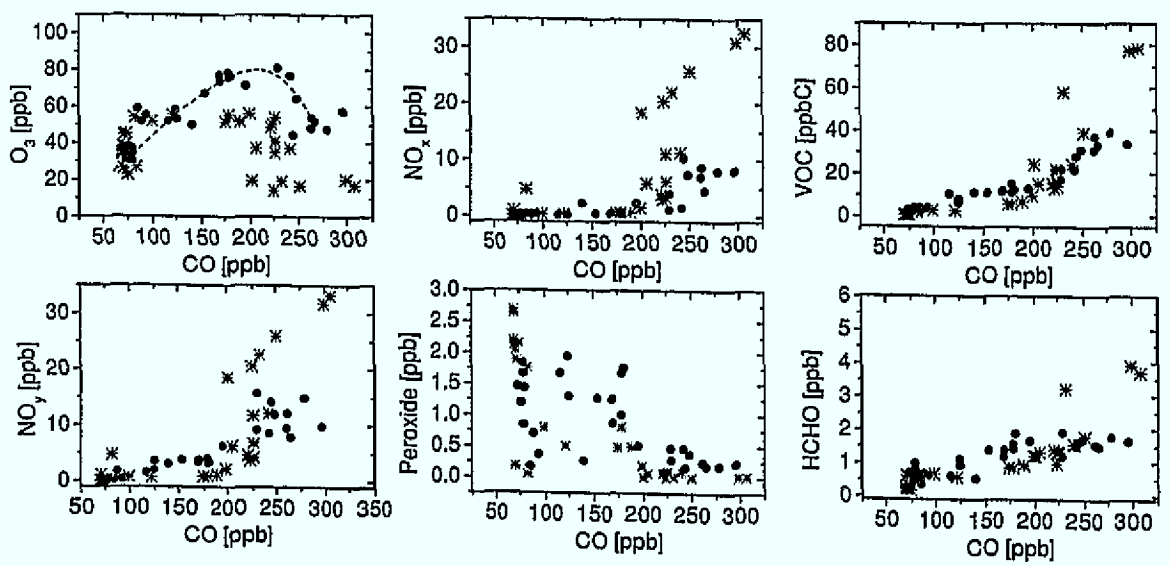

Figure 5.17: Relationship of O_3, NO_x, VOC, NO_y, H_2O_2 and HCHO to CO at the bottle sample locations of flight A581 (23rd September 1997). Measurement as black circles, model results as grey stars.

The most striking result from the model run is the obvious underestimation of ozone compared to the measurement and in relation to CO. This will be the subject of the discussion in the paragraphs following this one. Here, the discrepancy of model-to-observations will be merely described in detail.

High mixing ratios of ozone up to around 80 ppb were measured in the mid boundary layer (bottle samples at ~600 m altitude). The modelled O_3 values in this layer show mixing ratios between 40 and 60 ppb, barely higher than in free tropospheric layer. At the bottle sampling locations in the surface layer, 40-60 ppb O_3 were measured while the model gives lowest values of 10-20 ppb. Comparison with the modelled O_x values shows that a large fraction of the O_3 in this layer is tied up as NO_2, but still the modelled O_x underestimates the measurements by around 20-30 ppb. In relation to CO it is clearly shown that the observed photochemical ozone production, which led to the positive correlation between O_3 and CO below around 200 ppb, is not reproduced by the model. No net photochemical O_3 production can be seen from the model runs; in fact a even a decrease in O_3 for the highest CO mixing ratios is seen.

For VOC_i the comparison is difficult because the measurements do not represent all modelled hydrocarbons and the modelled hydrocarbons are lumped together into classes by application of aggregation factors. Therefore, a detailed comparison with single measured hydrocarbons will not be attempted. Instead, the sum of all measured hydrocarbons in ppbC is compared to the sum of modelled VOC classes, for which measurements exist. The agreement is generally quite good, which is also expressed by the high correlation coefficient of the time plot, apart from three individual samples for which the model overestimates the measurement by about a factor of two. These samples are all related to the surface layer and high CO mixing ratios.

Modelled NO and NO_2 are compared to the measurements as NO_x. The model clearly overestimates the measured NO_x levels for all bottle samples in the SL, and for part of the samples in the MPBL. While a good correlation between modelled and measured NO_x exists (r^2=0.75), the modelled mixing ratios are a factor 2-3 higher than the observations.

A variable often used to verify the NO_x budget in model calculations is NO_y (the sum of NO_x and its oxidation products) which is a conservative quantity in the absence of deposition. Unfortunately, the measurement of NO_y was subject to problems with the instrument's

inlet absorbing atmospheric HNO_3[28]. Therefore, the modelled (NO_y-HNO_3) is compared with the measured NO_y, although it is not clear yet, whether a fraction of the atmospheric HNO_3 passed the inlet and could have contributed to the measurement. Again, the modelled values overestimate the observations in the surface layer, while showing reasonable agreement for the rest of the bottle sample locations.

Interesting is the comparison between NO_x and NO_y for model and measurement. Relative to the measured NO_y (-HNO_3) the NO_x mixing ratios were low, indicating chemical ageing of the observed air masses, while in the model run NO_x and (NO_y-HNO_3) are almost the same. This indicates an underestimation of the chemical processing of the air masses by the model. An explanation for this is the very high NO_x levels in the model calculations, which suppress the availability of OH radicals. This is consistent with the lack of ozone production in the model results.

For formaldehyde (HCHO), the model mainly represents the observed levels, again with overestimation of a factor of two for the three bottle samples in the surface layer where the model overestimates VOC as well. The rather low correlation between modelled and measured values (r^2=0.43), can be attributed to the small range of the observed HCHO mixing ratios. This could be due to small atmospheric variability or the low time resolution of the HCHO instrument.

The comparison of measured to modelled peroxide reflects the large amounts of NO_x in the model calculations. Peroxides represent the dominant sink for free radicals in the NO_x-sensitive regime[29]. The model calculations yield peroxide levels close to zero in the surface layer and underestimate the measurements by about a factor of three in the MPBL, indicating that the modelled chemistry, caused by the high levels of modelled NO_x, is VOC limited. On the other hand the measured higher levels of peroxide in the MBL indicate more aged air and a transition to NO_x-limited ozone production. The cases where the modelled peroxide overestimates the measurement belong to bottle samples in the free troposphere, which are of no importance for this study.

The lower right panel of Figure 5.16 shows a very good agreement of modelled and observed relative humidity. This points to a good accuracy of the ECMWF analyses for the observed situation.

[28] Compare chapter 3.1.2
[29] Compare chapter 2.1.3.

5.2.3.2 *VOC/NO_x ratio*

As explained in chapter 2.1.3 the VOC- and NO_x-sensitive regimes of ozone formation mainly depend on the VOC/NO_x ratio. Figure 5.18 compares the measured VOC/NO_x relationship with the modelled one. The modelled VOC/NO_x ratio is more than 50% lower than the measured ratio. The difference is extremely important for the objective of this study, to investigate the relative roles of VOC and NO_x in forming ozone in a European continental plume. However, at this point the difference cannot clearly be attributed to a single reason. It could either be due to an incorrect VOC/NO_x ratio in the emission inventory, or to the extent of photochemical ageing. As has been discussed in chapter 5.2.1.2, the chemical aged air masses in the MPBL show a clearly higher VOC/NO_x ratio than those in the SL. Thus, the difference between measured and modelled VOC/NO_x ratio cannot be simply attributed to the emission ratios, but has to be analysed with respect to the photochemical processing. This will be discussed in more detail in the following chapters.

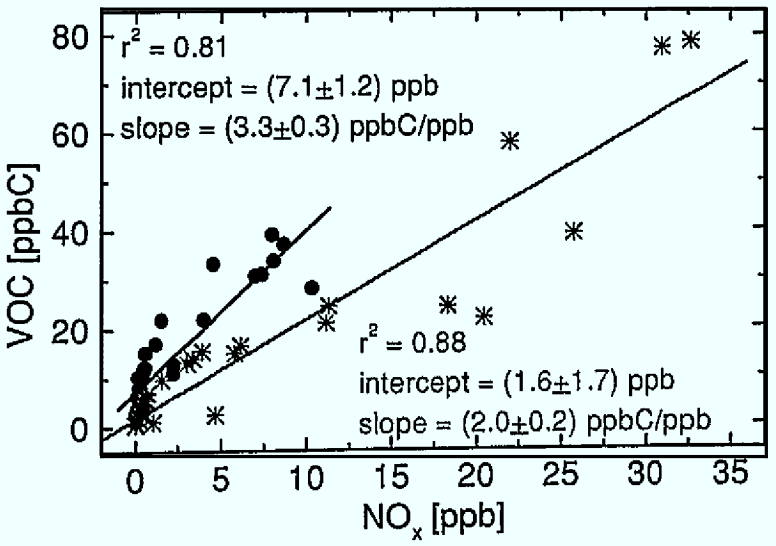

Figure 5.18: Relationship of VOC to NO_x at the bottle sample locations of flight A581 (23rd September 1997). Measurement as black circles, model results as grey stars.

5.2.3.3 *Photolysis rates*

The driving force for tropospheric photochemistry is the photolysis of photo-labile species. During the flight A581 the photolysis frequencies of jNO_2 and jO^1D were measured aboard the Hercules C-130. These measurements are compared to the frequencies calculated by photoRACM in Figure 5.19 and Figure 5.20, which show the time series of measurements and model calculations for the bottle sample location and the correlation between modelled

and measured photolysis rates. Part of the measurements took place under cloud leading to lower photolysis rates not represented by the model calculations, which are for clear sky only[30]. Those measurements are shown by open symbols in the correlation plot and are not included in the linear fit.

For the clear sky regions a good correlation between model and measurement is found (r^2=0.87 for jNO_2, and r^2=0.96 for jO^1D). Some scatter is due to the coarse altitude resolution of the photolysis model (1km levels). Nevertheless the slopes indicate that the model underestimates jNO_2 by around 20% and overestimates jO^1D also by around 20% compared to the measurements.

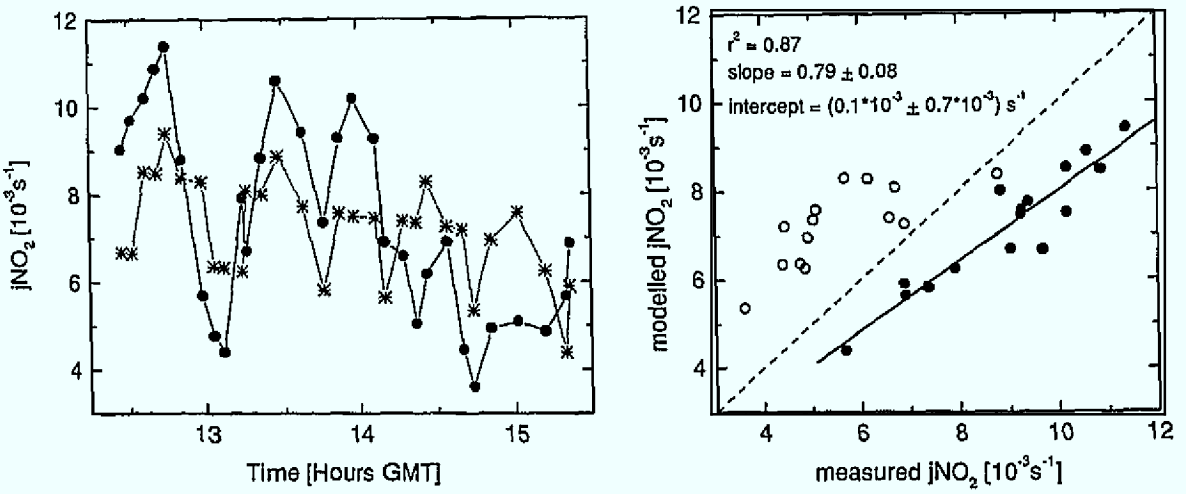

Figure 5.19: Comparison of measured and modelled NO_2 photolysis rates for the bottle sample locations. Left panel: time series. Black circles give the measured, grey stars the modelled jNO_2-frequencies. Right panel: correlation between modelled and measured jNO_2-frequencies for clear sky periods (filled circles). The solid line is the linear fit, the dashed line the one-to-one correspondence. The hollow circles represent measurements under clouds and are not included in the fit.

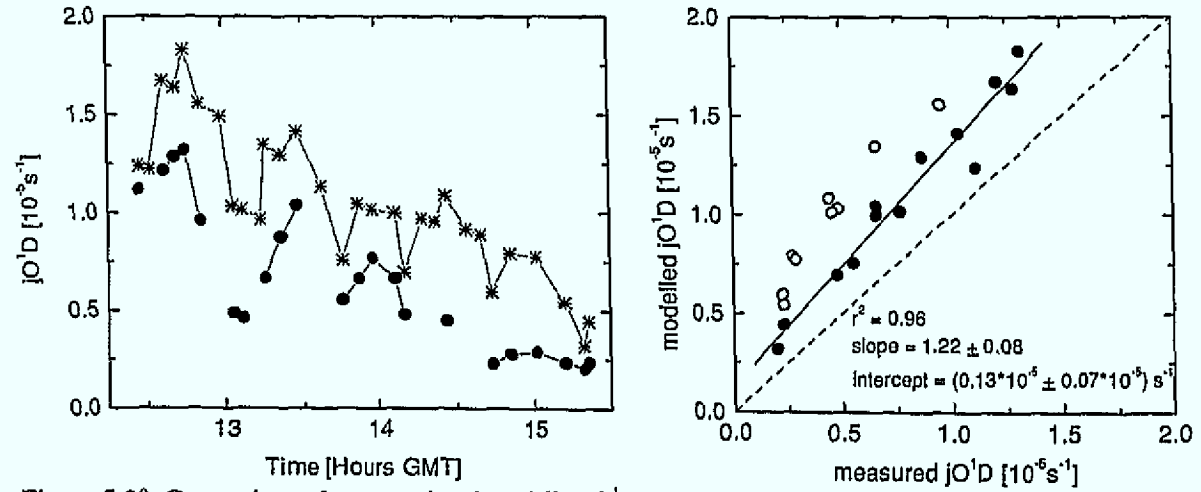

Figure 5.20: Comparison of measured and modelled O^1D photolysis rates for the bottle sample locations. Plots and symbols as in Figure 5.19.

[30] Compare chapter 4.2.3.

For jO^1D this result is still compatible with the measurements as the ACSOE/TACIA campaigns in the summer of 1997 represented the first deployment of the airborne jO^1D instruments and the accuracy of the measurements was estimated to be approximately 30% [*Hov et al.*, 1998]. However, jNO_2 was measured with an accuracy of 8%, independent of the meteorology (cloudy or clear sky) [*Volz-Thomas et al.*, 1996]. Consequently, the underestimation of the modelled jNO_2 is significant. Although the model proved its general ability to reproduce measured photolysis rates close to the surface [*Volz-Thomas et al.*, 1996], several factors can explain the differences between measured and modelled values. Surface albedo, aerosol distribution and water vapour all have a regional varying influence on the photolysis frequencies. The surface albedo in the model calculations is defined as wavelength dependent, but does not allow for different surfaces. Normally the albedo over the sea is found to be lower than over land, thus the modelled values should rather overestimate the measurements. Nevertheless, there was notable haze observed in the surface layer during the flight, which may increase the effective albedo and thus increase the observed photolysis rates. In this case the measurements would not tell much about the photolysis rates over land as the haze layer probably developed out of the increased water vapour in the marine boundary layer. Since the main part of photochemical processing happened over the European continent over which the air masses travelled for 3-4 days, compared to only half a day prior to the measurements over the sea, it was decided not to correct the modelled photolysis by the measurements. This introduces an uncertainty arising out of the deviation between modelled and measured photolysis rates which has to be kept in mind.

5.2.4 EKMA plot analysis

One objective of the project TACIA was to investigate whether it was possible to strengthen the knowledge of the relative roles of VOC and NO_x in forming ozone in an European plume over the North Atlantic, and whether measured concentrations of precursors and ozone are consistent with current European emission inventories. Obviously, the simulations discussed in the last chapter, based on the most recent available EMEP emission inventory for Europe, clearly underestimated the ozone production in the European plume observed during flight A581. Thus, the following will investigate whether the differences between modelled and measured chemical composition of the plume can be attributed to erroneous VOC and NO_x emissions.

5.2.4.1 EKMA plot calculations for interpretation of the measurements

The dependence of ozone formation on the ratio of VOC to NO_x is usually presented by an EKMA plot as described in chapter 2.1.3. EKMA plots are primarily a tool for sensitivity studies, and are normally not employed for the interpretation of measurements. This is due to the fact that simple chemical box model calculations are usually used for the generation of an EKMA plot. The simplifications of these calculations limit the transferability of the results to observations. Nevertheless, the large number of model runs performed for the different VOC to NO_x ratios require the time expenses for each model calculation to be kept small. Additionally, the simplifications allow for a better interpretation of the results than would be possible for a highly complex model set-up.

Therefore, the task for this study is to find simple model scenarios which allow the interpretation of sensitivity studies in the form of EKMA plots, but still represent the mean meteorological situations observed in the surface layer and in the MBL, respectively. The observed meteorological situation of an anticyclonic outflow from Europe is such that it can be approximated by a strongly simplified model set-up. As discussed before, the measurements are characterised by the observation of a distinct layering. Within a layer the observations of a parameter are quite homogeneous, but between the layers strong differences are found. Thus the simplified model scenario has to represent the observed differences between the layers.

5.2.4.1.1 Set up of the EKMA plot model calculations

In this chapter model scenarios are developed for each of the classes MPBL and surface layer, representing the main meteorological and chemical conditions that lead to the observed chemical signatures, but still simple enough for calculation and interpretation in an EKMA plot. The class FT is not discussed in this analysis as the transport analysis did not yield any European emission input for these air masses.

The model set-up for the EKMA plots is based on the back trajectories in the classes MPBL and SL shown in Figure 5.14. According to the travel time of the trajectories, 3 days of emission input over Europe are assumed for the class SL, and 4 days for the class MPBL. Constant daily emission input is assumed for Europe as a whole, with emissions during the night set as ¼ of the emissions during day. Because of the occurrence of the surface layer inversion no emission input is assumed for the class MBL from the last eve-

ning before the measurement. For the class SL the emissions stop at the last morning when the trajectories reach the Atlantic ocean. This emission scenario is compared in Figure 5.21 with the emission input given by the transport model for example trajectories in both classes. A reasonable agreement is found especially for the class mid PBL.

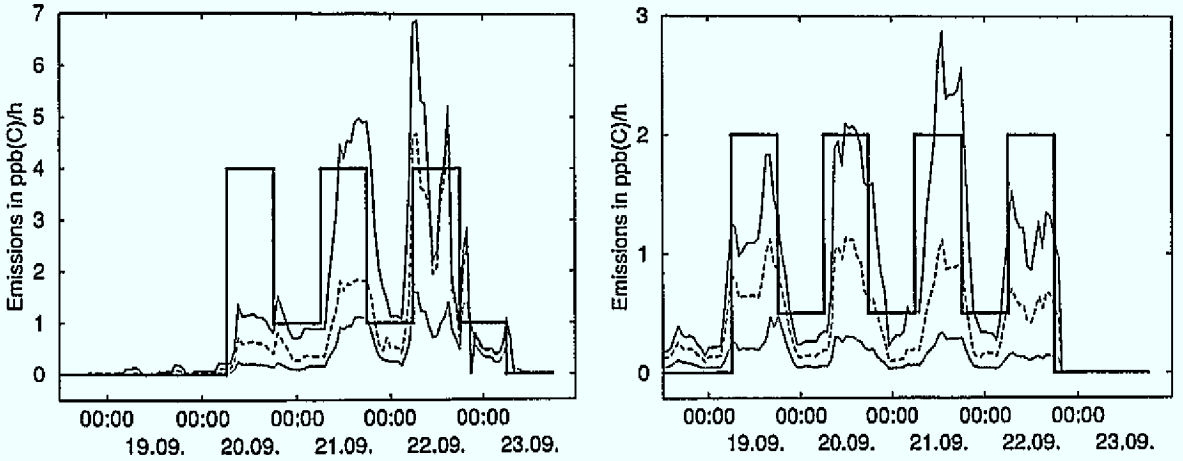

Figure 5.21: Comparison of the emission scenario used for the EKMA plot calculations in the classes SL (left) and MPBL (right) with emissions along example trajectories within the classes. The thick black line shows emission rates assumed for the EKMA plot calculations, whereby the amplitudes are varied in the EKMA plot calculations. Along the example trajectories (bottle sample no. 9 in the SL, respectively no.7 in the MPBL) emission rates of CO in ppb/h (solid line), VOC in ppbC/h (dashed line) and NO_x in ppb/h (dotted line) are plotted.

Deposition in the EKMA plot model calculations is assumed to occur whenever there are emissions, with separate deposition velocities for continental day and night respectively (chapter 4.2.4). For the class SL additional deposition over the ocean is assumed on the day of measurement. Photolysis rates are calculated as diurnal cycles for 50°N, 5°W at 1 km altitude for the class MPBL and at the surface level for the class SL.

Initialisation is as before provided by the mean initial concentrations for the classes MPBL and SL from the MCT model (University of Bergen) ten days prior to the measurements. The spin-up model runs without emissions are performed with temperature, pressure and photolysis rates adjusted to the mean position of the trajectories in the two classes.

5.2.4.1.2 Results

The model calculations were run for a large variety of VOC and NO_x volumetric emissions and the results are arranged in 2-dimensional maps as function of the amplitude[31] of the emission rates. Figure 5.22 shows the results of the model runs for the class MPBL, Figure 5.23 for the class SL. Plotted are isolines of the mixing ratios of ozone, NO_x, the sum of

[31] That means the emission rate during the day (in ppbC/h for VOC, respectively ppb/h for NO_x).

measured VOC, (NO_y-HNO_3), H_2O_2 and HCHO, each averaged from 12:00 – 16:00 GMT on the day of measurement corresponding to the time of the flight.

The question is, how to compare these fields of modelled mixing ratios with the observations. The aim of this comparison is to investigate if the deviations between model results and measurements, found for the bottle sample locations, are attributable to the absolute VOC and NO_x emissions from the EMEP emission inventory and their VOC/NO_x ratio. Therefore in the field of model results one point is selected which corresponds to the emission scenario for the corresponding trajectories. This is done by scaling the emission ratios between the emissions from the inventory with help of the measured CO as an inert tracer for anthropogenic emissions, as explained below:

In an EKMA plot the emission rates of VOC and NO_x are independent of each other. Whereas the emission inventory assumes correlation between the emissions of CO, VOC and NO_x, as can be seen in Figure 5.21.

Analysis of the emissions of VOC and NO_x along the bottle sample trajectories, according to the EMEP emission inventory for 1996, gives a mean VOC/NO_x emission ratio of 2.9 ppbC/ppb. This emission ratio is indicated in the EKMA plot by a solid diagonal line. The basis of the analysis is the fact that the emissions of VOC and NO_x are proportional to the CO emissions. Since CO can be assumed to be inert, the time integral of the CO emissions minus the atmospheric background concentration equals the mean CO mixing ratio in the respective class. Therefore, from the integrated CO emission, the emission rate of CO in ppb/h of the homogeneous European plume can be calculated. The absolute VOC and NO_x emissions are then obtained from the VOC/CO emission ratio of 0.56 ppbC/ppb and the NO_x/CO emission ratio of 0.19 ppb/ppb for the EMEP inventory. These are plotted in Figure 5.22 and Figure 5.23 respectively as a black circle and bar on the line of constant VOC/NO_x ratio = 2.9 ppbC/ppb. The dot corresponds to the mean of the observed CO mixing ratio for the respective class and the bar to the standard deviation.

Hence, marked by this is the emission scenario according to the emission ratios of the EMEP inventory and the measured CO for the absolute quantity. For ease of the discussion this will be referred to in the following as reference point. Outgoing from the reference points the observations of the species in the two classes can be compared to the EKMA plots.

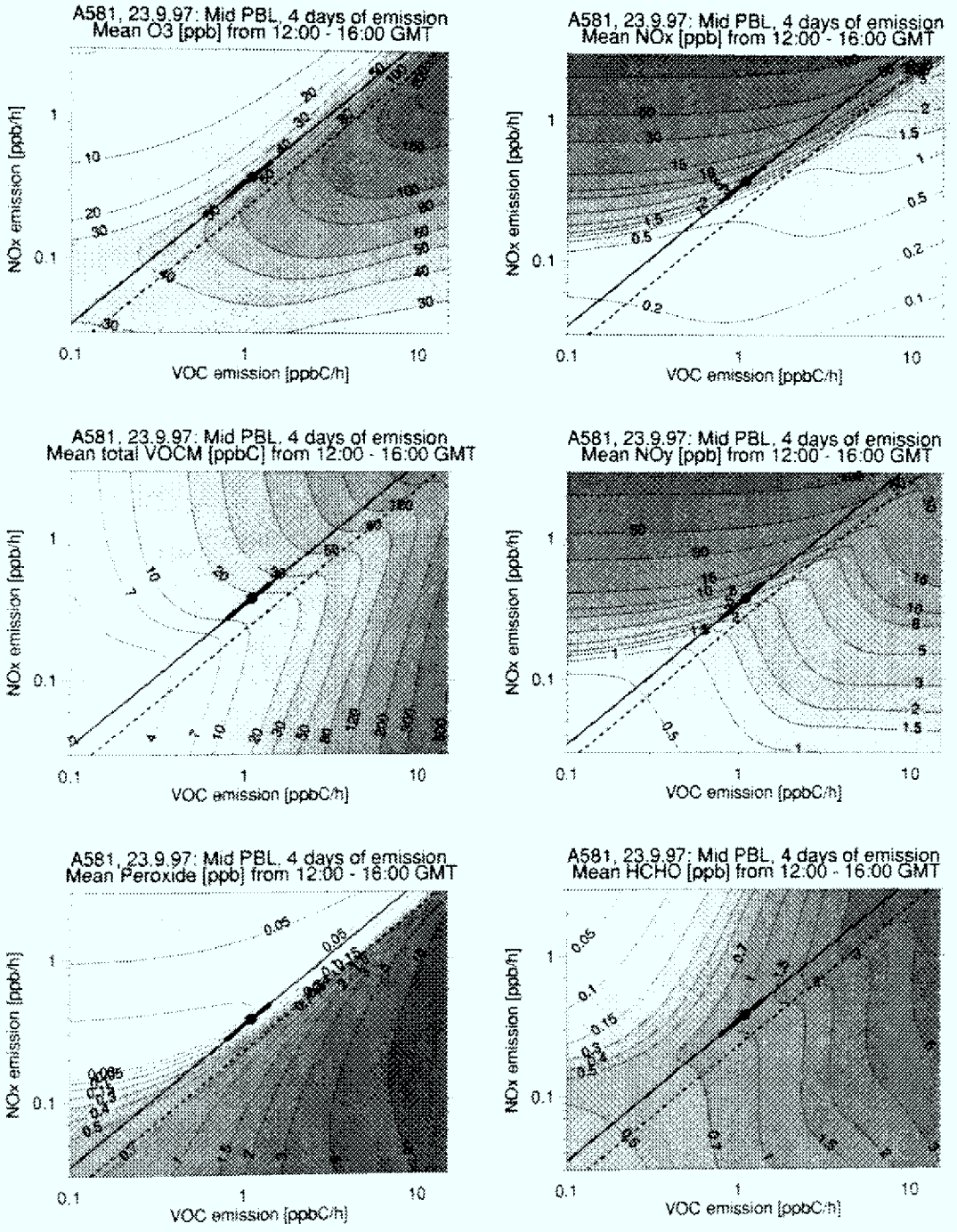

Figure 5.22: Modelled isolines of O_3, NO_x, sum of measured VOC (VOCM), NO_y, H_2O_2 and HCHO mixing ratios for the class MPBL, plotted against VOC (horizontal axis) and NO_x emissions (vertical axis). The solid line corresponds to $VOC/NO_x = 2.9$ emission ratios, as found from the EMEP emission inventory. The black dot and bar show the VOC and NO_x emissions that yield into the observed range of CO, given the ratios from the emission inventory. The dashed line indicates 50 % increased VOC/NO_x emission ratios.

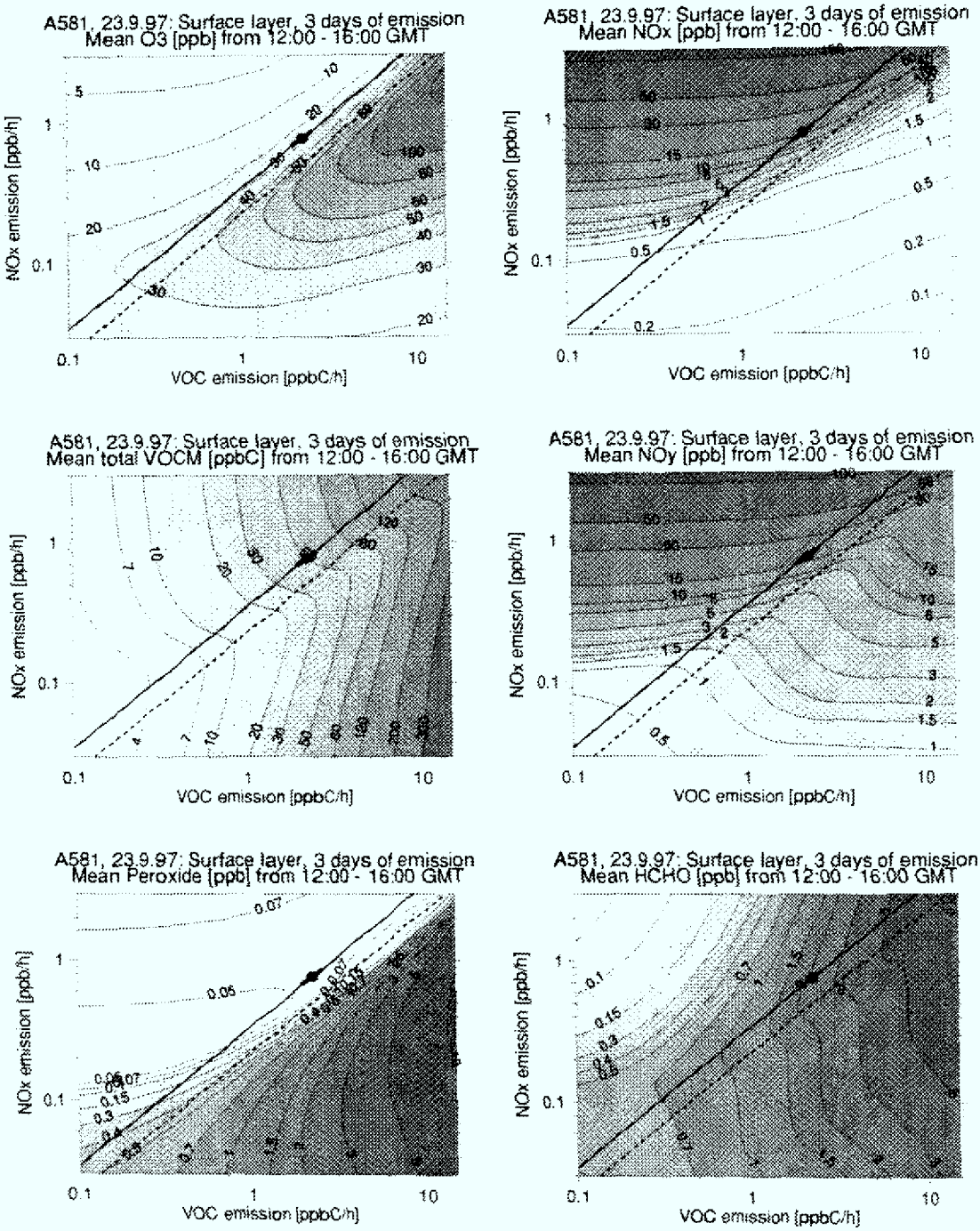

Figure 5.23: As Figure 5.22, but for the class SL.

This comparison is summarised in Table 5.1, which also shows the range of the results from the detailed model runs (for individual bottle samples) discussed in the last chapter for the classes MPBL and SL. Generally the same features for the reference point in the EKMA plots are found as for the detailed model runs. Again ozone is strongly underestimated by the model results, while NO_x is overestimated by about a factor of 2-3. From this is can be concluded that even under the simplification of the EKMA model set-up the main

differences between model calculations and measurements are correctly reproduced and, consequently, that the EKMA plot approach can be utilised for the further investigation.

Table 5.1: Comparison of the results from the EKMA plot calculations for the reference point with the range of detailed model results and observations in the classes MPBL and SL. The range is given by the lower and upper quartiles. The mixing ratios of the species are given in ppb, besides VOC (ppbC).

Species	SL			MPBL		
	EKMA-plot	Detailed model	Observa-tions	EKMA-plot	detailed model	Observa-tions
CO	257 – 298	233 – 299	262 – 279	164 – 232	189 – 226	179 – 229
O_3	25 – 26	17 – 20	48 – 54	40 – 44	37 – 52	76 – 78
NO_x	15 – 20	22 – 31	8.0 – 8.7	1.9 – 7.2	0.7 – 6.2	0.5 – 1.5
NO_y-HNO_3	16 – 22	23 – 32	9.8 – 14.1	2.7 – 8.4	1.1 – 6.8	3.5 – 8.5
VOC	44 – 58	39 – 77	33 – 37	10.9 - 26.7	6.9 – 16.5	11.5 – 17.0
HCHO	2.0 – 2.4	1.8 –3.7	1.5 – 1.7	0.9 – 1.3	0.9 – 1.3	1.4 – 1.7
Peroxide	0.05 – 0.06	0.01–0.02	0.18 - 0.23	0.04 – 0.1	0.09 – 0.48	0.5 – 1.3

Despite the large degree of abstraction, the results of the EKMA plot calculations can thus be compared to the measurements, and at the same time they are helpful for the elucidation of the relative roles of VOC and NO_x in the process of ozone production in the European plume. As described in chapter 2.1.3, the NO_x- and VOC-sensitive regimes in an EKMA plot become obvious from the change of O_3 concentrations with NO_x and VOC. They are divided by a ridge of high O_3, as well as strong gradients in NO_x and H_2O_2 mixing ratios.

Regarding the reference point it is seen that the model results are located in the VOC-sensitive regime. This is obvious for the surface layer (Figure 5.22), but also clearly valid for the MPBL class (Figure 5.23). On the other hand, the results of the measurements indicate that chemical processing in the MPBL is in the transition to NO_x-sensitivity[32].

In the VOC-sensitive part of the EKMA plot the ozone production depends not so much on the absolute emission rates but rather on the VOC/NO_x ratio. This can be easily inferred from the line of constant VOC/NO_x = 2.9 ppbC/ppb, which runs nearly parallel to the isolines of O_3. A better agreement with the observed O_3 would thus be found if the emission line is shifted towards higher VOC/NO_x ratios. A 50% increased emission ratio,

[32] Compare chapter 5.2.1.2

leading to VOC/NO_x = 4.5 ppbC/ppb, is indicated in the EKMA plots by the dotted line. For this emission ratio the serious underestimate of the observed O_3 mixing ratios is largely removed. Indeed, such emission ratios have been reported from German urban areas [*Kern et al.*, 1998; *Schmitz et al.*, 1997].

Nevertheless, this is only a qualitative analysis of the model results. Before this result can be considered quantitative, and used to constrain the uncertainties of the European VOC and NO_x emissions, it is necessary to analyse the significance of the deviation of the model results from the measurements for a given model scenario. This is the aim of the next chapter.

5.2.4.2 Significance Analysis of the deviation of model results and measurement

The idea is to analyse whether the deviation of the model results from the measurements for the reference point is significant, and if so, for which VOC and NO_x emission rates model and measurement would be consistent. The significance of deviations will be determined by taking into account the observed variability of the measurements within a specific class as well as the measurement errors. Each measurement in a class is assumed to fall under the same model scenario. The deviations among the measurements of a parameter in a class should then exhibit statistical behaviour, arising from the statistical error of the measurement itself and the variations from the model scenario as experienced by each measured air mass. These variations are caused by a multitude of parameters that may or may not have been acting on the measured air mass (like wind speed, wind direction, local turbulence and inhomogeneous emissions). Thus, they can be assumed to have a random character that can be described by a statistical distribution. Separately from this, the systematic error of the measurements has to be dealt with, i.e. the part of the error which arises for example from calibration inaccuracies. This error will be discussed later.

Ideally a model run should represent the expected mean of the associated class, with the measured parameter scattering around the modelled parameter. The frequency distribution of a measured parameter is assumed to be lognormal. This assumption cannot be proved due to the few data points available in each class (5 bottle samples in class 1, and 9 bottle samples in class 2), but a plausible argument for its applicability can be made. The lognormal distribution arises from a theory of elementary errors combined by a multiplicative process, just as the normal distribution arises from a theory of elementary errors combined by addition [*Aitchison and Brown*, 1966]. Nevertheless the main part of the deviation

within the measurements is due to differences in the specific history of the air parcels, about which a statement regarding the kind of the elementary errors is difficult. While changes in emissions are additive, the reduction of primary pollutants is due to multiplicative changes such as dilution and removal processes that are first order in the pollutant concentration [*Parrish et al.*, 1991]. Thus, an approximately lognormal distribution will be found if the processing of the air masses rather than the sources dominates the variability. This is the case if the sampled air masses are composed of more or less uniform sources of pollutants or are sampled far away from the sources. Since lognormal distributions have been widely used to represent the frequency distributions of the concentrations of air pollutants [*Georgopoulos and Seinfeld*, 1982], and have shown at least rough agreement with measurements at rural sites [*Parrish et al.*, 1991], this is a reasonable assumption.

5.2.4.2.1 Significance analysis for one measured parameter

The usefulness of the lognormal theory lies in the fact that the statistical properties of the normal distribution can be applied to the logarithm of the observations.

Thus the significance of the deviation of a model result from the measurements can be determined by a statistical test[33], which considers the estimated width of the frequency distribution of the parameter as well as the systematic error of the measurement. As explained in Appendix 9.1 for one parameter this is done by a t-test, with the systematic error allowed for by a non centrality parameter δ[34].

For the modelled parameter a significance value α is thereby determined. It gives the probability for an erroneous rejection of the null hypothesis that model observation differences are solely due to natural variability. Here rejection implies an incorrect model response. Thus the smaller α the more significant is the deviation between modelled and measured parameter.

For a statistical test a threshold in form of a significance level α_0 is normally defined, such that for $\alpha < \alpha_0$ the null hypothesis will be rejected. Common thresholds are significance levels of 1%, 5% or 10%. Analogously, a confidence interval is defined such that for

[33] A textbook for a review of the statistical test methods applied in this chapter is for example [*Seber*, 1984].
[34] The non centrality parameter δ has been estimated by using the accuracy of the measurements as an upper limit for the systematic error.

$\alpha \geq \alpha_0$ the modelled value is within the confidence interval given by the distribution of the measured parameter.

The significance values α were calculated for each modelled value in the EKMA plots of Figure 5.22 and Figure 5.23. These significance values are arranged again in 2-dimensional maps as function of the emission rates analogous to the EKMA plots. The result is given in Figure 5.24 and Figure 5.25 which show significance maps for the parameters O_3, NO_x, VOC, NO_y-HNO_3, H_2O_2 and HCHO. In each map isolines for $\alpha = \alpha_0$ are plotted, where α_0 is set to significance levels of 1%, 5%, 10% and 25%. The shaded areas are then regions in which the tested model parameter is within the confidence interval of the measurements for the respective significance level. Thus, for each parameter, confidence regions as a function of the VOC and NO_x emissions are obtained. Areas which are outside the isolines of a chosen significance level will then be rejected as possible emission scenarios for the tested parameter.

The general features of the confidence regions for each parameter in the two classes are best understood by comparison with the EKMA plots of Figure 5.22and Figure 5.23. The imaginary centre line of the confidence region for each parameter follows the model isolines of the observed trace species mixing ratio.

Since there is some tentativeness in the choice of a specific significance level as threshold, only areas outside the $\alpha = 1\%$ isoline will be rejected as possible emission scenarios. The other significance levels are still shown, as they indicate for which VOC and NO_x emissions the best agreement between modelled and measured parameters are found.

The confidence regions for each parameter will be discussed in the following with regard to the reference points.

Figure 5.24 and Figure 5.25 show that the reference point lies well outside the confidence region for ozone. Thus with regard to ozone, the assumed model scenario with VOC/NO_x = 2.9 emission ratios, following the EMEP inventory, has to be rejected with high probability. Conversely, regions of the model results that are within the confidence interval of the measurements are found for VOC/NO_x ratios about 50% higher than that of the emission inventory, as already indicated in the last chapter. Such emission ratios are marked by dashed lines in Figure 5.24 and Figure 5.25.

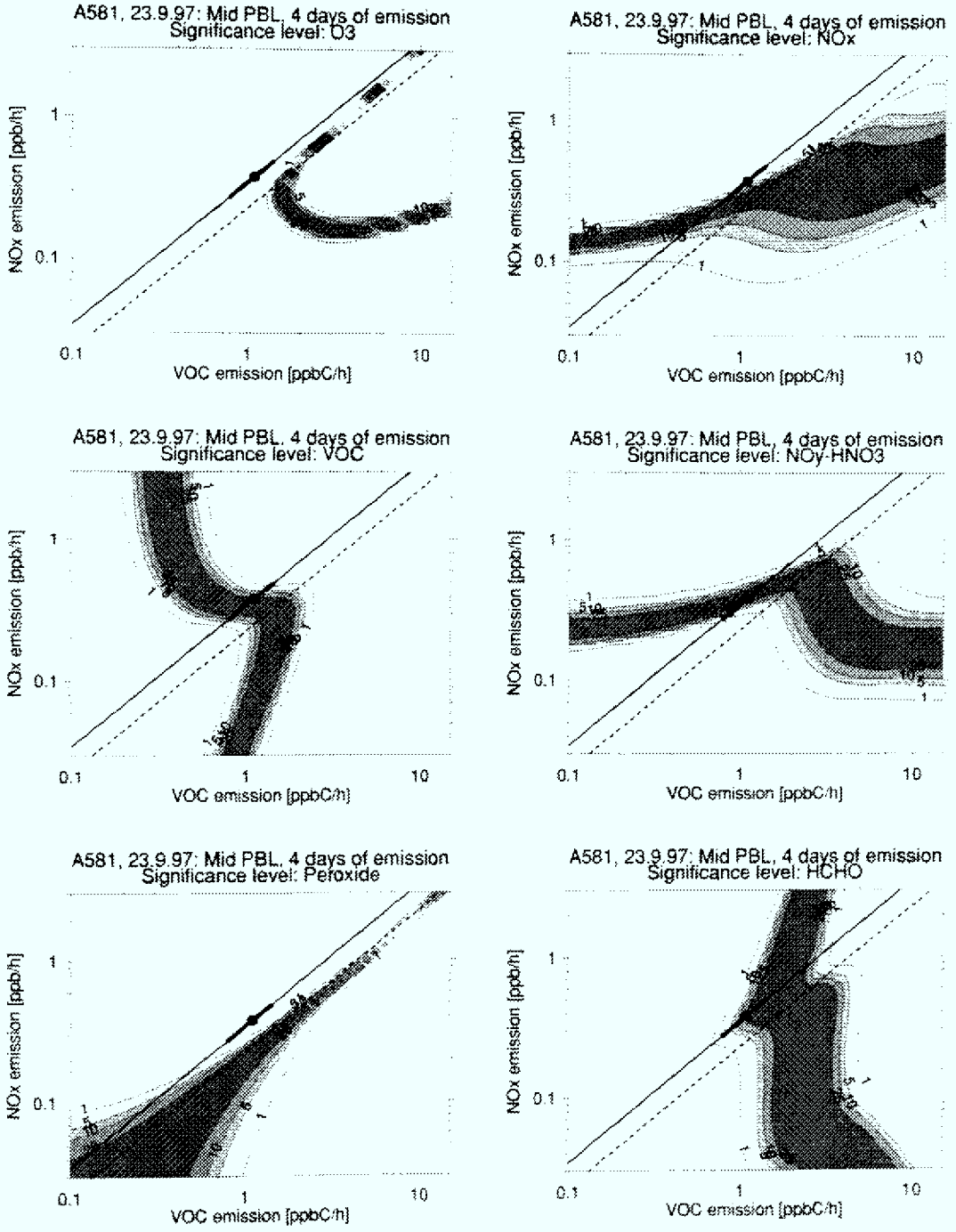

Figure 5.24: Isolines of the significance levels α = 1%, 5%, 10%, 25% for the null hypothesis that model-observation differences are solely due to statistical variability. Shown are the test results of the non central $t_{n-1,\delta}$-distribution for the parameters O_3, NO_x, VOC, NO_y-HNO_3, H_2O_2, HCHO (from left to right and top to bottom) in the class MPBL.

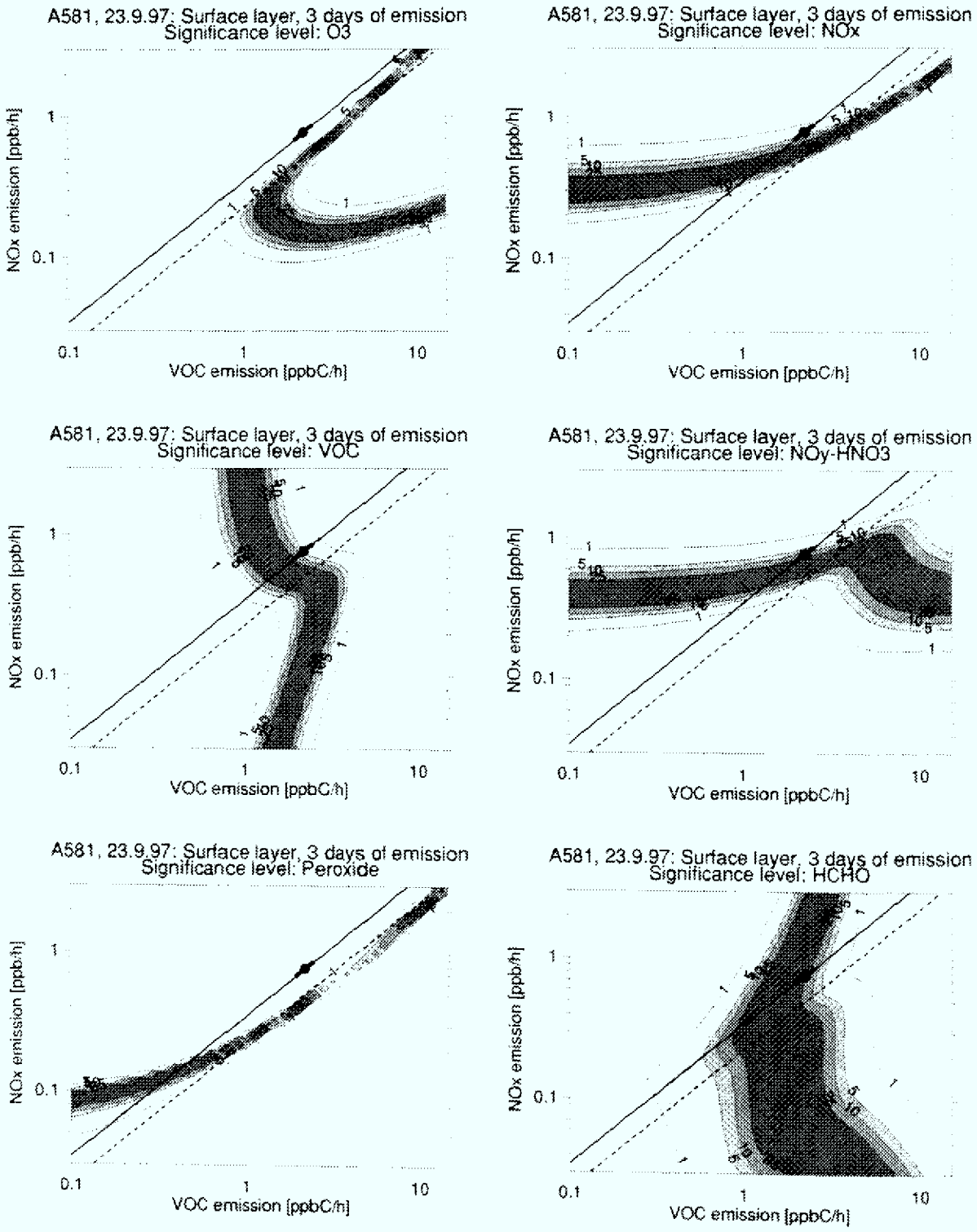

Figure 5.25: As Figure 5.24, but for the class SL.

For NO_x the reference point lies barely outside the 1% significance level. In this case, for a rejection of the hypothesis the measurement errors warrant a closer examination. Here too, higher VOC/NO_x emission ratios would yield better agreement with the measurements. The VOC mixing ratios are still within the statistical confidence region.

More difficult is the analysis for NO_y due to the problems with the measurement of HNO_3[35]. As discussed before, the model result of HNO_3-NO_y is tested against the measurement of NO_y. The assumed systematic error of the measurement does not include the uncertainty that parts of the HNO_3 may still pass the inlet, thus the measurement error is possibly too small. This must be kept in mind for the further analysis, although the modelled NO_y-HNO_3 does not significantly vary from the measurement.

Like ozone, the model results of peroxide show very significant deviations from the measurements for the reference point. Here even slightly more than the indicated 50% increase in VOC/NO_x ratios is necessary to obtain model results within the confidence interval of the measurements.

For HCHO a rather large uncertainty of the measurements had to be assumed, which leads to the wide confidence regions for this parameter in Figure 5.24 and Figure 5.25. Within these bounds no significant deviation between model and measurement is found.

On the whole, for both classes, MPBL and SL, significant deviations between model results and measurements are found for ozone and peroxide H_2O_2 if emissions of VOC and NO_x according to the reference point are assumed. Agreement with the measurements for these parameters is found for an increase of the VOC/NO_x emission ratio by at least 50%. For the other measured values no significant deviation is found, partly due to the allowance for the errors of the measurements. Still, an increase of the VOC/NO_x emission ratio would lead to higher significance values, for example for the modelled NO_x, and not disagree with the confidence regions for the other measured parameters.

5.2.4.2.2 Significance analysis for several measured parameter

To test the validity of a model, not a single modelled parameter alone should be tested against the measurements, but all reliable parameters together that are represented by the model. Consideration of the correlations between the different measured parameters then leads to a multivariate non-central F-distribution for the description of the tested hypothesis. Nevertheless, as shown in Appendix 9.2 the number of measurements within each class, especially in the SL, is too small for a precise estimation of the covariance matrix of the multivariate distribution.

[35] Compare chapter 3.1.2

Therefore, an alternative test method for several measured parameters is chosen, based on the combination of the univariate t-test results for each parameter. The idea for this is that we are looking for areas in the intersection of the confidence regions of all considered parameters. Expressed differently, a model result varies significantly from the measurements if at least one parameter varies significantly. The significance level α_0 for a number of p_0 tested parameters can be guaranteed by using the significance level α_0/p_0 for each single test, called Bonferroni correction (see e.g. [*Seber*, 1984]). Hence, the significance value α is determined by working with the $t_{n-1,\delta}$-distributions for each parameter, and then multiplying the minimum of the significance values with p_0:

$$\alpha = p_0 \cdot \min(\alpha_1, \ldots, \alpha_{p_0}) \tag{5.1}$$

The so-calculated significance values for different groups of measured parameters in the class MPBL are shown in Figure 5.26. As before, isolines for $\alpha = 1$, 5, 10, 25 % are shown. Comparison with Figure 5.25 illustrates the construction of the so-determined confidence regions as mainly the intersection of the confidence regions for the single parameters[36]. If only measured NO_x and VOC are compared to the model, the reference point lies just at the 1% significance level, which had been chosen as threshold for the confidence interval of the measurements. Thus, combined testing of the VOC and NO_x parameters does not generate a significant deviation of the model results from the measurements.

However, if ozone is considered in addition to VOC and NO_x, the reference point lies completely outside the 1% significance level. Even regarding uncertainties in the absolute determination of the significance levels, it can thus be stated that the model with this emission scenario differs significantly from the measurements. An increase of the VOC/NO_x ratio by 50%, as indicated by the dashed line, yields model results within the confidence region of the measurements. This is consistent with the findings from testing the model for ozone only. But by including NO_x and VOC in the test for the model results, the region of possible VOC and NO_x emissions is further confined. While the results for ozone only allow for a wide range of absolute emission rates along the line of 50% increased VOC/NO_x ratios, now the confidence region is limited to absolute values close to the emission rates at the reference point.

[36] Additionally, comparison with Figure 9.1 in the Appendix 9.2 shows that the so-determined confidence regions yield only minor differences to the results from the multivariate F-distribution in the class MPBL if the number of tested parameters is small enough (i.e. for up to three tested parameters).

A similar result is obtained when peroxide and HCHO, or additionally, NO_y-HNO_3 are included in the analysis.

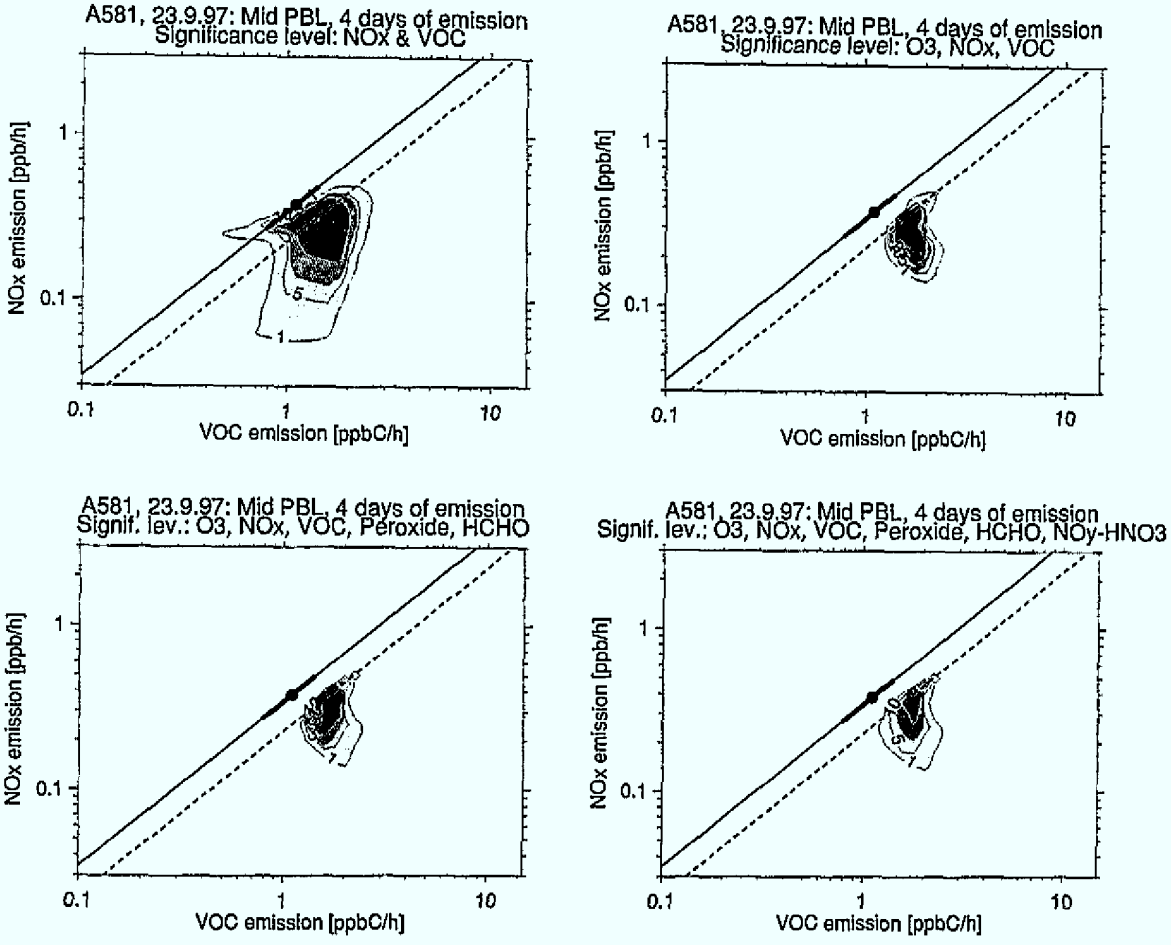

Figure 5.26: Isolines of the significance levels α = 1%, 5%, 10%, 25% for the null hypothesis that model-observation differences are solely due to statistical variability. Shown are the test results determined by $\alpha = p^*\min(\alpha_1,...,\alpha_p)$ in the class MPBL. The tested parameters are given in the header of each plot, NO_y has to be read as NO_y-HNO_3.

For the class of measurements in the surface layer the confidence interval is confined to a narrow range of VOC/NO_x ratios whenever O_3 is taken into account (Figure 5.27). This is due to the VOC-limited chemistry observed in the surface layer, where the ozone production depends strongly on the VOC/NO_x ratio. On the other hand, the relative insensitivity of VOC–limited O_3 production on the absolute emission rates leads to a rather wide range of the confidence region along the line of constant VOC/NO_x ratios.

Again, including peroxide, HCHO and (NO_y-HNO_3) in the analysis does not essentially change the results. The confidence region for the measurements in the surface layer class is centred along the dotted line, indicating 50% increased emission ratios with VOC/NO_x = 4.5 ppbC/ppb, while the reference point lies outside the 1% significance level.

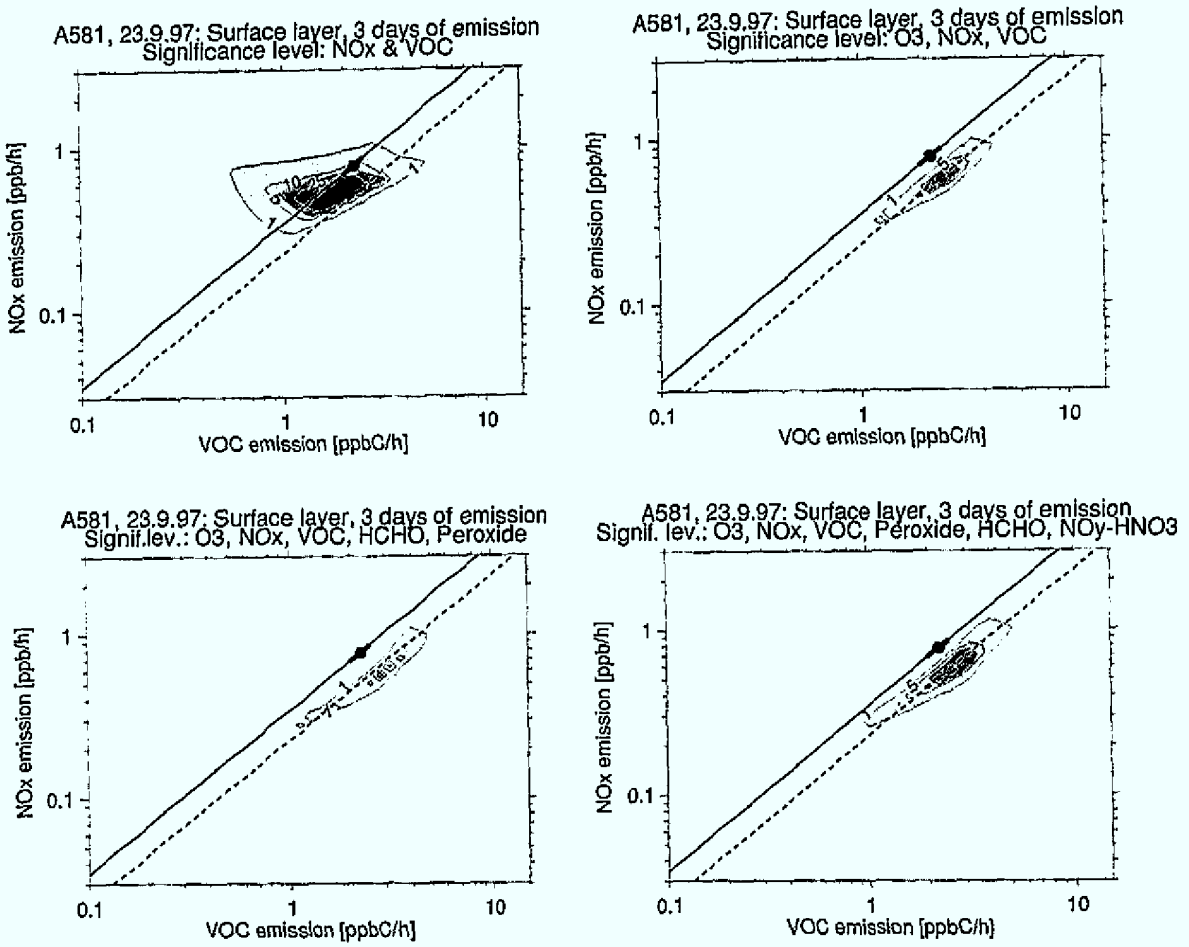

Figure 5.27: As Figure 5.26, but for the class SL.

5.2.4.3 Sensitivity studies

The EKMA plot analysis in the last chapter yielded a significant deviation of the modelled O_3, NO_x and VOC from the measurement if NO_x and VOC are assumed co-emitted to CO with ratios taken from the EMEP emission inventory for 1996. On the other hand, a good agreement between model results and these measured parameters within the statistical confidence interval is found under the assumption of about 50% higher VOC/NO_x ratios, i.e. VOC/NO_x ≈ 4-5 ppbC/ppb.

A possible model scenario that leads to results within the confidence region of the measurements is, for example, given by a 20 % reduction of the NO_x emissions combined with a 20% increase of the VOC emissions. These values are easily within the uncertainty range of the emissions. The overall uncertainty of emission inventories is difficult to assess, due to propagation of uncertainties from many assumptions and estimates. Thus, only a few studies of the uncertainty of emission inventories have been reported so far ([*Placet et al.*, 2000], and references therein). In a recent experiment to assess the uncertainty of CO, NO_x

and VOC emissions of a city (Augsburg) in Germany, the Evaluation of Emission Inventory Experiment (EVA), the standard deviation of calculated NO_x emissions was estimated as 40% [*Slemr et al.*, 2000]. Even higher uncertainties are assumed for the calculated VOC emissions, since for a main part of the VOC mix no information about the individual emitted compounds is available [*D .Klemp*, personal communication].

Thus, the emissions of VOC and NO_x are analysed as input parameters to the model that explain the deviations between model results and measurements in their uncertainty range. On the other hand, the idea was to investigate whether, from the observations in a European continental plume, the correctness of the VOC/NO_x ratio of the emission inventory can be determined and thus the uncertainty of the inventory confined. However, the significant deviation of the modelled ozone formation from the observations for NO_x and VOC emissions according to the inventory, does not automatically lead to rejection of the given emission inventory. In this context the question which has to be first answered is whether the deviation of the modelled trace gas concentration from the observations can be explained by uncertainties of the input parameters other than the emission rates of VOC and NO_x.

The uncertainty of atmospheric chemistry model calculations is difficult to assess. The problem lies in the high complexity due to the large number of input parameters and the many equations and parameterisations. A most widely used approach to investigate the uncertainties in modelling systems are sensitivity analysis procedures. In this approach the result of a base case run is compared to the results from additional simulations with one parameter value changed at a time [*Bergin et al.*, 1998]. The difficulty of this approach is that input variables of atmospheric chemistry models are often strongly correlated and the whole system is nonlinear. Therefore combined analysis of the different input uncertainties is useful to estimate the uncertainty of the model results.

Uncertainties are caused by input variables such as initial values, deposition and photolysis rates, and the reactivity of the VOC split assumed in the model calculation. The assumed uncertainties for these input variables of the model calculations are given in Table 5.2. It shows a selection of the overall model uncertainty only with respect to the choice of considered input variables. For example, the uncertainty of the whole chemical reaction group, including uncertainties of chemical rate constants and algorithms, is not taken into account. Also, the influence of variations in temperature and relative humidity do not have a significant impact [*Bergin et al.*, 1999], and was, therefore, not included in the analysis.

Table 5.2: Sensitivity analysis for assumed uncertainties of input variables of the model calculations

Input variable	Uncertainty range	Range in modelled O_3 [37]
Initial ozone concentration	± 25%	39-47 ppb
Mean reactivity of VOC split	± 20%	33-50 ppb
Photolysis rates	± 20%	33-55 ppb
Deposition velocity	± 50%	33-60 ppb

The uncertainties of input parameters for environmental models are generally not well known and are not often discussed in literature [*Hanna et al.*, 1998]. Therefore, the uncertainties given in Table 5.2 are only estimates, which have to be motivated in the following.

The initial ozone concentrations were determined by the mean of the start values for all bottle sample trajectories in a class, taken from the MCT model (University of Bergen) output[38]. Within the classes MPBL and SL, a standard deviation of the initial ozone mixing ratios of 20% is found. This gives an estimate of the uncertainty of initial ozone due to uncertainty in the origin of the air mass. The overall estimate of the uncertainty with 25% is slightly higher, to take into account uncertainties of the MCT model results. An estimate resulting from questionnaires answered by modelling experts [*Hanna et al.*, 1998] assumes ± 30 % uncertainty for the initial ozone concentrations, consistent with the estimate given here.

The modelled photolysis rates have been compared to observations of JNO_2 and JO^1D in chapter 5.2.3. It was found that the modelled frequencies for JNO_2 underestimate the measurements for clear sky regions by around 20%, probably due to haze in the marine boundary layer, which has not been considered in the photolysis model. This is taken into account as uncertainty of the modelled photolysis rates for this flight. Influence of clouds could yield even higher uncertainties, but would only be expected shortly before and during [39]the flight.

An important component of the uncertainty analysis is the mean reactivity of the VOC mix towards the primary degradation step by OH[40]. The mean reactivity is defined here as the

[37] Model run for the reference point of the EKMA plot scenario for the class MBL. Observed O_3 for this class: 76 ± 5 ppb.
[38] Compare chapter 5.2.2.4
[39] Compare chapter 5.2.2.2
[40] Compare chapter 2.1.2

mean rate constant of the VOC mix towards OH, weighted by the percentage of the individual species [*Schmitz et al.*, 1997]:

$$\langle k_{OH} \rangle = \frac{\sum k_{OH}^{i} \cdot [VOC_i]}{\sum [VOC_i]} \quad (5.2)$$

where $[VOC_i]$ is the concentration of a compound i of the VOC mix, and k^{i}_{OH} is its rate constant towards oxidation by OH. A higher reactivity of a VOC mix has a comparable effect on the photochemical ozone formation as an absolute increase of the VOC emissions. This is because the initial attack of VOC by OH is typically the rate-limiting step in the degradation cycle. Nevertheless during the ageing of the air masses the potential of oxidative material and different degradation paths become important, so a reactivity change is not completely equivalent to emission rate changes and so will be investigated here.

As no reliable estimates of the uncertainty of VOC splits exists [*Placet et al.*, 2000], the uncertainty of the mean reactivity in Table 5.2 can be nothing more than a rough estimate. For valuation, the Gaussian error of the mean reactivity from the standard deviation of the data in the VOC data base [*Mannschreck et al.*, 2000] used for the VOC split was calculated. This yields an uncertainty of the mean reactivity of the VOC mix of 10%. Additional uncertainty is given by the addition of carbonyls and organic acids not included in the data base from the GENEMIS split, as well as the uncertain amount of biogenic hydrocarbons, especially isoprene. Biogenic hydrocarbons were not included in the emissions for the model calculations because in the study area (N.W. Europe) man-made VOC emissions are thought to dominate over isoprene emissions [*Simpson*, 1995]. In addition, these should have lost importance in September, as isoprene emissions decline in concert with autumnal leaf senescence [*Fuentes and Wang*, 1999]. Nevertheless, not including biogenic hydrocarbons adds uncertainty to the mean reactivity of the VOC split.

The last variable studied in the uncertainty analysis is the deposition velocity. In the model only a coarse parameterisation of different deposition velocities is realised, distinguishing land and sea, as well as day and night. Model calculations and measurements have shown strong variations of deposition velocities as a function of month, time of day, surface type (e.g. vegetation or land-use) and meteorological parameters like wind speed, stability and insolation [*Brook et al.*, 1999]. Therefore an uncertainty of $\pm$ 50% was assumed, as stated in the above mentioned expert questionnaire [*Hanna et al.*, 1998].

The sensitivity of the modelled ozone to each of these uncertainties is given by the range of modelled O_3 in Table 5.2. Photolysis rates and deposition velocities are each treated as a group with uniform variation for all individual variables. The base case for this sensitivity analysis is the emission scenario for the reference point of the EKMA plot in the class MPBL. None of the uncertainties taken alone can explain the observed differences between modelled and measured ozone mixing ratios, as the range of modelled O_3 stays well below the measured 76 ± 5 ppb.

Still, it has to be investigated whether the combined influence of the uncertainties of these input variables yields results compatible with the measurements. Virtually all combinations of the input parameters within the uncertainty range are possible and have to be tested. One possibility for doing this is by Monte Carlo techniques [*Bergin et al.*, 1999; *Hanna et al.*, 1998]. Nevertheless, to keep the computing managable, here only a simple approximation was chosen. The range of the uncertainties was roughly estimated for each variable by three points: the base case value and the upper and lower uncertainty limits. Sensitivity runs were performed for all permutations of these values. The results of each sensitivity run is tested for significant deviation from the observations of O_3, NO_x and VOC by the significance analysis described in the last chapter. As the influence of the initial ozone concentrations was found to be rather small, this variable was neglected in the combined uncertainty analysis.

Table 5.3: Results of the sensitivity study for the combined influence of the uncertainty range of input variables. Shown are the modelled O_3, which has to be compared to the measurements of 76±5 ppb O_3, and the significance levels α for the null hypothesis that model-observation differences for O_3, NO_x and VOC are solely due to statistical variability. Photolysis rates, reactivity of the VOC split and deposition rates are varied relative to the base case as given in the table. Only results with $\alpha > 0.1$ are shown in the table

Photolysis rate	Reactivity	Deposition	O_3 [ppb]	α (O_3, NO_x, VOC)
+20%	Base case	-50%	76	**77.89**
Base case	+20%	-50%	69	**3.22**
+20%	+20%	-50%	83	**1.72**

This method gives a rough estimate of the overall uncertainty, as the combination of interim values is not taken into account. Nevertheless, it serves the purpose of investigating whether the uncertainty of the above described input variables allows for compatibility of model results and measurements without changing the rate of VOC and NO_x emissions. Indeed, combinations of the input values within their uncertainties are found which lead to

agreement of model results and measurements within the confidence region defined by an observed significance level $\alpha > 1$. These are found for the combinations of input variables given in Table 5.3.

At least a reduction of the deposition velocity, combined with an increase of photolysis rates and/or an increase of the mean reactivity of the VOC mix is responsible for the results in Table 5.3. The effect of these changes leads to higher availability of OH radicals in the system. It was shown in chapter 5.2.4.1.2 that the ozone production in the model calculations is strongly VOC limited. Under these conditions, the initial attack of VOC by OH is the rate-limiting step in the ozone formation. Thus, besides an increase in VOC or decrease in NO_x, a higher availability of OH radicals amplifies the ozone production for this regime. OH radicals are formed by photolysis of ozone itself, formaldehyde and other intermediate organics. Deposition again is a major sink for the precursors of OH like O_3. Thus a combination of increase in photolysis rates and decrease in deposition leads to an increase of the available OH radicals, which in turn amplify the ozone production. The effect of increasing the reactivity of the VOC mix is again an acceleration of the initial attack of VOC by OH, which can then lead to additional radical production during the oxidation chain.

Hence several possible combinations of input variables lead to an amplification of the photochemical processing in the model, which renders an agreement with the measurements within the statistical confidence. To validate this finding, Figure 5.28 and Figure 5.29 show the significance analysis for the case with 20% increased photolysis rates and 50% reduced deposition for the EKMA plot calculations in the classes surface layer and mid PBL. Shown are the confidence regions for O_3, as well as the combined confidence regions defined by equation (5.1) for NO_x and VOC, for the combination of these with O_3, and for all measured chemical species as discussed in chapter 5.2.4.2.2.

The results show that by changing the input parameters within their estimated uncertainties, the confidence region of agreement between model and measurement, dependent on the VOC and NO_x emissions, coincides with the reference point for the class MPBL (Figure 5.28), and touches it in the class SL (Figure 5.29). Thus, the deviation between the base case model run and the observations can be explained by uncertainties of different model parameters. These are, besides the emission rates of VOC and NO_x, combinations of other input variables. The combination of uncertainties in the photolysis rates and deposition velocities is chosen to demonstrate the impact of their uncertainties, as they are

independent of the emission rates. Though not shown here in form of an EKMA plot, the mean reactivity of the VOC split has a similar impact on the modelled trace gas composition.

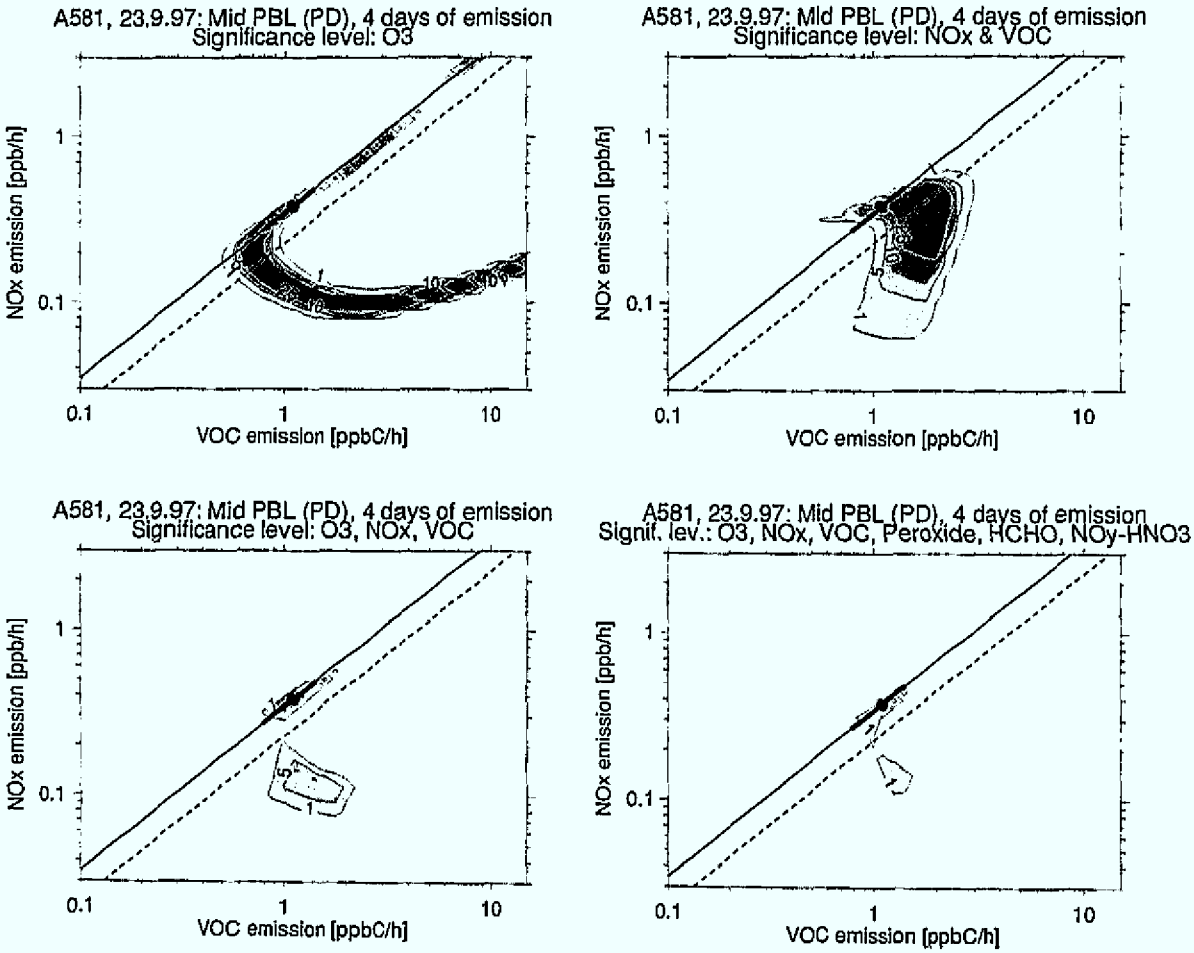

Figure 5.28: Isolines of the significance levels α = 1%, 5%, 10%, 25% for the null hypothesis that model-observation differences are solely due to statistical variability for an EKMA calculation with 20% increased photolysis rates and 50% reduced deposition relative to the base case. Shown are the test results of the non-central $t_{n-1,\delta}$-distribution for O_3, as well as the combined test result determined by $\alpha = 3*\min(\alpha_{O3}, \alpha_{NOx}, \alpha_{VOC})$ in the class MPBL. The tested parameters are given in the header of each plot.

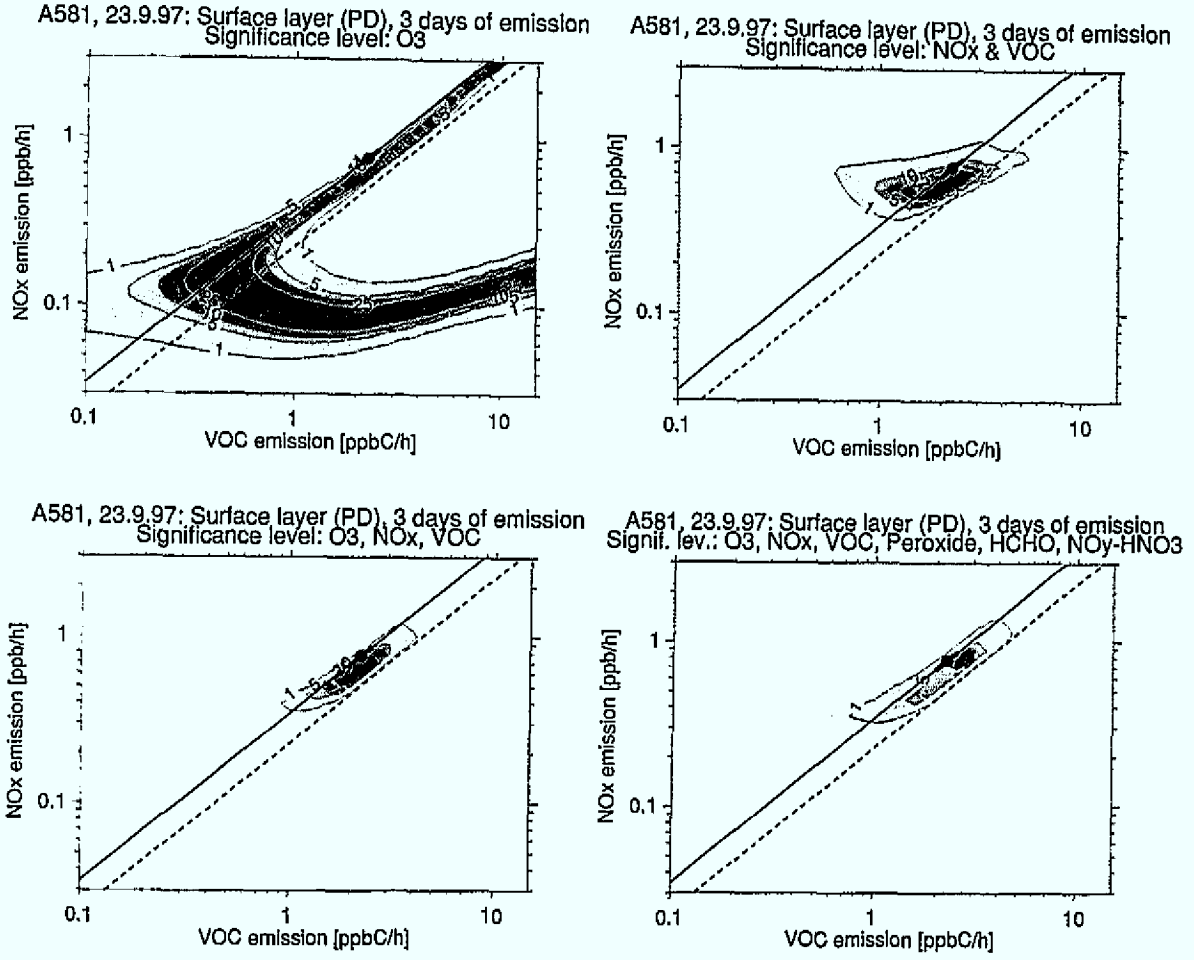

Figure 5.29: As Figure 5.28, but for the class SL.

5.2.5 Results from model calculations with changed input variables

The last step in this analysis is the transfer of the results of the EKMA plot analyses back on the explicit model runs along the bottle sample trajectories. The analysed sensitivity of the simplified EKMA model scenario to the uncertainties of VOC and NO_x emission rates, photolysis rates, mean reactivity of the VOC mix and deposition velocities, will be interpreted with respect to the detailed model set-up for individual measurements. According to the results from the last chapter, this will be shown for a model run with increased VOC/NO_x ratio, as well as for one with higher photolysis rates and less deposition.

Additionally, the high sensitivity of the model results to the reactivity of the VOC mix is considered. Due to this high sensitivity, biogenic emissions may be important for the observed situation, even if on average their emissions are thought not to be important for determining O_3 over Europe [*Simpson*, 1995].

Therefore, in the following model runs an increase of the reactivity of the VOC mix by biogenic emissions is approximated by taking into account biogenic isoprene. Its emissions are taken from global monthly emission fields [*Guenther et al.*, 1995] on a 1° by 1° grid. For simplicity, diurnal variations in isoprene emissions are approximated to be a quadratic with a maximum at solar noon and zero during the hours of darkness, as described in [*Evans*, 1999].

5.2.5.1 Increasing the VOC/NO_x emission ratio

From the EKMA plot analysis it was concluded that a 20% reduction of the NO_x emissions combined with a 20% increase of the VOC emissions should lead to model results consistent with the observations. This has been tested by a rerun of the model for all bottle sample locations, with the VOC and NO_x emissions along the trajectories changed accordingly to these factors. The results in Figure 5.30 and Figure 5.31 are presented in the same way and with the same scaling as in chapter 5.2.3.1, to enable easy comparison.

Obviously the net change of O_3 mixing ratios in the model gets much closer to the observations for the combination of increased VOC and reduced NO_x emissions. This can be seen in the improved correlation coefficient of $r^2 = 0.69$, as well as in the improved relation with CO. The observed ozone production for the bottle samples in the MPBL is now well reproduced by the model, as well as the decrease in ozone for high CO mixing ratios in the surface layer. Nevertheless, some underestimation of the modelled ozone in the surface layer is still apparent.

With the changed emissions, also modelled precursor NO_x, VOC and NO_y concentrations now show an overall good consistency with the measurements. The strong overestimation of NO_x, as found in the base case model results, has clearly disappeared. Still, some deviations are found in the surface layer, with overestimation of VOC by a factor of two for three of the bottle samples. As for the base case model run, this overestimation is seen likewise for the modelled formaldehyde. Besides these three bottle samples in the surface layer, the range of modelled HCHO mixing ratios compares well with the measurements, especially in relation to CO as emission tracer.

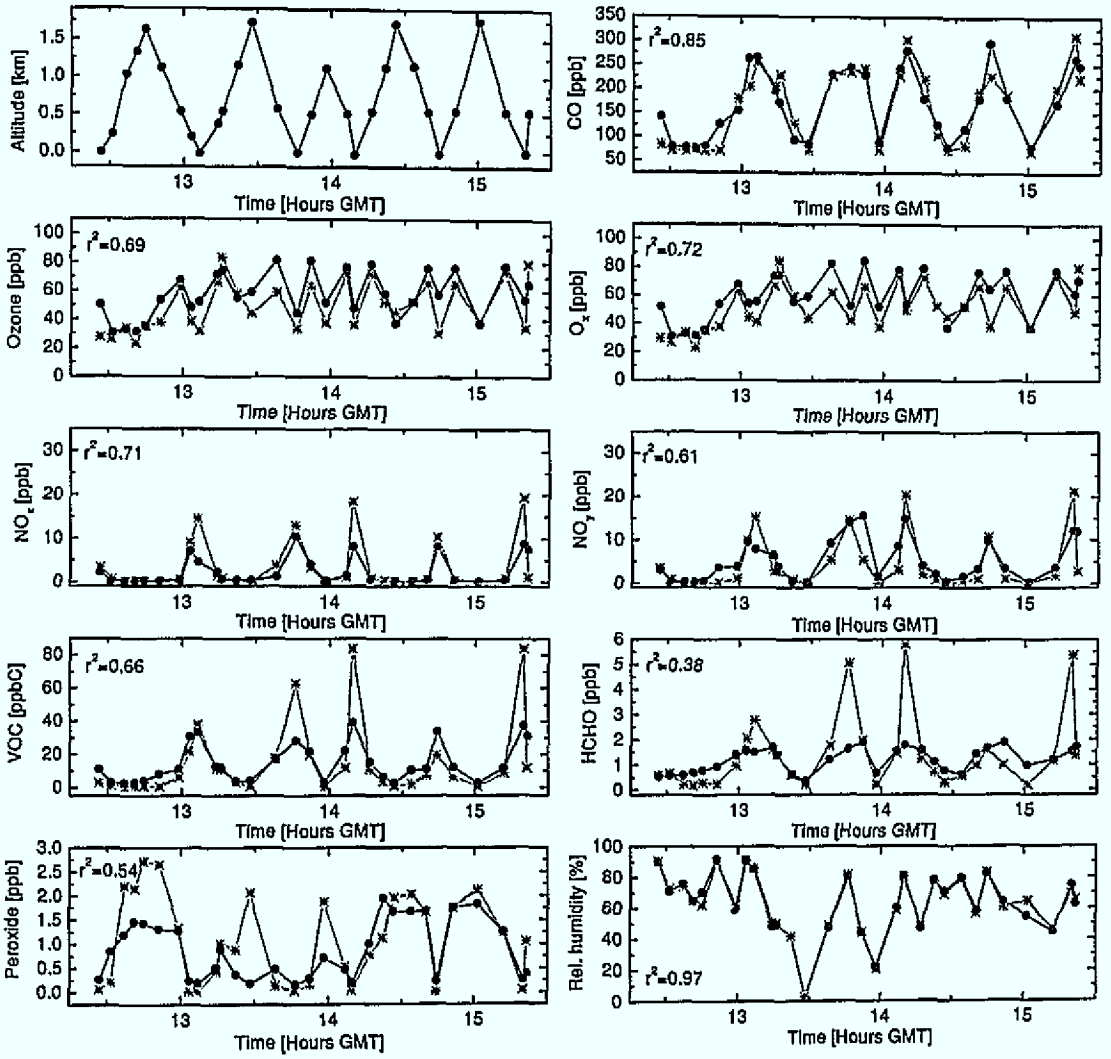

Figure 5.30: Time series of measured and modelled values at the bottle sample locations of flight A581 (23rd September 1997). Measurement as black circles, modelled values as grey stars. Model run with biogenic hydrocarbon emissions [*Guenther et al.*, 1995], 20% increased anthropogenic hydrocarbon emissions, and 20% decreased anthropogenic NO_x emissions.

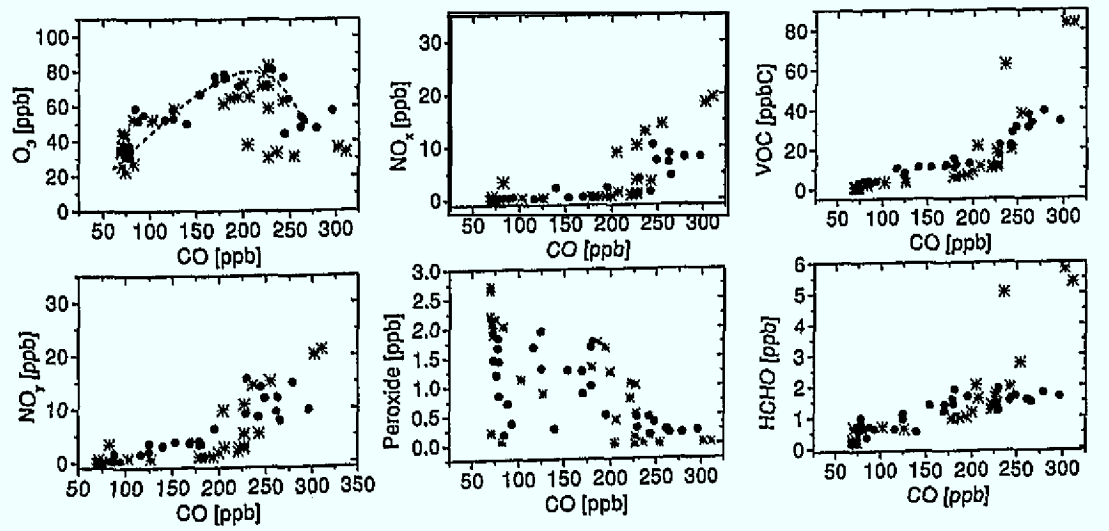

Figure 5.31: Relationship of O_3, NO_x, VOC, NO_y, H_2O_2 and HCHO to CO at the bottle sample locations of flight A581 (23rd September 1997). Measurement as black circles, model results as grey stars. Model run with biogenic hydrocarbon emissions [*Guenther et al.*, 1995], 20% increased anthropogenic hydrocarbon emissions, and 20% decreased anthropogenic NO_x emissions.

Also, the modelled peroxide now compares much better to the measurements than for the base case model run. In contrast to the base case, the model with changed VOC/NO_x emission ratio reproduces the observed peroxide production in the MPBL, indicating a correct representation of the relative roles of VOC and NO_x in the ozone production. Still peroxide is overestimated for part of the bottle samples observed in the free troposphere. These bottle samples are not affected by European emissions and thus are of no importance for this analysis.

Altogether a good agreement of the model results for increased VOC/NO_x emission ratios with the measurements is found, as predicted by the EKMA plot analysis. That the same degree of agreement is not found for some of the bottle samples in the surface layer as supposed from the EKMA plot results, may be due to a deviation of the scenario for the emission input in the EKMA plot compared to the individual trajectories. In the EKMA plot homogeneous emission input over the last three days before the measurement was assumed, while for individual bottle samples in the SL the model shows an increasing emission input with the time, with higher emissions shortly before the measurement[41].Thus, for these bottle samples photochemical processing of the precursor emissions was not given enough time in the model runs.

5.2.5.2 Increasing the photolysis rates and decreasing the deposition

The second scenario from the EKMA plot analysis that will be investigated for individual bottle sample locations, is a 20% increase of the photolysis rates, combined with a 50% reduction of the deposition velocities. The results in Figure 5.32 and Figure 5.33 are very similar to the results obtained for the increased VOC/NO_x emission ratio. This is consistent to the conclusions from the EKMA plot analysis. Here, only some of the observed deviations will be discussed.

The ozone production for the bottle samples in the MPBL is further increased, with highest values up to 100 ppb even exceeding the observations, while in the SL layer the modelled ozone is still slightly too low. Despite this slight overestimation of the range of modelled ozone concentrations, the form of the observed relationship between ozone and CO is reproduced very well by the model scenario.

[41] This can, for example, be seen for the modelled emission input for bottle sample no. 9 in the SL layer, shown in Figure 5.21.

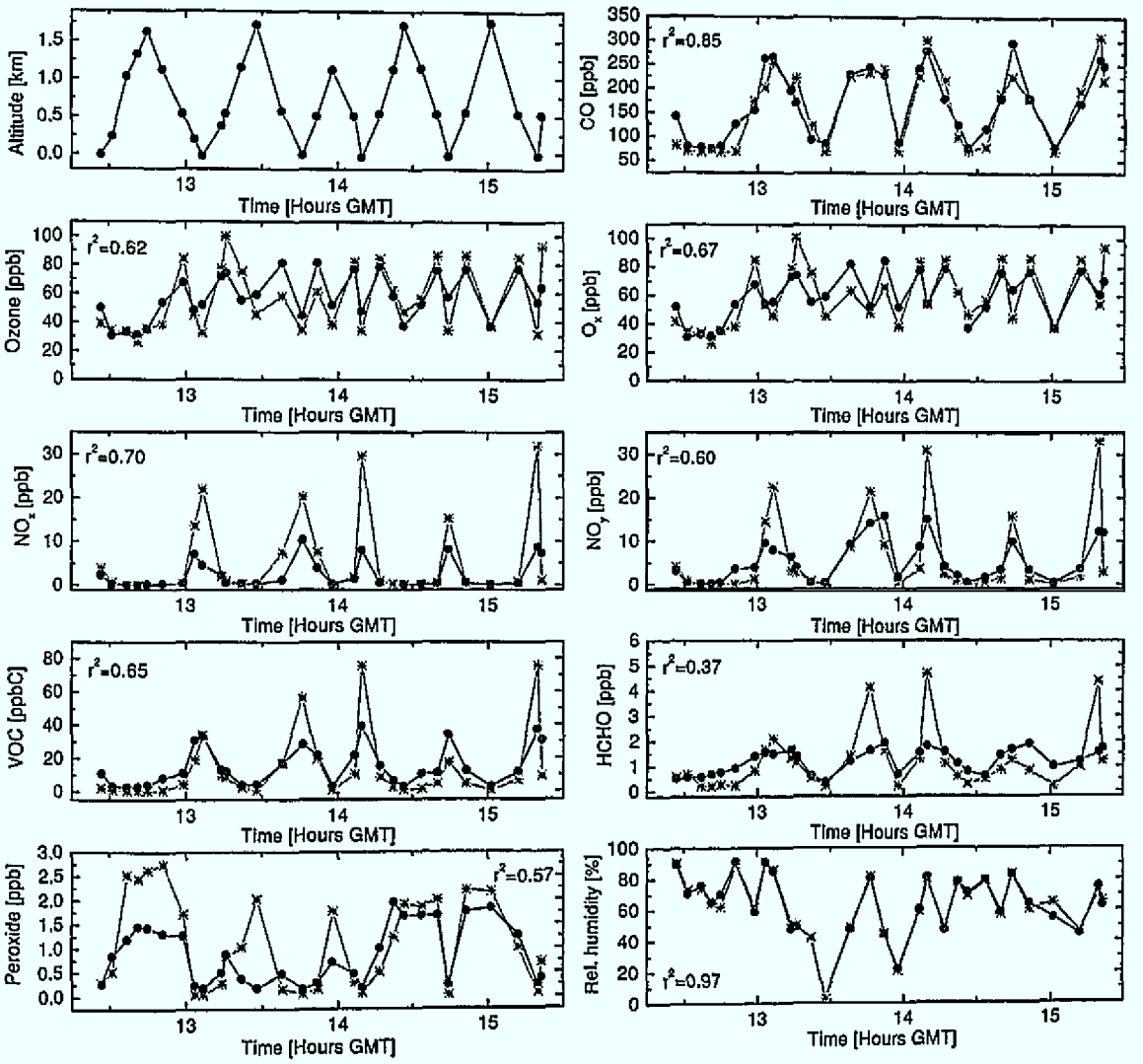

Figure 5.32: Time series of measured and modelled values at the bottle sample locations of flight A581 (23rd September 1997). Symbols like Figure 5.30. Model run with biogenic hydrocarbon emissions [*Guenther et al.*, 1995], 20% increased photolysis rates, and 50% reduced deposition velocities.

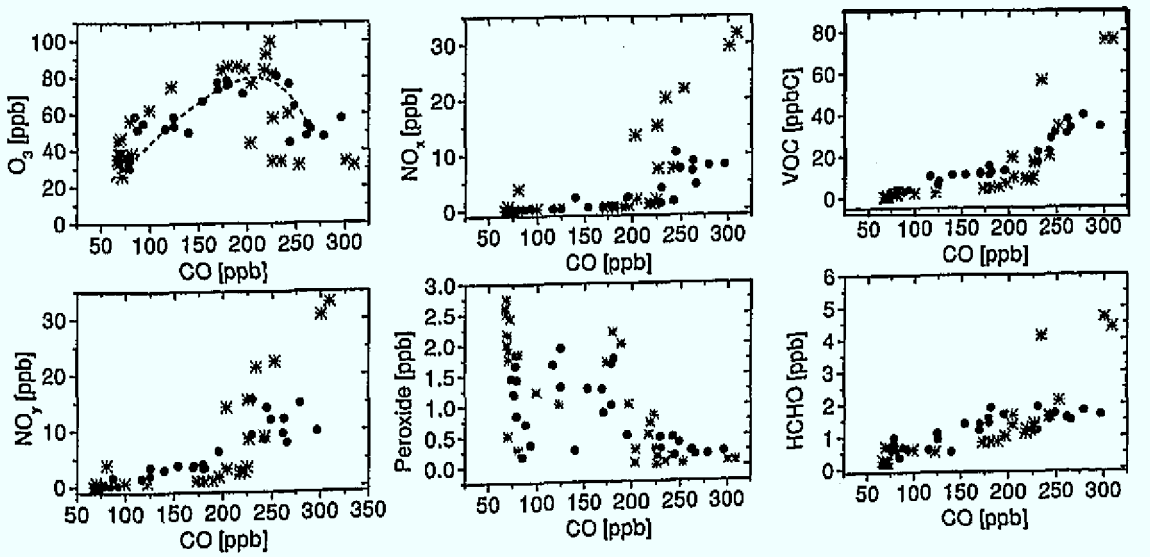

Figure 5.33: Relationship of O_3, NO_x, VOC, NO_y, peroxide and HCHO to CO at the bottle sample locations of flight A581 (23rd September 1997). Symbols like Figure 5.31. Model run with biogenic hydrocarbon emissions [*Guenther et al.*, 1995], 20% increased photolysis rates, and 50% reduced deposition velocities.

However, in contrast to the results with changed VOC and NO_x emissions, a strong overestimate for the VOC and NO_x model results in the surface layer still exists. The difference to the results with reduced NO_x emissions (Figure 5.30) is more than the 20% reduction of NO_x. The additional difference can be explained by reduced NO_2 deposition.

On the whole, the model set-up with increased photolysis rates and reduced deposition is also capable of reproducing the main features of the observed ozone production. Thus, as indicated by the sensitivity studies, the uncertainties of the model parameters allow for several model set-ups that are able to explain the observations.

5.3 Conclusions

The aim of the analysis of the TACIA flights was to investigate whether it is possible to strengthen the knowledge of the relative roles of VOC and NO_x in forming ozone in a European plume over the North Atlantic, and whether measured precursors and ozone are consistent with current European emission inventories.

A major problem for this analysis is the accurate reconstruction of the transport and emission inputs into the plume, which is the prerequisite for the correct analysis of chemical processing. It turns out that the newly developed transport module, in combination with the CO observations as inert tracer for anthropogenic emissions, is a useful tool for the analysis of the European emission/transport problem. Thereby one flight could be selected for which the meteorological conditions allow for a very good description of the observed tracer transport with the model.

For this flight, A581 on 23rd September 1997, the chemical processing in the observed plumes is analysed with the help of model calculations. A clear underestimation of the modelled ozone production was found. The separate tracer analysis enables transport to be excluded as a reason for the deviation of the model results from the observations.

Transport analysis in combination with the chemical observation was used to cluster the observations into three classes according to observed layering (surface layer, mid boundary layer and free troposphere) which enabled the formulation of simplified model scenarios.

These model scenarios were used for EKMA plot calculations in an extensive sensitivity study of the relative role of VOC and NO_x emissions. It could be shown that, despite the large degree of abstraction, the results of the EKMA plot calculations can be compared to

the measurements. Thereby a helpful tool for the interpretation of the observation with respect to the relative roles of VOC and NO_x could be set up.

The base case EKMA model scenario, with emission ratios taken from the EMEP emission inventory of 1996 and scaled to the measured CO mixing ratios, did not reproduce the observed ozone formation. Instead, the model results reveal VOC limitation for the surface layer as well as for the mid boundary layer, the latter not supported by the observations.

A central point of this study is the use of statistical tests to analyse the significance of the deviation between model results and measurement. In doing so it became possible to assess whether the comparison of model results and measurements can constrain the uncertainty of possible VOC and NO_x emission scenarios in Europe.

The statistical tests showed that the deviations between model results and measurements are significant if the input parameters of the model calculations are regarded as true values. However, if the uncertainties of these input variables are taken into account, the model results move into the confidence region of the measurements. The analysed uncertainties include the uncertainty of VOC and NO_x emission rates relative to the CO emissions, and certain combinations of the uncertainties of photolysis rates, mean reactivity of the VOC mix and deposition velocities. Different combinations of the input variables within their uncertainties were shown to produce model results statistically consistent with the measurements.

The results from the statistical analysis of the EKMA framework have been transferred to detailed model runs for the individual measurements. Thereby, for two different combinations of input variables within the confidence region of the EKMA calculations, a good agreement was also shown with the individual measurements. These scenarios are a 20% increase of anthropogenic VOC emissions, combined with 20% reduction in NO_x emission, resulting in a 50% increase of the VOC/NO_x emission ratio, as well as a combination of 20% increase in the photolysis rates with 50% decrease in the deposition velocities. Since both scenarios are within the estimated uncertainties of the input parameters, they cannot be distinguished in their effect on the observed ozone formation. Thus from this study no conclusion about the consistency of European emission inventories with TACIA observations is possible.

The uncertainties in the input variables included in the sensitivity analysis have to be counted for in the same way in more complex three dimensional atmospheric chemistry models. Thus, the use of more complex models would not yield a different conclusion in this study. Therefore, to learn more about a single input variable of a model by observations in an ageing plume, more constraints have to be put on the rest of the input variables. If it is possible to further constrain these input variables, it could become possible to validate European emission inventories by TACIA like observations.

6 Discussion of transport and chemistry during ACSOE

6.1 Introduction

While with the data from the TACIA experiment rather fresh emissions in the lower part of the troposphere and close to the continent could be analysed, the ACSOE data can and will be used for the analysis of long range transport of primary pollutants and ozone in the remote free troposphere. These air masses were identified in chapter 3.3.2 by a positive correlation between O_3 and CO, which points to photochemical production of ozone from anthropogenic emissions. Slopes of correlation plots between O_3 and CO have already been used in recent papers to estimate the amount of ozone produced photochemically in an ageing plume since the time of emission [*Parrish et al.*, 1993]. Interestingly, the observed slope of the O_3-CO correlation during ACSOE is significantly higher than that found in the lower troposphere during TACIA. Thus the observations indicate a more effective production of ozone in the free troposphere than in the PBL. Since larger slopes of O_3-CO correlations in the free troposphere than in the PBL have been reported from several different locations and times [*Gerbig et al., 1997*], such observations are probably significant and of importance for understanding the ozone budget of the free troposphere.

A prerequisite for the interpretation of the observed correlation between ozone and CO in the context of the ozone production efficiency in the free troposphere is the analysis of the origin of the observed ozone plume. The question is whether the enhanced ozone was photochemically produced in the free troposphere or produced in the boundary layer, followed by venting to the free troposphere with subsequent long-range transport.

The principal problem is similar to that described in chapter 5 for the analysis of fresh plumes in the lower part of the troposphere: the history of the air masses has to be analysed before more can be learned about the chemical processing of an anthropogenic plume in the different parts of the troposphere from the observed trace gas compositions. Again, the strategy will be to separate chemistry from transport. In a first step the transport of an observed plume will be analysed by running the model described in chapter 4 with CO as an inert tracer. Provided that source region and upward transport can be identified by the tracer experiment, the ozone production in the free troposphere versus ozone export from the planetary boundary layer can be estimated.

A condition for such an analysis is the identification of a pronounced plume, marked by clearly elevated CO mixing ratios. This plume has to be large enough in scale to allow its representation by the transport module. Important indicators for the chemical processing of a plume are the amount and composition of hydrocarbons. Therefore, observations of VOCs are needed, that can still be related to the emission input, which means that acetylene and long-lived alkanes should exhibit a clear correlation to CO as tracer of anthropogenic emissions.

Those conditions were best met by the observations during the flight A575 on September 14th 1997.

6.2 Observations

The flight A575 took place south-south-west of the Azores[42], east of Hurricane Erika. A number of deep profiles, from about 7 km altitude to 15 m above sea level, were performed. Within each of these profiles short horizontal runs were carried out, in order to take a total of 40 flask samples.

In the latter part of the flight (profile 5 onwards), strongly enhanced O_3 mixing ratios at about 5–7 km altitude were observed in correlation with increased concentrations of CO, NO_y and long-lived hydrocarbons. This is illustrated in Figure 6.1 where the observed O_3, CO, NO_y, NO, the sum of measured VOC, H_2O_2, dew point and temperature are plotted against altitude for profile 7.

This profile exhibits a strong increase with altitude of ozone and CO with distinct highly correlated layering between both species. Furthermore, layers of only a few hundred meters thickness with enhanced O_3 are matched by synchronous increase of NO_y. The slope for the correlation between O_3 and CO for some layers reaches up to more than 1 ppbO_3/ppbCO (compare Figure 6.2). These air masses (above 3 km) are relatively dry, which indicates descending air. A contribution of stratospheric air masses to the observed enhancement in ozone can be excluded despite the low humidity. The distinct layering with sharp gradients indicates high stability of the air masses, which inhibit strong vertical mixing. Thus, ozone of recent stratospheric origin would stay in separate layers with low humidity and low CO [*Newell et al.*, 1999]. The observed positive correlation of O_3 with

[42] Compare Figure 3.4 and Table 3.4.

CO for the distinct layers speaks against this. Hence, the observations of O_3, CO, NO_y and water vapour suggest upward transport of a continental air mass, loaded with anthropogenic emissions, to an altitude of at least 8 km (corresponding to a dew point of 240 K), with subsequent descent during the transport towards the Azores.

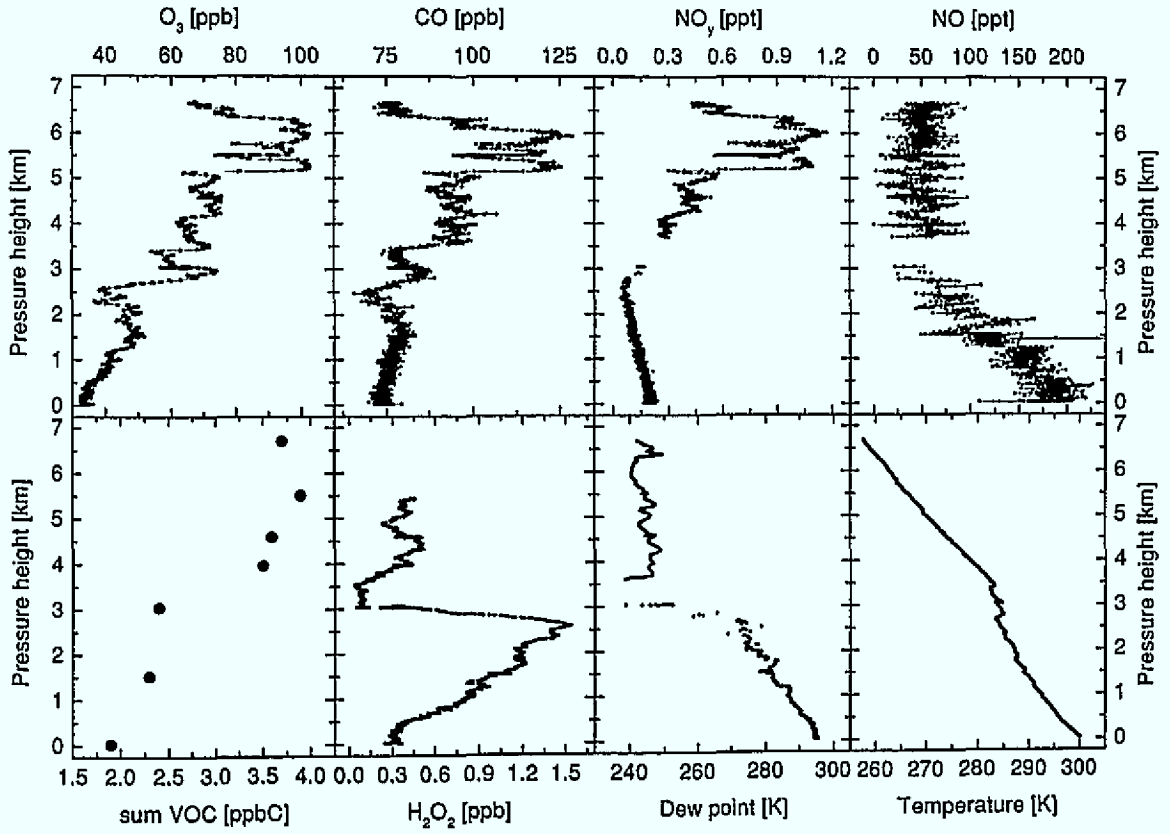

Figure 6.1: Profile 7 measured during the ACSOE flight A575 on 14th September south west of the Azores. Shown are O_3, CO, NO_y, NO, sum of measured VOC, H_2O_2, dew point and temperature.

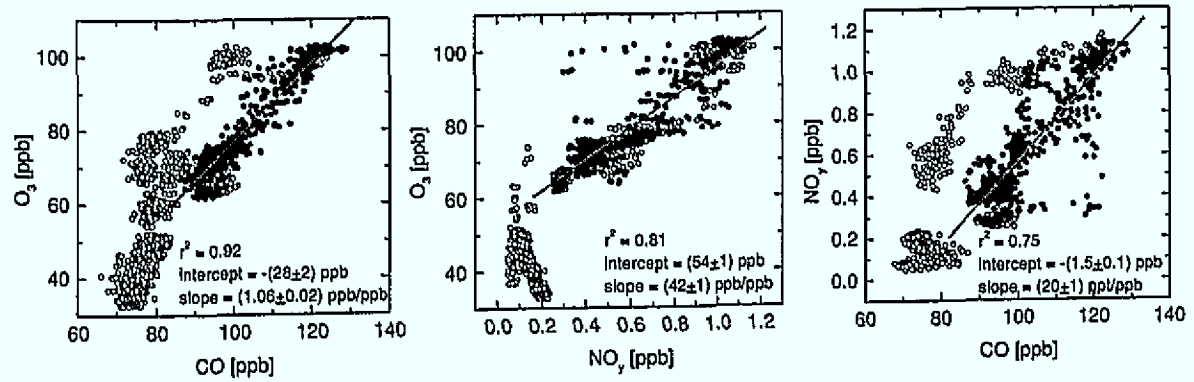

Figure 6.2: Correlation of O_3 with CO (left), of O_3 with NO_y (middle), and of NO_y with CO (right) for profile 7 of flight A575. The filled circles mark data at 4-6 km altitude and constitute the regression.

While the observed NO_y[43] closely matches the gradients of O_3 in the polluted layers, the measurements of NO are near the detection limit of 50 ppt. The information content of the

[43] Note that the observed NO_y is likely to be (NO_y-HNO_3), as explained in chapter 3.1.2.

NO profile above 3 km is therefore practically nothing. However, the upper limit of 50 ppt is close enough to zero to allow the conclusion that the process of ozone formation at the time of observation has already finished and nearly all initially present NO_x has been converted to higher forms of oxides of nitrogen.

H_2O_2 shows generally low values in the relatively dry air above 3 km, with mixing ratios below 0.5 ppb. In the more humid air masses below 3 km higher H_2O_2 mixing ratios up to 1.5 ppb are observed, which decrease towards the surface, presumably as a result of dry deposition [*Reeves et al.*, 2000].

The formaldehyde measurements obtained during this flight are likely to be too high, due to a problem with the instrument's zeros [*G.Mills*, private communication][44]. Therefore they are not included in the analysis.

The above observations of air masses between 5-7 km, marked by elevated CO mixing ratios above 90 ppb adjoint with O_3 mixing ratios above 70 ppb, are used to define a continental plume. Figure 6.3 shows its extent. As can be seen from the highlighted points on the flight track, this plume was encountered during all profiles at the latter part of the flight, i.e. over a horizontal range of several hundred kilometres.

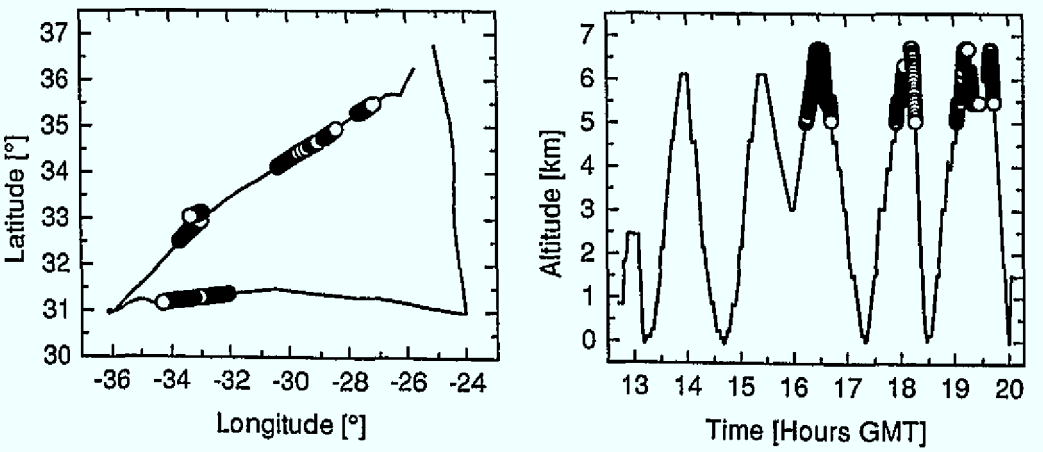

Figure 6.3: Flight path of the ACSOE flight A575 on 14th September 1997. Highlighted points correspond to observed air masses between 5-7 km altitude with CO > 90 ppb and O_3 > 70 ppb. Shown are 10 s means.

The chemical signature of the plume is given in Table 6.1 by the statistical parameters of the observed trace gases.

[44] Compare chapter 3.1.2.

Table 6.1: Chemical characteristics of the continental plume observed during flight A575. Included in the distribution are air masses between 5-7 km altitude, with CO > 90 ppb and O_3 > 70 ppb. Note that only 5 flask samples were taken inside the plume for the determination of VOC mixing ratios.

Species	mean	median	1. quartile	3. quartile	5 percentile	95 percentile
O_3 [ppb]	81	80	76	83	73	99
CO [ppb]	105	104	98	112	92	122
NO_y [ppb]	0.69	0.65	0.60	0.74	0.54	1.03
NO [ppt]	43	41	28	56	8	76
H_2O_2 [ppb]	0.21	0.19	0.15	0.27	0.07	0.38
VOC [ppbC]	4.4	4.6	3.9	4.9	3.6	5.3

Hydrocarbon mixing ratios are shown only as sums of measured VOC in Figure 6.1 and Table 6.1. As discussed in chapter 3.3.3 the mixing ratios of long lived hydrocarbons, especially those of some alkanes and acetylene, are in the range of some hundred ppt and are closely correlated to CO. Conversely, hydrocarbons with lifetimes of hours to a few days are already widely removed. This was used in chapter 3.3.3 to establish a photochemical age of the plume of several days.

A similar approach for the determination of the photochemical plume age makes use of the acetylene/CO ratios. From measurements over the Pacific [*Gregory et al.*, 1996] it was suggested that acetylene/CO ratios (units of ppt/ppb) of less then 0.5 should be representative of well aged air (more then 10 days old), while values greater than 1.0 should be indicative of emissions of only a few days back in time. Figure 6.4 shows the observed correlation between acetylene and CO. The bottle samples collected at enhanced CO mixing ratios exhibit a range of acetylene/CO ratios of 0.8 to 1.2, with a mean of 1.0. Provided that the emission ratios valid for the plume are similar to those in the case discussed by *Gregory et al.* [1996] this indicates that emissions occurred several days, but not before ten days, prior to the VOC measurements over the Azores. Therefore, it should be possible to trace the air masses back to the emission areas within the range of ten-day back trajectories.

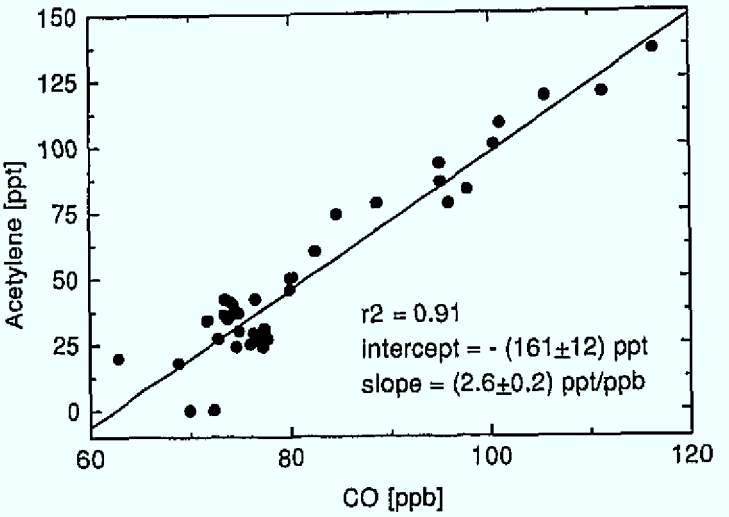

Figure 6.4: Correlation between acetylene and CO observed during flight A575.

6.3 Tracer Analysis for validation of the dynamics

For analysis of the transport of the observed plumes, the model described in chapter 4 was run with CO as inert tracer. The general set-up is similar to the tracer analysis described in chapter 5.1. However, in contrast to TACIA, where only European emissions had to be considered, in the ACSOE case emissions from nearly all of the northern hemisphere, especially from North America, have to be considered. As described in chapter 4.1.3 the CO emissions outside Europe are scaled to NO_x emissions from the global GEIA inventory. This adds some uncertainty to the total amount of emitted CO, as the emission ratios of NO_x/CO can depend on the emission region. The coarse resolution of the GEIA inventory (1° x 1°) is sufficient for this study because the long distance between source and receptor region does not call for a more detailed analysis.

No mixing height fields were available for regions outside of Europe. Thus, the mixing height in the model was adjusted to 1.5 km as a first guess for the average depth of the boundary layer over the United States [*Thompson et al.*, 1994][45].

A mean regional background, corresponding to the lowest 5 percentiles of the measurements during ACSOE[46], was used to initialise the model CO concentration. With 67 ppb, this is slightly lower than that used for the TACIA flights.

[45] taken from [*Holzworth*, 1964]
[46] compare Figure 3.5.

6.3.1 Results

Model results are compared in Figure 6.5 to the measured CO values. Data and model results are averaged over the corresponding boxes given by the trajectory clusters along the flight track. As described in chapter 5.1.1, time series of measured and modelled mixing ratios are compared, as well as the parameters of their statistical distribution over the respective altitude ranges. For the latter, only data after 16 GMT are included in the comparison since mainly CO background concentrations were sampled before this time.

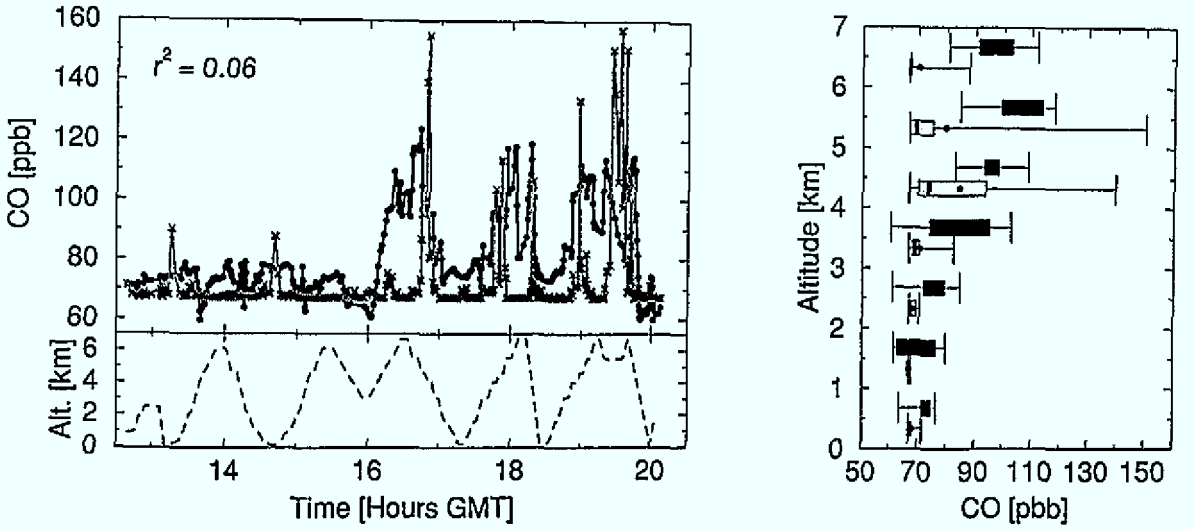

Figure 6.5: Measured and modelled CO mixing ratios for flight A575. Left panel: time series with modelled CO as grey crosses, measurements as black circles. The dashed line shows the aircraft altitude. Right panel: distribution of modelled (lighter grey) and measured (darker grey) CO mixing ratios for altitude classes of 1 km each. Only data after 16 GMT are included. The central 50% are given by the box, the 5 and 95 percentiles by the bars. The bar within the box marks the median, and the dot the mean of the distribution.

The comparison results show no correlation between measured and modelled CO (r^2 = 0.06). The model yields mainly CO background concentrations. Occasionally, some spikes of enhanced CO mixing ratios are modelled. Those are found for the observed layer of elevated CO mixing ratios during the latter part of the flight at 4-6 km altitude. In the statistical distribution these spikes are found in the strongly elevated 95 percentiles of the CO mixing ratio at this altitude range. However, the modelled median concentrations are barely elevated over the background values, and do not reproduce the observed layers of elevated CO mixing ratios at 4-7 km altitude as represented by the measured mean and median concentrations.

In order to understand the low model performance the trajectories were analysed. The upper left panel of Figure 6.6 shows example trajectories, where the mean positions of every 10^{th} trajectory cluster along the flight track are marked. A considerable degree of variabil-

ity in the trajectories is apparent. However, a principal flow from the North American continent to the observation area is evident.

Based on the CO observations and model results, the trajectories were partitioned into three groups for which example trajectories are shown in Figure 6.6.

- Case one shows trajectories that belong to measurements of clean background air. This includes observations at all altitudes during the first part of the flight and at low altitudes (below about 3 km) during the latter part. These trajectories indicate air masses of oceanic or northern African origin, which did not travel over CO-emitting areas within the last ten days. Consequently, the model shows mainly background concentrations of CO.

- Case two includes trajectories where the modelled CO concentrations show distinguished spikes. Those trajectories originate at low altitude over the USA, passing over the regions with strong emission along the east coast, where they are uplifted about 5-6 days before the measurement.

- Case three depicts trajectories of air masses with enhanced observed CO concentrations that are not reproduced in the model. They passed over the east coast of the US like the trajectories of case two, which pick up emissions. But in contrast to these trajectories they stay at high altitudes far above the model mixing height of 1.5 km over the American continent. Consequently in the model set-up (mixing height = 1.5 km) these trajectories do not see any emission input from the North American continent.

The vast majority of the back trajectories starting from points within the observed plume belong to case three. Since these trajectories miss the American emission input, the observed plume cannot be represented in the model calculations shown in Figure 6.5. Thus, for the analysis of the origin of the observed anthropogenic emissions, the following investigates when and how the continental boundary layer air is brought up to the middle troposphere for these trajectories.

Emission inputs older than ten days, and thus out of the range of the trajectories, are unlikely since the analysis of the hydrocarbon/CO correlations, especially that of the acetylene/CO ratio, indicates emissions only several days ago.

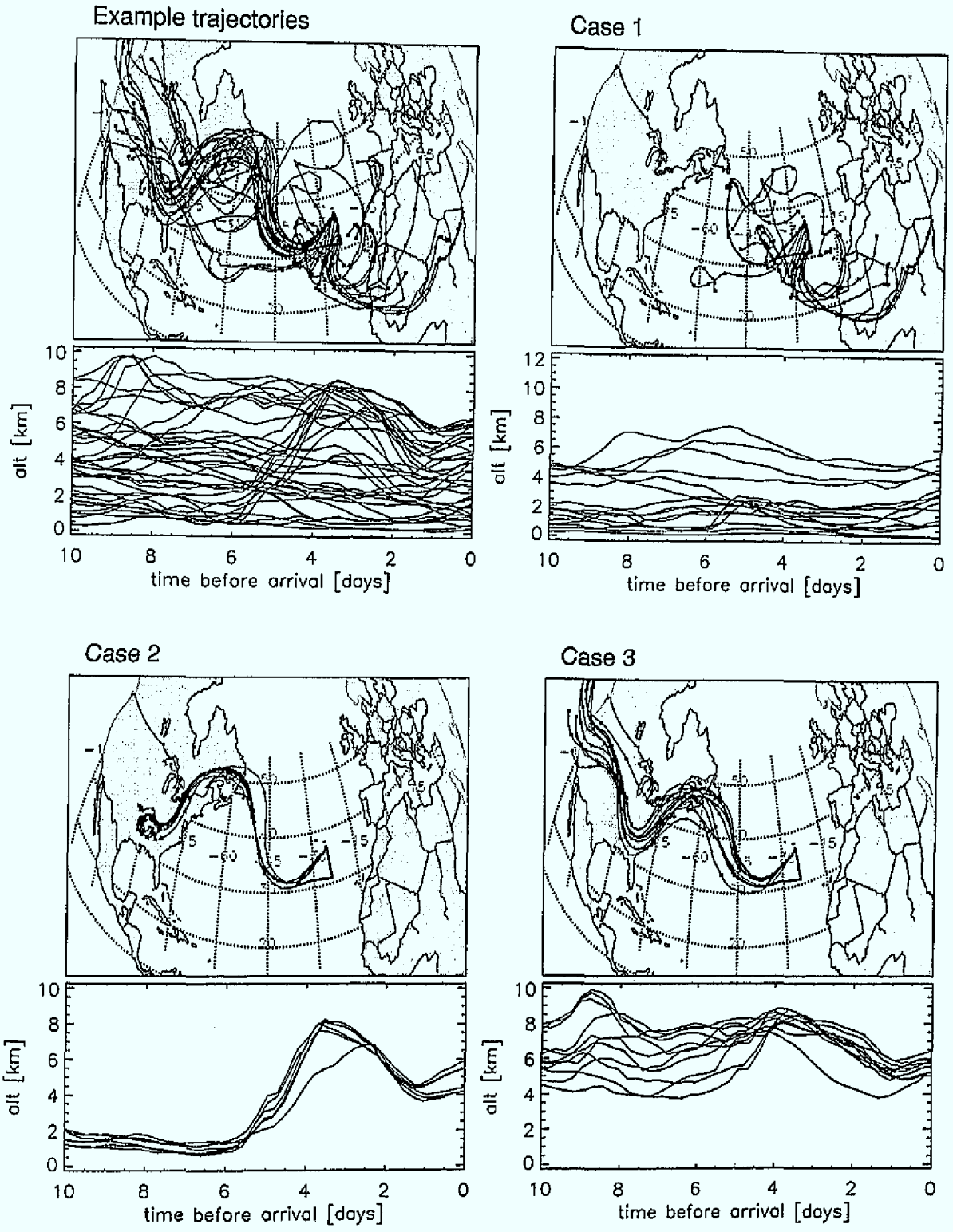

Figure 6.6: Example trajectories of the mean position of the clusters for flight A575 on September 14th 1997. Thick black line shows the flight path of the plane. Crosses show every 24 hours along the horizontal displacement of the trajectories. Panels: upper left shows every 10th mean trajectory. Upper right (case 1): observation of clean background air. Lower left (case 2): spikes of high modelled CO. Lower right (case 3): trajectories of air masses with enhanced observed CO concentrations which are not reproduced in the model.

This strongly suggests an origin of the observed CO concentrations from emissions in North America. However, the vertical or quasi-vertical transport of CO into the free troposphere obviously does not reach up to the trajectory heights and is therefore missed by the trajectories. To test this, the model mixing height was varied in order to find the best correlation between measured and modelled CO values. The results in Figure 6.7 show a monotonous rise of this correlation with increasing emission mixing height up to 9 km. By far the best correlation (r^2=0.65) between model and measurements is found for model mixing heights between 9-12 km, and no differences are found within the 9-12 km height range.

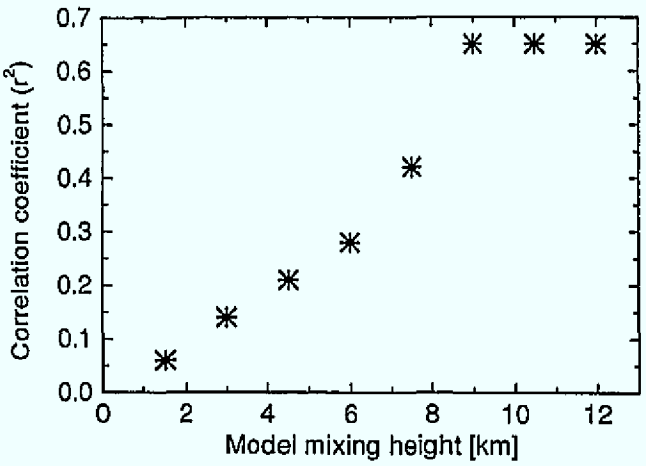

Figure 6.7: Dependency of the correlation coefficient (r^2) on the mixing height applied in the model run for flight A575.

The results for a model run, where the emissions are mixed up to a maximum height of 9 km, are shown in Figure 6.8. The observed CO layers are represented well by the adjusted model. However, it is clear that a model mixing height of 9 km does not represent any physical boundary layer height. Therefore, the adjusted model does not describe a physical uplift experienced by the emissions but it approximates the observations far away where it is only observed that boundary layer air has been vented into the free troposphere, independent of when and where.

The model results indicate that the vertical transport of emissions into the free troposphere has been rapid, as it is not represented by the trajectories. As discussed in chapter 2.2.3, fast vertical transport occurs in the cores of convective cumulus clouds, or by frontal uplifting in conjunction with a cold front. The applied three-dimensional trajectories based on ECMWF winds follow synoptic-scale vertical movements, whence they cannot resolve vertical transport in convective clouds. The tracer experiment with increased mixing height

indicates that almost all of the observed CO in the free troposphere is resulting from just such rapid uplift over the emitting regions of eastern USA.

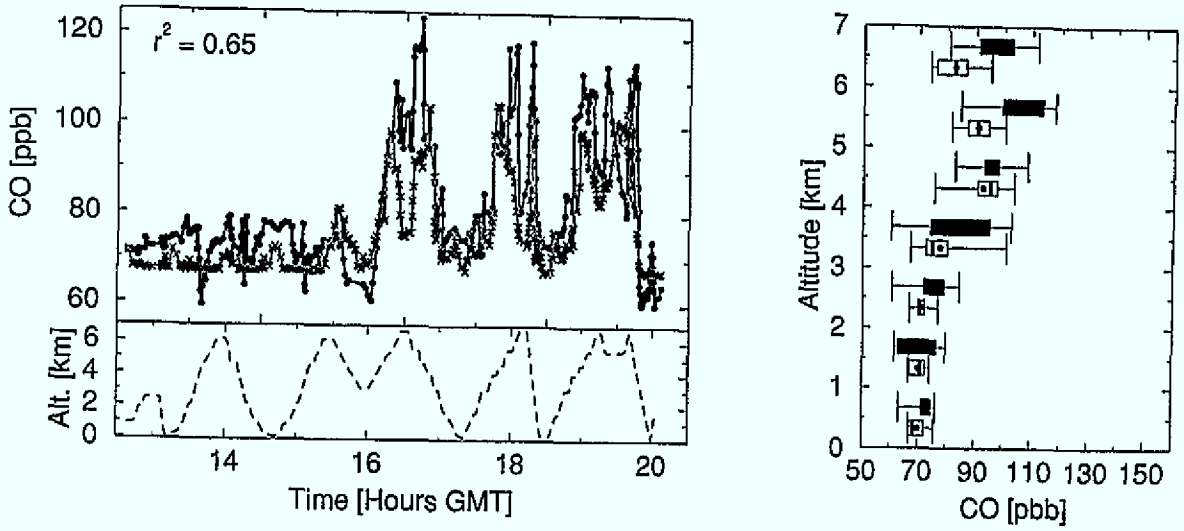

Figure 6.8: Measured and modelled CO mixing ratios for flight A575, with mixing height of emissions set to 9 km in the model run. Plots and symbols as in Figure 6.5.

Since convective activity and frontal uplift are associated with high cumulus type clouds, the next step of the transport analysis was to investigate whether high convective clouds were present within the trajectories' domains at the time of emission.

6.3.2 Analysis of areas with possible convective influence using satellite data

For identifying convective activity in conjunction with trajectories, satellite images have proved to be a valuable tool [*Brunner et al.*, 1998]

Images of cloud brightness temperatures analysed from GOES-8 infrared satellite data are used[47]. The cloud brightness temperature gives a measure of the height of the cloud top, given an optically thick cloud. Besides the height of the cloud, the criterion for convective upward transport is the cloud type. Convective clouds are cumulus and cumulonimbus type, while stratiform or cirrus clouds are not representative of convective activity. To extract convective clouds from satellite data several schemes have been proposed which mostly utilise high resolution data from different IR, namely IR and visible channels[48]. However, the problem of spatially high resolution satellite data is the limited number of satellite overpasses over the observation area during a day. Typically, convective clouds with a lifetime of typically only a few hours cannot be traced. For this work, coarse images

[47] The analysed satellite images were kindly provided by NASA GSFC/Ames Meteorology, USA. They are analysed from channel 4 of GOES-8, which works in the 11 µm range.
[48] See [*van Hees et al.*, 1999] and references therein for a review.

(resolution 0.1° x 0.1°) of cloud brightness temperatures from GOES-8 data were used as they were available every hour[49].

A simple approximation for the determination of convective clouds from such satellite images is the use of a threshold method, which assumes clouds colder than a certain threshold temperature to be convective [*Mapes and Houze Jr.*, 1993]. This criterion is usually used in connection with deep convection, where only clouds with tops near the tropopause are considered. At these high altitudes the threshold scheme works rather well to distinguish high convective clouds. The most abundant other cloud type at high altitudes is cirrus, which is usually thin enough to have higher brightness temperature than the temperature at the cloud top, and thus falls below the threshold.

As indicated by the trajectory model study (Figure 6.7), convective clouds of at least 8-9 km height have to be looked for. An alternative way to estimate the height of the clouds makes use of the dew point temperature within the observed plume. An average dew point of 240 K was observed in the layers with enhanced CO and O_3. Assuming water vapour as a conservative tracer during the transport, this procedure gives the condensation height of the upward transported air masses. For this work, if the brightness temperature of a cloud was at least 5 degrees colder than the measured dew point, the cloud was considered of sufficient height and thickness to have convectively contributed to the observed layer. The threshold temperature of 235 K corresponds to a height of 8-9 km according to the U.S. Standard Atmosphere, consistent with the estimated height from the trajectory analyses. This height should be sufficient to distinguish convective clouds by the threshold method, without making too much error because of cirrus.

A so-defined high and cold enough cloud is assumed to potentially influence an observed air mass if it is found within the trajectory cluster box at the respective time. In Figure 6.9, incidents of high (cold) clouds that were found along and during the passage of example trajectories (from profile 7), and which corresponded to the layer of enhanced O_3 and CO, are marked by a white point[50]. An accumulation of such points in the South Eastern states

[49] Only for some hours the satellite images were missing.

[50] In Appendix 9.3 some images of cloud brightness temperatures are shown, in which boxes corresponding to trajectory clusters for the layers of elevated CO are plotted. Cold (high) parts of the clouds with brightness temperatures below 235 K are highlighted by colours according to the temperature. Thus whenever a coloured point is found in such a box, this is interpreted as possible convective influence of the respective air mass.

of the United States is noted. Further convective activity is recognised during the travel of trajectories over the main emission areas along the east coast.

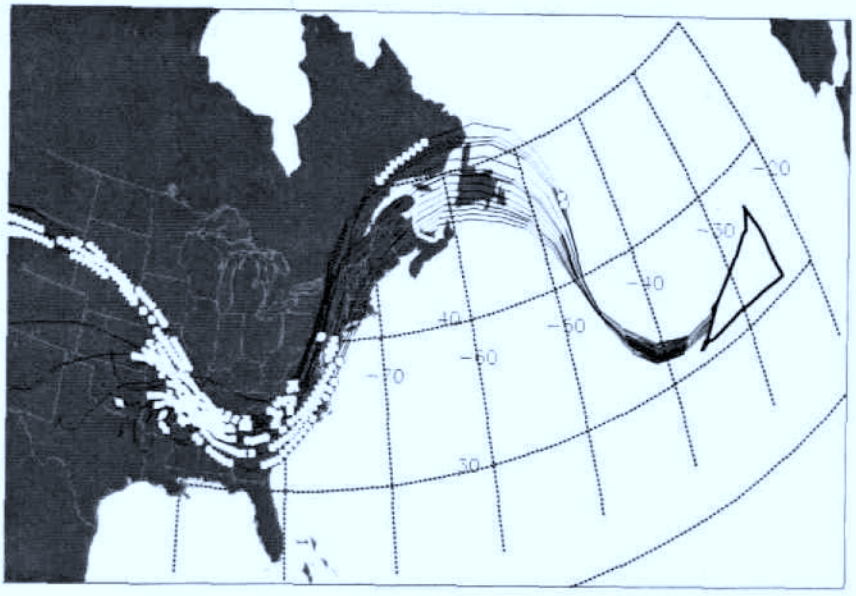

Figure 6.9: Example trajectories for the layer of enhanced O_3 and CO mixing ratios. Highlighted points: cold (high) clouds with brightness temperatures below 235 K found within the influencing area of the trajectories.

Closer analysis of the satellite images (Appendix 9.3), together with weather maps, show that the accumulation of points with convective activity in Figure 6.9 corresponds to a fast developing mesoscale convective complex (MCC) over the central Mississippi region. This was caused by advection of cold air from the north and advection of warm humid air from the Golf of Mexico. This meteorological situation leads to the development of convective and synoptic vertical winds, and to the formation of very large and high clouds 6 days before the measurement, at about 21 GMT of September 8^{th} 1997. As can be seen from the respective satellite images in Appendix 9.3, this massive complex of clouds with brightness temperatures down to 220 K covers nearly all areas defined by the plotted trajectory boxes. Within this MCC, strong vertical mixing can be assumed throughout the troposphere, which would destroy any existing distinct trace gas layers. Consequently, the observed distinct layers of CO and O_3 cannot be older than 6 days. The trajectories cannot be followed further back in time as they lose their identity in the extended vertical redistribution associated with this event.

Mesoscale convective systems consist of convective updrafts and, additionally, slantwise mesoscale ascending and descending branches of air [*Cotton et al.*, 1995]. These organised flow branches lead to the additional development of a mesoscale cold front, with synoptical uplift of warm air ahead of the front. This explains the uplift indicated by some of the

trajectories from the boundary layer up to about 8km from day 6 to day 4 before the measurement (compare Figure 6.6, case 2).

The synoptical uplift in conjunction with the mesoscale cold front also led to large amounts of cloud and convective cells along the east coast of the United States on 9th and 10th of September. The trajectories passed this region at 6 to 8 km altitude. As shown by the composite images of cloud brightness temperatures and trajectory boxes for these days in appendix 9.3, further convective contribution to the observed air masses from those convective cells cannot be excluded.

From the 11th September the observed air masses left the cloud area over the east coast and were transported eastwards following the jet stream. This transport occurred largely in cloud free areas, until 14th September when the trajectories are seen to travel around the back of hurricane Erica to the observation area.

6.3.3 Conclusions from the tracer analysis

The aim of the transport analysis was to identify the source region and upward transport of the observed plumes. In short, the back trajectories indicate an origin of the polluted air masses over the North American continent. High and cold clouds over the south-east and along the east coast of the United States were found within the influencing area of the trajectories 4-6 days before the measurement. This strongly indicates convective venting of boundary layer air. The applied three-dimensional trajectories, based on ECMWF winds, follow synoptic-scale vertical movements but cannot resolve vertical transport of air in convective clouds. Only in a few cases did the model trajectories originate in the continental boundary layer. Satellite images in conjunction with trajectories are therefore invaluable tools for the identification of convective events for this work.

Nevertheless, the combined analysis of trajectories and satellite images yields only statistical results. It cannot be decided which convective event exactly contributed to the observed pollutant loading in the plume. The uncertainty of the back trajectories at 4-6 days before the measurement allows for the possible contribution of several convective events.

An additional constraint, that could be used for identifying possible convective contribution to the observed plume, is the existence of anthropogenic emissions in the updraft area of the convective events. This would mean connecting the information about convective influence with the information of tracer transport, like CO. However, in this case it is not

only the emission rate at the time and location of the cloud that has to be considered for possible upward transport, but also the history of air masses within the updraft area.

The above demands more complex modelling than can be done with the simple transport module utilised for this study. However, it can be concluded already from this qualitative analysis that the observed layers originate from fast vertical transport of North American emissions in conjunction with clouds 4-6 days prior to the measurement. The exact time of emission and transport should be of minor significance when compared to the subsequent long range transport over the North Atlantic. In the following, the chemical processing and ozone production of such polluted air masses in the free troposphere is analysed.

6.4 Ozone production within the free troposphere

This chapter investigates whether the observed ozone can be produced in the free troposphere from precursors transported upward by convection. The upward transport of precursors within the cores of convective cumulus clouds is fast, i.e. within a time scale of about one hour[51]. Thus, the chemical production in the free troposphere can be assumed to start in the outflow region of the convective cloud.

The air masses are assumed to be transported, after convective input of *CO*, *VOC* and NO_x, to the observation area following the trajectories without further mixing with surrounding air. This assumption is motivated by the observed distinct layering, combined with the high coherency of the associated plume trajectories between the east coast of the United States and the observation area[52]. High coherency implies that chemical constituents remain confined within the same air mass since neighbouring particles stay close to each other, inhibiting possible mixing with other air masses [*Stohl*, 2000].

Under such conditions the precursor concentrations at the outflow region of the cloud can be scaled relative to the measured CO mixing ratios. However, prerequisites for such an approach are, firstly, the knowledge of the emission inventory over the emitting area and, secondly, an estimate of the degree of photochemical processing which has taken place inside the PBL and before convection lifts the partially processed air masses to the upper troposphere. The uncertainty of the precursor ratios in the cloud outflow will be investigated by considering a range of initial concentrations for NO_y and VOC in the model cal-

[51] Compare chapter 2.2.3
[52] Compare Figure 6.9

culations. Finally, the possible initial concentrations for NO_y and VOC can be further constrained by comparison of the model results with the measurements. The ozone formation is thus modelled as a function of the initial NO_y and VOC concentrations[53], which will be presented as before in form of EKMA plots.

6.4.1 Set up of the EKMA plot model calculations

The model runs are initialised 6 days before measurement, at 20 GMT of September 8th 1997. This is the time when the composition from satellite images and trajectory clusters indicates venting of boundary layer air into the upper troposphere by a mesoscale convective complex, and thus represents an upper limit of the age of the observed plume in the free troposphere.

The initial composition of NO_y in the outflow region of the cloud is assumed as 20% NO, 40% NO_2, 30% PAN and 10% organic nitrates, as supposed by [*Jaeglé et al.*, 1998], based on 3-D model calculations of the NO_y budget over the United States [*Liang et al.*, 1998]. HNO_3, the main depositing component of NO_y, is assumed to be efficiently scavenged by the wet convection.

As the speciation of VOC emissions for the US may differ significantly from Europe, the German urban split was not applied as for the TACIA model calculations[54]. Instead an aggregated VOC mix based on the NAPAP[55] anthropogenic VOC emissions for the US [*Middleton et al.*, 1990] was used. Degradation of reactive VOC in the PBL before the convective upward transport was simulated by assuming oxidation of the VOC by an integrated OH concentration, $\int [OH]dt = 5.4 \cdot 10^{10}\,s\,cm^{-3}$. This corresponds to about ½ day of photochemical ageing, assuming daily average integrated OH concentration according to [*Stockwell et al.*, 1990][56]. The resulting VOC split used for the model calculations is shown in Table 6.2.

[53] Here initial NO_y concentrations, and not as usually NO_x, are assumed, to account for the partition of NO_x emissions that is transported into the free troposphere as PAN or organic nitrates.
[54] Compare chapter 4.2.2
[55] National Acid Precipitation Assessment Program
[56] Compare chapter 4.2.2

Table 6.2: Specification of the initial VOC concentrations into RACM model species in volume percent. The sum differs from a hundred percent due to assumed photochemical ageing by oxidation with $\int [OH]\, dt = 5.4 * 10^{10}$ s cm^{-3}.

RACM class	ppb %	RACM class	ppb %
ETH	5.3	TOL	5.0
HC3	18.6	OLT	1.2
HC5	10.4	OLI	0.1
HC8	5.9	HCHO	2.2
ETE	10.1	ALD	0.4
XYL	1.6	KET	1.6

The height of the outflow region of the cloud is estimated by the average dew point of the observed plume[57]. With about 240 K this corresponds to a condensation height of approximately 8 km. This is set as the start height for the model calculations. The water vapour in the model calculations is fixed to 0.12%, accordingly to the observed H_2O in the polluted layer.

Photolysis rates, temperature and pressure for the chemical box model are forced by the mean position of the trajectories at each day of transport. The values are shown in Table 6.3.

Table 6.3: Mean daily position of the trajectories for the observed layers of elevated O_3 and CO. Values used to force the photolysis rates, as well as temperature, pressure and water vapour in the chemical box model calculations with RACM

Date	Latitude	Longitude	Altitude [km]	Pressure [mbar]	Temperature [K]
08.09.97	38 N	94 W	8	350	240
09.09.97	35 N	88 W	8	350	240
10.09.97	37 N	79 W	8	350	240
11.09.97	45 N	69 W	8	350	244
12.09.97	45 N	57 W	7	400	252
13.09.97	38 N	47 W	6	500	265
14.09.97	33 N	36 W	6	500	266

The initial ozone concentration is assumed as 60 ppb. Given about 55 ppb O_3 background concentration observed during the ACSOE flights in September 1997 between 7-9 km, this

[57] Compare chapter 6.3.2

may be already an overestimation, as it includes moderate O_3 enhancement within the PBL. If no O_3 production is assumed to have taken place within the PBL, the convective venting should lead to an initial O_3 deficiency in the convective plume (e.g. [*Hauf et al.*, 1995; *Kley et al.*, 1997]).

For CO an initial concentration of 110 ppb is assumed, based on the average observations within the polluted layers.

H_2O_2 is highly soluble and thus likely to be largely scavenged during wet convection. Thus, it is initialised to zero at the cloud outflow. Recent discussion that convective transport of H_2O_2 may nonetheless be an important HO_x source in the upper troposphere [*Folkins et al.*, 1998; *Jaeglé et al.*, 1997; *Prather and Jacob*, 1997]. However, this source should be of minor importance for the convective outflow of polluted surface air with elevated concentrations of HO_x precursors.

6.4.2 Results

Figure 6.10 shows isolines of modelled O_3 mixing ratios averaged from 16-20 GMT for the day of the measurement, corresponding to the time of the plume observetion, as a function of initial VOC and NO_y concentrations. In contrast to the usual practise, initial NO_y (not NO_x) mixing ratios are used in order to account for the fraction of PAN and ONIT that is assumed to have already been produced in the PBL prior to the convective uplift.

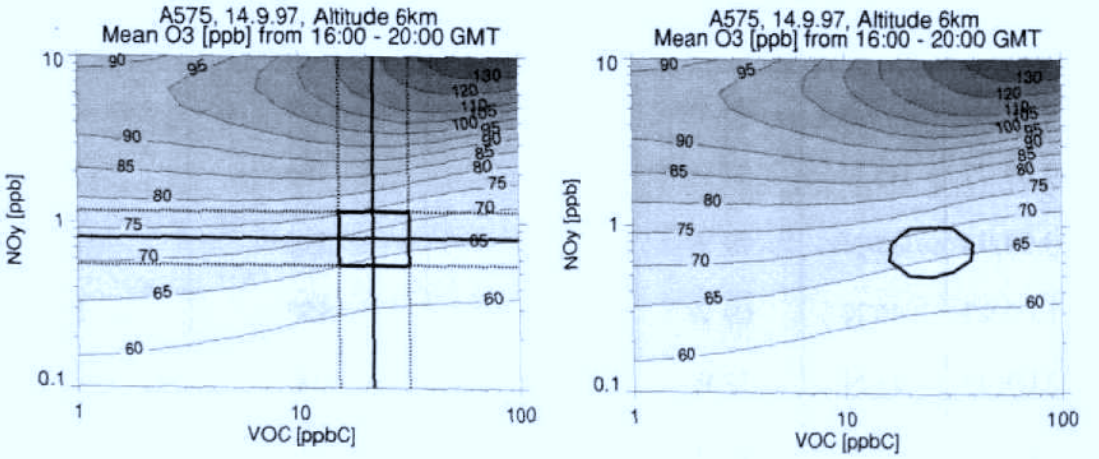

Figure 6.10: Modelled isolines of O_3 as a function of initial VOC (horizontal axis) and NO_y (vertical axis) concentrations in ppbC and ppb respectively. In the left plot the range of VOC and NO_y start values is marked that corresponds to the median and the 5 respectively 95 percentiles of observed CO (see text). In the right plot the region of initial VOC and NO_y is marked that leads to agreement of the modelled VOC and (NO_y-HNO_3) with the observations. Shown is the 1% significant level (ellipsoid), with the confidence region of allowed start values inside the ellipsoid and significant deviation outside.

The NO_x/CO ratio from anthropogenic sources in the United States is around 0.1 ppbNO_x/ppbCO [*EPA*, 1995]. The $\Delta NO_y/\Delta CO$ ratio in the outflow region of a convective cloud is usually much smaller, due to loss of HNO_3 by deposition in the boundary layer and by scavenging in the wet convection. *Jaeglé et al.* [1998] assume the $\Delta NO_y/\Delta CO$ ratio in convective plumes to be only 20% of the NO_x/CO source ratio in the US, based on a 3-D model calculation of the springtime NO_y budget over the United States [*Liang et al.*, 1998]. This is adopted for the estimation of the initial NO_y concentration. According to the assumption of CO as an inert tracer and zero dilution, ΔCO is given by the observed CO mixing ratio after subtraction of the background concentration. For NO_y the background is assumed as zero. Then, the initial NO_y concentration in ppb is given by $NO_y = 0.02*\Delta CO$. The NO_y start values are marked in the EKMA plot according to the observed median CO concentration in the plume (solid horizontal line), as well as for the 5 and 95 percentiles (dotted horizontal lines).

The initial VOC concentrations are estimated in a similar manner. An emission ratio of VOC = CO/2.4 by mass is assumed, as analysed by [*Flatoy et al.*, 1996] from the NAPAP inventory for the eastern United States for 1985. The ratio is reduced by 35% due to the photochemical ageing of the VOC mix before upward transport. This yields the initial VOC concentration in ppbC as $VOC = 0.55*\Delta CO$. It was assumed that the background concentration of VOC is negligibly small. The vertical solid and dotted lines mark these VOC start values for the median and percentiles of the observed CO.

The uncertainty of the degree of photochemical processing that the air masses have already experienced while still in the boundary layer, adds uncertainty to the so-determined start concentration of VOC and NO_y. An attempt was made to utilise the measured VOC and NO_y mixing ratios at the time of observation over the Azores for the determination of their initial values, i.e. their concentrations after they had been lofted to the upper troposphere. In absence of further washout and deposition, NO_y is a conservative quantity in the free troposphere and could therefore be used directly for the estimation of the initial concentration. Unfortunately, because of the uncertain amount of HNO_3 sampled by the NO_y instrument [*S.Bauguitte*, personal communication], it is not possible to use the quantity NO_y.

Instead, the results of the EKMA modelling for VOC and (NO_y-HNO_3) are compared to the measurements of VOC and NO_y[58]. *Initial concentrations* of VOC and NO_x in the EKMA calculation are assumed as possible model scenarios for the observed plume, if the *resulting concentrations* of VOC and (NO_y-HNO_3) agree with the respective observations. As described in chapter 5.2.4.2, agreement between modelled and measured concentrations is defined by the confidence interval of the measurements. The confidence interval is again determined for each parameter by a t-test that considers the variance of the measurements within the observed plume as well as the systematic error of the measurements. It is noted that the number of VOC measurements with 5 bottle samples is rather small, which increases the width of the confidence interval. The combined confidence region for both parameters, VOC and (NO_y-HNO_3), is then determined as described in chapter 5.2.4.2.2.

The so-defined confidence region is shown in the right panel of Figure 6.10 for the 1% significance level, superimposed on the isolines of ozone mixing ratios. The area within the ellipsoid (isoline of 1% significance level) then gives the region of initial concentrations which lead to modelled VOC and (NO_y-HNO_3) concentrations compatible with the measurements. As can be seen from comparison of the panels of Figure 6.10, this region agrees rather well with the region marked by the estimation of the initial concentrations from the CO observations (left panel). The agreement between the two independent methods of determining the start values lends confidence to the assumptions about the initial $NO_y/\Delta CO$ and $VOC/\Delta CO$ ratios. These included the assumption that a considerable degree of photochemical processing of the VOC and NO_x emissions takes place in the PBL prior to the convective transport. This is confirmed by the comparison of model results and measurements for VOC and (NO_y-HNO_3).

The next step is to compare the modelled ozone concentrations, for the region set up with initial VOC and NO_y concentrations, to the ozone measurements in the layer. Considering the range of initial values scaled to the CO observations (left panel), the modelled O_3 concentrations are about 63-75 ppb, and 63-71 ppb for the confidence region of VOC and (NO_y-HNO_3) observations (right panel). In both cases this is notably lower than the observed values of 73-99 ppb. Since the initial model O_3 mixing ratio was 60 ppb, this means that the model produces 3-15 ppb O_3 during the 6 day transport in the free troposphere.

[58] As described for the TACIA model calculations (chapter 5.2), the modelled (NO_y-HNO_3) is compared to the measured NO_y, which contains an unknown fraction of HNO_3.

The EKMA plots in Figure 6.10 show that the O_3 production for the given range of initial VOC and NO_y concentrations is strongly NO_x limited. While the production of O_3 increases with increasing NO_y, the latter being equivalent to increasing NO_x start values, the O_3 production slightly decreases with increasing VOC start concentrations. From photochemical modelling studies it was suggested that the O_3 production in the upper troposphere approaches the NO_x-saturated regime for NO_x concentrations above a few hundred ppt (e.g. [*Brasseur et al.*, 1998]), somewhat at variance with the present results from the ACSOE campaign. However, it has to be taken into account that in the EKMA plots of figure 6.10 the integrated net O_3 production over about six days of transport in the free troposphere is given and not the instantaneous O_3 production rate. Over the 6 day time that the air mass needs to travel from the U.S. east cost to the Azores, NO_x is soon oxidised and the O_3 production becomes NO_x limited.

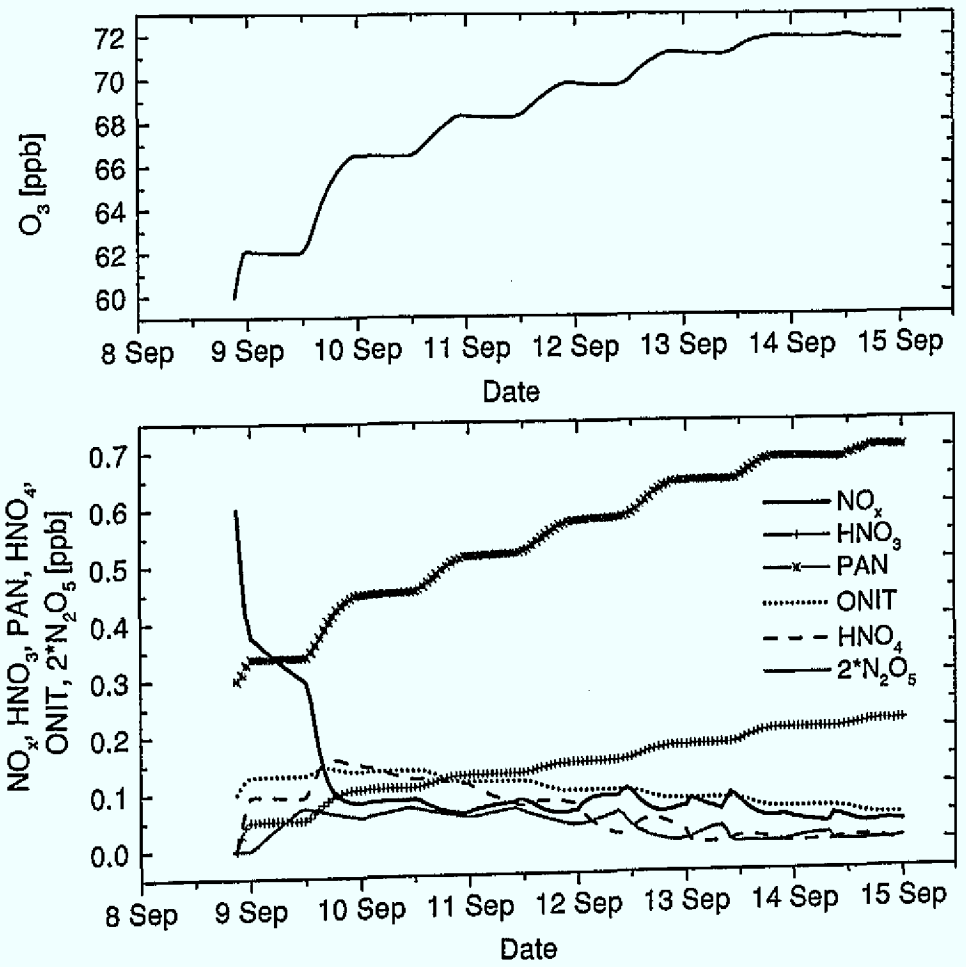

Figure 6.11: Evolution of the concentration of O_3 and the NO_y constituents NO_x, HNO_3, PAN, ONIT, HNO_4 and N_2O_5 along the model trajectory. Shown are the model results for initial concentrations of 1 ppb NO_y and 20 ppbC VOC.

This is seen in Figure 6.11 which shows the evolution of O_3 and the individual NO_y constituents over a model run with initial concentrations of 1 ppb NO_y and 20 ppbC VOC. Clearly, the main O_3 production in the free troposphere takes place within the first two days after the upward transport. During the further transport the net O_3 production successively declines, down to zero net production on 14th September, the day of measurement.

The reason for the levelling off of the ozone production is the rapid oxidation of NO_x, which is shown in the lower panel of Figure 6.11. As soon as the second model day the NO_x concentration declines to below 100 ppt, from where it further decreases more slowly to around 30 ppt on the day of measurement. This low NO_x concentration is consistent with the measurement of NO_x, which was at the detection limit of 50 ppt. The main product of the NO_x oxidation is PAN, which accounts for around 70% of the final NO_y, while the HNO_3 yield is only about 20%. Although PAN principally is a NO_x reservoir which releases NO_x back into the system by photolysis or thermal decomposition, it acts as an effective NO_x sink due to low temperatures.

The high amount of model-produced PAN cannot be compared to direct measurements, since, unfortunately, no quantitative PAN measurements for the campaign exist[59]. A comparison with literature data is difficult because the respective conditions are important. The modelled NO_y composition is at variance with the measured composition of NO_y species in upper tropospheric air during the SONEX[60] mission over the North Atlantic in October/November 1997. In SONEX, median values of the compounds of NO_y were reported as: $NO_x \approx 25\%$, $HNO_3 \approx 35\%$ and PAN $\approx 17\%$ [*Talbot et al.*, 1999]. However, a substantial amount of the NO_y observed during the SONEX study was associated with aircraft exhaust and lightning-produced NO_x. Since the amount of NO_x that is converted to PAN is strongly dependent on the availability of VOC, which is not emitted by aircraft or produced during lightning, the NO_x oxidation under the SONEX conditions favours HNO_3 over PAN production.

The comparison of the measured and modelled O_3 concentrations for initial values of VOC and NO_y, within the confidence region of the respective measurement, only compares the mean ozone concentration within the width of the frequency distribution of the measure-

[59] Compare chapter 3.1.2.

[60] The SASS (Subsonic Assessment) Ozone and NO_x Experiment (SONEX) was an airborne field campaign conducted in October-November 1997 in the vicinity of the North Atlantic Flight Corridor to study the impact of aircraft emissions on NO_x and ozone [*Singh et al.*, 1999].

ments. However, additional information about the ozone production can be gained from the observed slope between O_3/NO_y. Figure 6.12 presents a scatter plot of the O_3/NO_y observations as well as model results[61]. Only those model results are included that yield VOC values between 3.6 and 5.3 ppbC, corresponding to the 5 and 95 percentiles of the measurements, respectively. A linear relation between O_3 and (NO_y-HNO_3) is obtained. This is caused by the strong NO_x-limitation, which leads to a linear dependency of the O_3 production on NO_y, nearly independent of the VOC concentration in this regime. However, the slope of the modelled correlation between O_3 and (NO_y-HNO_3) is found to be 16.4±0.4 ppb/ppb, which is a factor of three smaller than the observed slope of 48±2 ppb/ppb.

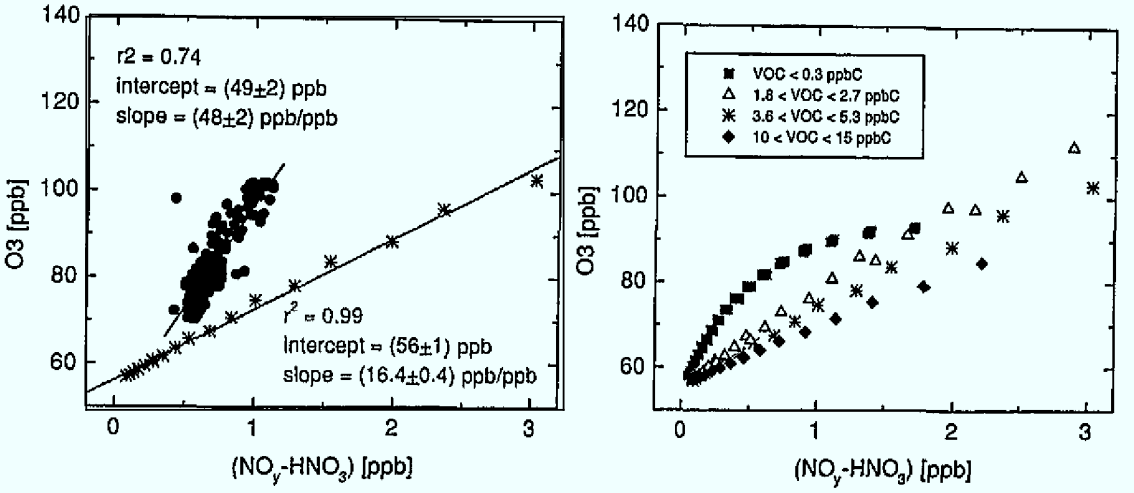

Figure 6.12: Left panel: correlation between O_3 and (NO_y-HNO_3) for the measurements (black dots) and from the EKMA model calculations (grey stars). Only model calculations are included, which yield a sum of measured VOC between 3.6 and 5.3 ppbC, corresponding to the 5 and 95 percentiles of the measurements. Right panel: modelled relationship between O_3 and (NO_y- HNO_3) for different ranges of the resulting sum of measured VOC.

This strong underprediction cannot be explained by measurement uncertainties. The uncertainty of the fraction of HNO_3 in the NO_y measurement is approximated by the use of the quantity (NO_y-HNO_3) which is a lower limit for NO_y and, thus, represents the largest possible error with respect to HNO_3. Therefore, this gives an upper limit for the slope between O_3 and NO_y. Additional uncertainties of the NO_y measurements due to calibration and artefacts are estimated as 17% at 1 ppb (Table 3.3). Thus, the modelled underprediction of the slope is much larger than the above uncertainty.

The right panel of Figure 6.12 shows the modelled O_3 versus (NO_y–HNO_3), as on the left panel, but for a range of the resulting VOC mixing ratios. It is seen that a change by a fac-

[61] As before, modelled (NO_y-HNO_3) is plotted in figure 6.12

tor of two in the VOC mixing ratios does not significantly change the modelled slope between O_3 and (NO_y-HNO_3). The observed slope is only approximately produced by the model if unrealistically low VOC concentrations (< 0.3 ppb) are used. The increase in slope by a decrease of VOC levels can be explained by the reduction of PAN formation. Higher VOC concentrations increase the production of PAN, thereby reducing the NO_x concentration that is available for O_3 production. Additionally, the PAN production is in competition to the production of HNO_3. Therefore, high VOC concentrations with high PAN production increase the resulting concentration of (NO_y-HNO_3) compared to model calculations with low VOC concentrations. In summary, modelled slopes between O_3 and (NO_y-HNO_3) that are comparable to the measurement are only found for extremely low resulting VOC concentrations below 0.3 ppbC. However, in this case the O_3 production becomes NO_x-saturated at around 1 ppb NO_y-HNO_3, which prevents further O_3 production.

The intercomparison with the NOAA P3 aircraft during the ACSOE campaign revealed that the measured alkanes were up to a factor two lower than that measured by NOAA[62].This indicates that the VOC concentrations in the model results are more likely too low than too high. Consequently, the modelled slopes of the O_3/(NO_y-HNO_3) correlation represent upper limits given the uncertainties of VOC and of measured HNO_3 amounts.

In summary, the model calculations cannot explain the observed O_3 in relation to the measured precursor mixing ratios of CO, NO_y and VOC.

6.4.3 Discussion of uncertainties

In chapter 5 a strong influence of uncertainties in the input variables on the model results was ascertained. Thus, a relevant question is whether the deviation of the modelled O_3 production from the observations in the free troposphere might be due to such uncertainties. However, it is noted that the meteorological and chemical regime for the free troposphere case is significantly different from the boundary layer study in chapter 5. Hence the uncertainties analysed there do not have to have the same effect in the free troposphere.

First, no emission and surface deposition rates have to be considered in the free troposphere. Deposition could only occur on aerosols, or in form of wet deposition if the air masses cool off below the saturation point or pass clouds. Wet deposition can mainly be

[62] Compare chapter 3.1.2

excluded, as the satellite images in Appendix 9.3 do not indicate any raining clouds passed by the air mass trajectories after leaving the North American continent. The low humidity and the descending movement of the air masses also exclude wet deposition due to condensation.

The uncertainties in the photolysis rates have only a minor impact on the results as the ozone production is strongly NO_x limited. The same accounts for the reactivity of the VOC split. In the NO_x-limited regime the ozone formation is almost independent of small changes in VOC concentration and reactivity, or in the photolysis rates [*Hess et al.*, 1992].

Wild et al. [1996] have reported a strong sensitivity of the net O_3 production in the NO_x-limited regime on the water vapour mixing ratio. Drier air masses have shown greater net O_3 production due to minor importance of the destruction pathway $O(^1D) + H_2O$. The same is found in this study, with a change from the net O_3 production to net loss during the transport, if the water vapour mixing ratio is increased. On the other hand, according to the observed low humidity, the H_2O mixing ratio in the model calculations is already low (0.12 %). Thus a further reduction would not yield a significant gain in ozone.

Dilution effects were neglected in this study. Assessing the impact of dilution does not yield any increase in the O_3 concentration after six days. Although dilution would imply increased initial concentrations, so that the observed CO mixing ratio could still result, the effect of a resulting higher O_3 production in the first days is more than compensated by the subsequent dilution of the produced O_3 against lower background concentrations. Similar results were found by [*Mauzerall et al.*, 1998; *Wild et al.*, 1996].

6.4.3.1 Results for initialisation with "fresh" emission input

A major uncertainty in the model set-up is the degree of photochemical processing that the air masses have already experienced within the boundary layer prior to their convective uplift. For the model calculations, the initial $NO_y/\Delta CO$ mixing ratios at the outflow region were assumed to be 20% of the NO_x/CO source ratio, with NO_x constituting 60% of the initial NO_y. Consequently, the NO_x available for O_3 production in the free troposphere is only 12% of the NO_x emissions in the boundary layer, relative to CO. This has to be taken into account if the observed enhanced slope of O_3/CO is to be explained by a more efficient O_3 production from NO_x on a per-molecule basis in the free troposphere. The observed slope of O_3/CO in the polluted free tropospheric plume of up to 1 $ppbO_3/ppbCO$ is roughly a factor of 2-3 higher than the observed slopes of about 0.3 $ppbO_3/ppbCO$ during

TACIA. Given the asssumed NO_x/CO ratio in the convective outflow as only 12% of the NO_x/CO source ratio, this means that the O_3 production from NO_x on a per-molecule basis in the free troposphere would have to be enhanced by a factor of 25 compared to the PBL in order to explain the observed slope of O_3/CO. *Liang et al.* [1998] estimate the O_3 production efficiency[63] in the free troposphere over the United States in fall to be 42 compared to 9 in the boundary layer. This gives an enhancement of only a factor 4-5 in the free troposphere. Consistent with the above presented model results, this factor is too small to explain the observed slope of O_3/CO for an export of 12% NO_x relative to CO.

In order to explain the observed O_3/CO ratio from production in the free troposphere, a higher ratio of exported NO_x/CO has to be assumed. This could be the case if the convectively upward transported pollution is very young, that is if NO_x would not yet have been oxidised. This scenario was modelled by repeating the EKMA plot calculations assuming fresh emission input into the convective updraft. The initial NO_y concentrations were assumed as 100% NO_x (33% NO, 67% NO_2), and the VOC mix was directly taken from [*Middleton et al.*, 1990] without prior degradation.

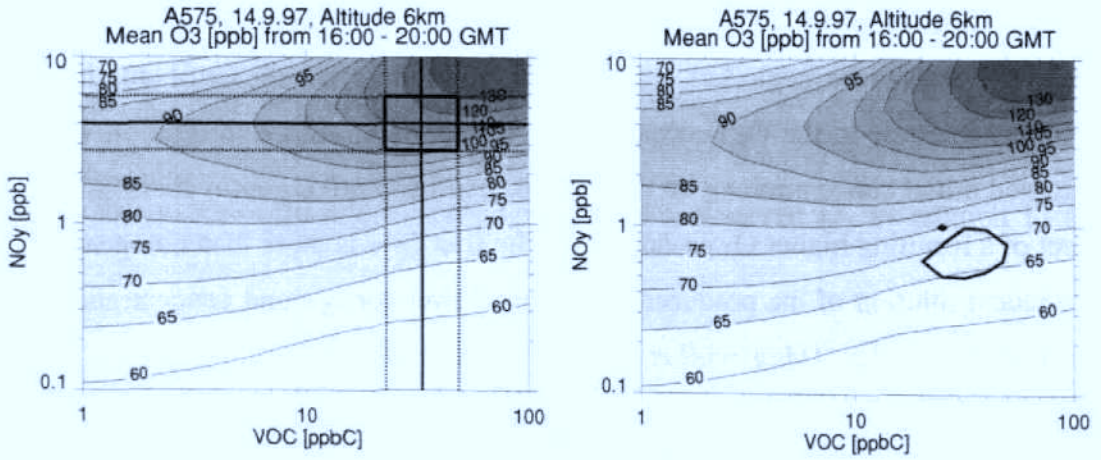

Figure 6.13: As Figure 6.10, but for initialisation with fresh pollution vented from the boundary layer (initial NO_y set as 100% NO_x, initial VOC mix according to emission split [*Middleton et al.*, 1990]). Consequently, in the left panel the initial concentrations of NO_y and VOC scaled to the observed CO shift to higher values.

However, the so-defined initial concentrations of NO_y and VOC for fresh emission input are strongly contradicted by the observations of (NO_y-HNO_3) and VOC. The right panel shows, as before, the confidence region, where the start values lead to modelled VOC and

[63] The O_3 production efficiency is defined as the gross number of O_x molecules produced from a NO_x before it is oxidised to HNO_3.

(NO_y-HNO_3) concentrations compatible with the measurements for the 1% significance level. Comparison with Figure 6.10 shows almost no change of this region compared to the base case scenario. Thus, the observed concentrations of VOC and (NO_y-HNO_3) largely determine the start values of NO_y and VOC, irrespective of changes in the individual composition of these start values by photochemical processing prior to the uplift in the free troposphere. High initial NO_y/CO ratios, as given by the assumed NO_x/CO emission ratios, can therefore be excluded as a possible model scenario, since the resulting (NO_y-HNO_3) is about a factor 4-5 higher than the confidence region of the measurement allows.

Within the confidence region of VOC and (NO_y-HNO_3) marked in the right panel of Figure 6.13, the resulting O_3 concentration of 64-74 ppb slightly enhanced compared to the base case study (Figure 6.10). The slight enhancement is due to the higher amount of available NO_x for the same initial NO_y concentration, as the initial NO_y concentrations are assumed as 100% NO_x. Even so the model results are significantly below the observed O_3 concentrations.

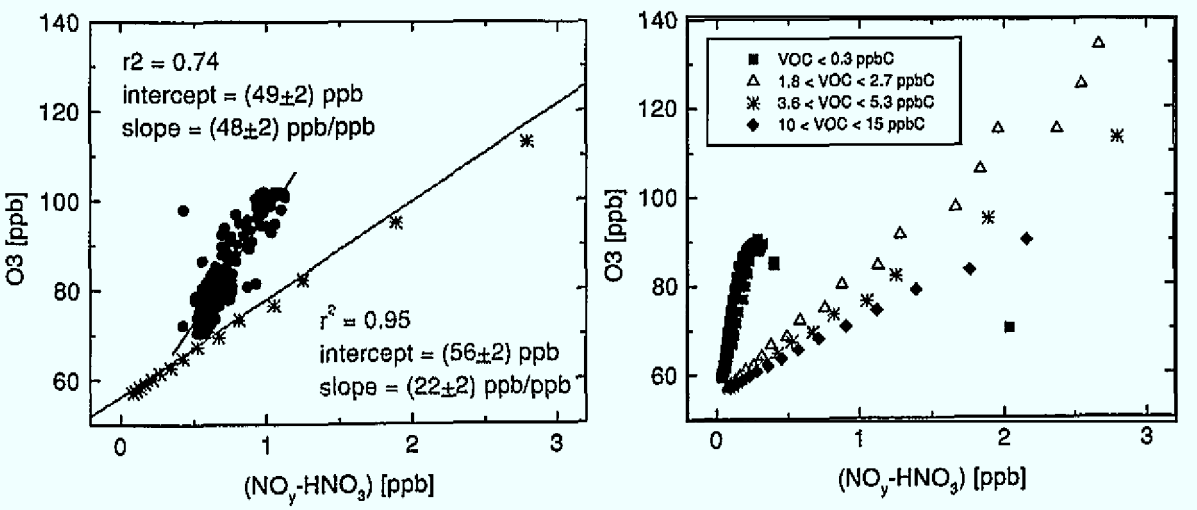

Figure 6.14: As Figure 6.12, but for initialisation with fresh pollution vented from the boundary layer (initial NO_y set as 100% NO_x, initial VOC mix according to emission split [*Middleton et al.*, 1990]).

The underprediction can also be clearly seen from the correlation between O_3 and (NO_y-HNO_3) shown in Figure 6.14. The slope of the modelled correlation between O_3 and NO_y-HNO_3 still underestimates the measurements by more than a factor of two (left panel). Agreement is obtained (right panel), like before (Figure 6.12, right panel), if the VOC concentrations are decreased by about a factor of four, which again is neither compatible with the VOC measurements nor with the VOC/CO emission ratio.

Thus, even the assumption of convective flux of fresh emissions into the free troposphere cannot explain the observed O_3 regarding the simultaneous observations of VOC and NO_y.

Another possibility that has been frequently discussed is the influence of possible lightning-produced NO_x that the air mass might have gained during the convective transport (e.g. [*Huntrieser et al.*, 1998] and references therein). Still the argument stays the same in the sense that the amount of lightning-produced NO_x is limited by the observation of NO_y-HNO_3 in the plume at the time of observation. The only difference to the model calculation discussed above is that in this case fresh NO_x is added to already PBL-aged VOC concentrations. A model calculation for this scenario, assuming initial NO_y concentrations as 100% NO_x in the cloud outflow, combined with aged initial VOC emissions as in the base case study, though yielding slightly increased resulting O_3 production, still underestimates the slope of $O_3/(NO_y\text{-}HNO_3)$ by nearly a factor of two (not shown).

In summary, it is concluded that the model calculations, in conjunction with the (NO_y-HNO_3) and VOC observations in their uncertainty range, cannot explain the observed enhanced ratio of O_3/CO in the free troposphere.

6.5 Venting of boundary layer ozone to the free troposphere

The question posed at the beginning of this chapter was, whether the observed ozone was photochemically produced in the free troposphere or produced in the boundary layer followed by venting to the free troposphere with subsequent long range transport. An explanation of the observed O_3 mixing ratios by O_3 production in the FT is negated by the model calculations. The remaining question is whether PBL produced ozone, followed by convective transfer to the free troposphere, can account for the observations. Therefore, O_3 observations from ground stations were investigated to see if such venting was possible.

Hourly observation of ozone concentrations at ground stations were obtained from the AIRS (Aerometric Information Retrieval System) database of the U.S. Environmental Protection Agency (EPA) [*EPA*, 1997] [64]. For estimation of possible venting of O_3 from the boundary layer, the observations had to be merged in time and space with the convective events that were analysed to potentially contribute to the observed polluted layer. In Figure 6.15 some examples of composite images are plotted, which include the observed O_3 con-

[64] These data were kindly provided by A.Fiore, Harvard University, Cambridge, USA.

centrations at the ground stations (marked by colours), clouds with brightness temperatures less than 235 K (marked by grey areas), and example trajectory cluster boxes corresponding to the polluted layer (red rectangles), all at the respective times given in the header. Additionally, the mean path of the example trajectories is shown by black lines, and the maximum observed O_3 concentrations from all ground stations at the given hour is plotted at the place of observation (red number).

These composite images were created for every hour of September 7th to September 10th, the time of the trajectory overpass over the eastern United States.

For a first estimate of possible venting of O_3 from the boundary layer, only the observed ozone concentrations, which were found within the box of a trajectory cluster and, simultaneously, underneath clouds with brightness temperatures below 235 K, were considered. This yielded a maximum O_3 concentration of about 80 ppb, considering all trajectories that correspond to the observed plume, and all coincidences with high clouds. The mean observed O_3 concentration underneath clouds was found to be rather small with about 40 ppb.

However, the ozone concentrations under the influence of the convective updraft may still be higher than the mixing ratio reported from ground stations at the respective time. This could, for example, be due to titration of ozone with NO under the condition of low photolysis rates underneath the clouds. Titration effects could not be examined as no simultaneous NO_x observations at the ground stations were available. Nevertheless, some indication for titration is suggested by frequent, extremely low minimum ozone concentrations (below 10 ppb), reported from ground stations underneath high clouds.

A better estimate of the likely ozone concentrations in the convective updraft areas within the PBL, can be obtained through the examination of the observed maximum O_3 concentrations in the path of the trajectories before the convective venting. Figure 6.15 shows that high O_3 concentrations are found for cloud free areas along the path of the trajectories on September 7th and September 8th (upper two panels). Thereby, the reported O_3 at most of the ground stations range from about 70 ppb up to the maximum reported values of 139 ppb ozone on September 7th, and 133 ppb on September 8th. The high ozone concentrations on September 8th are found in the cloud free area ahead of the mesoscale convective complex. These high values could well persist in the residual layer until the pass of the MCC and its associated mesoscale cold front in the night from September 8th to 9th.

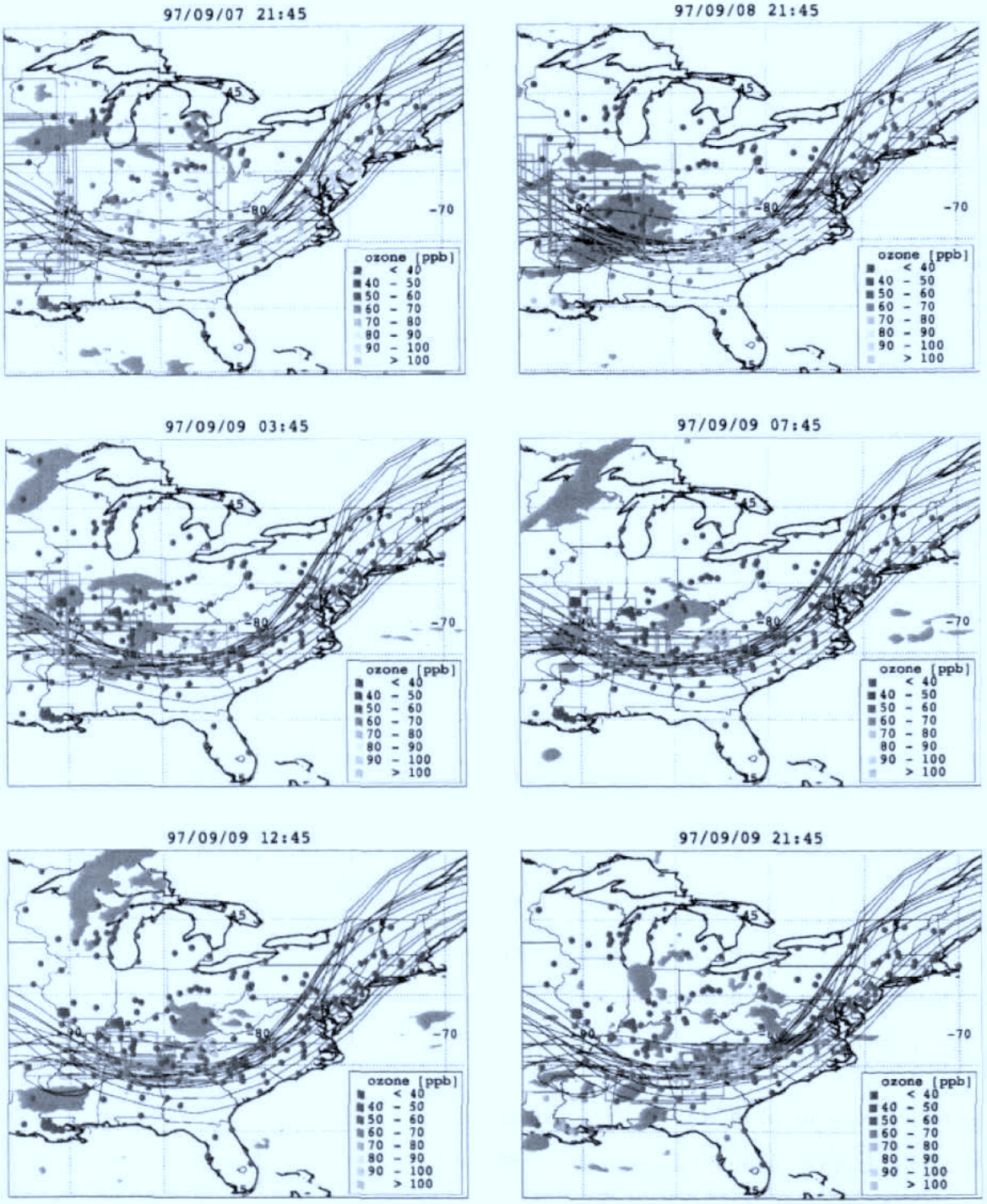

Figure 6.15: Composite images showing the hourly ground station ozone observation (coloured circles, see legend), the maximum observed O_3 concentration (red number at the place of observation), clouds with brightness temperatures below 235 K (grey areas), example trajectory cluster boxes (profile 7) corresponding to the polluted layer (red rectangles), all at the respective times given in the header. The mean path of the example trajectories is shown by black lines.

A more detailed analysis of a contribution by cloud venting to the observed high ozone levels in the FT, would require more ground observations of chemical tracers and a detailed cloud model for the investigation of the upward transport, including dilution with surrounding air. This is beyond the scope of this work.

An important question concerning the venting of boundary layer ozone is, whether the observed slope up to 1 ppbO_3/ppbCO in the FT exists in the PBL air masses at the time of convective uplift. As discussed before[65], average summertime slopes of 0.3-0.4 ppbO_3/ppbCO were found during TACIA and at four Canadian surface sites [*Parrish et al.*, 1998]. However, in both cases the observation area was further north than the region of interest for the convective uplift (South Eastern United States). This could have influenced the O_3 production rates and thereby the slope of O_3/CO as well. Nevertheless, this has to stay speculative for this work as no CO and NO_y data from operational ground stations were available with sufficient resolution for this study. The observation of O_3/CO slopes in PBL air masses before and after cloud venting to the free troposphere, and after further transport in the FT, could be a helpful constraint for future work.

6.6 Conclusions

During the ACSOE flight A575, long range transport of primary pollutants and ozone was observed in the remote free troposphere. It was investigated whether the observed O_3 in the air masses should be attributed to in situ production of O_3 in the FT from exported precursors, or, conversely, to substantial venting of boundary layer ozone over industrialised areas to the FT with subsequent long range transport is the cause.

To answer this question the source region and upward transport of the observed plumes were analysed by means of a newly developed transport module in combination with CO as inert tracer for anthropogenic emissions. Comparison of the model results with observed CO indicates rapid vertical transport of emissions into the free troposphere that is not resolved by the trajectories. By combining of the back trajectories with cloud brightness temperatures, analysed from GOES –8 infrared satellite data, convective events over the south-east and along the east coast of the US were found within the influencing area of the trajectories 4-6 days prior to the measurements. Thus, it is concluded that the observed polluted layers in the remote free troposphere originate from convective transport of North American emissions. The exact time and region of emission and upward transport could not be identified due to the uncertainties in the trajectory position.

[65] Compare chapter 3.3.2

The production of ozone in the FT from precursors, transported upward by convection, was modelled as a function of the initial NO_y and VOC concentrations in the outflow of the convective event, with the results presented in form of EKMA plots. Comparison of the model results with the observations was obtained by two different methods. Firstly, the initial concentrations of NO_y and VOC were scaled to the observed CO as tracer for anthropogenic emissions. The scaling was based on emission ratios from the NAPAP emission inventory for eastern U.S., considering reduction of the initial NO_y/CO and VOC/CO ratios due to photochemical losses in the PBL and scavenging during the convective transport. Secondly, possible initial NO_y and VOC concentrations were determined from comparison of the model results with the observed (NO_y-HNO_3) and VOC in the plume. The statistical confidence region was calculated, for which the start values lead to modelled VOC and (NO_y-HNO_3) concentrations compatible with the measurements at the 1% significance level. An excellent agreement of the initial NO_y and VOC concentrations in the polluted free tropospheric layer determined by both methods was found.

The results indicate that the upward transported air masses were already photochemically aged, with $NO_y/\Delta CO$ ratios in the convective outflow of about 20 % of the emission ratio. The modelled O_3 production was found to be strongly NO_x limited, and the modelled O_3 concentrations significantly lower than the measurements. The modelled correlation between O_3 and (NO_y-HNO_3) was found to be by about a factor of three too low relative to the observed slope of O_3/(NO_y-HNO_3). Given the above $NO_y/\Delta CO$ ratio, the slope of O_3/CO from the model calculations, of about 0.2-0.3 $ppbO_3$/ppbCO, is also about a factor of three smaller than the observations.

Assuming fresh emission input into the FT, with a higher ratio of exported NO_y/CO, increased the produced O_3 in relation to CO in the FT. However, at the same time the resulting (NO_y-HNO_3) increased, which is at odds with the observations. The significance analyses of modelled and measured concentrations for VOC and (NO_y-HNO_3) showed that initial NO_y/CO concentrations, that would be high enough to explain the observed O_3 concentrations, can be excluded.

It is concluded that the observed O_3 in the FT with the given slopes of O_3/CO and O_3/(NO_y-HNO_3) cannot be explained solely by in-situ production during the long range transport in the FT according to the model calculations.

Consequently, a substantial part of the observed O_3 has to come from venting of boundary layer ozone over industrialised areas to the FT with subsequent long-range transport. O_3 observations from ground stations were examined to investigate if such venting was possible. Maximum O_3 concentrations up to nearly 140 ppb were found in the path of the trajectories, though not coincident with the cloud venting. This indicated a weather situation favourable for formation of high O_3 concentrations within the PBL before the development of the convective events, allowing the possibility that substantial parts of the observed O_3 in the free troposphere could have been vented from the boundary layer. More detailed observations and extended model studies, particularly regarding the relation of ozone to precursor concentrations before the uplift, would improve our knowledge about the role of cloud venting for the ozone budget of the free troposphere.

7 Summary and general conclusions

The objective of this work was to analyse the ozone formation in continental plumes transported into source free maritime areas. This was investigated using airborne measurements aboard the United Kingdom Meteorological Office (UKMO) C-130 Hercules aircraft obtained during the European project TACIA (Testing Atmospheric Chemistry in Anticyclones) and the UK project ACSOE (Atmospheric Chemistry Studies in Oceanic Environment). High resolution measurements of CO as a quasi inert tracer of anthropogenic emissions were made and interpreted.

The relative roles of anthropogenic VOC and NO_x emissions in forming ozone in a continental plume in the lower part of the troposphere were investigated using the observations of rather fresh emissions close to the European continent during TACIA. Ozone formation and long range transport in the free troposphere were analysed from the observations of primary pollutants and ozone in the remote free troposphere during ACSOE.

A heuristic model was developed as a tool for the analysis of the history of air masses observed in source free areas. The model set-up, with modules for transport and chemistry, allows for a separation of these processes in the analysis. A Lagrangian formulation was chosen for the transport module, centred on clusters of back trajectories. The cluster formulation allowed for a highly parameterised description of atmospheric mixing processes based on synoptical scale motions. This procedure yielded good results at distances far enough from the source regions, where sub-scale mixing can be neglected.

This transport module in combination with the CO observations proved to be a useful tool for the analysis of emissions and transport. Excellent agreement between measured and modelled CO mixing ratios in the PBL was found for a stable flow situation in conjunction with anticyclonic conditions close to the emitting area (European continent) during the TACIA flight A581.

The transport module in conjunction with cloud brightness temperatures was found to be a valuable tool for the identification of convective events. Layers of enhanced CO and ozone, observed in the remote free troposphere near the Azores during ACSOE flight A575, could be identified as caused by long range transport from the eastern United States.

With the prerequisite of unambiguous transport situations correctly described by the model, these two flights allowed for the investigation of the chemical processing and ozone formation in continental plumes in the PBL (A581) and the free troposphere (A575).

The interpretation of observations distant from the source regions, with respect to the influence of anthropogenic NO_x and VOC emissions on the ozone formation in a plume, was done by an indirect inverse modelling approach. The method involves extensive sensitivity studies regarding VOC and NO_x emissions and their initial concentrations, in an EKMA framework. Despite the large degree of abstraction, the results of EKMA plot calculations can be compared to the measurements with help of CO as emission tracer and enables the dependency of the observed O_3 on anthropogenic VOC and NO_x emissions to be analysed.

A central point of this study is the use of statistical test methods for the analysis of the significance of deviations between model results and measurements. Sensitivity studies, regarding the dependence of model results on the variability of input parameters, were analysed with respect to confidence regions of the observations.

With these means, the following general conclusions regarding ozone formation in continental plumes transported into source free maritime areas are obtained:

- The layers of enhanced CO and O_3 in the FT, observed during ACSOE flight A575, can only partly be explained by in-situ production of ozone in the FT. Higher O_3 production efficiencies on a per-molecule basis of NO_x in the FT compared to the PBL were found to be compensated by the reduced NO_x availability in the free troposphere, related to CO. Thus, PBL-produced O_3 is found not only to be important close to source regions, but also for long range transport within the FT in connection with cloud venting, where it contributes to the tropospheric budget of ozone.

- The O_3 formation within the PBL depends on a multitude of parameters. It was shown for the example of the TACIA flight A581, that the natural variability and uncertainties of these parameters are still too high for an unambiguous interpretation of observed O_3 formation in a continental plume with respect to anthropogenic NO_x and VOC emissions. This complicates the task of estimating the influence of export of pollution-derived ozone and its precursors on the remote troposphere.

These conclusions have repercussions on future experiments, if the influence of anthropogenic emissions on tropospheric ozone is to be more quantitatively understood:

Estimations of the influence of PBL-produced O_3 on the global troposphere calls for model simulations. However, in order to get reliable results these have to be constrained by observations. It was shown that such constraints cannot be obtained if the degrees of freedom in the comparison of observations from field campaigns with model results are too large. Consequently, field campaigns should be designed in a way that the observations constrain the natural variability and uncertainties of parameters that have a significant impact on the model results in the investigated situation. The combination of sensitivity studies with statistical test methods discussed in this thesis offers a possible method for analysing the significance of the variability in input parameters on the results. Including such analyses as part of the strategy planning of a field campaign would significantly improve the interpretability of the obtained results. This could help to further improve our understanding of the processes involved in the controlling of tropospheric ozone.

8 References

Abraham, H.-J., P. Lenzschow, M. Lutz, W. Reichenbächer, E. Reimer, B. Scherer, and B. Stark, Flugzeug- und Bodenmessungen von Ozon und Vorläuferstoffen zu Abschätzung der Wirksamkeit von emissionsmindernden Maßnahmen im Großraum Berlin-Brandenburg (FluMOB-Projekt Abschlußbericht), 1994.

Aitchison, J., and J.A.C. Brown, The Lognormal Distribution, Cambridge University Press, Cambridge, 1966.

Albritton, D.L., F.C. Fehsenfeld, and A.F. Truck, Instrumental requirements for global atmopheric chemistry, *Science, 250*, 75-81, 1990.

Atkinson, R., D.L. Baulch, R.A. Cox, R.F. Hampson Jr., J.A. Kerr, M.J. Rossi, and J. Troe, Evaluated Kinetic Photochemical and Heterogenous Data for Atmospheric Chemistry: SupplementV, *J. Phys. Chem. Ref. Data, 26*, 521, 1997.

Atkinson, R., Gas-Phase Tropospheric Chemistry of Organic Compounds: A Review, *Atmospheric Environment, 24A*, 1-41, 1990.

Bauguitte, S., Measurements of nitrogen oxides, in Testing Atmospheric Chemistry in Anticyclones (TACIA), Final Report, R&D Programme Environment and Climate, Area: Environment Technologies, Topic: Environment and climate, tropospheric chemistry, Contract No ENV4-CT95-0038, edited by O. Hov, pp. 83-94, 1998.

Benkovitz, C.M., M.T. Scholtz, J. Pacyna, L. Tarrason, J. Dignon, E.C. Voldner, P.A. Spiro, J.A. Logan, and T.E. Graedel, Global gridded inventories of anthropogenic emissions of sulfur and nitrogen, *Journal of Geophysical Research, 101*, 29239-29253, 1996.

Berge, E., MSC-W Status Report 1997, Emissions, dispersion and trends of acidifying and eutrophying agents, Norwegian Meteorol. Inst., Oslo, Norway, 1997.

Bergin, M.S., A.G. Russell, W.P.L. Carter, B.E. Croes, and J.H. Seinfeld, VOC Reactivity and Urban Ozone Control, in Encyclopedia of Environmental Analysis and Remediation, John Wiley & Sons, New York, 1998.

Bergin, M.S., G.S. Noblet, K. Petrini, J.R. Dhieux, J.B. Milford, and R.A. Harley, Formal Uncertainty Analysis of a Lagrangian Photochemical Air Pollution Model, *Environmental Science & Technology, 33*, 1116-1126, 1999.

Bethan, S., G. Vaughan, C. Gerbig, A. Volz-Thomas, H. Richter, and D.A. Tiddeman, Chemical air mass differences near fronts, *Journal of Geophysical Research, 103*, 13413-13434, 1998.

Bougeault, P., S. Belair, J.M. Carriére, J. Cuxart, V. Ducroq, C. Fischer, P. Héreil, J.P. Lafore, P. Mascart, V. Masson, J.P. Pinty, E. Richard, and J. Stein, The Meso-NH Atmospheric Simulation System: Scientific documentation., Meteo-France and CNRS, Toulouse, France, 1995.

Brasseur, G.P. et.al., European scientific assessment of the atmospheric effects of aircraft emissions, *Atmospheric Environment, 32*, 2327-2422, 1998.

Brasseur, G.P., J.J. Orlando, and G.S. Tyndall, Atmospheric Chemistry and Global Change, Oxford University Press, Inc., New York, 1999.

Brook, J.R., L. Zhang, Y. Li, and D. Johnson, Description and evaluation of a model of deposition velocities for routine estimates of air pollutant dry deposition over North America. Part II: review of past measurements and model results, *Atmospheric Environment, 33*, 5053-5070, 1999.

Bruckmann, P., R. Beier, and S. Krautscheid, Immissionsmessungen von Kohlenwasserstoffen in den Belastungsgebieten Rhein-Ruhr, *Staub-Reinhalt. Luft, 43*, 404-410, 1983.

Bruckmann, P., W. Kersten, W. Funcke, E. Balfanz, J. König, J. Theisen, M. Ball, and O. Päpke, The Occurrence of Chlorinated and Other Organic Trace Compounds in Urban Air, *Chemosphere, 17*, 2363-2380, 1988.

Brunner, D., J. Staehelin, and D. Jeker, Large-Scale Nitrogen Oxide Plumes in the Tropopause Region and Implications for Ozone, *Science, 282*, 1305-1309, 1998.

Chang, J.S., F.S. Binkowski, N.L. Seaman, J.N. McHenry, P.J. Samson, W.R. Stockwell, C.J. Walcek, S. Madronich, P.B. Middleton, J.E. Pleim, and H.H. Lansford, The Regional Acid Deposition Model and Engineering Model, National Acid Precipitation Assessment Program, Washington D.C., 1989.

Chatfield, R.B., J.A. Vastano, L. Li, G.W. Sachse, and V.S. Connors, The Great African plume from biomass burning: Generalizations from a three-dimensional study of TRACE A carbon monoxide, *Journal of Geophysical Research, 103*, 28059-28077, 1998.

Chaumerliac, N., R. Rosset, M. Renard, and E.C. Nickerson, The transport and redistribution of atmospheric gases in regions of frontal rain, *Journal of Amospheric Chemistry, 14*, 43-51, 1992.

Chin, M., D.J. Jacob, J.W. Munger, D.D. Parrish, and B.G. Doddridge, Relationship of ozone and carbon monoxide over North America, *Journal of Geophysical Research, 99*, 14565-14573, 1994.

Conny, J.M., The isotopic characterization of carbon monoxide in the troposphere, *Atmospheric Environment, 32*, 2669-2683, 1998.

Cotton, W.R., G.D. Alexander, R. Hertenstein, R.L. Walko, R.L. McAnelly, and M. Nicholls, Cloud venting - A review and some new global annual estimates, *Earth-Science Reviews, 39*, 169-206, 1995.

Crutzen, P.J., and P.H. Zimmerman, The changing chemistry of the troposphere, *Tellus, 43AB*, 136-151, 1991.

Crutzen, P.J., The Role of NO and NO_2 in the Chemistry of the Troposphere and Stratosphere, *Annual Review of Earth and Planetary Sciences, 7*, 443-472, 1979.

Danielsen, E.F., and V.A. Mohnen, Project Dustorm Report: Ozone Transport, in Situ Measurements, and Meteorological Analyses of Tropopause Folding, *Journal of Geophysical Research, 82*, 5867-5877, 1977.

Derwent, R.G., and M.E. Jenkin, Hydrocarbons and the long-range transport of ozone and PAN across Europe, *Atmospheric Environment, 25A*, 1661-1678, 1991.

Dickerson, R.R. et al., Thunderstorms: An important mechanism in the transport of air pollutants, *Science, 235*, 460-465, 1987.

Dodge, M.C., Combined Use of Modelling Techniques and Smog Chamber Data to Derive Ozone-Precursor Relationships, in International Conference on Photochemical Oxidant Pollution and its Control, edited by B. Dimitriades, pp. 881-889, 1977.

Draxler, R.R., and G.D. Hess, An Overview of the HYSPLIT_4 Modelling System for Trajectories, Dispersion, and Deposition, *Australian Meteorological Magazine, 47*, 295-308, 1998.

Ebel, A., R. Friedrich, and H. Rodhe, Tropospheric Modelling and Emission Estimation, in Transport and Chemical Transformation of Pollutants in the Troposphere, edited by P. Borell, P.M. Borrell, T. Cvitas, K. Kelly, and W. Seiler, Springer-Verlag Berlin Heidelberg, 1997.

ECMWF, The Description Of The ECMWF/WCRP Level III - A global atmospheric data archive, 1995.

Ellermann, K., S. Herkelmann, D. Gladtke, and H.U. Pfeffer, LIMES-Jahresbericht, Landesumweltamt NRW, 1995.

EPA (U.S. Environmental Protection Agency), National air pollution and emission trends 1900-1994, EPA, Research Triangle Park, NC, 1995.

EPA (U.S. Environmental Protection Agency), National Air Quality and Emissions Trends Report, 1997, 1997.

Evans, M.J., Lagrangian modelling of tropospheric field measurements, Dissertation thesis, University of Cambridge, Cambridge, 1999.

Finlayson-Pitts, B.J., and J.N. Pitts, Atmospheric Chemistry: Fundamentals and Experimental Techniques, John Wiley and Sons, New York, 1986.

Fishman, J., and W. Seiler, Correlative Nature of Ozone and Carbon Monoxide in the Troposphere: Implications for the Tropospheric Ozone Budget, *Journal of Geophysical Research, 88*, 3662-3670, 1983.

Flatoy, F., O. Hov, and H. Smit, Three-dimensional model studies of exchange processes of ozone in the troposphere over Europe, *Journal of Geophysical Research, 100*, 11,465-11,481, 1995.

Flatoy, F., O. Hov, C. Gerbig, and S.J. Oltmans, Model Studies of the meteorology and chemical composition of the troposphere over the North Atlantic during August 18-30, 1993, *Journal of Geophysical Research, 101*, 29317-29334, 1996.

Folkins, I., R. Chatfield, H. Singh, Y. Chen, and B. Heikes, Ozone production efficiencies of acetone and peroxides in the upper troposphere, *Geophysical Research Letters, 25*, 1305-1308, 1998.

Fuentes, J.D., and D. Wang, On the seasonality of isoprene emissions from a mixed temperate forest, *Ecological Applications, 9*, 1118-1131, 1999.

Georgopoulos, G.P., and J.H. Seinfeld, Statistical distribution of air pollutant concentrations, *Environ. Sci. Technol., 15*, 401A-416A, 1982.

Gerbig, C., D. Kley, A. Volz-Thomas, and D.S. McKenna, Zur Ozonbilanz in der Troposphäre: Flugzeuggestützte Messungen von Ozon, CO, und NO_y, Berichte des Forschungszentrum Jülich, Jülich, 1997.

Gerbig, C., D. Kley, A. Volz-Thomas, J. Kent, K. Dewey, and D.S. McKenna, Fast-response resonance fluorescence CO measurements aboard the C-130: Instrument characterisation and measurements made during NARE '93, *Journal of Geophysical Research, 101*, 29229-29238, 1996.

Gerbig, C., J.C. Lin, B.C. Daube, S.C. Wofsy, P.S. Bakwin, D.F. Hurst, P.C. Novelli, K.J. Davis, and S. Schmitgen, Development of a Simple Trajectory Transport Model to Assess Regional CO_2 Fluxes from Aircraft and Tower Measurements, in AGU Fall Meeting, San Francisco, California, USA, 1999a.

Gerbig, C., S. Schmitgen, D. Kley, A. Volz-Thomas, K. Dewey, and Haaks, An improved fast-response vacuum-UV resonance fluorescence CO instrument, *Journal of Geophysical Research, 104*, 1699-1704, 1999b.

Gidel, L.T., Cumulus cloud transport of transient tracers, *Journal of Geophysical Research, 88*, 6587-6599, 1983.

Graedel, T.E., and P.J. Crutzen, Atmospheric change: An Earth System Perspective, W. H. Freeman and Company, New York, 1993.

Gregory, G.L., A.S. Bachmeier, D.R. Blake, B.G. Heikes, D.C. Thornton, A.R. Bandy, J.D. Bradshaw, and Y. Kondo, Chemical signatures of aged Pacific marine air: Mixed layer and free troposphere as measured during PEM-West A, *Journal of Geophysical Research, 101*, 1727-1742, 1996.

Guenther, A., C.N. Hewitt, D. Erickson, D. Fall, C. Geron, T. Graedel, P. Harley, L. Klinger, M. Lerdau, W.A. McKay, T. Pierce, B. Scholes, R. Steinbrecher, R. Tallamraju, J. Taylor, and P. Zimmermann, A global model of natural volatile organic compound emissions, *Journal of Geophysical Research, 100*, 8873- 8892, 1995.

Guicherit, R., Ozone on an urban and regional scale - with special reference to the situation in the Netherlands, in Tropospheric Ozone - Regional and Global Scale Interactions, edited by I.S.A. Isaksen, pp. 49-62, Reidel, D., Dodrecht, The Netherlands, 1988.

Haagen-Smit, A.J., Chemistry and Physiology of Los Angeles Smog, *Industrial and Engineering Chemistry, 44*, 1342-1346, 1952.

Hanna, S.R., J.C. Chang, and M.E. Fernau, Monte Carlo estimates of uncertainties in predictions by a photochemical grid model (UAM-IV) due to uncertainties in input variables, *Atmospheric Environment, 32*, 3619-3628, 1998.

Hass, H., H.J. Jakobs, and M. Memmesheimer, Analysis of a regional model (EURAD) near surface gas concentration predictions using observations from networks, *Meteorol. Atmos. Phys., 57*, 173-200, 1995.

Hauf, T., P. Schulte, R. Alheit, and H. Schlager, Rapid vertical trace gas transport by an isolated midlatitude thunderstorm, *Journal of Geophysical Research, 100*, 22,957-22,970, 1995.

Hess, G.D., F. Carnovale, M.E. Cope, and G.M. Johnson, The evaluation of some pohotochemical smog reaction mechanisms - I. Temperature and initial composition effects, *Atmospheric Environment, 26A*, 625 - 641, 1992.

Hipskind, R.S., G.L. Gregory, G.W. Sachse, G.F. Hill, and E.F. Danielsen, Correlations between Ozone and Carbon Monoxide in the lower Stratosphere, Folded Tropopause, and maritime Troposphere, *Journal of Geophysical Research, 92*, 2121-2130, 1987.

Holloway, J.S., R.O. Jacoubek, D.D. Parrish, A. Fried, B. Wert, B. Henry, J.R. Drummond, C. Gerbig, A. Volz-Thomas, and S. Schmitgen, Airborne Intercomparison of Vacuum Ultraviolet Fluorescence and Tunable Diode Laser Absorption Measurements of Tropospheric Carbon Monoxide, *Journal of Geophysical Research, in press, 2000.*

Holton, J.R., An introduction to dynamic meteorology, 511 pp., Academic Press, San Diego, California, USA, 1992.

Holzworth, G.C., Estimates of mean mixing depths in the contiguous United States, *Monthly Weather Review, 92*, 235-247, 1964.

Hough, A.M., The development of a two-dimensional tropospheric model: The model chemistry, *Journal of Geophysical Research, 96*, 7325-7362, 1991.

Hov, O., F. Flatoy, J.S. Foot, K. Dewey, H. Richer, A. Kaye, J. Kent, D. Tiddeman, I. Hawke, D. Kley, C. Gerbig, S. Schmitgen, S. Penkett, G. Mills, S. Bauguitte, J.M. Baker, B. Bandy, R. Burgess, T. Green, P.S. Monks, H.M. McIntyre, C. Reeves, F. Stordal, N. Schmidbauer, S. Solberg, M. Beekmann, E. Dugault, M. Lattuati, K. Law, J. Pyle, M. Evans, M. Cahill, P.-H. Plantevin, and D. Shallcross, Testing Atmospheric Chemistry in Anticyclones (TACIA), Final Report, R&D Programme Environment and Climate, Area: Environment Technologies, Topic: Environment and climate, tropospheric chemistry, Contract No ENV4-CT95-0038, 1998.

Huntrieser, H., H. Schlager, C. Feigl, and H. Höller, Transport and production of NO_x in electrified thunderstorms: Survey of previous studies and new observations at midlatitudes, *Journal of Geophysical Research, 103*, 28,247-28,264, 1998.

Jaeglé, L., D.J. Jacob, P.O. Wennberg, C.M. Spivakovsky, T.F. Hanisco, E.J. Lanzendorf, E.J. Hintsa, D.W. Fahey, E.R. Keim, M.H. Proffitt, E.L. Atlas, F. Flocke, S. Schauffler, C.T. McElroy, C. Midwinter, L. Pfister, and J.C. Wilson, Observed OH

and HO_2 in the upper troposphere suggest a major source from convective injection of peroxides, *Geophysical Research Letters, 24*, 3181-3184, 1997.

Jaeglé, L., D.J. Jacob, Y. Wang, A.J. Weinheimer, B.A. Ridley, T.L. Campos, G.W. Sachse, and D.E. Hagen, Sources and chemistry of NO_x in the upper troposphere over the United States, *Geophysical Research Letters, 25*, 1705-1708, 1998.

James, I.N., The global atmospheric circulation, in Physics and chemistry of the atmospheres of the Earth and other objects of the solar system, edited by C. Boutron, pp. 1-37, Les Editions de Physique, Les Ulis, 1996.

Joseph, J.H., W.J. Wiscombe, and J.A. Weinman, The delta-Eddington approximation for radiative flux transfer, *Journal of Atmospheric Science, 33*, 2452-2458, 1976.

Junkermann, W. et al., *Journal of Atmospheric Chemistry, 8*, 203-227, 1989.

Kern, T., N. Metz, and D. Kley, Untersuchungen von Verkehrsabgasemissionen insbesondere im Hinblick auf die Ozonbildung, Forschungszentrum Jülich, Jülich, 1998.

Khalil, M.A.K., and R.A. Rasmussen, The global cycle of carbon monoxide: trends and mass balance, *Chemosphere, 20*, 227-242, 1990.

Klemp, D., D. Kley, F. Kramp, H.J. Buers, G. Pilwat, F. Flocke, W. Paetz, and A. Volz-Thomas, Long-Term Measurements of Light Hydrocarbons (C2 - C5) at Schauinsland (Black Forest), *Journal of Atmospheric Chemistry, 28*, 153-171, 1997.

Kley, D., H. Geiß, and V.A. Mohnen, Tropospheric Ozone at Elevated Sites and Precursor Emissions in the United States and Europe, *Atmospheric Environment Part A - General Topics, 28A*, 149-158, 1994.

Kley, D., H.G.J. Smit, H. Vömel, H. Grassl, V. Ramanathan, P.J. Crutzen, S. Williams, J. Meywerk, and S. Oltmans, Tropospheric Water Vapor and Ozone Cross Sections in a Zonal Plane Over the Central Equatorial Pacific, *Quart. J. Roy Met. Soc., 123*, 2009-2040, 1997.

Kley, D., Tropospheric Chemistry and Transport, *Science, 276*, 1043-1045, 1997.

Kley, D., Tropospheric ozone in the global, regional and subregional context, in Topics in Atmospheric and Interstellar Physics and Chemistry, edited by C.F. Boutron, pp. 161-184, Les Editions de Physique, Les Ulis, 1994.

Lattuati, M., Impact des Émissions Européennes sur le bilans de l'ozone troposphèrique l'interface de l'Europe et de l'Atlantique Nord: rapport de la modèlisation lagrangienne et des mesures en altitude, Thèse de doctorat thesis, Université Paris 6, Paris, France, 1997.

Lazrus, A.L., G.L. Kok, S.N. Gitlin, J.A. Lind, and S.E. McLaren, Automated fluorimetric method for hydrogen peroxide in air, *Analytical Chemistry, 58*, 594-597, 1986.

Leighton, P.A., Photochemistry of Air Pollution, Academic Press, San Diego, California, USA, 1961.

Lelieveld, J., and P.J. Crutzen, Role of deep cloud convection in the ozone budget of the troposphere, *Science, 264*, 1759-1761, 1994.

Liang, J., L.W. Horowitz, D.J. Jacob, Y. Wang, A.M. Fiore, J.A. Logan, G.M. Gardner, and J.W. Munger, Seasonal budgets of reactive nitrogen species and ozone over the United States, and export fluxes to the global atmosphere, *Journal of Geophysical Research, 103*, 13435-13450, 1998.

Liu, S.C., D. Kley, M. McFarland, J.D. Mahlman, and H. Levy, On the Origin of Tropospheric Ozone, *Journal of Geophysical Research, 85*, 7546-7552, 1980.

Liu, S.C., M. Trainer, F.C. Fehsenfeld, D.D. Parrish, E.J. Williams, D.W. Fahey, G. Hubler, and P.C. Murphy, Ozone production in the rural troposphere and the implications for regional and global ozone distributions, *Journal of Geophysical Research, 92*, 4191-4207, 1987.

Logan, J.A., M.J. Prather, S.C. Wofsy, and M.B. McElroy, Tropospheric chemistry: a global perspective, *Journal of Geophysical Research, 86*, 7210-7254, 1981.

Madronich, S., Photodissociation in the Atmosphere. 1. Actinic Flux and the Effects of Ground Reflections and clouds, *Journal of Geophysical Research, 92*, 9740-9752, 1987.

Mannschreck, K., K. Bächmann, I. Barnes, K.H. Becker, T. Heil, R. Kurtenbach, M. Memmesheimer, V. Mohnen, T. Schmitz, R. Steinbrecher, A. Obermeier, D. Poppe, A. Volz-Thomas, and F. Zabel, A VOC-Database, *Journal of Atmospheric Chemistry, submitted*, 2000.

Mapes, B.E., and R.A. Houze Jr., Cloud clusters and superclusters over the oceanic warm pool, *Monthly Weather Review, 121*, 1398-1415, 1993.

Marenco, A., V. Thouret, P. Nedelec, H. Smit, M. Helten, D. Kley, F. Karcher, P. Simon, K. Law, J. Pyle, G. Poschmann, R. Von Wrede, C. Hume, and T. Cook, Measurement of ozone and water vapor by Airbus in-service aircraft: The MOZAIC airborne program, An overview, *Journal of Geophysical Research, 103*, 25631-25642, 1998.

Mauzerall, D.L., J.A. Logan, D.J. Jacob, B.E. Anderson, D.R. Blake, J.D. Bradshaw, B. Heikes, G.W. Sachse, H. Singh, and B. Talbot, Photochemistry in biomass burning plumes and implications for tropospheric ozone over the tropical South Atlantic, *Journal of Geophysical Research, 103*, 8401-8423, 1998.

McKenna, D.S., A. Volz-Thomas, S. Penkett, G. Vaughan, H. Fischer, and F. Stordal, Oxidising Capacity of the Tropospheric Atmosphere: Final Report to the European Comission on contract EVSV-CT91-0042, EU, 1995.

Memmesheimer, M., J. Tippke, A. Ebel, H. Hass, H.J. Jakobs, and M. Laube, On the use of EMEP emission inventories for European scale air plooution modelling with the EURAD model, in EMEP workshop on photooxidant modelling for long range transport in relation to abatement strategies, pp. 307-324, Berlin, 1991.

Menut, R. Vautard, M. Beekmann, and C. Honore, Adjoint modelling for sensitivity of atmospheric pollution peaks over the Paris area, *Journal of Geophysical Research, in press*, 2000.

Methven, J., Offline Trajectories: Calculation and Accuracy., Dept. Meteorology, Uni. Reading, UK, 1997.

Middleton, P., W.R. Stockwell, and W.P.L. Carter, Aggregation and analysis of volatile organic compound emissions for regional modeling, *Atmospheric Environment, 24A*, 1107-1133, 1990.

Muller, J.-F., Geographical distribution and seasonal variation of surface emissions and deposition velocities of atmospheric trace gases, *Journal of Geophysical Research, 97*, 3787-3804, 1992.

Newell, R.E., V. Thouret, J.Y.N. Cho, P. Stoller, A. Marenco, and H.G. Smit, Ubiquity of quasi-horizontal layers in the troposphere, *Nature, 398*, 316-319, 1999.

Novelli, P.C., L.P. Steele, and P.P. Tans, Mixing Ratios of Carbon Monoxide in the Troposphere, *Journal of Geophysical Research, 97*, 20731-20750, 1992.

Parrish, D.D., J.S. Holloway, M. Trainer, P.C. Murphy, G.L. Forbes, and F.C. Fehsenfeld, Export of North American ozone pollution to the North Atlantic Ocean, *Science, 259*, 1436-1439, 1993.

Parrish, D.D., M. Trainer, J.S. Holloway, J.E. Yee, M.S. Warshawsky, F.C. Fehsenfeld, G.L. Forbes, and J.L. Moody, Relationships between ozone and carbon monoxide at surface sites in the North Atlantic region, *Journal of Geophysical Research, 103*, 13357-13376, 1998.

Parrish, D.D., M. Trainer, M.P. Buhr, B.A. Watkins, and F.C. Fehsenfeld, Carbon monoxide concentrations and their relation to concentrations of total reactive oxidized nitrogen at two rural U.S. sites, *Journal of Geophysical Research, 96*, 9309-9320, 1991.

Paulson, S.E., The tropospheric Oxidation of Organic Compounds: Recent Developments in OH, O_3, and NO_3 Reactions with Isoprene and other Hydrocarbons, in Progress and Problems in Atmospheric Chemistry, edited by J.R. Barker, World Scientific, Singapore, 1995.

Penkett, S.A., B.J. Bandy, C.E. Reeves, D. McKenna, and P. Hignett, Measurements of peroxides in the atmosphere and their relevance to the understanding of global tropospheric chemistry, *Faraday Discuss., 100*, 155-174, 1995.

Penkett, S.A., N.J. Blake, P. Lightman, A.R.W. Marsh, P. Anwyl, and G. Butcher, The seasonal variation of nonmethane hydrocarbons in the free troposphere over the North Atlantic Ocean: Evidence for extensive reaction of hydrocarbons with the nitrate radical, *Journal of Geophysical Research, 98*, 2865-2885, 1993.

Pickering, K.E., A.M. Thompson, W.K. Tao, and T.L. Kucsera, Upper Tropospheric Ozone Production Following Mesoscale Convection During STEP/EMEX, *Journal of Geophysical Research, 98*, 8737-8749, 1993.

Pickering, K.E., J.R. Scala, A.M. Thompson, W.K. Tao, and J. Simpson, Free Tropospheric Ozone Production following entrainment of Urban Plumes into Deep Convection, *Journal of Geophysical Research., 97*, 17985-18000, 1992.

Pickering, K.E., R.R. Dickerson, G.J. Huffman, J.F. Boatman, and A. Schanot, Trace Gas Transport in the Vicinity of Frontal Convective Clouds, *Journal of Geophysical Research, 93*, 759-773, 1988.

Pickering, K.E., R.R. Dickerson, W.T. Luke, and L.J. Nunnermacker, Clear.Sky vertical profiles of trace gases as influenced by upstream convective activity, *Journal of Geophysical Research, 94*, 14,879-14,892, 1989.

Placet, M., C.O. Mann, R.O. Gilbert, and M.J. Niefer, Emissions of ozone precursors from stationary sources: a critical review, *Atmospheric Environment, 34*, 2183-2204, 2000.

Prather, M.J., and D.J. Jacob, A persistent imbalance in HO_x and NO_x photochemistry of the upper troposphere driven by deep tropical convection, *Geophysical Research Letters, 24*, 3189-3192, 1997.

Reeves, C.E., S. Penkett, B. Bandy, G. Mills, S. Bauguitte, R. Burgess, M. Evans, T. Green, K. Law, P. Monks, H. Richer, and S. Schmitgen, Investigation of Tropospheric Photo-Oxidation Using Peroxide and Formaldehyde Data Collected Over the North Atlantic and Generated by an Observationbally Constrained Box Model as Part of the ACSOE Programme, draft, 2000.

Richer, H.R., J.S. Foot, R.G. Derwent, S. Schmitgen, D. Kley, O. Hov, N. Schmidbauer, S.A. Penkett, B. Bandy, G. Mills, S. Bauguitte, P.S. Monks, and M. Evans, Fast Photochemical Balance Calculations On Aircraft Data, collected during TACIA, draft, 2000.

Röckmann, T., C.A.M. Brenninkmeijer, P. Neeb, and P.J. Crutzen, Ozonolysis of Nonmethane Hydrocarbons as a Source of the Observed Mass Independent Oxygen Isotope Enrichment in Tropospheric CO, *Journal of Geophysical Research, 103*, 1463-1470, 1998.

Sachse, G.W., G.F. Hill, L.O. Wade, and M.G. Perry, Fast-Response, High-Precision Carbon Monoxide Sensor Using a Tunable Diode Laser Absorption Technique, *Journal of Geophysical Research., 92*, 2071-2081, 1987.

Saylor, R.D., R.C. Easter, and E.G. Chapman, Simulation of the tropospheric distribution of carbon monoxide during the 1984 MAPS experiment, *Atmospheric Environment, 33*, 4675-4694, 1999.

Schmitz, T., D. Klemp, and D. Kley, Messungen der Immissionskonzentrationen verschiedener Ozonvorläufersubstanzen in Ballungsgebieten und an Autobahnen, Berichte des Forschungszentrum Jülich GmbH, 1997.

Seber, G.A.F., Multivariate observations, John Wiley & Sons, New York, 1984.

Seibert, P., F. Beyrich, S.-E. Gryning, S. Joffre, A. Rasmussen, and P. Tercier, Review and intercomparison of operational methods for the determination of the mixing height, *Atmospheric Environment, 34*, 1001-1027, 2000.

Seinfeld, J.H., Atmospheric Chemistry and Physics of Air Pollution, Wiley, New York, 1986.

Seinfeld, J.H., Chemistry of Ozone in the Urban and Regional Atmosphere, in Progress and Problems in Atmospheric Chemistry, edited by J.R. Barker, World Scientific, Singapore, 1995.

Shetter, R.E., A.H. McDaniel, C.A. Cantrell, S. Madronich, and J.G. Calvert, Actinometer and Eppley Radiometer Measurements of the NO2-photolysis rate coefficient during the Manua Loa Observatory Photochemistry Experiment, *Journal of Geophysical Research, 97*, 10,349-10,360, 1992.

Sillman, S., The relation between ozone, NO_x and hydrocarbons in urban and polluted rural environments, *Atmospheric Environment, 33*, 1821-1845, 1999.

Sillman, S., The use of NO_y; H_2O_2 and HNO_3 as indicators for O_3-NO_x-VOC sensitivity in urban locations, *Journal of Geophysical Research, 100*, 14175-14188, 1995.

Simpson, D., Biogenic emissions in Europe, 2. Implications for ozone control strategies, *Journal of Geophysical Research, 100*, 22891-22906, 1995.

Singh, H.B., A.M. Thompson, and H. Schlager, SONEX airborne mission and coordinated POLINAT-2 activity: overview and accomplishments, *Geophysical Research Letters, 26*, 3053-3056, 1999.

Slemr, F., G. Baumbach, U. Corsmeier, R. Friedrich, N. Kalthoff, D. Klemp, K. Mannschreck, M. Möllmann-Coers, P. Rabl, and J. Slemr, Evaluation of calculated, spatially and temporaly highly resolved emission inventories of photosmog precursors for a city: The experiment and its major results, Draft, 2000.

Stamnes, K.S., S.-C. Tsay, W. Wiscombe, and K. Jayaweera, Numerically stable algorithm for discrete-ordinate-method radiative transfer in multiple scattering and emitting layered media, *Appl. Opt., 27*, 2501-2509, 1988.

Stevenson, D.S., C.E. Johnson, W.J. Collins, R.G. Derwent, K.P. Shine, and J.M. Edwards, Evolution of tropospheric ozone radiative forcing, *Geophysical Research Letters, 25*, 3819-3822, 1998.

Stockwell, W.R., F. Kirchner, M. Kuhn, and S. Seefeld, A new mechanism for regional atmospheric chemistry modeling, *Journal of Geophysical Research, 102*, 25847-25879, 1997.

Stockwell, W.R., P. Middleton, J.S. Chang, and X. Tang, The Second Generation Regional Acid Deposition Model Chemical Mechanism for Regional Air Quality Modeling, *Journal of Geophysical Research, 95*, 16,343-16,367, 1990.

Stohl, A., A one-year Lagrangian "climatology" of airstreams in the northern hemisphere troposphere and lowermost stratosphere, Draft, 2000.

Stohl, A., Computation, accuracy and applications of trajectories - A review and bibliography, *Atmospheric Environment, 32*, 947-966, 1998.

Stull, R.B., An Introduction to Boundary Layer Meteorology, Kluwer Academic Press, Dordrecht, 1988.

Sturges, W.T., C.E. Reeves, S.A. Penkett, P.S. Liss, T.W. Choularton, W.J. Broadgate, K.N. Bower, K.S. Law, L.J. Gray, and G.G. McFadyen, ACSOE Implementation Plan, University of East Anglia, Norwich, UK, 1996.

Talbot, R.W., J.E. Dibb, E.M. Scheuer, Y. Kondo, M. Koike, H.B. Singh, L.B. Salas, Y. Fukui, J.O. Ballenthin, R.F. Meads, T.M. Miller, D.E. Hunton, A.A. Viggiano, D.R. Blake, N.J. Blake, E. Atlas, F. Flocke, D.J. Jacob, and L. Jaeglé, Reactive Nitrogen Budget During the NASA SONEX mission, *Geophysical Research Letters, 26*, 3057-3060, 1999.

Tao, W.-K., and J. Simpson, Goddard cumulus ensemble model, I, Model description, *Terr. Atmos. Oceanic Sci., 50*, 673-690, 1993.

Thijsse, T.R., and R.F. van Oss, TNO-Bericht, 1997.

Thompson, A.M., K.E. Pickering, R.R. Dickerson, W.G. Ellis, D.J. Jacob, J.R. Scala, W.-K. Tao, D.P. McNamara, and J. Simpson, Convective transport over the central United States and its role in regional CO and ozone budgets., *Journal of Geophysical Research, 99*, 18703-18711, 1994.

Thompson, A.M., The oxidising capacity of the Earth's atmosphere: Probable past and future changes, *Science, 256*, 1157-1168, 1992.

Trainer, M., et al., Correlation of ozone with NO_y in photochemically aged air, *Journal of Geophysical Research, 98*, 2917-2925, 1993.

Umweltschutz, B.L.f., Abschlußbericht zum Forschungsvorhaben "Bestimmung von leichtflüchtigen organischen Schadstoffen in Stadtluft (BOSS)", 1994.

van Hees, R.M., J. Lelieveld, and W.D. Collins, Detecting tropical convection using AVHRR satellite data, *Journal of Geophysical Research, 104*, 9213-9228, 1999.

Vogel, B., F. Fiedler, and H. Vogel, Influence of topography and biogenic volatile organic compounds emission in the state of Baden-Württemberg on ozone concentrations during episodes of high air temperatures., *Journal of Geophysical Research, 100*, 22907-22928, 1995.

Volz, A., and D. Kley, A Resonance Fluorescence Instrument for the In-Situ Measurement of Atmospheric Carbon Monoxide, *Journal of Atmospheric Chemistry, 2*, 345-357, 1985.

Volz-Thomas, A., A. Lerner, H.W. Pätz, M. Schultz, D.S. McKenna, R. Schmitt, S. Madronich, and E.P. Röth, Airborne Measurements of the Photolysis Frequency of NO2, *Journal of Geophysical Research., 101*, 18613-18627, 1996.

Volz-Thomas, A., B.A. Ridley, M.O. Andreae, R.G. Chameides, R.G. Derwent, I.E. Galbally, J. Lelieveld, S.A. Penkett, M.O. Radgers, M. Trainer, G. Vaughan, and X.J. Zhou, Tropospheric Ozone, in Assessment of Ozone Depletion, edited by R.L. Albritton, R.T. Watson, and P.J. Aucamp, WMO, 1995.

Warneck, P., Chemistry of the Natural Atmosphere, Academic Press, San Diego, 1988.

Weseley, M.L., Parametrisation of surface resistances to gaseous dry deposition in regional scale numerical models, *Atmospheric Environment, 23*, 1293-1304, 1989.

Wild, O., K.S. Law, D.S. McKenna, B.J. Bandy, S.A. Penkett, and J.A. Pyle, Photochemical trajectory modeling studies of the North Atlantic Region During August 1993, *Journal of Geophysical Research, 101*, 29269-29288, 1996.

WMO (World Meteorological Organization), Scientific Assessment of Ozone Depletion: 1998, Global Ozone Reseach and Monitoring Project - Report 37, Geneva, 1999.

9 Appendix

9.1 t-test for the significance of the deviation between modelled and measured values for one parameter

Be X_p the variate of a measured parameter p (p = O3, NOx, VOC, ...), then

(9.1) $$Y_p = \ln(X_p)$$

shall be normally distributed with the mean μ_p and the variance σ_p^2.

As μ_p and σ_p^2 are not known, they are estimated from the measurements[66]:

(9.2) $$\hat{\mu}_p = \bar{y}_p = (1/n)\sum_{i=1}^{n} y_{pi}$$

(9.3) $$\hat{\sigma}_p^{\,2} = s_p^{\,2} = \frac{1}{n-1}\sum_{i=1}^{n}(y_{pi} - \bar{y}_p)^2$$

The estimated standard error of the mean $\bar{y}_p$ is then given by:

(9.4) $$\hat{\sigma}_{\bar{y}_p} = \sqrt{\frac{\hat{\sigma}_p^{\,2}}{n}}$$

It shall be analysed, whether the modelled values μ_{Mp} are within the confidence interval of the measured parameters. That is, we are testing the null hypothesis that the model-observation differences are explicable by natural variability, while rejection of this hypothesis implies an incorrect model response. For unknown variance σ_p^2 this is done by the t-test, defined by the measure:

(9.5) $$t = T(y_{p_1}, \ldots, y_{p_n}) = \frac{\bar{y}_p - \mu_{Mp}}{\hat{\sigma}_{\bar{y}_p}}$$

where the test statistic T is t-distributed with n-1 degrees of freedom.

[66] The estimated values are denoted by a " ^ ".

Additionally, the systematic error of the measurements has to be counted for. This error results in a deviation of $\bar{y}_p$ from the true mean. If the systematic error of the measurement x_p is given by $\varepsilon_p \cdot x_p$ then the mean that is tested for is shifted by $\ln(1+\varepsilon_p)$. Hence the test statistic T becomes non central distributed with the non centrality parameter δ:

(9.6) $$T \sim t_{n-1,\delta} \qquad \text{with:} \quad \delta = (\ln(1+\varepsilon_p)/\sigma_{\bar{y}_p})^2$$

The task of testing this null hypothesis is to give the probability that we erroneously reject the true hypothesis (type-1-error). This probability is called the significance level of a test. Common thresholds are significance levels of 1%, 5% or 10%.

The problem can be mathematically formulated in the following definition:

(9.7) $$P(|t| < k) = 1 - \alpha_0$$

where α_0 is the significance level, and k defines the bounds of the so called confidence interval, such that for $|t| \geq k$ the null hypothesis will be rejected.

Equivalently, this can be formulated by defining an α-value, which gives the probability that the test statistic T exceeds the test value t, with rejection of the null hypothesis if $\alpha < \alpha_0$:

(9.8) $$\alpha = P(|T| > |t|) < \alpha_0$$

Hence α gives the smallest value, for which the model-observation differences are still significant. This is the observed significance level of the tested model value.

The smaller α the more significant is the deviation between modelled and measured parameter. For example if $\alpha < 1\%$ for a tested model value, the probability that the measured values originate from a distribution with modelled mean is less then one percent. This means that even for a significance level $\alpha_0 = 1\%$, which is statistically interpreted as a very significant deviation, this leads to the rejection of the hypothesis. Whereas the higher α is, the higher is the probability that the observed deviation between measured and modelled parameter can be explained by statistical variability, thus is not significant.

9.2 F-test for the significance of the deviation between modelled and measured values for several parameter

In analogy to the univariate case Y is defined as the vector of the variates Y_p

(9.9) $$Y = (Y_{p_1}, \ldots, Y_{p_{p_0}}) = (\ln(X_{p_1}), \ldots, \ln(X_{p_{p_0}}))$$

where p_0 is the number of considered measured parameters p. Then Y shall be multivariate normally distributed with a mean vector μ and the covariance matrix Σ. For the measured samples the mean is estimated by $\bar{y} = (\bar{y}_{p_1}, \ldots, \bar{y}_{p_{p_0}})$, and the covariance matrix by:

(9.10) $$\hat{\Sigma} = (\hat{\sigma}_{ij})_{p_0 \times p_0} \qquad \text{with } \hat{\sigma}_{ij} = \frac{1}{n-1} \sum_{k=1}^{n} (y_{p_i k} - \bar{y}_{p_i})(y_{p_j k} - \bar{y}_{p_j})$$

The hypothesis that the vector μ_M of the model results for p_0 parameters is equal to the mean vector μ leads then to Hotelling's T^2 test statistic defined as:

(9.11) $$T^2 = n(\bar{y} - \mu_M)^T \hat{\Sigma}^{-1} (\bar{y} - \mu_M)$$

where $n \geq p_0 + 1$, to ensure that $\hat{\Sigma}$ admits an inverse. Under the hypothesis $\mu = \mu_M$ a T^2 value can be tested for significance using an F-distribution with degrees of freedom p_0 and $n - p_0$, given by the following relation:

(9.12) $$F_{(p_0, n-p_0)} = \frac{n - p_0}{p_0 (n-1)} T^2$$

For the univariate case $p_0 = 1$ this F-distribution is just the square of the t-distribution. As well analogous to the univariate case, the systematic errors of the measurements are allowed for by a non centrality parameter of the F-distribution, which in the multivariate case takes the form:

(9.13) $$\delta = n \cdot \varepsilon^T \Sigma^{-1} \varepsilon \qquad \text{with } \varepsilon = (\ln(1+\varepsilon_{p_1}), \ldots, \ln(1+\varepsilon_{p_{p_0}}))$$

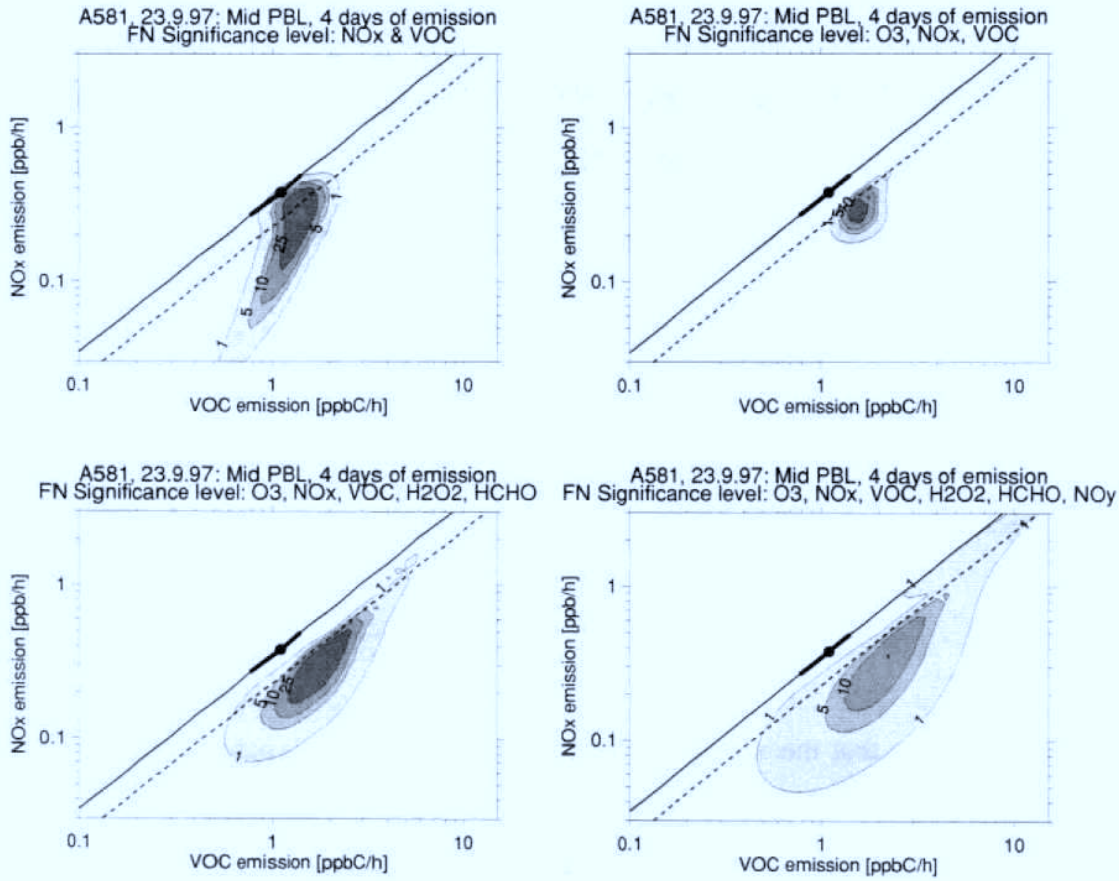

Figure 9.1: Isolines of the significance levels α = 1%, 5%, 10%, 25% for the null hypothesis that model-observation differences are solely due to statistical variability. Shown are the test results of the non central $F_{(p,n-p,\delta)}$-distribution (FN) in the class MPBL. The tested parameters are given in the header of each plot, NO_y has to be read as NO_y-HNO_3.

Figure 9.1 and Figure 9.2 show the test results for different groups of parameters in the classes MPBL and SL. These plots illustrate a main problem of the multivariate test approach for these observations. The $F_{(p_0,n-p_0)}$-distribution is only defined if the number of tested parameters, p_0, is smaller than the number of samples, n. In the class MPBL nine bottle samples , in the class SL only five bottle samples are available, which can be used to estimate the covariance matrix of the distribution. Hence no results for five and more parameters exist in the class SL. But already for fewer parameters the non centrality parameter becomes very large, due to small eigenvalues of the covariance matrix. This can be caused by a strong correlation of the measured parameters, or more likely in this case by the small number of observations which result in a questionable estimation of the covariance matrix $\hat{\Sigma}$. Due to the large non centrality parameter the test value becomes very conservative, thus inhibiting nearly every significance statement. The more parameters are included in the test, the larger become the confidence regions defined by the 1% significance level in the results presented for the classes MPBL and SL. In Figure 9.2 the

test results for the group of O_3, NO_x and VOC lie above the 1% significance level for the major part of the EKMA plot.

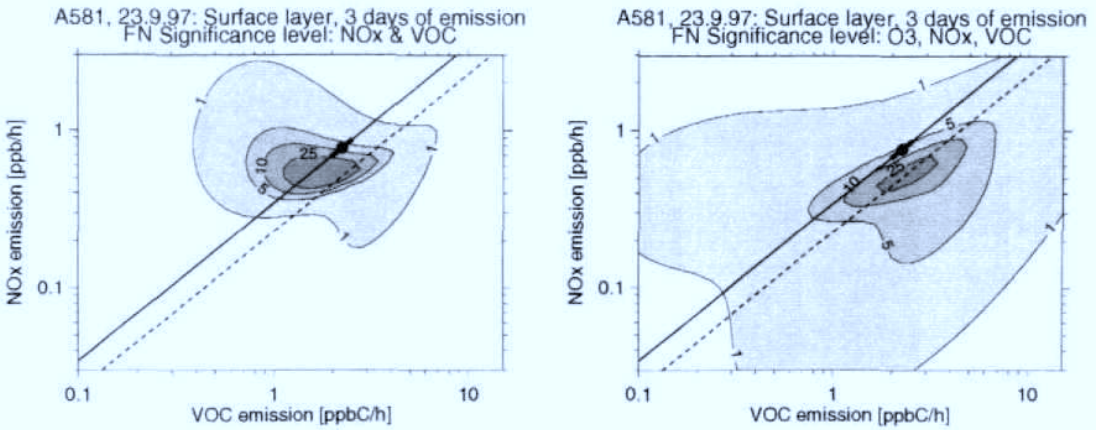

Figure 9.2: Like Figure 9.1, but for the class SL. Due to the limited number of samples in this class, no results for 5 and more parameters exist.

Thus the multivariate non central F-distribution, though it gives a correct description of the tested hypothesis, yield a good test parameter only when the number of samples is sufficiently larger than the number of tested parameters.

9.3 Composite images of cloud brightness temperatures and example trajectory cluster boxes

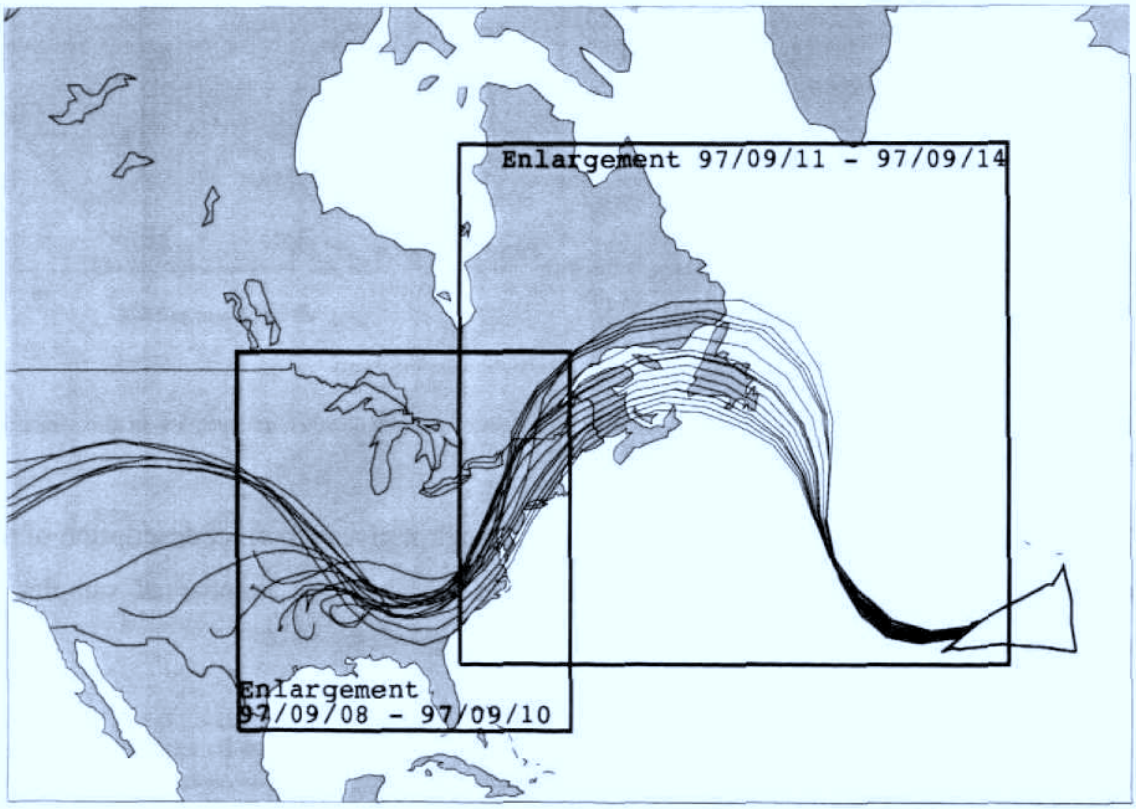

Figure 9.3: Map of the area of investigation. Shown are the mean position of the example trajectories included in the analysis, and the flight track. Marked by boxes are the enlargement areas shown in the composite images of GOES-8 cloud brightness temperatures and trajectory boxes, for the days 97/09/08 – 97/09/10 (Figure 9.5 and 9.6), and the days 97/09/11 – 97/09/14 (Figure 9.7 and 9.8)

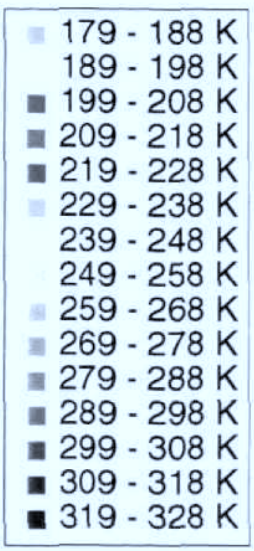

Figure 9.4: Colourtable of the cloud brightness temperatures shown in Figure 9.5 – 9.8.

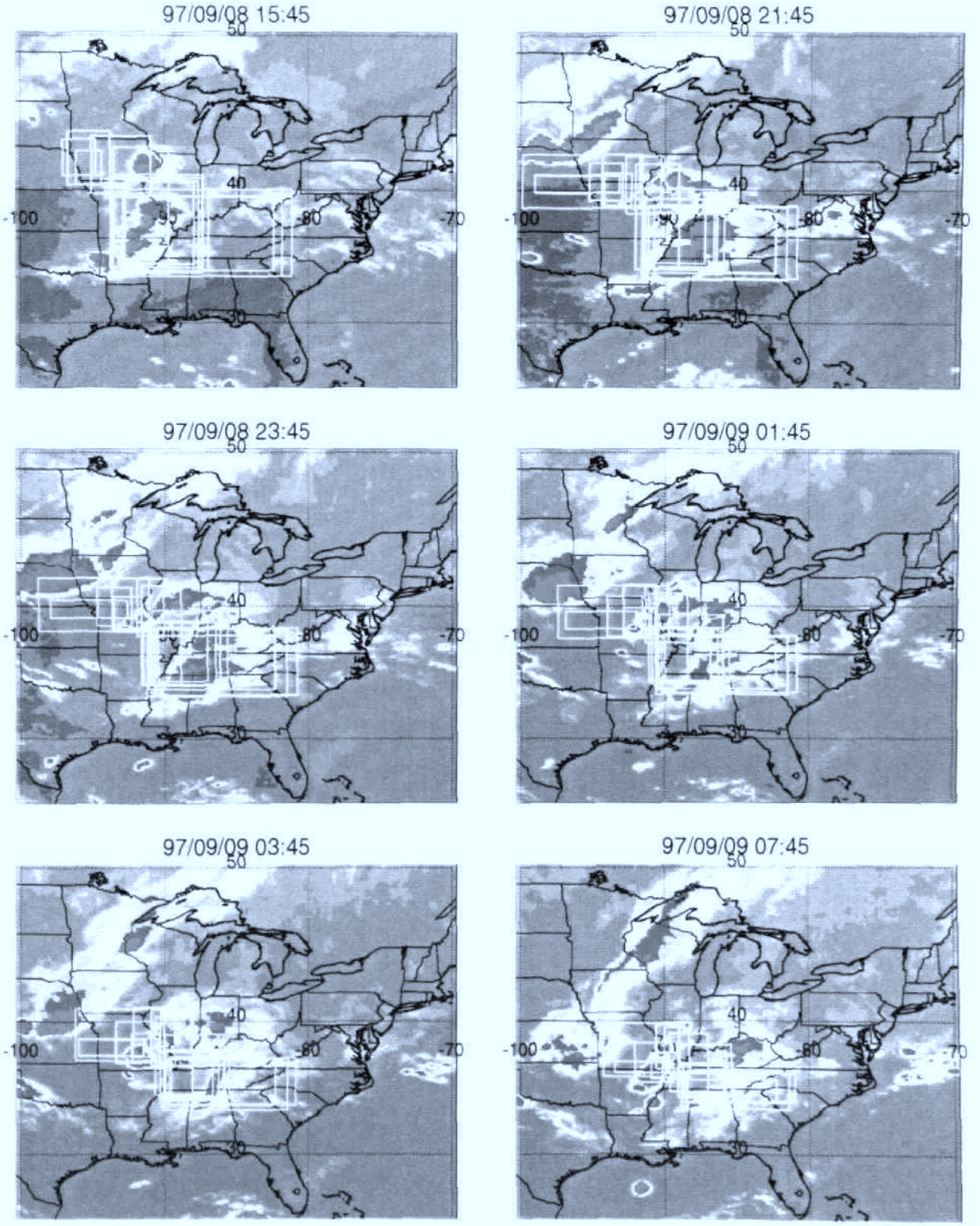

Figure 9.5: Composite images of GOES-8 cloud brightness temperatures and example trajectory cluster boxes for corresponding to the polluted layer in the FT. The respective date and time is given in the header.

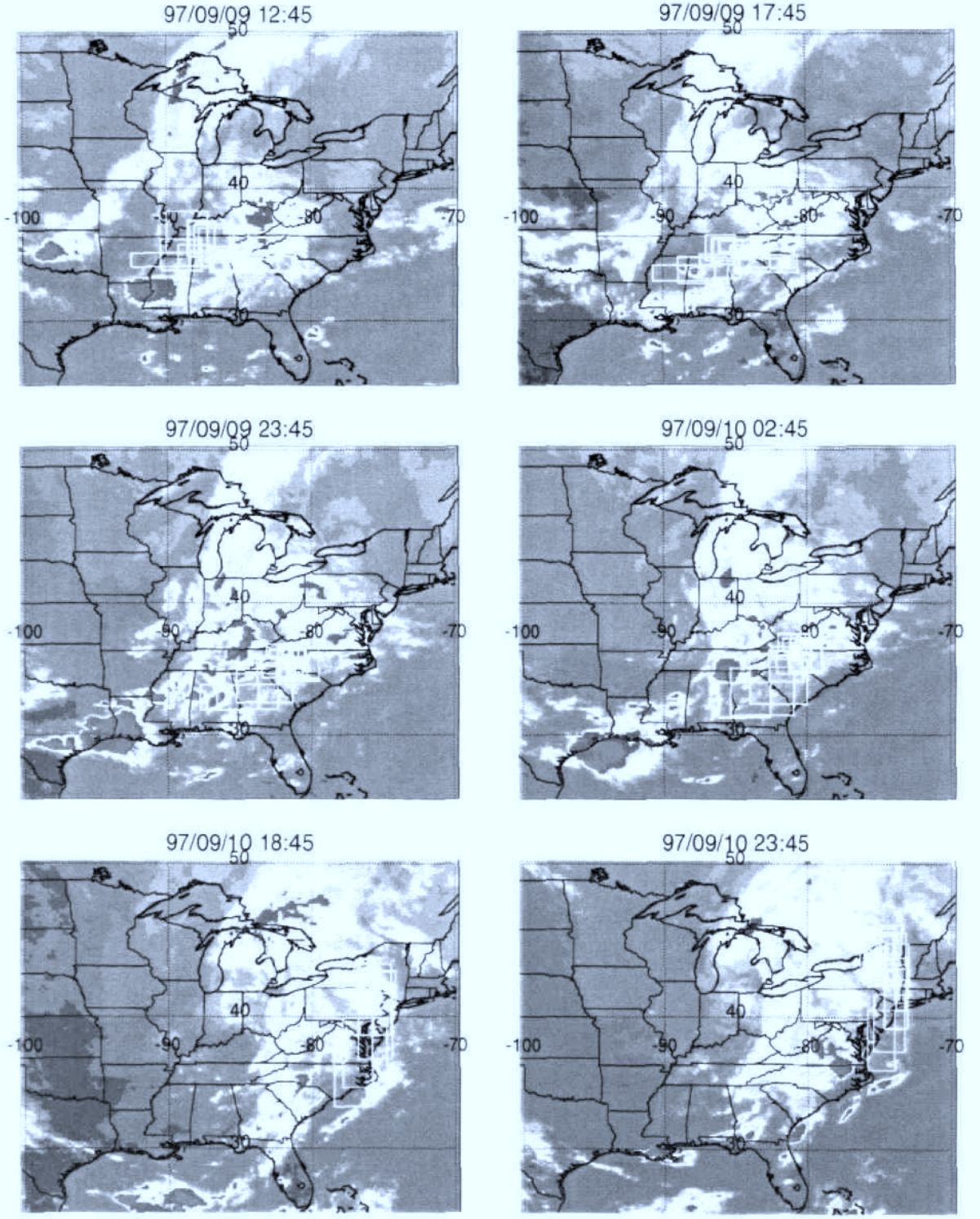

Figure 9.6: Composite images of GOES-8 cloud brightness temperatures and example trajectory cluster boxes for corresponding to the polluted layer in the FT. The respective date and time is given in the header.

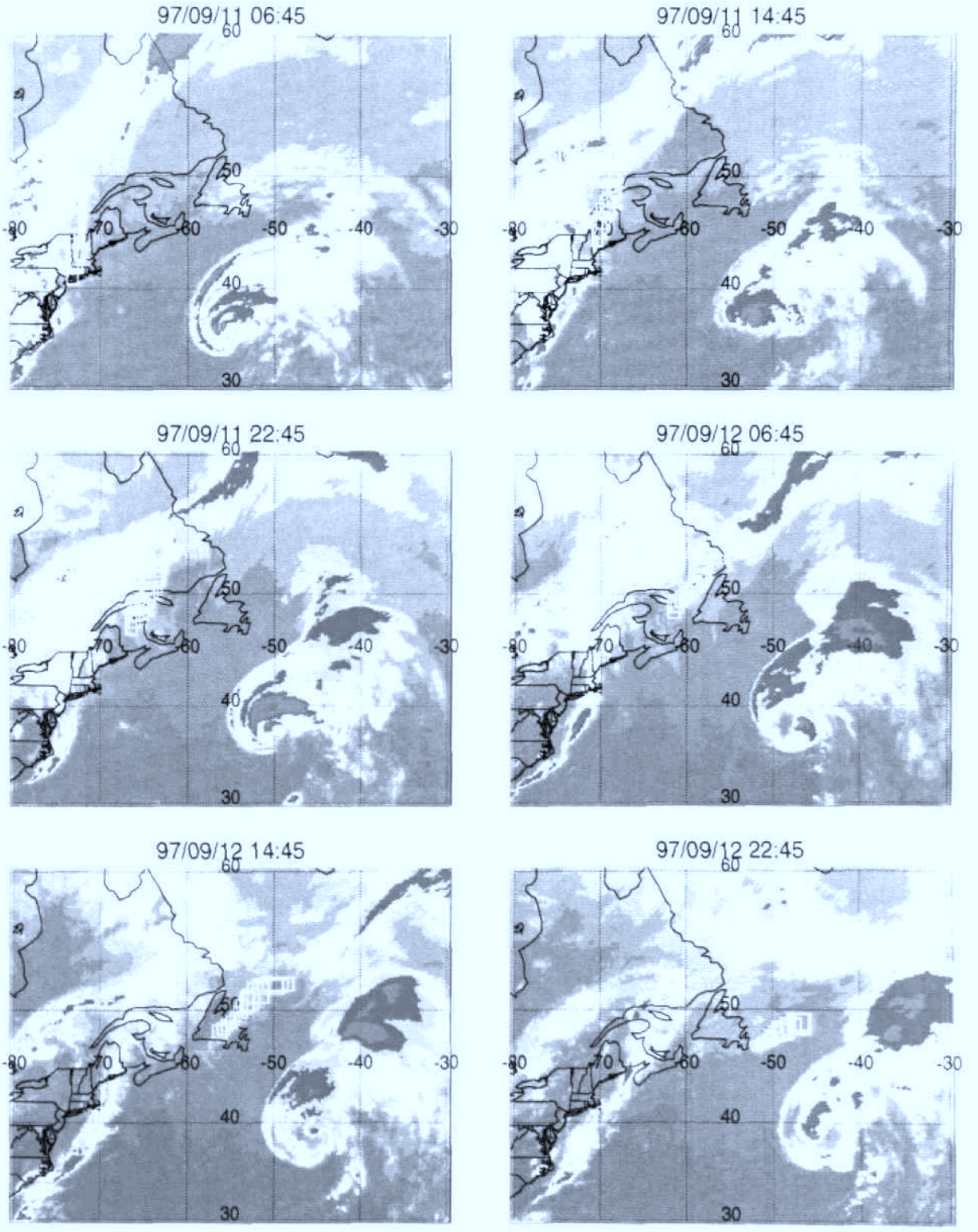

Figure 9.7: Composite images of GOES-8 cloud brightness temperatures and example trajectory cluster boxes for corresponding to the polluted layer in the FT. The respective date and time is given in the header.

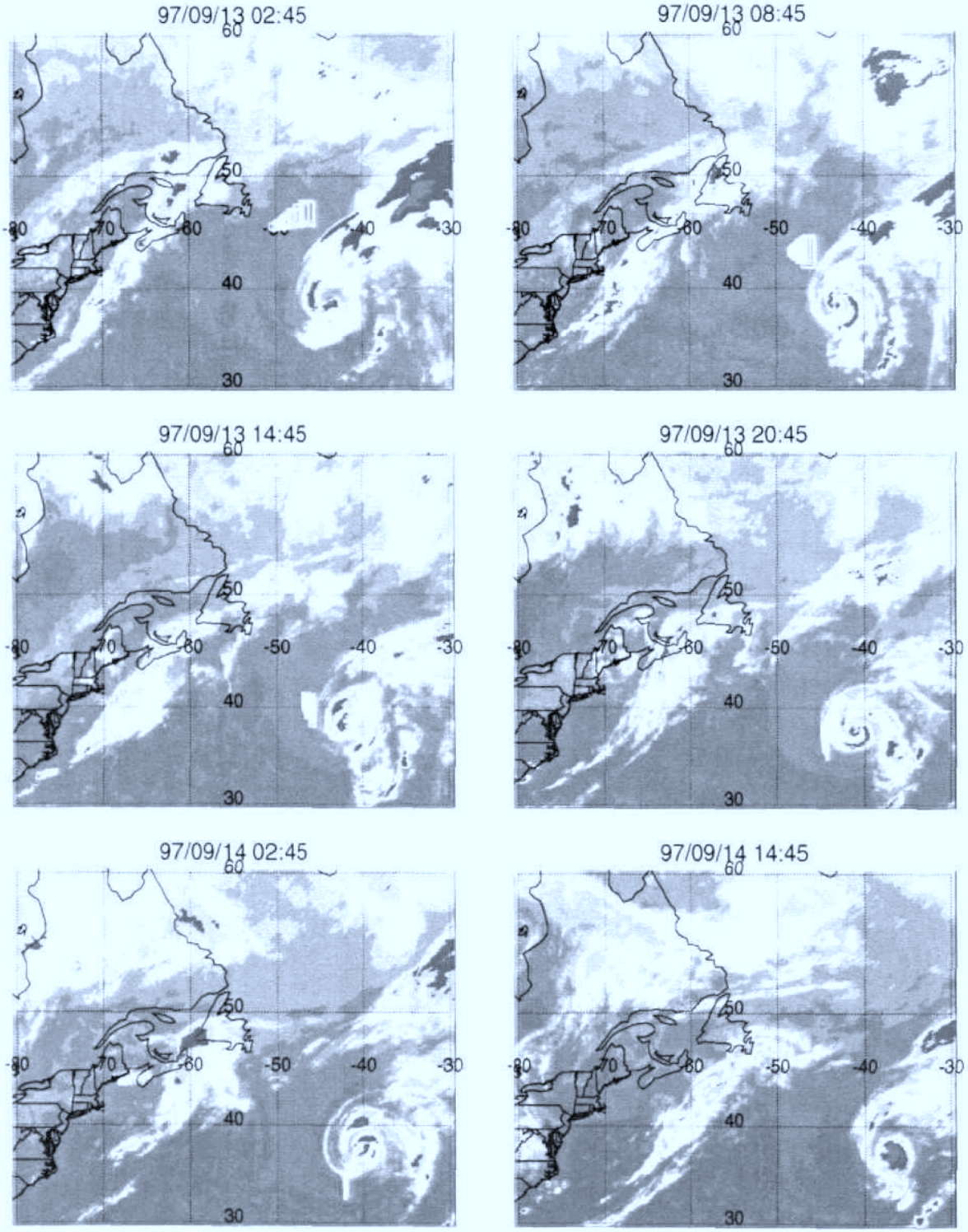

Figure 9.8: Composite images of GOES-8 cloud brightness temperatures and example trajectory cluster boxes for corresponding to the polluted layer in the FT. The respective date and time is given in the header.

9.4 List of abbreviations

ACSOE	Atmospheric Chemistry Studies in Oceanic Environment, UK project
AIRS	Aerometric Information Retrieval System
ASP	Air sampling pipe
ECMWF	European Centre for Medium-range Weather Forecasting
EKMA	Empirical Kinetic Modelling Approach
EMEP	Co-operative Program for Monitoring and Evaluation of the Long Range Transmission of Air Pollutants in Europe
EPA	U.S. Environmental Protection Agency
FT	Free troposphere
FZJ	Forschungszentrum Jülich
GEIA	Global Emission Inventory Activity
GENEMIS	Generation of European Emission Data for Episodes
GMT	Greenwich Mean Time
HO_x	$OH + HO_2$
LFC	Level of free convection
MAPS	Measurement of Air Pollution from Satellite
MCC	Mesoscale convective complex
MELCHIOR	Modéle Lagrangien de la Chimie de l'Ozone l'Èchelle Régionale
MH	Mixing height
MOZAIC	Measurement of ozone and water vapour by airbus in-service aircraft
MPBL	Mid planetary boundary layer
MRF	Meteorological Research Flight
NAPAP	National Acid Precipitation Assessment Program
NILU	Norwegian Institute for Air Research
NOAA	National Oceanic and Atmospheric Administration
NO_x	$NO + NO_2$
O_x	$O_3 + NO_2$
PAN	Peroxyacetylnitrate
PBL	Planetary boundary layer
PMT	Photo multiplier tube
RACM	Regional Atmospheric Chemistry Mechanism
RADM2	The second generation Regional Acid Deposition Model

RF	Resonance fluorescence
SL	Surface layer
TACIA	Testing Atmospheric Chemistry in Anticyclones, EU project
TDLAS	Tunable diode laser absorption spectroscopy
UEA	University of East Anglia
UKMO	United Kingdom Meteorological Office
VOC	Volatile Organic Compound
VURF	Vacuum ultraviolet resonance fluorescence

Acknowledgements

First of all, I wish to acknowledge the support of Prof. Dr. D. Kley, my supervisor, who enabled the international collaborations, from which this thesis has largely benefited and which I enjoyed very much. Also I wish to thank him for his interest and helpful suggestions, as well as for his critical review of this thesis.

I wish to thank Prof. Dr. D. McKenna who kindly agreed to becoming co-referee of this work.

There are many other people who have helped make this thesis what it is. My warmest appreciation must go to Dr. Christoph Gerbig who first introduced me to this field and always helped me with advice and comment. I have very much enjoyed our joint work.

Heiner Geiß became more and more involved in this work, as it shifted from experimental to modelling problems, and I would especially like to thank him for his constant support and the many fruitful discussions.

Many of the diagrams and computations were prepared with the assistance of Sabine Schröder, for whose help and patience I am very grateful.

I would like to express my appreciation to Dr. Wolfgang Meier, who was able to understand my experimental ideas from a mathematical point of view, and with whose help statistical test methods became a central part of this thesis.

All my colleagues at the ICG-2 I would like to thank for their permanent cooperation.

Much of this work has been based on measurements collected during the TACIA and ACSOE programme. I wish to thank the people involved in this program, particularly those I have worked with in field campaigns. The MRF group I would like to thank for the fruitful collaboration and especially their hospitality, which made the field campaigns one of the highlights of my PhD.

An important and enjoyable part of this thesis was my research stay at the Service d'Aeronomie in Paris. I would especially like to thank Dr. Matthias Beekmann and Dr. Johanna Kowol-Santen, from whose collaboration I have greatly benefited.

The helpful comments and co-operation of many people from different institutions have been greatly appreciated. Particularly, I wish to thank all the people who helped to provide me with data without which this thesis would not have been possible.

I also owe a big "thank you" to Ian Dwyer for proof-reading this thesis.

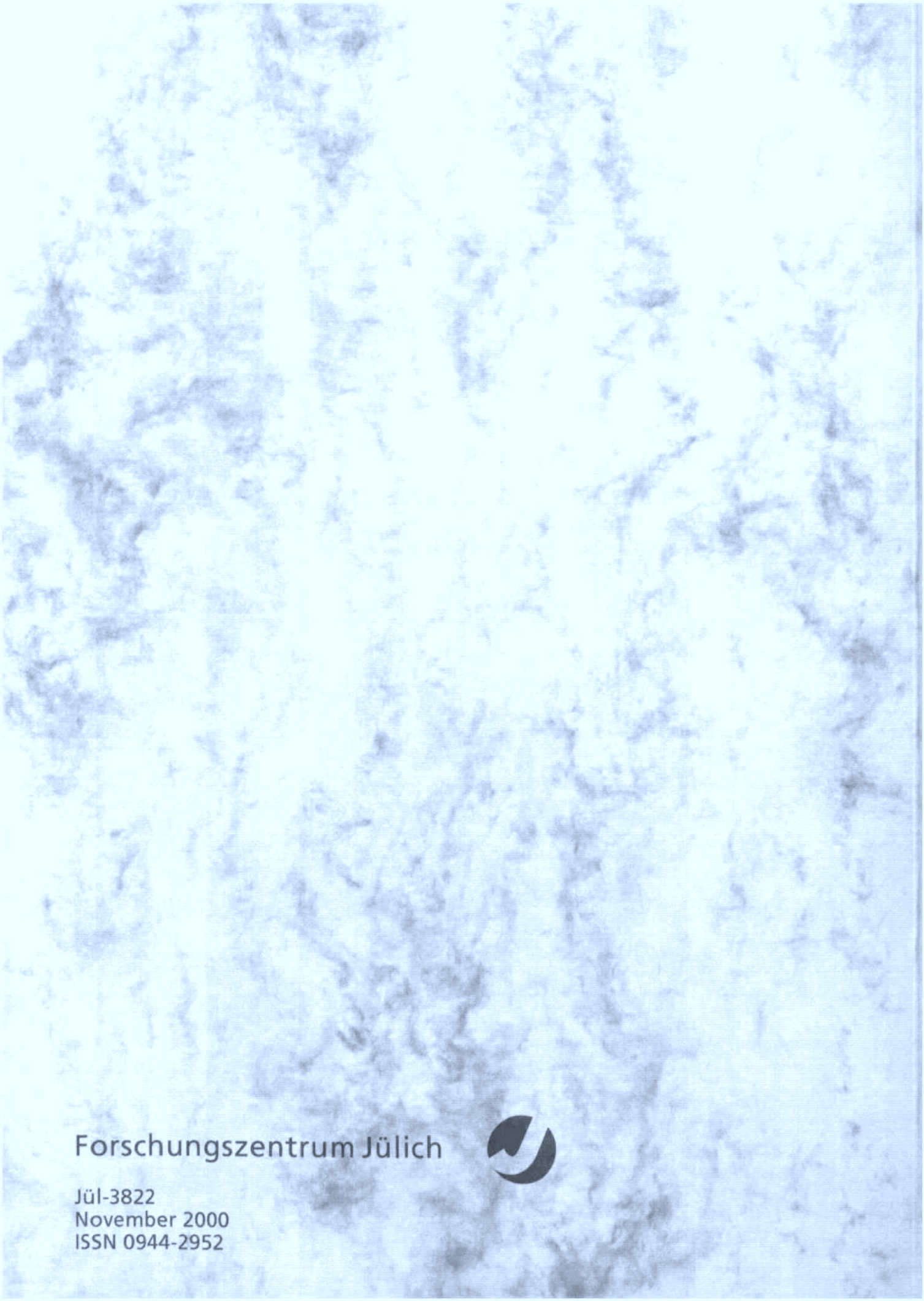

Forschungszentrum Jülich

Jül-3822
November 2000
ISSN 0944-2952